Load Testing, Analysis, and Design of a New Box Culvert Wing Tab

by

Pavlo Voitenko

A dissertation submitted to the Graduate Faculty of
Auburn University
in partial fulfillment of the
requirements for the Degree of
Doctor of Philosophy

Auburn, Alabama
August 4, 2018

Keywords: Culvert, Wing Wall, Soil-Structure Interaction, Finite Element, Plaxis 3D

Approved by

J. Brian Anderson, Chair, Associate Professor of Civil Engineering
Andrzej Nowak, Elton & Lois G. Huff Eminent Scholar, Professor of Civil Engineering
Robert W. Barnes, Associate Professor of Civil Engineering
James S. Davidson, Gottlieb Professor of Civil Engineering
Nathaniel B. Hardy, Assistant Professor of Entomology and Plant Pathology

Abstract

Culverts are critical hydraulic and transportation structures. They are often subjected to complex load conditions such as backfill earth pressure and traffic live load. Culverts may experience total and differential soil settlement of underlying soils, hydrostatic pressure, and aggradation/degradation scour. Any of these may lead to damage, usually in the form of cracking, often immediately after construction. One way to mitigate this problem is to alter the wing wall-to-culvert connection. This research project focused on studying the behavior of a new tabbed wing wall-to-culvert connection design and developing the design guidelines for it.

Three culverts with tabbed wing wall-to-culvert connection were constructed in Alabama. During the construction, earth pressure cells were installed on each tab to monitor the changes in the compression pressure that was generated within the tab. This data was used to support the numerical results in predicting the theoretical force normal to the tab surface.

The failure mechanism of the wing wall was studied using a non-linear three dimensional finite element analysis. A number of models with different geometries, material properties, design loads, and extreme events were developed. Stage analysis was used to replicate the construction process and model scour development. Distribution of stresses normal to the contraction joint surface and movement of the wing wall were

studied. These results were used to predict the maximum forces acting on the tab overlapping surface and state after which the wing wall can no longer perform its function.

The design procedure for the new wing wall tab design was developed to articulate with the AASHTO LRFD Bridge Design Specifications (2014). Load and resistance factors were determined using the reliability based procedure involving variability of soil and structure material parameters.

Acknowledgements

This dissertation is dedicated to my Wife and my Daughter who have been a great source of inspiration and support.

First, I would like to thank my incredibly supportive wife, Olga. Her encouragement and love always helped me to overcome all difficulties and find the right way in the darkest time. I want to thank my little girl, Sofia, whose appearance in my life provided unending inspiration. I feel fortunate to have them in my life.

I would like to express my sincere appreciation and gratitude to my advisor, Dr. J Brian Anderson for his support, guidance and mentorship throughout this research. He taught me to think out of the box and that the rational result is a derivative of all my thoughts and ideas despite their unrealities.

I would like to thank Dr. Andrzej Nowak for introducing me to the Reliability theory and valuable guidance and invaluable suggestions throughout this project. Thanks to Dr. James Davidson for his expert consultations and explanations of numerical modeling approaches and philosophies. I also want to thank Dr. Robert Barnes for his thorough guidance through the design of concrete structures and contributions for this project.

I would also like to acknowledge my partner in research, Herman Lester Lee. I appreciate all his assistance during field testing and shared materials, but more importantly, I appreciate his friendship.

My special gratitude goes to Dr. Eugene Gotsulyak, Dr. Alexander Gorodetsky, and Dr. Valeriy Maksymenko. They taught me that numerical results are only just numbers until the researcher gives them a meaning.

Finally, I would like to acknowledge the Alabama Department of Transportation for funding this research, and an opportunity to instrument three constructed culverts with tabbed wing wall connection.

Table of Contents

List of Tables

List of Figures

List of Abbreviations

ASD	Allowable Stress Design
CDF	Cumulative Distribution Function
CIP	Cast In-place Concrete
COV	Coefficient of Variation
DC	Dead Load of Structural Components
DW	Dead Load of Wearing Surface
EH	Horizontal Earth Fill Pressure
EV	Vertical Earth Fill Pressure
ES	Earth Structural Load
FE	Finite Element
HS	Hardening Soil
LS	Live Load Surcharge
LRFD	Load and Resistance Factor Design
MC	Mohr-Coulomb
SF	Safety Facto
SPT	Standard Penetration Test
WA	Water Pressure

Chapter 1. Introduction

Culverts play an important role in highway infrastructure as hydraulic and transportation structures. In certain conditions culverts may be more economically attractive than bridges or provide resistance to higher stream velocities or resistance to ice loading. Culvert failures are less critical in comparison to bridge failures due to smaller scale and location beneath the road embankment. Nevertheless, significant damage or failure of the culvert component may interrupt highway services (Scanlon 2012).

Culverts as a type of hydraulic structure are distinguished from bridges by being embedded into the soil (MNDOT 2000). When the structure is more than 10-ft wide in the direction parallel to the roadway, it is classified as a special category of bridge (MNDOT 2000, Scanlon 2012). This definition corresponds to the classification by ALDOT (2008) and FDOT (2011), except the maximum span length for a culvert should not exceed 20ft.

The retaining structures located on both sides of the culvert at the waterway opening are commonly referred to as wing walls and are key elements of a culvert. The primary functions of wing walls are to hold the backfill from the entrance and protect the soil from erosion (FHWA 1983). Unlike the culvert barrel, the wing walls are rarely directly affected by traffic loads. The wing wall is usually cast-in-place and situated at an angle to the box, and they are subjected to less lateral soil pressure than a retaining wall of the same size. Since the soil conditions are unique for each site, specifically designed CIP wing walls are recommended (FDOT 2011), but can also be precast. Wing walls may or may not be

attached to the headwall. However, for large culverts, the headwalls and wing walls should always be separated by a structural expansion joint (FHWA 1983).

During their service life, bridge type culverts are exposed to cycles of traffic load, hydrostatic pressures, and non-uniform soil pressures which can result in damage of the structural components and loss of serviceability. Since the backfill soil usually consists of different layered components (various types of soil), there is a probability of uneven settlement under the applied load. These deformations are often the cause of crack formation in culverts. Because of contact with the water under the roadway, these structures are subject to constant deterioration and therefore must be designed, constructed and maintained appropriately (Scanlon 2012).

1.1 Problem statement

Cracking along the vertical wing joint in newly built culverts was recently reported in Alabama (ALDOT 2012a). The culvert, located on AL49 near Dadeville, has cracked along the wing-to-tab joint after construction (Figure 1-1).

Figure 1-1. Culvert distress on AL 49 near Dadeville, AL

A second culvert, near Centerville, cracked after the formwork was removed and before backfill was placed (Figure 1-2). Uneven settlement of the soil foundation under

the culvert and wing wall, as well as inappropriate/inadequate curing, were reported as possible reasons for the rapid crack formation after construction.

Figure 1-2. Culvert distress near Centerville, AL

Substantial cracking, shown in

Figure 1-3, was noticed during an inspection of the large culvert 50-47-51.36 located 12 miles east of US 150 near Mitchell, IN. Part of the wing wall had many stress cracks at both ends/entrances of the structure. The vertical crack propagation led to the total failure of the wing wall-to-culvert connection. More cracks through the slab top at the northeast side were indicated during inspection with the maximum opening of ¼-in (INDOT 2012).

Figure 1-3. Large Culvert 50-47-51.36

Considering these distresses at the joint between headwall and wing wall, a new design proposed to disconnect the members to eliminate the stress transfer between them. The project described herein is a part of a larger overall effort by the Alabama Department of Transportation (ALDOT) to investigate a new method of culvert construction in response to crack formation often seen in newly built culverts immediately after construction.

1.2 Objectives

The proposed solution to the problem of cracking along the wing-to-culvert joint is by involves changing both the footing width and the wing wall-to-culvert connection (Figure 1-4). The new design eliminates the connection and leaves the wing wall to deflect separately from the barrel, as cantilever retaining wall with a pin support along one side.

The objectives of this study were to:

1. Determine the mechanism that causes cracking at the culvert to wing wall connection
2. Determine the critical stress distribution on the culvert wing tab surface
3. Develop an LRFD design procedure for the culvert wing tab to determine dimensions and reinforcing steel details
4. Develop reliability factors for the design procedure

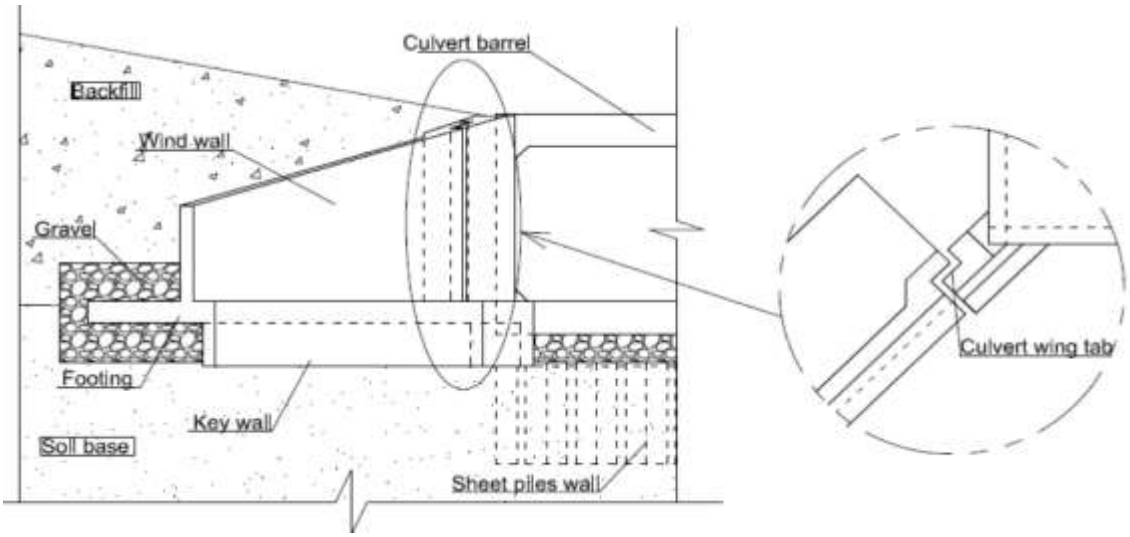

Figure 1-4. Front and plan view of the wing wall-to-culvert joint

1.3 Scope of Work

The research objectives were accomplished by the following scope of work:

1. A detailed literature review was conducted
2. Three dimensional finite element analysis was used to simulate culvert construction
    a. Numerical models were developed for three constructed culverts
    b. Stresses and displacements were determined along the tab surface for different stages of construction
    c. The procedure to evaluate the magnitude of shear force acting on the tab surface was developed using the results of numerical simulation
3. To evaluate the numerical model, the verification was performed with theoretical solutions and laboratory tests
    a. Lateral earth pressure distribution
    b. Behavior of interface element

    c. The material model was calibrated to simulate the behavior of filling material realistically

4. A field study was conducted in parallel to determine the stresses on the culvert tab at full scale under real conditions
5. The results of tasks 1-3 were used to develop a design procedure based on treating the culvert tab as a corbel
6. A reliability study was conducted
    a. Sensitivity analysis was performed to determine the impact of dimensions of the structure and main design material parameters
    b. The structural performance of three constructed culverts was evaluated in terms of reliability index
    c. The load and resistance factors were calculated for the culvert tab design using reliability procedure

Chapter 2. Background and Literature Review

2.1. Overview

Structural behavior of culverts under various loads depends on the category of the culvert. Culverts are categorized as arch, box, circular and masonry (Scanlon 2012).

The shape of a culvert depends mostly on hydrostatic conditions but mostly on depth and headwall elevation. All culverts may be divided into five main groups (ALDOT 2008; ConnDOT 2000):

- Pipe-Arch – not a typical structural shape that is mostly used for limited clearness and cover height. Usually made with the same materials as circular.
- Arches – bottomless, arch-shaped structures with natural stream bottom. Cast-in-place concrete is a preferable material.
- Box Section – rectangular or square (CIP or precast concrete) cross section can be adjusted to any site conditions. Because of angular corners, box cross-section is not hydraulically efficient in comparison with a circular.
- Multiple Barrels – common shape for wide waterways or low embankment. The walls between openings may cause clogging by catching debris.

Culverts are typically made of reinforced concrete (ConnDOT 2000). However, steel, and more recently, polyethylene, and reinforced plastic are used. In accordance with Coghlan, B. K. (1916) wooden, cast-iron, vitrified clay pipe and stone box culverts were used in construction. Concrete culverts, either cast-in-place (CIP) or precast, are preferable

over other materials due to relatively high resistance to applied loads, resistance to environmental hazards (such as corrosion or temperature changes during freeze-thaw periods) and low maintenance costs (FDOT 2011).

Depending on the complexity of the design, concrete culverts can be constructed with precast members or cast-in-place. While precast sections are standardized regarding their shape and the size, cast-in-place concrete construction can be specially designed to meet the in-situ requirements. Unlike precast, which are produced for several specific strength classes, CIP box culverts can be manufactured for various load and environmental conditions. In the case of CIP construction, box culverts are usually built on site using ready-mixed concrete. Thus, the structure can be constructed without joints that reduce the risk of corrosion (ConnDOT 2000; KYTC 2011). Since CIP culverts are designed for specific load conditions, additional reinforcement can be placed in high stress locations.

A number of cases of early cracking of the structural components of culverts were reported, as well as techniques to analyze the behavior of the damaged structure. Some culverts were instrumented and rehabilitated recently (Ahmed, B. et al. 2003; Hurd 1991; IODOT 2013; Musser 1995). Finite element modeling was used along with laboratory tests to investigate the behavior of these culverts. To understand the reasons that lead to structural distress numerical analysis was repeated multiple times for different material properties and load combinations.

2.2. Background

2.2.1. Earth pressure theory

Stand-alone culvert wing walls are retaining structures that protect backfill from eroding into the culvert entrance. Being fully disconnected from the culvert barrel, their

behavior is similar to cantilever retaining walls. To properly design and construct these structures, the lateral earth pressure acting on the retaining structures from the soil must be predicted. The lateral earth pressure estimate is based on the state of plastic equilibrium as defined by the Rankine (Rankine 1857), and the assumption that the active pressure develops in the soil on the heel side of the wall and the passive pressure on the toe side. The passive and active pressure develop with sufficient wall movement so that the full shear strength of the backfill soil occurs (Huntington 1957). The third type of soil pressure acting on the buried structures is At-Rest earth pressure which requires no wall movement.

The lateral earth pressures can be expressed as:

$$\sigma_h = K \cdot \sigma_v \qquad \text{Equation 2-1}$$

where:

σ_v – effective normal stress on the base: $\sigma_v = \gamma \cdot H$

γ – unit weight of soil

H – depth below the surface of earth

K – coefficient of lateral earth pressure

The coefficient of lateral earth pressure expresses the ratio of the effective horizontal stresses to the effective vertical stress. After natural or artificial compaction of backfill, the value of K takes the form of K_o known as the coefficient of earth pressure at rest. With the horizontal expansion of the soil, the value of K decreases until it becomes equal to K_A, known as an active earth pressure coefficient. The horizontal compression of the soil mass increases the value of K until it becomes equal to the passive earth pressure coefficient K_P (Terzaghi et al. 1996).

Distinctions between various methods to estimate the coefficient of lateral earth pressure are explained in this section.

2.2.1.1. At-Rest Earth Pressure Coefficient (K_0)

At-Rest earth pressure (Figure 2-1) is lateral pressure acting on a rigid body, represented by a horizontal earth pressure coefficient, K_0. For cohesionless soils, its value can be approximated using Equation 2-2. In cohesive soils, the lateral earth pressure will not be developed till some depth, so the K_0 can be calculated using elastic theory through Poisson's Ratio (Equation 2-3).

For cohesionless soils (Jaky 1948):

$$K_0 = 1 - \sin\varphi \qquad \textbf{Equation 2-2}$$

For cohesive soils (Tschebotarioff 1973):

$$K_0 = \frac{\nu}{1-\nu} \qquad \textbf{Equation 2-3}$$

For overconsolidated soil (Mayne and Kulhawy 1982):

$$K_0(OC) = K_0 \cdot OCR^{\sin\varphi} \qquad \textbf{Equation 2-4}$$

where:

φ – effective friction angle of soil

ν – Poisons ratio

OCR – overconsolidation ratio

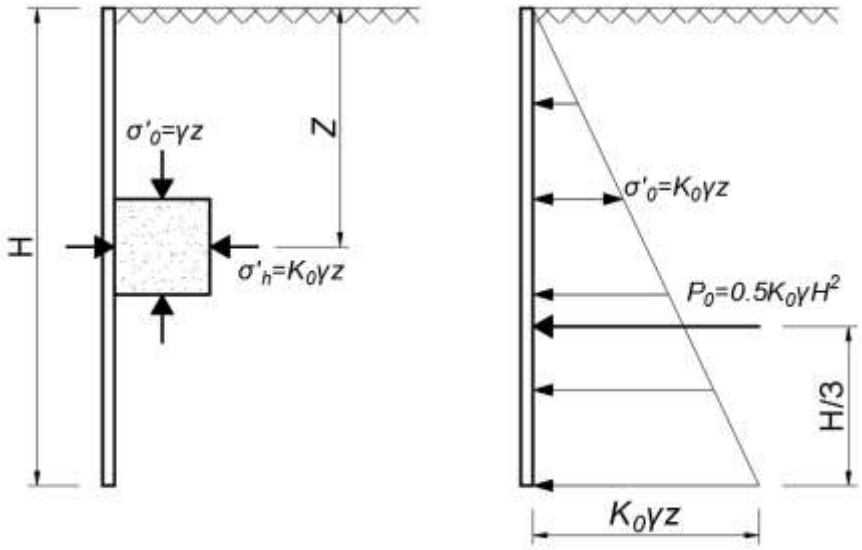

Figure 2-1. Distribution of lateral earth pressures at rest

2.2.1.2. Active and passive pressure (Rankine, Coulomb)

Active and Passive Earth Pressures (Figure 2-2) are the most significant stresses in retaining structure design. Active is an earth pressure on the retaining system that develops when the retaining structure tends to move away from the soil fill to the excavation. Unlike active, passive pressure is caused by the movement of structure elements toward the soil. Approximate ratios of these required movements relative to wall height are given in Table 2-1 of the AASHTO LRFD (2014).

Table 2-1. Approximate values of relative movements required to reach active or passive pressure conditions (*AASHTO LRFD* 2014)

Type of Backfill	Values of Δ/H	
	Active	Passive
Dense sand	0.001	0.01
Medium dense sand	0.002	0.02
Loose sand	0.004	0.04
Compacted silt	0.002	0.02
Compacted lean clay	0.010	0.05
Compacted fat clay	0.010	0.05

Coulomb (1776) and Rankine (1857) theories are most commonly used to determine active and passive earth coefficients. Coulomb theory states that in the active state of stress develops behind the wall and the soil within the failure wedge is in the state of plastic (force) equilibrium (Figure 2-2). The values of K_A and K_P are obtained assuming plane strain conditions, uniform shear resistance along the rupture surface, inclined wall geometry and friction develops between the wall and the soil.

The distribution of active (Figure 2-2) and passive pressure is linear with the resultant force acting at the distance of one-third of the wall height above its base.

$$K_A = \frac{\sin^2(\theta+\varphi)}{\sin^2\theta \cdot \sin(\theta-\delta) \cdot \left[1+\sqrt{\frac{\sin(\varphi+\delta)\cdot\sin(\varphi-\beta)}{\sin(\theta-\delta)\cdot\sin(\theta+\beta)}}\right]^2} \qquad \textbf{Equation 2-5}$$

$$K_P = \frac{\sin^2(\theta+\varphi)}{\sin^2\theta \cdot \sin(\theta+\delta) \cdot \left[1-\sqrt{\frac{\sin(\varphi+\delta)\cdot\sin(\varphi-\beta)}{\sin(\theta+\delta)\cdot\sin(\theta+\beta)}}\right]^2} \qquad \textbf{Equation 2-6}$$

where:

φ - friction angle of soil

δ - friction angle between fill and wall

β - the angle of fill to the horizontal

θ - the angle of the back face of the wall to horizontal

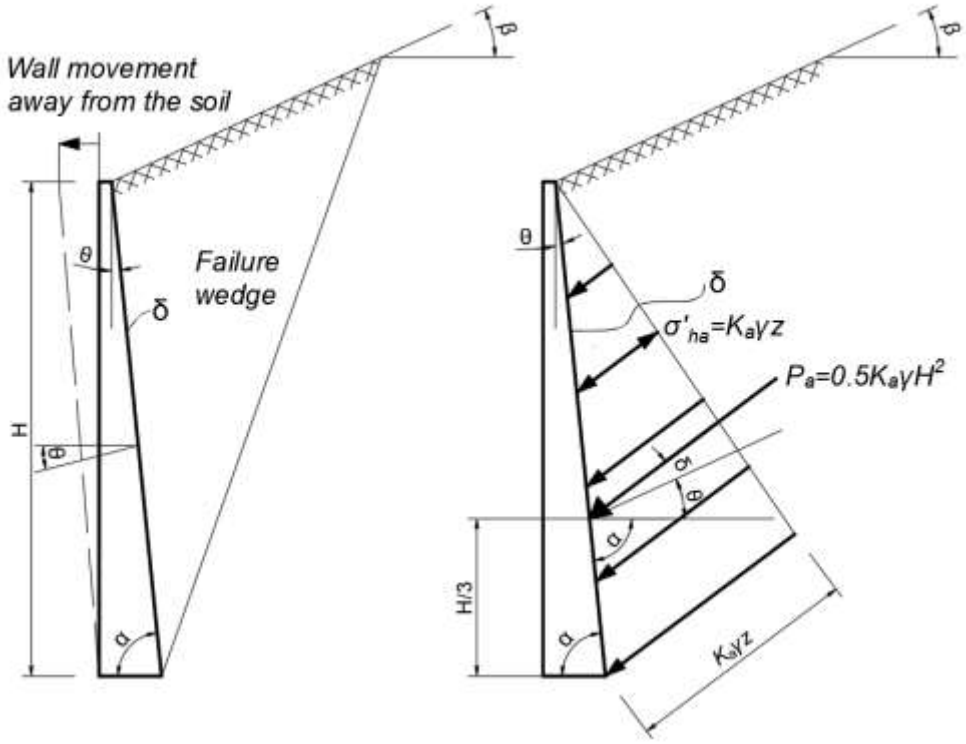

Figure 2-2. Failure wedge and distribution of lateral active Coulomb earth pressures

Rankine's theory was developed considering the same assumptions as Coulomb, except the frictionless interface between soil and the structure. Without soil - structure friction the resultant force from active earth pressure is parallel to backfill surface (Figure 2-3). The failure happens when one of the principal stresses reaches the maximum compression stress (Bruner et al. 1983). The limitation of this theory for the structures with substantial wall friction (Rankine 1857).

The Rankine equation for the coefficients of active and passive earth pressure with inclined backfill are:

$$K_A = \cos\beta \cdot \left[\frac{\cos\beta - \sqrt{(\cos^2\beta - \cos^2\varphi)}}{\cos\beta + \sqrt{(\cos^2\beta - \cos^2\varphi)}} \right] \quad \textbf{Equation 2-7}$$

$$K_P = \cos\beta \cdot \left[\frac{\cos\beta + \sqrt{(\cos^2\beta - \cos^2\varphi)}}{\cos\beta - \sqrt{(\cos^2\beta - \cos^2\varphi)}} \right] \quad \textbf{Equation 2-8}$$

where:

φ - friction angle of soil;

β - the angle of fill to the horizontal

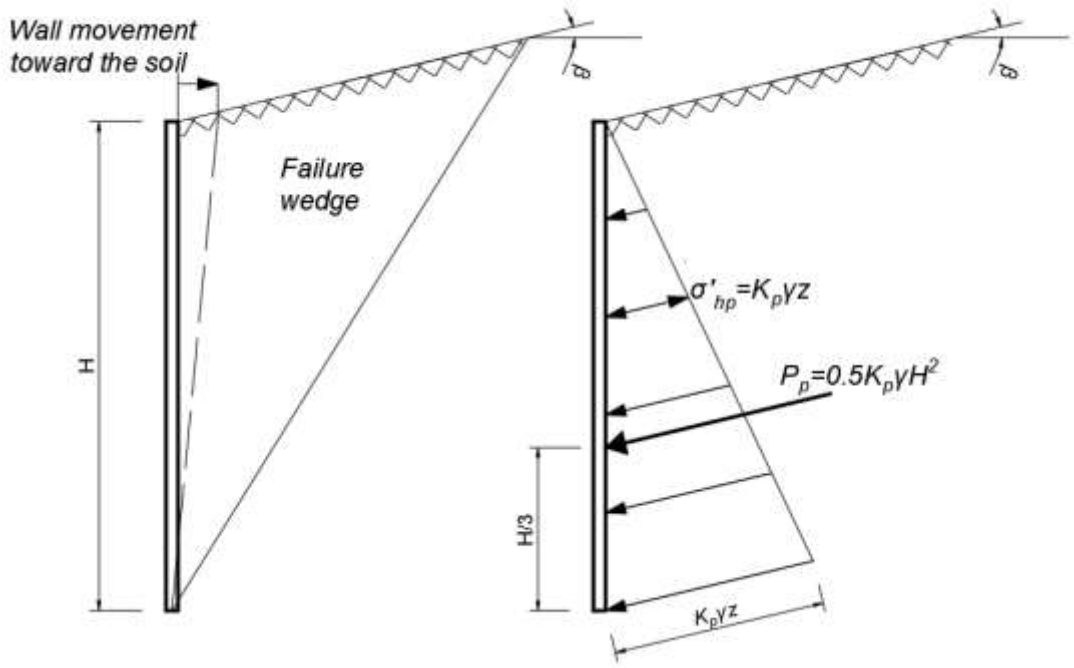

Figure 2-3. Failure wedge and distribution of lateral passive Rankine earth pressures

AASHTO LRFD (2014) allows either Coulomb theory or Rankine theory be used to calculate the value of lateral earth pressure coefficient. It is recommended to neglect any contribution from passive earth pressure in stability calculations as its development requires up to ten times larger movement then for active pressure. Exceptions may be made for the cases when the structure is deeper than the theoretical depth of the soil that could be weakened or removed due to scour, erosion, freeze-thaw, or any other means. In the

calculations, only the effective embedment depth, the depth below the disturbed soil, shall be considered (*AASHTO LRFD* 2014).

2.2.1.3. Surcharge Load

Surcharge loads are additional vertical loads acting on the soil behind the retaining structure. By its definition, these can be permanent loads (dead load) or temporary (live loads). The dead loads are caused by the soil layers above the top of the wall (backfill), adjacent structures or pavement. Live loads mostly result from highway traffic or parked cars.

The theory of elasticity can be used to estimate the lateral pressure from point (Figure 2-4a), line (Figure 2-4b), strip (Figure 2-4c), and uniform surcharge loads (Bowles 1988). The equations developed by Boussinesq (1885), for rigid structures, are incorporated in AASHTO LRFD (2014) to estimate the horizontal pressure from these loads. This approach involves the load position in respect to the structure and Poisson's Ratio to characterize the soil.

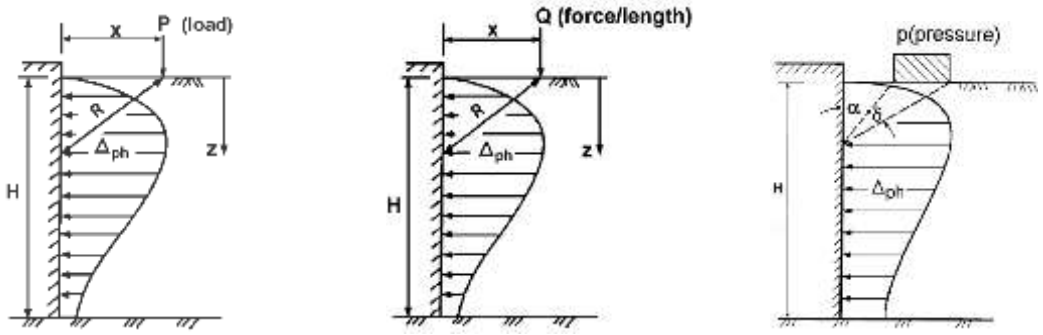

a b c

Figure 2-4. Horizontal pressure on the wall (*AASHTO LRFD*, 2014)

For a uniformly distributed load, the horizontal pressure can be calculated using the coefficients of lateral earth pressure (*AASHTO LRFD* 2014):

$$\Delta_p = K_s \cdot q_s \qquad \textbf{Equation 2-9}$$

where:

q_s – uniform surcharge load.

K_s – coefficient of earth pressure due to a surcharge load. Can be equal to K_o, K_A, K_P depending on the case.

The horizontal pressure on the wall from the point load (Figure 2-4a) can be calculated, as (*AASHTO LRFD* 2014):

$$\Delta_{ph} = \frac{P}{\pi \cdot R^2} \cdot \left[\frac{3 \cdot Z \cdot X^2}{R^3} - \frac{R \cdot (1 - 2 \cdot \nu)}{R + Z} \right] \qquad \textbf{Equation 2-10}$$

where:

P – point load

R – radius distance from the point of load application to the considering point on the wall as shown on Figure 2-4a

X – distance from the wall to the point of load application

Z – depth to the considering point on the wall

ν – Poisson's ratio

The horizontal pressure on the wall from the infinitely long line load (Figure 2-4b) can be calculated, as (*AASHTO LRFD* 2014):

$$\Delta_{ph} = \frac{4 \cdot Q}{\pi} \left[\frac{Z \cdot X^2}{R^4} \right] \qquad \textbf{Equation 2-11}$$

where:

Q – line load

The horizontal pressure from the uniformly loaded strip (Figure 2-4c) parallel to the wall can be calculated, as (*AASHTO LRFD* 2014):

$$\Delta_{ph} = \frac{4 \cdot p}{\pi}\left[\delta - \sin\delta \cdot \cos(\delta + 2\alpha)\right] \qquad \textbf{Equation 2-12}$$

where:

p – uniform load on a strip

α, δ – angles shown on Figure 2-4c

2.2.1.4. Hydrostatic Load

The typical design of retaining structures, which do not retain any water, eliminate the development of hydrostatic pressure on the wall (*AASHTO LRFD*, 2014). However, in case the groundwater level increases due to flooding, heavy rain or any other event, the hydrostatic pressure can develop behind an undrained wall (Figure 2-5). Since water does not change volume under the applied load, it generates equal stresses in all directions. Thus, the water pressure develops linearly with increasing the depth (Bowles 1988).

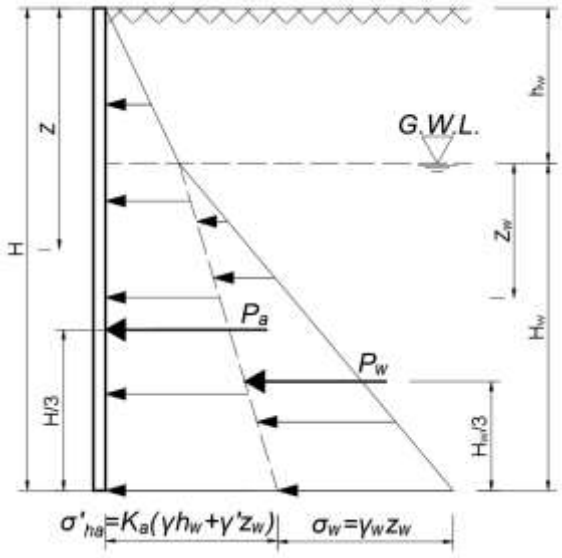

Figure 2-5. Lateral pressure from groundwater table

2.2.2. Scour

The erosion of soil due to the flow of water in the stream bed is often referred as scour (Arneson et al. 2012). Scour can be characterized as:

- Aggradation. Defined by an overall increase of the stream bed due to the accumulation of sediments.
- Degradation. Unlike aggradation, is a decrease of the stream bed height due to erosion by the stream flow.
- Contraction scour. It occurs with the presence of a structure in the stream. A structure interrupts the natural stream flow forcing it to change direction and speed.
- Local scour. Refers to the scour due to increasing water acceleration around the structure that obstructs the flow.

AASHTO LRFD (2014) defines the Extreme Event II (Table 2-2) load combination to analyze structural stability of the culvert due to scour. The possible scour depth should be estimated by hydraulic and subsurface exploration if the structure located in a flood prone area. Also, the provisions of Section 2.6.4.4.2 of AASHTO LRFD (2014) shall be applied for the design against scour.

In this study, a scour is considered as an extreme event that may damage or render the disconnected wing wall unserviceable. To investigate the effect of scour, soil elements were incrementally removed beneath the wing wall.

2.2.3. Design of Retaining Structures

The traditional design of a cast in place box culvert considers the culvert and wing wall integral as one system (*AASHTO LRFD* 2014; IODOT 2013; NYSDOT 2012). The

connection between the culvert and wing walls may be designed with or without an expansion joint. However, while culvert barrels are designed similar to bridges (*AASHTO LRFD* 2014), wing walls are usually designed as cantilevered retaining walls to resist out-of-plane backfill pressures (FHWA 1983).

Wing walls, as cantilever retaining walls, are designed for the strength and extreme event limit states (*AASHTO LRFD* 2014). The strength limit state includes calculation of structural failure, bearing capacity failure (Figure 2-6a), lateral sliding (Figure 2-6b), and loss of base contact due to eccentric loading (Figure 2-6c). At the extreme event limit state, the structure shall be investigated for overall stability failure (Figure 2-6d).

Overturning stability analysis is accomplished by comparing the moments produced by the force that tends to overturn the wall and the moments of the resisting forces. As it is specified in Section 11.6.3.3 of AASHTO (2014), the resultant eccentricity of the loads acting on the structure determines the overturning resistance of the structure. The allowable eccentricity e is limited to 1/6 of the footing width B on either side of the center of footing (Figure 2-7).

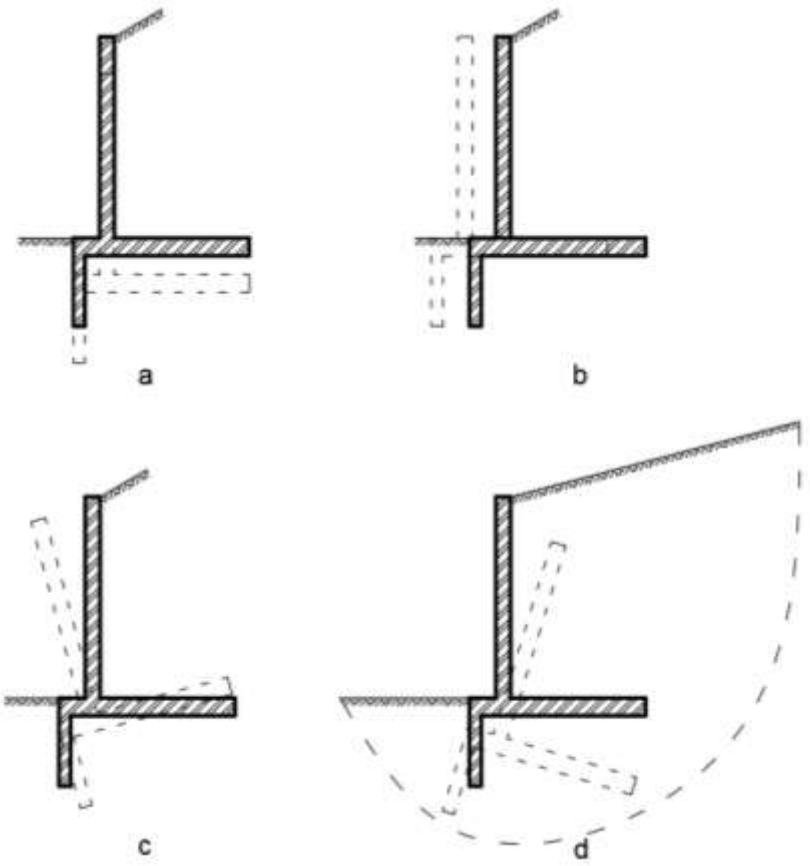

Figure 2-6. Forms of stability failure: a) sliding, b) overturning, c) bearing d) and overall

The dimensions of the footing should be prescribed to provide sufficient contact surface to distribute the acting pressure without exceeding the bearing capacity of the soil. Bearing resistance shall be evaluated in accordance with the provisions of Section 11.6.3.2 of AASHTO LRFD (2014). For retaining structures supported by a soil foundation, the stress distribution under the footing should be assumed uniformly distributed (Figure 2-7) and calculate as follows:

$$\sigma_v = \frac{\sum V}{B - 2 \cdot e} \qquad \textbf{Equation 2-13}$$

where:

ΣV – Summation of vertical forces

B – Footing base width

e – eccentricity

The factored bearing resistance q_r shall be calculated in accordance with Section 10.6.3.1 of AASHTO (2014) using following equation:

$$q_r = \phi_b \cdot q_n > \sigma_v \qquad \textbf{Equation 2-14}$$

where:

q_r – Factored bearing resistance

q_n – Nominal bearing resistance (AASHTO 10.6.3.1.2a-1)

σ_v – Vertical stress (Equation 2-13)

The sliding failure limit state of CIP cantilever walls prevents the excessive movement of the structure. The safety margin is provided by reducing the shear resistance along the interface through the load factor. The factored resistance against failure shall be calculated following the provision of Section 10.6.3.4 of AASHTO LRFD (2014):

$$R_r = \phi R_r = \phi_\tau R_\tau + \phi_{ep} \mathrm{R}_{ep} \qquad \textbf{Equation 2-15}$$

where:

R_r – Factored resistance against failure by sliding

R_n – Nominal sliding resistance against failure by sliding

ϕ_τ – Resistance factor for shear between soil and foundation

R_τ – Nominal sliding resistance between soil and foundation (AASHTO LRFD Eq. 10.6.3.4-2)

ϕ_{ep} – Resistance factor for passive resistance

R_{ep} – Nominal passive resistance of soil throughout the life of the structure

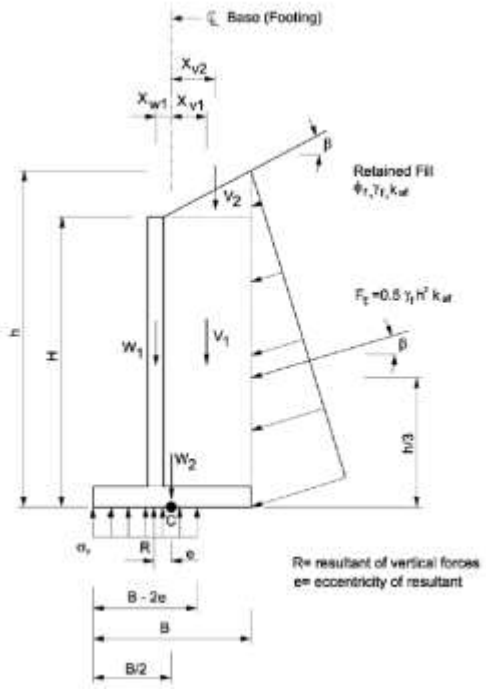

Figure 2-7. Bearing stress criteria for CIP cantilever walls on soil (*AASHTO LRFD 2014)*

The resistance provided by passive earth pressure R_{ep} should be neglected in the design if the soil in front of the wall can be removed due to erosion.

The global stability of a cantilever wall is closely related to the failure of the retained slope. Thus, a stability analysis must be performed to produce a single factor of safety *FS* as specified in Section 10.6.2.3 of AASHTO LRFD (2014). The resistance factor *φ d*epends on the quality of in-situ soil investigation and obtained geotechnical parameters as well as on presents of surcharge elements. It can take the value of 0.75 for well-defined soil parameters and 0.6 in case of limited information.

The loads considered in wing wall design (Figure 2-8), are the following:

- self weight, dead load of structural components (DC)
- self weight of future wearing surface (DW)

- vertical earth pressure (EV)
- horizontal earth pressure (EH)
- earth surcharge load (ES)
- water pressure (WA)
- live load (LL)

Load factors for considered load combinations are outlined in Section 3.4.1 of AASHTO LRFD (2014) and summarized in Table 2-2. Load factors for Strength I and Extreme II load combinations are applicable for sliding and eccentricity limit states analysis. The notations “a” and “b” refer to minimum and the maximum values of load factors, respectively. The minimum load factors were applied to the vertical loads representing resistance while maximum load factors, to the horizontal loads, which represent load component in the design formula. For the bearing limit state, maximum load factors for both vertical and horizontal loads applied depending on Strength Ib, Extreme IV, and Extreme IIb load combinations (*AASHTO LRFD* 2014).

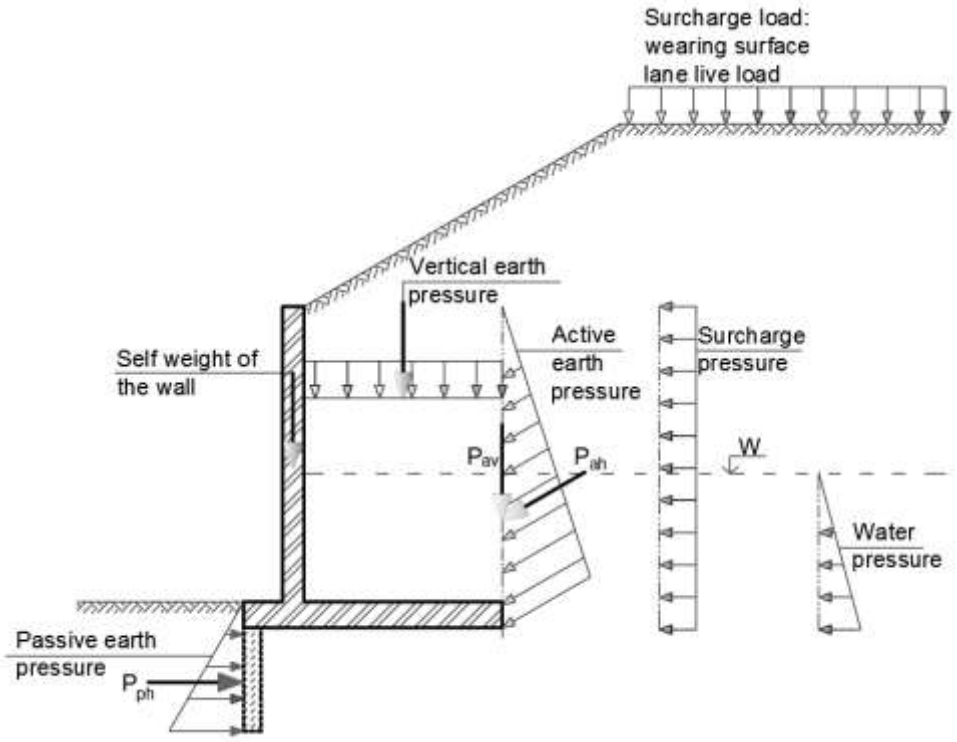

Figure 2-8. Considered load components

Table 2-2. Load factors

Load Combination Limit State	Load factors					Application
	DC, γ_{DC}	EV, γ_{EV}	LL_V, γ_{LL_V}	LL_H, γ_{LL_H}	EH, γ_{EH}	
Strength Ia	0.90	1.00	-	1.75	1.50	Sliding, Eccentricity
Strength Ib	1.25	1.35	-	1.75	1.50	Bearing, Strength, Design
Strength IV	1.50	1.35	-	-	1.50	Bearing, Strength, Design
Extreme IIa	0.50	1.00	-	-	-	Sliding, Eccentricity
Extreme IIb	1.25	1.35	-	-	-	Bearing

Geotechnical resistance factors for shallow foundations specified in Section 10.5.5.2.2. of AASHTO LRFD (2014) depend on soil type and type of concrete wall. Applicable factors for bearing and sliding limit states are summarized in Table 2-3.

Table 2-3. Resistance factors for geotechnical resistance (*AASHTO LRFD*, 2014)

Method/Soil/Condition			Resistance Factor
Bearing Resistance	ϕ_b	Theoretical method (Munkafakh et al., 2001), in clay	0.5
		Theoretical method (Munkafakh et al., 2001), in sand, using CPT	0.5
		Theoretical method (Munkafakh et al., 2001), in sand, using SPT	0.45
		Semi-empirical method (Meyerhof, 1957), all soils	0.45
		Footing on rock	0.45
		Plate Load Test	0.55
Sliding Resistance	ϕ_τ	Cast-in-Place Concrete on sand	0.8
		Cast-in-Place Concrete on clay	0.85
	ϕ_{ep}	Passive earth pressure component of sliding resistance	0.5

2.2.4. Corbel Design

A corbel (Figure 2-9) is a short cantilever reinforced concrete member, cast monolithically with the column or wall element, used to support concentrated loads or beam reactions. The potential failure modes of a corbel are (Mattock 1976; Powell and Foster 1996):

- yielding of a tensile tie due to a combination of the flexural and axial load
- shear interface failure of the contact surface with the column
- flexural failure leading to the diagonal splitting of the concrete
- splitting of the end anchorage of the tensile tie

In accordance with design provisions summarized in Section 5.13.2.4 of AASHTO LRFD (2014), the potential failure modes of corbels include the loss of flexural or shear

capacity, crushing or splitting of the compression strut and failure of the end anchorage of the tensile tie. Failure modes of corbels are shown in Figure 2-10. A shear crack occurs near the point of application of the concentrated force and propagates to the bottom corner of the corbel interface (Figure 2-10a). It can also start at the upper corner of the tab and proceed vertically to the bottom fiber (Figure 2-10b). Failure due to the splitting of concrete around the tensile reinforcement may occur if the anchorage length is insufficient (Figure 2-10c). Inadequate proportions of the tab can result in failure due crushing of the concrete under concentrated load (Figure 2-10d) (Ashari 2014; Mattock 1976).

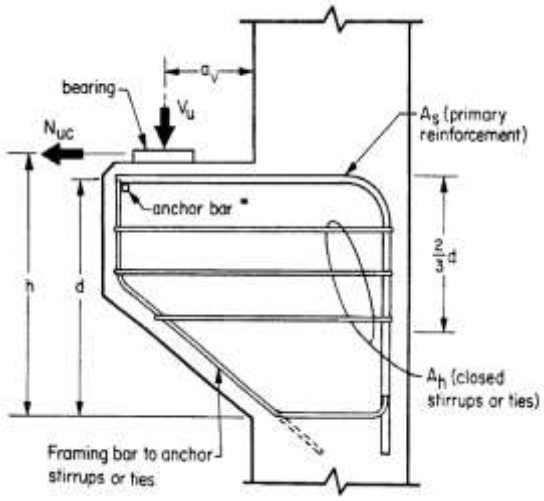

Figure 2-9. Corbel with typical reinforcement (*AASHTO LRFD* 2014)

General provisions for corbel design are laid out by AASHTO (*AASHTO LRFD* 2014) as follows:

- The position of ultimate shear force a_v should not be greater than the effective depth d of the corbel section.
- The section at the face of support shall be designed to simultaneously resist a factored shear force V_u, factored moment M_u, and horizontal tensile force N_{uc}.

- The magnitude of horizontal tensile force N_{uc}, unless any specific provisions applied, shall not be taken less than $0.2V_u$.
- The area of reinforcement A_{vf} to resist factored shear force shall be calculated using the provisions of Section 5.8 of AASHTO LRFD (2014).
- The area of reinforcement A_n to resist factored horizontal tensile force shall be calculated using the provisions of Section 5.13 of AASHTO LRFD (2014).
- The area of main reinforcement A_s shell be calculated using the provisions of Section 5.13 of AASHTO LRFD (2014).
- The area of closed stirrups A_h shell be calculated using the provisions of Section 5.13 of AASHTO LRFD (2014).
- The reinforcement ratio ρ sell not be smaller than the ration $0.04(f_c'/f_y)$ as specified in the provisions of Section 5.13 of AASHTO LRFD (2014).
- The tensile reinforcement shall be anchored in accordance with provisions of Section 5.11 of AASHTO LRFD (2014) as close to the outer face of the tab as allowed by cover requirements.

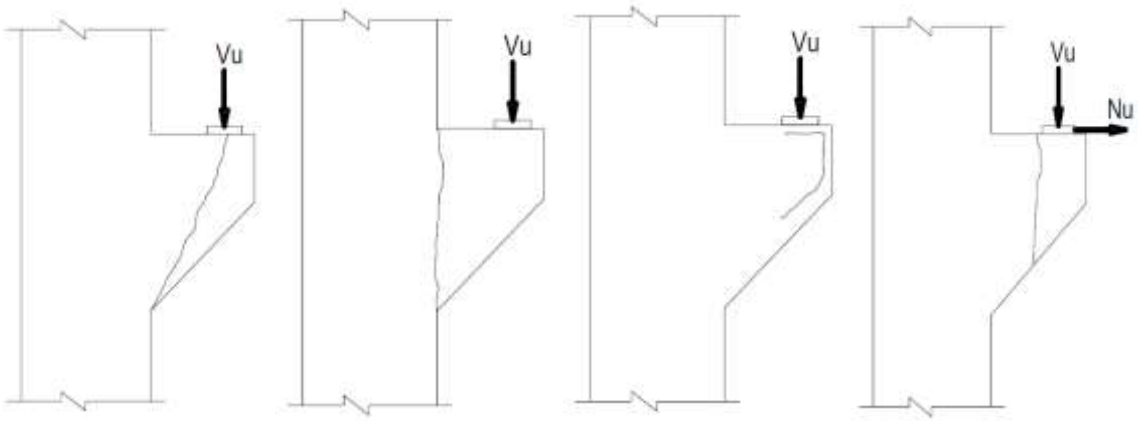

Figure 2-10. Modes of failure of corbel (Ashari 2014)

2.2.5. Reliability Theory

Reliability analysis is used to account for uncertainties associated with load and resistance in structural design. Most of the parameters considered in design and evaluation procedures are not deterministic quantities but random variables or functions of them (Nowak and Collins 2012). Determination of the load carrying capacity of a structure involves estimation of the load and resistance components. The difference between load (Q) and resistance (R) components defines the probability of failure P_f (probability of the situation when the load component exceeds the nominal resistance) (Figure 2-11).

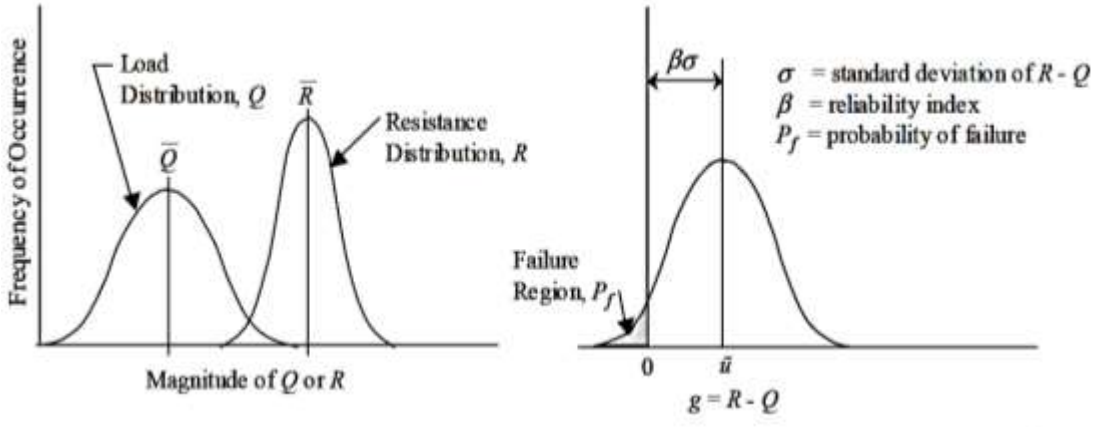

a) **b)**

Figure 2-11: Probability density functions of a) load and resistance components and b) limit state function values (Nowak and Collins, 2012)

New generation design codes, such as AASHTO LRFD (2014) provide a safety margin due to load and resistance factors determined using reliability-based calibration procedures (Nowak and Lind 1979), and (Nowak and Collins 2012). Such probabilistic analysis requires available statistical parameters of the load and resistance in each considered case. The performance of the structure is evaluated in terms of the reliability

index, β and its closeness to the target reliability β_T. The fundamental design formula used in load and resistance factor design is:

$$\phi R = \sum \gamma_i \cdot Q_i \qquad \textbf{Equation 2-16}$$

where:

R – nominal resistance

Q_i – nominal load component

ϕ – resistance factor

γ_i - load factor for particular component

From equation (Equation 2-16), the nominal load consists of several components which best represent the operational rather than ultimate condition of the structure (Bathurst et al. 2012; Harr 1987). The safety margin is provided by the factors that underestimate the capacity and overestimate the load components to the extent that the target reliability criterion is satisfied.

Numerous procedures have been developed to measure structural reliability (Ang and Tang 1984; Benjamin 1970; Nowak and Collins 2012). The overall reliability-based calibration procedure includes the following tasks (Nowak et al. 2005):

- Formulation of the limit state function
- Analysis of the available load and resistance statistics
- Development of the reliability analysis procedure
- Selection of the target reliability index
- Determination of the load and resistance factors to satisfy the target reliability criteria

Development of the load and resistance probabilistic model requires collection and analysis of the available data. The statistical parameters, such as mean value, standard deviation, and coefficient of variation can be extracted directly from the distribution function. Direct data plotting in the form of cumulative probability function allows easier interpretation, estimation of uncertainties and prediction of the extreme values in certain periods of time. The procedure is also dependent on the type of random variable which is defined by the shape of the distribution function (Nowak and Collins 2012).

2.2.5.1. Target Reliability

The key point in the calibration procedure is selection of the target reliability, which would adequately represent the desired safety margin. Currently, there is no specific guidance available for target reliability selection. However, the important criteria to determine the appropriate level of safety and the corresponding target reliability index is the successful past practice of safe design and limit state. The first one can be defined with the safety factor (SF) used in the Allowable Stress Design (ASD) practice. The corresponding target reliability factor can be calculated or simulated using the Monte Carlo method applying Equation 2-17:

$$\frac{R_n}{SF} - \sum Q_i \geq 0 \qquad \textbf{Equation 2-17}$$

The resultant β, however, can vary due to the different statistics applied in the design methods (Allen et al. 2005; Barker et al. 1991). Thus, another important criterion comes into play. The desired probability of failure can be selected depending on the type of the limit state (service, strength, fatigue, and extreme event). Structural components should satisfy the target reliability of $\beta_T = 3.5$ and correspond $P_f = 0.0002$ for strength limit

states (Allen et al. 2005). At the same time, past geotechnical practice has proved the appropriateness of $\beta_T = 3.0$ and $P_f = 0.001$ for foundation design (Withiam et al. 1998).

Another important factor to consider is the redundancy a component in the structural system. In other words, a lower reliability index is acceptable for members that, in the case of collapse, do not lead to progressive destruction of the whole system (Zhang et al. 2001). Concurrently, the required probability of failure can still be reached for the group of members. As an example, pile foundations, as well as reinforced retaining soil walls, will not fail due to the collapse of a single component. The ability of the soil to re-distribute the load for the structural components allows the use of lower reliability acceptance criteria for geotechnical structures (Zhang et al. 2001).

Recommendations regarding the appropriate target reliability level are available in many sources. The proposed value of the target reliability index β_T for a group of piles based on ASD varied from 2.0 to 2.5 (Barker et al. 1991). Phoon et al. (2003) recommended the target reliability index, β_T, for semi-gravity retaining walls in the range from 3.0 to 3.2 for all limit states. At the same time, the desired reliability for footings and drilled shafts are 3.5 ($P_f = 0.0002$) and 2.5-3.0 ($P_f = 0.001$), respectively (Allen et al. 2005; Barker et al. 1991). According to Allen et al. (2005), the desired reliability for reinforced soil retaining walls (pullout limit state) was chosen to be equal to 2.33 ($P_f = 0.01$) due to inherent redundancy (Bathurst et al. 2012). The failure of one layer reinforcement will not cause the failure of the whole structure due to the load being redistributed over the other layers. Similarly, a group of piles as a parallel system will retain remaining load even in the case of a single pile collapse. The desired failure probability according to (Paikowsky 2004) is $\beta = 2.0$-2.5. However, the number of piles in a group should be at least five to consider the

effect of redundancy. Serial system behavior, when the entire bridge pier is supported by one foundation was considered in the same research by Barker et al. (1991). The recommended value of target reliability index $\beta_T = 3.5$ (P_f=0.0002). In addition to the consideration of a redundant/non-redundant system, the selection of the desired reliability should be validated with similar structures successfully constructed and operated in the past.

2.2.5.2. Limit States

According to Section 11 of AASHTO LRFD (2014), failure of reinforced concrete cantilever semi-gravity walls can be described by the following limit states:

Sliding (Figure 2-6, b) – failure occurs when the horizontal component of the total force acting on the wall exceeds the factored shear soil resistance.

Bearing resistance (Figure 2-6, a) – failure due to the total vertical forces including eccentricity.

Overturning failure (Figure 2-6, c) – failure due to the loss of wall stability.

The sliding resistance of the wall is formulated in Equation 2-18. Cohesion should not be taken into consideration due to the possible shrinkage of the interface between the soil and foundation. If the soil is cohesionless, the nominal sliding resistance can be determined as:

$$R_\tau = V \cdot \tan\delta \qquad \textbf{Equation 2-18}$$

where:

V – total vertical force

δ – internal friction angle of drained soil (ϕ_f) – for CIP walls

When the footing rests on cohesive soil, the nominal bearing capacity is equal to the lesser of the undrained shear strength of the soil or 50% of the effective vertical stress. The bearing resistance can be determined based on the soil pressure distribution depending on the type of the foundation (soil or rock) (*AASHTO LRFD* 2014) The vertical capacity of the soil foundation can be determined using Equation 2-13.

The overturning capacity of the wall can be evaluated as the ratio of the factored resisting and overturning moments acting on the structure (Campos 2004). The ratio of the moment is expressed as the eccentricity of the resultant force acting on the footing (Equation 2-20):

$$e = \frac{\frac{RB}{2} + F_t \cdot \cos\beta - F_t \cdot \sin\beta + W_1 \cdot x_{w1} - V_1 \cdot x_{v1} - V_2 \cdot x_{v2}}{R} \qquad \textbf{Equation 2-19}$$

where:

V_1 – resultant of the weight of the soil carried by wall heel (Figure 2-7)

V_2 – resultant of the weight of the soil surcharge directly above wall heel (Figure 2-7)

W_1 – weight of wall stems(Figure 2-7)

F_t – resultant force of active lateral earth pressure (Figure 2-7)

β - the inclination of the ground slope behind the face of the wall (Figure 2-7);

2.2.5.3. Statistical Parameters

Since most of the parameters in soil mechanics are biased (properties are highly variable from site to site), including bias factors helps to exclude random variation of the parameters and increase the quality of the data. Three sources of uncertainties that affect

the accuracy of soil test results include inherent variability, measurement errors and transformation uncertainties (Phoon et al. 1995). These factors have a substantial effect on the actual coefficient of variation (COV) used in the geotechnical design. Primary uncertainty is affected by the natural geological, environmental and chemical processes involved in the formation of the soil layer. The error that accumulated at the testing-transforming stages, as well as variation of the inherent variability of the soil properties, were evaluated by Phoon et al. (1995).

When data is gathered from different sources, knowledge of bias statistics allows consistent and accurate interpretation. Consistent input data features a low coefficient of variation (COV) and bias factor close to one. The function which demonstrates the best fit to the data distribution is also important. If the shape of the cumulative distribution function (CDF) is a straight line (probability plot), the distribution can be classified as normal (Gaussian). To generalize the statistics, the bias factor (ratio of the mean measured value to the nominal value) is applicable (Nowak and Collins 2012). The probability scale can be changed to the standard normal variable scale (Z) to evaluate the variation in standard deviations. The examples of a CDF's of the soil unit weight plotted on probability paper versus corresponding standard normal variable on the vertical axis are shown in Figure 2-12, for 12.6 and 3.6-m (41 and 11.8-ft) high retaining walls respectively (Allen et al. 1992).

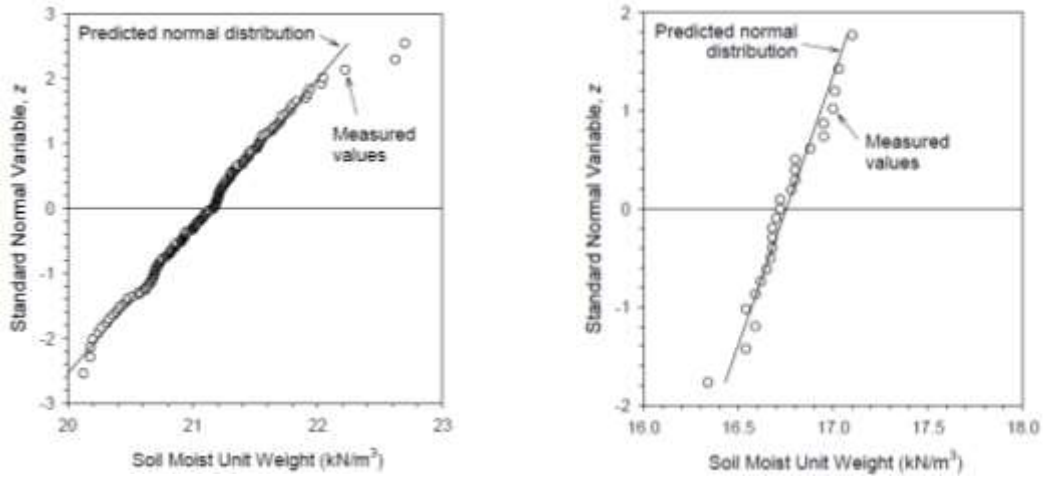

a b

Figure 2-12: CDF's for soil unit weight in engineered fills for a typical 12.6-m high (a), and 3.6m high (b) wall reinforced soil wall (Allen et al. 1992)

Many recent studies have been published providing a large amount of test data on retaining wall resistance (Bathurst et al. 2012), (Bathurst et al. 2011), (Bathurst et al. 2009). The necessary statistical parameters for the geotechnical design components were collected and summarized by Castillo et al. (2004), Duncan (2000), Harr (1987), Kulhawy and Phoon (2002), Ranganathan (1999), Sivakumar and Basha (2008), Wisniewski et al. (2016). The statistical parameters for the main components of the geotechnical design are summarized in Table 2-4.

Table 2-4: Statistical parameters of the soil properties

Random variable	Mean Value	COV	Type of distribution	Reference
Unit weight of soil, γ_s, kN/m^3	21.2	0.021	Normal	(Allen et al. 2005)
	16	0.07	Normal	(Castillo et al. 2004)
Soil of backfill	18	0.07	Normal	(Sivakumar and Basha 2008)
	19	0.07	-	(Harr, 1987)
Soil under base	19	0.07	Normal	(Sivakumar and Basha 2008)
	16	0.07	-	(Harr, 1987)
Angle of internal soil friction, φ, degrees	30	0.10	Normal	(Castillo et al. 2004)
Friction angle of the backfill soil	30	0.05-0.10	Lognormal	(Sivakumar and Basha 2008)
	32	0.10	-	(Harr, 1987)
Friction angle of the soil base	20	0.05	Lognormal	(Sivakumar and Basha 2008)
	28	0.28	-	(Harr, 1987)
	28	0.13	-	(Kulhawy 1992)
Coefficient of friction, μ	0.5	0.15	Normal	(Castillo et al. 2004)
Unit weight of concrete, γ_c, kN/m^3	17	0.2	Normal	(Ranganathan 1999)
Cohesion of soil base, c, kN/m^2	17	0.2	Normal	(Sivakumar and Basha 2008)
	30	0.3	Lognormal	(Harr 1987)
Angle of friction of soil below toe and heel, φ_2	14	0.10	Normal	(Sivakumar and Basha 2008)

2.3. Review of Pertinent Literature

2.3.1. Numerical Analysis of Culvert Behavior

2.3.1.1. Culvert Barrels

Numerical methods, such as finite element modeling, are widely used to investigate the behavior of culvert members under applied loads. The basic idea of stiffness or displacement method applied for the design of box culvert members was discussed in FDOT (1993). A wide variety of software packages exists to provide both effective design of new and detailed investigation of existing culvert structures. In particular, NYSDOT, (2012) discusses methods of using field and laboratory test results in the design and numerical investigation. ETCulvert developed by Eriksson Technologies (2017) is currently in use by the NYC DOT Office of Structures as well as the Precast Concrete Association of New York (PCANY 2017; NYSDOT 2012).

Convergence of physical test and numerical results is not always possible to achieve due to structural imperfections, unpredictable soil-structure behavior, and stress-strain conditions due to the variability of soil properties. In many cases, however, the conduction of the scaled laboratory based test is not available leaving numerical analysis as the only option.

Various modeling techniques have been applied to simulate the actual behavior of culvert components. For comparison, a large-scale lab test of a concrete box culvert with sand backfill was conducted to determine the load distribution and stress-strain behavior of the members (Dasgupta and Sengupta 1991). The comparison of load distribution on the box culvert surface was done with Marston theories (Spangler 1960). An analytical

model was developed in CYBER 180-840A (1986) using plane-strain elements for sand fill and 2-noded beam elements for culvert details. The sand backfill was meshed more refined in the contact zone to provide adequate distribution of stresses and deflection. Soil properties, such as modulus of elasticity, friction coefficient, cohesion and unit weight, were determined by lab tests and applied in the model depending on the depth of the backfill. The difference of pressure distribution obtained from numerical simulation and the experimental test was within 5%.

A similar study to compare field testing and computer modeling results were conducted by McGrath et al. (1996). Concrete arch culvert deflection and crack evolution were investigated under external backfill and live loads, which exceed HS-20 truck by 30%. After a two-year field test was completed, the obtained actual results were compared to the FEM model developed in the CANDE (Katona 2017) software package. The numerical and test results agreed on the structural behavior of the culvert except for the displacement. The actual measured effect of the live load was five-times smaller than predicted in the design from live load due to HS-20 truck. This relationship was observed in the model with soil pressure as well.

Alkhrdaji T (2001) investigated problem related to the corrosion of the culvert reinforcing steel and substituting fiber reinforced polymers bars for the steel was considered. Numerical analysis of the buried reinforced box culvert was conducted using BOXCAR software (ACPA 1983), specially developed for the Federal Highway Administration (FHWA). Stresses in the critical locations were determined using the stiffness matrix method considering 32 load conditions, including an HS15 truck load as one of them (FHWA 1983). The box culvert was modeled linear-elastic with shell elements

using Visual Analysis software (IES 2017). The crack formation was simulated by decreasing the element stiffness in the crack zones. Observed deflection, during the test, were less than 1 mm and this confirms the linear elastic bridge behavior under the design loads. Under the applied load the safety margin is about 40%, since the stresses are 40% below the yield point.

The behavior of a reinforced concrete box culvert was analyzed in ABAQUS by Garg and Abolmaali, (2009). The culvert body was simulated using the 3D shell and solid elements. The position and size of the reinforcing steel were modeled using special rebar elements. The contact surface was simulated using non-linear node-to-surface contact elements. The load was applied to the culvert section and gradually increased during the analysis to capture the moment of failure. The magnitude of the load at crack initiation on the inside surface predicted by FE results was 38-kip versus 42-kip obtained from the physical test. Proof load test proved it. Also, the pattern of crack propagation through the slab thickness was similar. The shear cracks appeared under the load twice large than the factored design load, which include surcharge and live loads.

B. Ahmed (Ahmed, B. et al. 2003) analyzed the crack development in a box culvert and an underpass located approximately 3.5 km away from the West End of Jamuna Multipurpose Bridge (JMB). Two and three dimensional FEM analysis in SAP90 was used to determine the main causes of cracking. In the model, the live load combination of HB and HA according to (BS 5400-2 1978) was applied directly to the structure. The comparison between simplified load distribution using Rankine theory and load distribution based on Marston theories (Spangler 1960) was done for each set of models. The soil and culvert members were simulated using 8-noded brick elements and 4-noded

plate elements respectively. The interaction between soil and structure was modeled using special “link” elements (active only in compression stages). The modulus of elasticity of the soil estimated using Bowles (1988). Contours of developed stresses show that the highest magnitude appears at the bottom due to the elastic settlement without a live load. It was concluded that the effect of the soil settlement produces a “beam like” effect on the whole structure in a direction perpendicular to traffic. High density soil may result in significant pressure on the head and wing walls due to arching action in the lateral direction (Terzaghi 1947).

One of the recent studies using numerical analysis was conducted by Abuhajar et al. (2017) using FLAC 2D (Itasca 2017). The effect of soil arching action on the development of stresses and deflections in the culvert barrel was analyzed, along with the culvert-soil interaction. Different geometries of the culvert components were considered in order to evaluate the sensitivity of the vertical and horizontal stresses. The linear elastic material model was chosen to simulate the box culvert. Elastic-perfectly plastic behavior was assigned to the soil elements. The numerical model was verified with centrifuge test results. The centrifuge test was used to perform static parametric analysis of the soil-culvert interaction. It was observed that stresses at the corner of the box increase with decreasing thickness of the walls. The results of the parametric study can be used to estimate the actual stress distribution on the culvert under static loads.

2.3.1.2. Retaining Wing Walls

The main purpose of culvert wing walls is to retain the soil of the backfill and direct the water flow. The design provisions and structural behavior of the wing walls are very similar to the retaining walls. A number of research projects focused on analysis of the

strength and stability of different types of the retaining walls based on finite element analysis (Abuhajar et al. 2017; Bentler and Labuz 2006; Chugh et al. 2016; Clough and Duncan 1971; Goh 1993; Kulhawy 1992; Senthil et al. 2014).

However, several researchers such as (Clough and Duncan 1971; Kulhawy 1992) pointed out the importance of including the retaining wall movement and the actual distribution of stress in the design. In these studies, the response of 6-m high gravity retaining wall was computed using the finite element simulation. Terzaghi, (1934) previously analyzed this problem. At the same time, Casagrande, (1973) indicated a certain level of redundancy in strength and stability of the retaining gravity wall which could be caused by the overconservative design based on classical theories. It revealed a strong need in the application of numerical analysis to evaluate the actual behavior of the structure in conjunction with the surrounding soil.

The conventional design of retaining structures utilizes simplified assumptions about active pressure conditions behind the wall based on lateral earth force and pressure theories attributed to Coulomb (1776) and Rankine (1858). These assumptions allowed for satisfactorily conservative design when there were an insufficient test and numerical results available. The distribution of the active pressure according to these theories was recently verified by Nisha et al., (2011) using Plaxis (2017). The elastoplastic material model based on Mohr-Coulomb failure criteria for the soil was chosen for this analysis. The magnitude and distribution the earth pressure was found to be close to the theoretical.

Goh, (1993) employed the FE analysis in order to evaluate the development of stresses and displacements in cantilever concrete retaining walls. The author criticized the traditional approach based on Coulomb (1776) and Rankine (1858) theories regarding the

active earth pressure distribution. These conventional approaches ignore the impact of flexibility and boundary conditions of the structure on the lateral pressure distribution. The lateral pressure is especially sensitive to the level of compaction of the backfill. In order to analyze the behavior of the structure and predict possible deformations in more detail, non-linearity of the material was included in the numerical modeling. The backfill and base sandy soil were simulated using 8-node isoperimetric finite elements along with a linear elastic perfectly plastic Mohr-Coulomb material model. The retaining wall structure was modeled linear elastic using the same type of elements. For soil-concrete interaction, 6-node interface elements were selected similarly to the Clough and Duncan (1971) approach. The results indicated complex movement of the wall, including rotation over the toe caused by non-uniform stiffness of the wall and soil base. Consequently, the distribution of lateral soil pressure was different than predicted by the theoretical solution. The effect of the roughness of the concrete surface underestimated in conventional theory, lead to a reduction of the lateral pressure. Although the author does not perform the experiment based validation of the FE model, a simplified guideline for the retaining wall design is proposed, that closely reflects the actual behavior of the structure.

The results of a study by Bentler and Labuz, (2006) instrumenting a reinforced concrete cantilever retaining wall corresponds to the observations made in the previous study by Goh (1993). The authors examined the distribution of active pressure by monitoring the behavior of the cantilever retaining wall during 12 months of construction. The development of the active condition occurred once the top of the stem displaced on the order of 0.1% of the backfill height. This is a much smaller movement than suggested by Terzaghi's (1934) classic large-scale tests. Out of plane rotation of the whole structure

and vertical translation of the whole structure were noticed during monitoring of the instrumentation. This was primarily caused by the difference between the vertical stresses under the base of the wall. The structure rotated towards the backfill while the top of the wall tended to deflect away from it. The relative flexibility of the structure, which is not included in the theoretical analysis, contributed to this complex rotation of the wall. Also, the measured magnitude of the horizontal passive pressure acting on the key wall was 10% less than the corresponding design value. During backfill compaction, the sensors recorded a significant increase (by twice) of the lateral backfill pressure. The results also confirmed the importance of the horizontal stresses on the toe in the total resistance of the structure against sliding. Thus, it was recommended to modify the factor of safety in the traditional stability analysis and design for sliding, unless the soil in front of a toe will be removed.

Senthil et al., (2014) used three dimensional finite element modeling with ABAQUS to evaluate the behavior of a 15m high retaining wall under active earth pressure. Cantilever and counterfort type retaining walls were considered in this study. In the FE model, the resultant force of the active earth pressure was applied at the level of 35 to 50% of the wall height due to the assumption that the active earth pressure in sandy soils is trapezoidally distributed. The material models for the concrete, steel and soil components were linear elastic. Results showed the pressure distribution varies along with the changing geometry of retaining wall components. The configuration of the cantilever wall with a short toe and a longer heel was found least stable, while the opposite developed the maximum stresses.

The group of researchers led by Chugh et al., (2016) used the finite difference code FLAC (Itasca 2017) along with the test results in order to evaluate the effect of the

structural properties and geometry of retaining walls on the development of active and passive pressures. An important aspect of this study was the use of interface elements for soil-structure interaction. In order to reflect the stages of construction, layers of backfill were added step-by-step. It was concluded that the increase of the backfill height does not necessarily lead to a direct increase of the retaining wall deformation. The stage of construction when the wall was installed before the backfilling was the most critical, as the deformations initiated at this stage progressed significantly with increase of the backfill height.

2.3.2. Reliability analysis

A few studies set out to optimize current traditional design provisions for retaining walls (Rhomberg and Street 1981; Sarıbaş Aşkın and Erbatur Fuat 1996). However, most of the approaches ignored the natural variability of the load and resistance design parameters by treating them as deterministic values. Some researchers emphasized a need to apply the probabilistic approach in order to account for uncontrolled uncertainties during the design of retaining walls (Castillo et al. 2004; Chalermyanont and Benson 2004; Duncan 2000; Hoeg and Murarka 1974; Phoon et al. 1995; Whitman 2000).

There are a number of researchers who integrated reliability-based analysis into their studies (Christian John T. et al. 1994; Duncan 2000; Fenton et al. 2005; Goh A. T. et al. 2009; Low 2007; Mandali et al. 2011; Sivakumar and Basha 2008; Tang et al. 1999). A brief review of the recent studies including reliability analysis follows.

Duncan (2000) emphasized the need to involve the principles of structural reliability in the problems related to the stability and uneven settlement of retaining structures. He also mentioned the accessibility of the statistical parameters, such as

standard deviation, based on existing databases. The simplified reliability-based approach was proposed to substitute the conventional deterministic analysis and evaluate the level of safety in the geotechnical problem. The recommended safety factors were developed on the basis of including the natural variability of the geotechnical parameters involved in the design. Sliding of the retaining wall, slope failure, consolidation due to settlement, and settlement of footings on sand was the considered in his research. For all these problems, the statistical parameters were estimated using available information about variability of concrete and soil material properties (Wolff 1994). The derivation of the statistical parameters, such as standard deviation for most variable parameters was provided. Based on sensitivity analysis, the effect of the variability on the safety factor for each considered problem was evaluated. In particular, the most likely value (mean) of safety factor against sliding of the retaining wall was computed as 1.5 with a variation of 17%.

The objective of the study done by Felton (2005) included determining the spatial variability of soil properties used in retaining wall design. The traditional practice of retaining wall design employs either Rankine or Coulomb theory for the development of earth pressure that considering a uniform soil mass. The authors applied non-linear FE modeling to evaluate the effect of soil unevenness on soil pressure and used a Monte Carlo simulation (Nowak and Collins 2012) to evaluate the reliability of the current design. Three properties were considered as random variables in this design: effective friction angle of the soil, unit weight of the soil and unit weight of the concrete (all log-normally distributed since they cannot be negative). The same spatial correlation was assumed for these random fields. The rest of the parameters were assumed to be deterministic values in both FE model and Monte Carlo simulation. The sensitivity analysis was performed to track the impact of

variability of safety factors for considered design (resistance-to-active earth pressure ratio). For different combinations of mean and standard deviation of the coefficient of correlation between friction angle and unit weight field the factor-of safety varied from 1.5 to 3.0. It was concluded that there exists a substantial difference between the behavior of the spatially variable soil continuum and that simplified by Rankine or Coulomb theories. The authors also emphasized the positive effect of correlation on structural safety in terms of probability of failure. However, the case when the unit weight and friction angle are independent random variables was a more conservative approach**.**

The traditional factor-of-safety based approach to the retaining wall design was challenged in research by Low (2007). This method involved a simplified two-dimensional graphical procedure for random variables, where the "design point" was located at the intersection of the limit state function and the one-standard-deviation dispersion ellipse. Two limit states for retaining wall design were considered: sliding and overturning. The internal soil friction and soil-wall interface friction angles were treated as random variables with different coefficients of correlation. The authors applied the Hasofer-Lind reliability index (Hasofer and Lind 1974) and the first-order second moment reliability method (FORM) in order to evaluate the reliability of traditional retaining wall design. The design components were considered normally and non-normally (lognormal and beta) distributed. The Monte Carlo simulation (Nowak and Collins 2012) was used determine the probability of failure for each case considered. Similar to Fenton et al. (2005) it was concluded, that including the natural positive correlation between the resistance parameters (unit weight of the soil and internal friction angle) lead to an unconservative design. At the same time, the positive correlation (ρ=0.8) between angles of internal soil friction and soil-wall surface

friction should be included as a more conservative case. Based on the Monte Carlo simulation, reliability indices β for the overrunning and sliding limit states were equal to 2.491 and 3.102 respectively. Therefore, the overturning limit states control the overall stability of a semi-gravity retaining wall.

Sivakumar and Basha (2008) present the reliability procedure based on the target reliability concept to assess the optimum design for cantilever retaining walls. The stability limit states evaluated in this study were sliding of the retaining wall base, out-of-plane overturning and bearing capacity of the wall. The properties of backfill and foundation soil were assumed to be random variables, as well as the dimensions of the retaining wall. This study also collected the available information about the statistics (mean, coefficient of variation and type of distribution) of the design parameters. The target reliability index, β_T, was in the range from 3.0 to 3.2 for all limit states considered by Phoon et al. (2003). The results of design targeting reliability index and traditional provisions defined in the specification were compared and discussed. According to the results of sensitivity analysis, the geometry had a significant effect on structural reliability in the cases of overturning, sliding and bearing failure. At the same time, the statistical parameters of the soil properties had a lesser impact on reliability index for the same limit states.

Mandali et al. (2011) employed the First-order reliability methods, Second-order reliability methods, and Monte Carlo Simulation to evaluate the design of counterfort retaining walls in terms of the probability of failure, P_f, and reliability index, β. The sliding, overturning and bearing capacities of the retaining wall were analyzed as possible geotechnical modes of failure. The authors also considered the structural moment and shear failure modes for the stem, heel, and toe of the wall. The design parameters such as the unit

weight of the concrete, unit weight of the soil, internal friction angle, cohesion were assumed to be normal random variables with the statistics obtained from the literature. Based on the sensitivity analysis conducted, the angle of internal friction was the most influential design parameter. The reliability index for geotechnical modes of failure varied from 2.8 (for sliding) to 8.4 for overturning. In all cases, the traditional deterministic safety factor SF=1.5 was applied. Therefore, the authors recommended using a safety factor of 1.7 in order to obtain an acceptable reliability index $\beta=3$. For structural modes, the controlling structural element was the heel with the β ranging from 2.5 to 5.1.

Goh et al. (2009) compared the traditional design approach, which covers all the uncertainties incorporated in the design parameters into a single conservative safety factor, with the reliability-based approach. The concept of "partial factor of safety on shear strength" was applied to evaluate the effect of variability in geometry on the design of cantilever retaining wall in granular soil. The Monte Carlo simulation method was used for sensitivity analysis. The target probability of failure was taken as a measure of structural safety. The impact of the internal friction angle on the probability of failure was evaluated for a nominal surcharge load of 10-kPa/m. The results showed a substantial effect of the empirical depth of embedment of the retaining wall on the probability of failure. Based on this research, the authors also recommended optimum factors of safety in the range from 1.2 to 1.25 for P_{fT} =0.01.

Chapter 3. Tabbed Wing Wall-to-Culvert Connection

3.1 Introduction

As it was mentioned in previous chapters, the need to study the behavior of the wing wall-to-culvert connection was caused by the rapid cracking of the newly built cast-in-place culvert and the alternative design developed by ALDOT engineers to prevent it. Therefore, the analysis presented herein is focused on CIP multiple barrels box culvert with wing walls using finite element (FE) simulation techniques. The details of the newly developed design are presented and discussed in this chapter.

3.2. Novel Wing Wall-to-Culvert Connection Design

There is a high stress concentration zone located in the monolithic connection between the wing wall and culvert barrel. The new culvert design proposed by ALDOT engineers allows the wing wall and concrete barrel to move independently in the vertical direction. The plan view of the culvert constructed according to the new design is shown in Figure 3-1 and Figure 3-2. In particular, the changes made to the wing wall design are listed below:

- The width of the footing was increased.
- A key wall was included to provide additional sliding stability in case of scour.

- Overlapping culvert and wing wall tab extensions were added.

Since the wing wall was disconnected from the culvert barrel, it was further re-designed as a free-standing cantilever retaining wall. To provide the overall stability of the wing wall and effectively distribute the weight to the foundation soil, the footing width was increased.

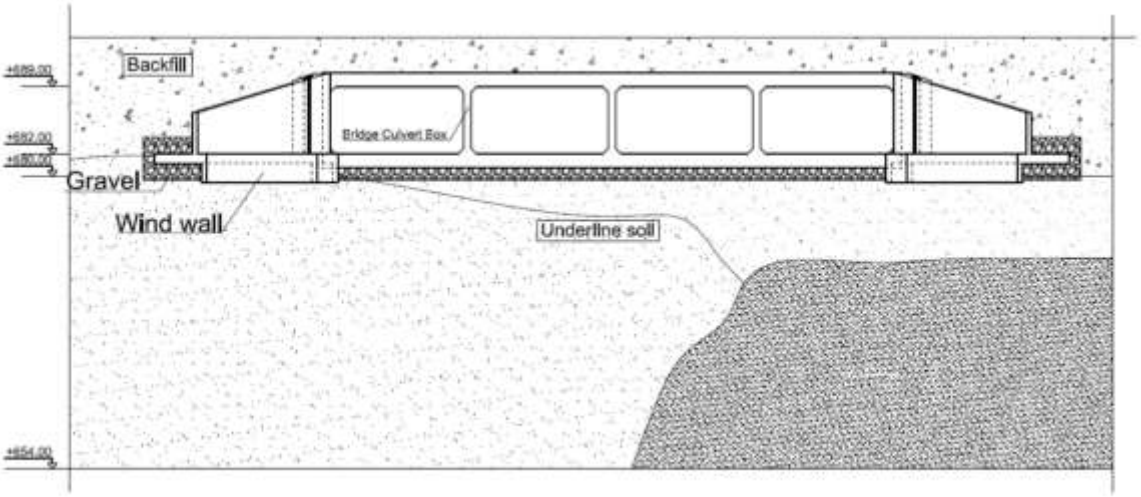

Figure 3-1 Tabbed culvert design.

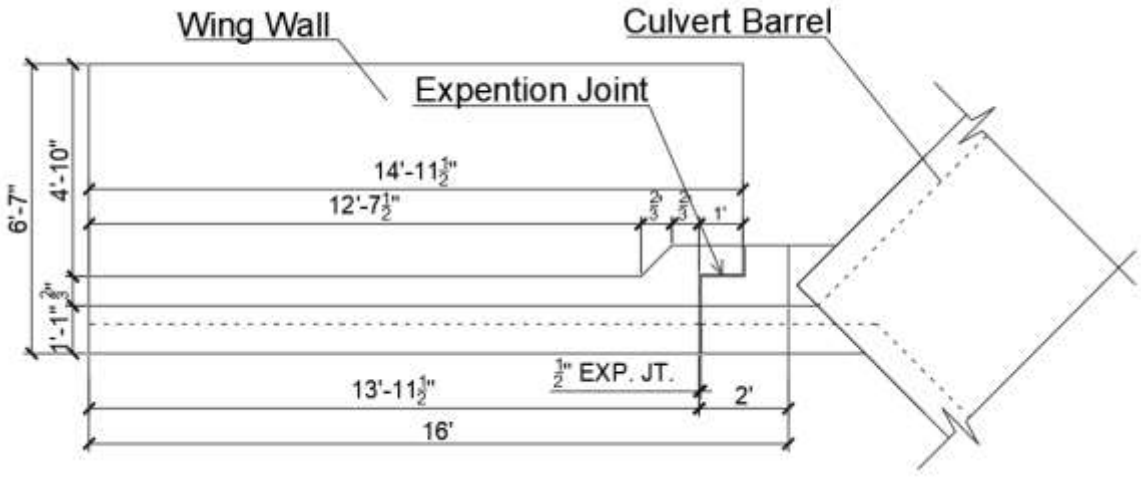

Figure 3-2. Tabbed wing wall-to-culvert connection.

According to the AASHTO LRFD (2014), the stability of a free-standing wing wall depends not only on structural resistance but on sliding, bearing and overturning capacity

of the soil-structure system. In this case, the dimensions of the footing were controlled by bearing capacity of the soil. Thus, the stronger soil allowed for narrower footing dimensions, while weaker types of soil required an increased footing width. The soil base properties are presented in Chapter 5.4 and summarized in Appendix B.

As the wing wall was designed as a cantilever retaining wall, it may settle and rotate independently from the barrel. Due to this movement, some compression forces could be transferred between two overlapping tab extensions. In terms of sufficient anchorage length of horizontal reinforcement, both tabs were designed 12-in (1-ft) deep (Figure 3-2). The new tab design is discussed in detail in Chapter 3.2.

These improvements allow differential settlement to occur without generating large stresses at the connection zone. Thus, the probability of crack formation along the joint decreases.

3.3. Tab Extension Design

The changes to the current design, discussed in the previous chapter, were offered by ALDOT in order to solve the problem of cracking along the wing wall-to-culvert joint. By eliminating the rigid connection, the stress concentration zone was removed and both structural components were allowed to move independently. Without the rigid connection, the wing wall behaves as a short cantilever retaining wall with pin support along one side. This also decreases the excessive stresses that lead to the rapid crack formation. Thus, the durability service life of the structure is increased.

An overlapping tab extension was added to each corner of the body of the culvert to serve as a horizontal bearing support for the wing walls to ensure the two structural elements continued to perform jointly in resisting the loads associated with backfill. In

this way, the wing walls still benefit from the lateral stiffness of the culvert, but restraint is removed from what was previously a concentration of stress. Also, the newly designed tabbed connection allows for the translation of loads from the wing wall to culvert barrel horizontally. The dimensioned plan view of the wing wall-to-culvert joint is shown in Figure 3-3.

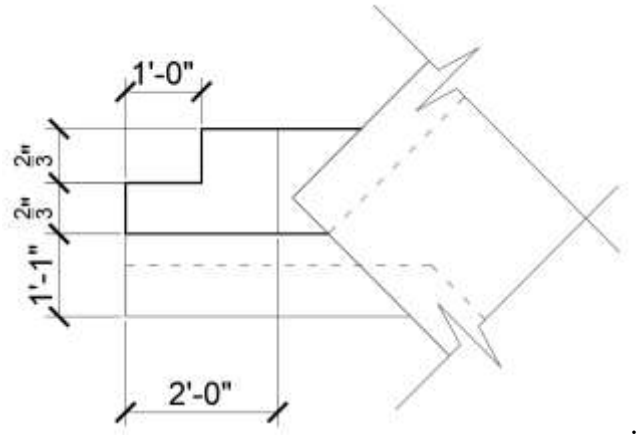

Figure 3-3. Scheme of the tab extension.

Initially, the depth of the tab extension was 8-in based on the new experimental design. These dimensions were chosen to be sufficient for an effective transfer of stresses from the wing wall to the barrel. It was also suitable in terms of sufficient anchorage length for the horizontal reinforcement. Further on, the actual wing wall-to-culvert connection was designed with 12-in (1-ft) tab extension. The ½-in gap between overlapping tab extension was filled with a layer of bituminous material in order to provide the independent movement of the structures, transfer of stresses from the wing wall to the culvert and prevent the soil ingress into the joint. For three different culverts constructed according to the new design, the thickness of the tab was the same as the wall thickness and equal to 8, 9, and 10-in respectively (Appendix A).

The filling material was an important component in this design since it provides the transfer of the horizontal stresses from the wing wall to the culvert barrel. Two conditions of bitumen impregnated fiberboard were considered: saturated and unsaturated. The saturated state was simulated since it produces the critical horizontal deflection of the wing wall due to higher compressibility. Therefore, the filling material is fully compressed, and the stresses are transferred directly to the culvert tab. In case of unsaturated conditions, the highest stresses occur along the joint.

3.4. Constructed Culverts

ALDOT designed three new culverts in conjunction with county engineers for testing as part of this project. The culverts were located in reasonable proximity to Auburn, AL: Chambers County Road 258, Lee County Road 156 and Coosa County Road 68. In all three cases, the novel tab connection was implemented. Thus, the cast-in-place wing wall and barrel were constructed separately opposite to the traditional design.

The first culvert was built on Chambers County Road 258, located over Whatley Creek, in April 2016. It is shown in Figure 3-4. This culvert consists of four barrels with total outer dimensions of 44-ft by 51-ft in the directions along and transverse to the stream, respectively. The depth of the culvert barrel is 8.4-ft, which is the smallest depth of all locations. The 1.25-ft deep key wall was added to each side to prevent soil erosion under the barrel and increase the overall stability of the structure.

Figure 3-4. Location of Chambers County culvert ("Google Maps" 2017a)

Four identical free-standing wing walls were cast with an angle of 45° to the barrel. The height of the wing walls varied from 7.16-ft at the connection with the barrel to 4.5-ft at the opposite side. The total length of the wall was 15-ft with the total width of the footing (toe with a heel) of 6.5-ft. The key wall attached to the wing wall was 1.5-ft deeper than the bottom of the footing. After construction, the backfill 1.16-ft above the culvert top slab was added along with the pavement. The detailed drawings of the culvert at Chambers County are shown in Figure 3-5 and Figure A-1-4 (Appendix A).

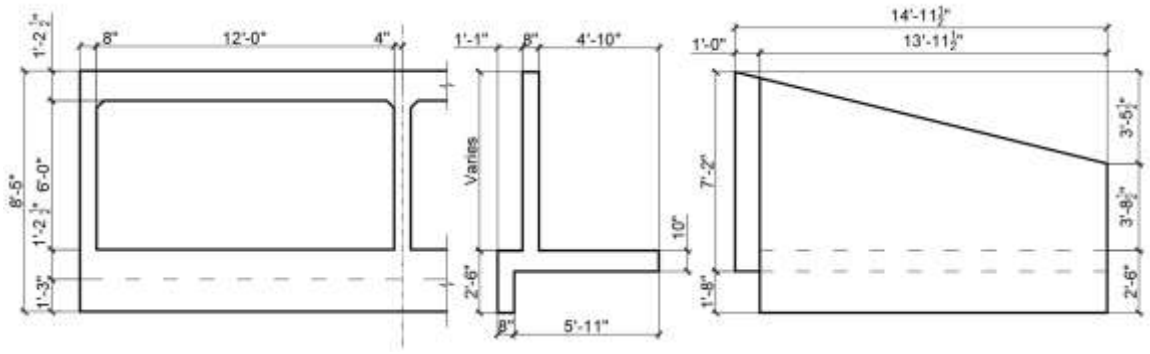

Figure 3-5. Outer dimensions of the Chambers County culvert

The second culvert, located in Lee County Road 156, was built in September 2016 (Figure 3-6).

Figure 3-6. Location of Lee County culvert ("Google Maps" 2017b)

This structure consists of three equal size barrels with 10-ft by 8-ft waterway openings. The total length of the culvert along the stream was 44-ft, while the total width transverse to the stream is 32.6-ft. The depth of the culvert was 10.16-ft extended with a 1.3-ft key wall. Similar to the previous case, four wing walls were constructed at an angle

of 45° to the barrel which is skewed by 15°. While the heights of the wing walls were greater than those in Chambers County (9-ft), the length of the wing walls were 4-ft shorter. The height of the wing wall gradually decreased from 9.5-ft at the barrel side to 4.6-ft at the outer edge. The total width of footing (toe with a heel) was 8.25-ft. The key wall attached to the wing wall extends 1.6-ft deeper than the bottom of the footing. The backfill was 1.2-ft above the culvert top slab with the wearing surface above. The dimensioned drawings of this culvert are shown in Figure 3-7 and Figure A-5-8 (Appendix A).

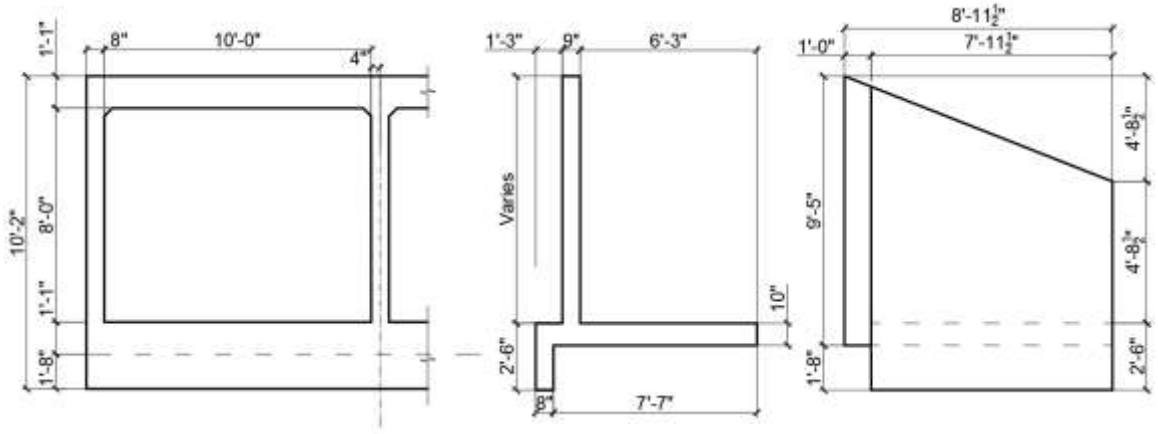

Figure 3-7. Outer dimensions of the Lee County culvert

Construction of the third culvert over Shelton Creek on Coosa County Road 68 was completed in October 2016 (Figure 3-8). This culvert was the largest considered in this study. It consisted of four CIP barrels with 14-ft by 10-ft waterway openings. The total dimensions of the culvert were 44-ft by 60-ft in the direction along and across the stream, respectively.

Figure 3-8. Location of Coosa County culvert ("Google Maps" 2017c)

The depth of this culvert was 12.25-ft extended with a 3.8-ft deep key wall. Each diagonal pair of wing walls had slightly different geometry, but all of them were constructed at an angle of 45° to the culvert barrel. The difference was only in footing width, which for the first pair was 10-ft, and for the second was 8.5-ft. The wing wall was 11-ft long. The height of the wall gradually decreased from 11.5-ft at the culvert side to 5.5-ft at the outer edge. The key wall was the same as in the barrel and 3.8-ft deeper than the footing bottom. Unlike others, this culvert had backfill only to top of the wall. Pavement placed directly on the culvert box. The detailed drawings of this culvert are shown in Figure 3-9 and in Figure A-9-12 (Appendix A).

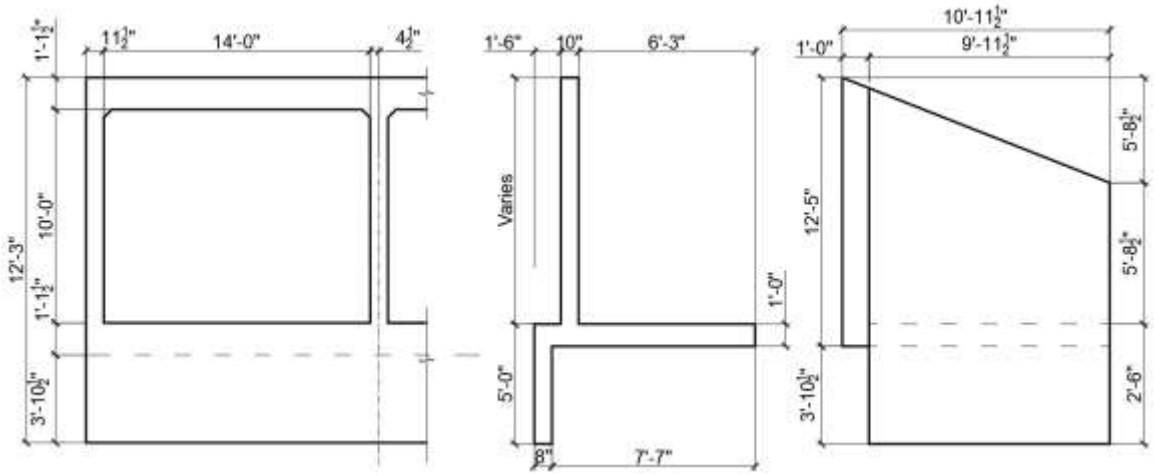

Figure 3-9. Outer dimensions of the Coosa County culvert

Chapter 4. Finite Element Simulation

4.1. Introduction

Plaxis 3D was selected for this study, as it is one of the most commonly used numerical programs for geotechnical engineering. Plaxis3D is equipped with abilities to calculating static elastic-plastic deformations, stability analysis, safety-analysis, consolidation and steady-state groundwater flow. Also, it is suited to efficiently and properly model soil-structure interaction for complex geotechnical structures. With the ability to divide analyses process into a number of separate modeling phases, it is capable of modeling the actual construction process.

In this study, FE models were created for the three constructed culverts and for additional theoretical cases with deeper culverts. The culvert barrel, wing walls, filling material, and surrounding soil were modeled using 3D soil elements. The interfaces between different materials were modeled using 3D shell elements. The applied surcharge and traffic loads were distributed through corresponding areas. The construction stages included building the culvert, backfilling, traffic load, and scour erosion.

4.2. Finite Elements

Two types of FE were used in the analysis. Soil and concrete were modeled using 3D 10-node tetrahedral elements (Figure 4-1) formulated in local coordinate system ζ, η, and ξ. This type of element provides a second-order interpolation of displacements in the

nodes. The shape function N_i was formulated for each node with unity value and zero at the other nodes (Equation 4-1). To calculate stresses and strains, 4-point Gaussian integration is used (Table 4-1) (Plaxis bv 2015a). Such element has three degrees of freedom per node: u_x, u_y and u_z.

$$N_1 = (1-\xi-\eta-\zeta)(1-2\xi-2\eta-2\zeta); N_2 = \zeta(2\zeta-1); N_3 = \xi(2\xi-1);$$
$$N_4 = \eta(2\eta-1); N_5 = 4\zeta(1-\xi-\eta-\zeta); N_6 = 4\zeta\xi; N_7 = 4\xi(1-\xi-\eta-\zeta); \quad \textbf{Equation 4-1}$$
$$N_8 = 4\eta(1-\xi-\eta-\zeta); N_9 = 4\eta\zeta; N_{10} = 4\xi\eta$$

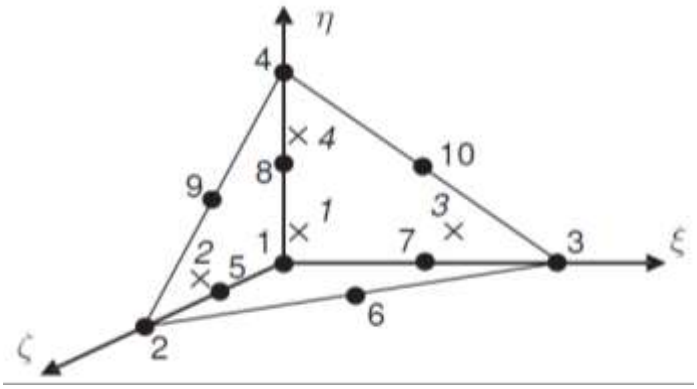

Figure 4-1. Local numbering and position of nodes (•) and integration points (x) of 10-node wedge element. (Plaxis bv 2015a)

Interfaces were modeled using a 6-node plate triangular element (Figure 4-2). Unlike ordinary plate elements, the interface element is different in terms of having coupled nodes instead of a single node. The distance between two "sub-nodes" of a node pair is zero. Each node has only three translation degrees of freedom (u_x, u_y and u_z). Thus, this element allows slipping and gapping between coupled nodes. The interface elements are numerically integrated using 6-point Gauss integration (Table 4-2). (Dunavant 1985; Plaxis bv 2015a). Interfaces after meshing were composed to 12-node interface elements.

Table 4-1. Gaussian integration for the 10-node tetrahedral element. (Plaxis bv 2015a)

Point	ξ_i	η_i	ζ_i	Wj
1	1/4-1/20√5	1/4-1/20√5	1/4-1/20√5	1/24
2	1/4-1/20√5	1/4-1/20√5	1/4+3/20√5	1/24
3	1/4+3/20√5	1/4-1/20√5	1/4-1/20√5	1/24
4	1/4-1/20√5	1/4+3/20√5	1/4-1/20√5	1/24

To eliminate a discontinuity between structural elements, the corner node pair of an interface element contracts to a single node. This may result in sharp high stresses around the corners of rigid elements (Figure 4-3). To eliminate this problem of non-physical stress distribution, the additional interface should be added inside the structural element (Figure 4-3), the stiffness of which should be assigned appropriately not to create unrealistically weak soil (Van Langen and Vermeer 1991). In this study, this feature of interface elements was utilized around all sharp edges of the culvert.

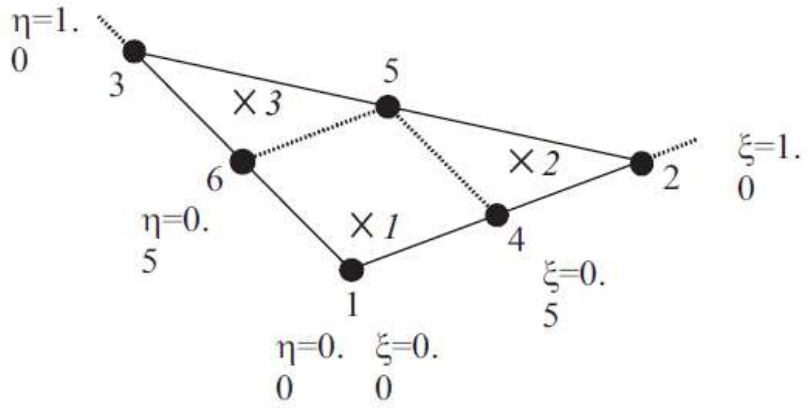

Figure 4-2. Local numbering and position of nodes (•) and integration points (x) of a 6-node plate triangle. (Plaxis bv 2015a)

Table 4-2. Gaussing integration for 12-node triangular element. (Plaxis bv 2015a)

Point	ξ_i	η_i	Wj
1	0.091576	0.816848	0.109952
2	0.091576	0.091576	0.109952
3	0.816848	0.091576	0.109952
4	0.108103	0.445948	0.223382
5	0.445948	0.108103	0.223382
6	0.445948	0.445948	0.223382

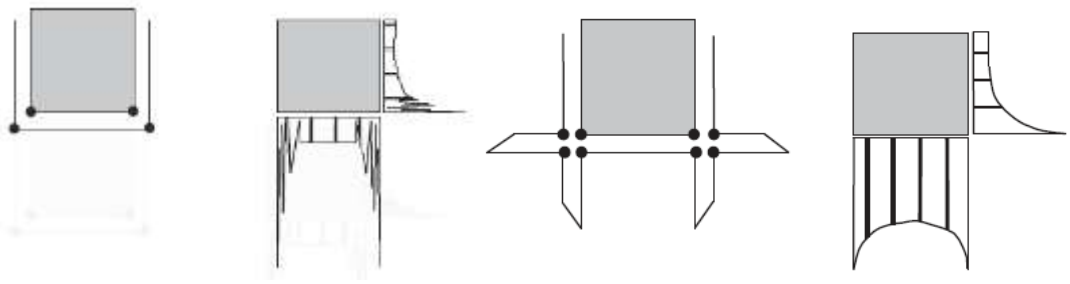

a b

Figure 4-3. Inflexible corner point: a) one surface interface; b) double surface interface. (Plaxis bv 2015b)

4.3. Meshing

With defined geometry, loads, and boundary conditions the model needs to be divided into finite elements. Plaxis 3D has an embedded fully automatic mesh generator. To obtain the accurate results without excessive calculation time, the appropriate coarseness must be defined. The finite element size is represented by the target element size, l_e (Equation 4-2). This size depends on the outer dimensions of the model and relative element size factor, r_e, which can be separately specified for each structural element.

To improve quality of the mesh, especially in the contact zone of elements with different coarseness, the enhanced mesh refinement was used. It automatically refines the element size to the default value of r_e=0.5 or other manually specified numbers around boundaries, interfaces, and applied load.

$$l_e = \frac{r_e}{20}\sqrt{(x_{\max} - x_{\min})^2 + (y_{\max} - y_{\min})^2 + (z_{\max} - z_{\min})^2} \qquad \textbf{Equation 4-2}$$

where:

r_e - relative element size factor;

$(x, y, z)_{max,\ min}$ – coordinates of the outer edge of the model.

4.4. Constitutive Models

To investigate the distribution of stresses causing rapid cracking on the culvert wing tab, three types of material models were considered. A simple Linear-Elastic (LE) model (Figure 4-4) was applied to the structural elements (wing walls and a culvert barrel) to obtain the stress distributions along the contact surface without overloading the model. The Mohr-Coulomb (MC) (Figure 4-5) and Hardening Soil (HS) (Figure 4-7) material models are applied for soil elements (Plaxis bv 2015c). The compressible filling material of the gap was modeled using HS model.

4.4.1. Linear Elastic Model

The Linear Elastic model is the simplest material model available in Plaxis 3D. This model is based on Hooke's law of isotropic elasticity. It involves two basic parameters: Young modulus *E,* which represents the slope of the stress-strain curve (Figure 4-4), and Poisson's Ratio *v,* which represents the relationship between stresses in different

directions (Plaxis bv 2015c). This model may be used to simulate the stiff volumes in the soil such as concrete walls.

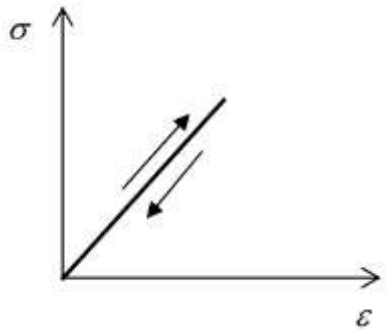

Figure 4-4. Basic idea of a linear elastic model

Due to the large linear region of the LE model, it cannot be used to simulate the soil material as it behaves in a non-linear manner, and even small distortions are irreversible. Using this model, the stresses are not limited and may show material strength beyond its real parameters.

4.4.2. Mohr-Coulomb Model

The Mohr-Coulomb (MC) model is the simplest linear elastic perfectly plastic model (Figure 4-5). This model represents a first-order approximation of soil behavior. The stiffness of each layer is based on constant average values or linearly increases with depth (Plaxis bv 2015c).

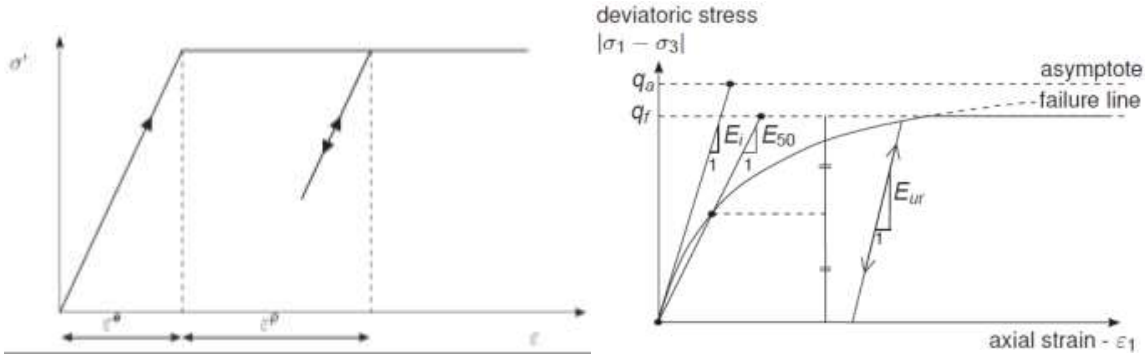

a) **b)**

Figure 4-5. Elastic perfectly plastic model (a); hyperbolic stress-strain relation (b) (Plaxis bv 2015c)

The basic principle of elastoplasticity is that the strains include elastic and plastic components. Stresses are related to the strains through The Hooke's Law (Plaxis bv 2015c).

$$\underline{\varepsilon} = \underline{\varepsilon}^{\theta} + \underline{\varepsilon}^{p} \qquad \textbf{Equation 4-3}$$

$$\underline{\underline{\sigma}}' = \underline{D}^{\theta}(\underline{\varepsilon} - \underline{\varepsilon}^{p}) \qquad \textbf{Equation 4-4}$$

where:

$\underline{\varepsilon}$ – total strain

$\underline{\varepsilon}^{\theta}$ – elastic strain

$\underline{\varepsilon}^{p}$ – plastic strain

$\underline{\sigma}'$ - effective stresses

$\underline{D}^{\theta}$ – elastic stiffness matrix

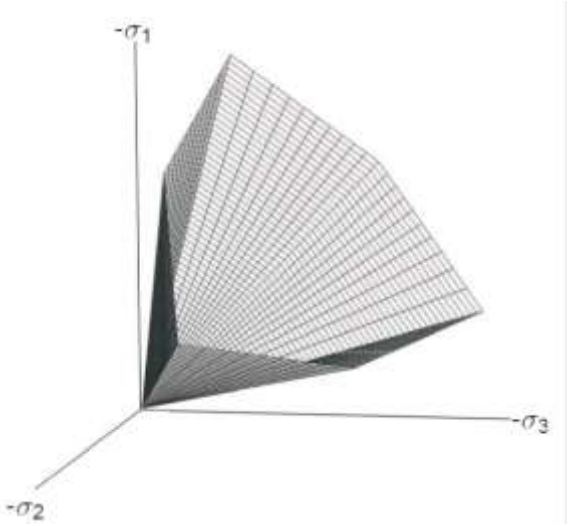

Figure 4-6. The Mohr-Coulomb yield surface (Plaxis bv 2015c)

The Mohr-Coulomb yielding criterion is an extension to 3D conditions of Coulomb's friction law (Figure 4-6). This means that this law is obeyed within a material element. The yield surface of MC model looks like a hexagonal cone with sharp edges

along the intersection of two yield surfaces. Unlike other programs where these transitions are smoothed, Plaxis 3D (Plaxis bv 2015a) has the exact form of the full MC model with the sharp transition between the yield surfaces (Koiter 1960; Van Langen and Vermeer 1990).

The MC yield conditions consist of three functions formulated in terms of principal stresses (Smith and Griffiths 2004):

$$f_1 = \frac{1}{2}(\sigma'_2 - \sigma'_3) + \frac{1}{2}(\sigma'_2 + \sigma'_3)\cdot\sin\varphi - c\cdot\cos\varphi \le 0$$
$$f_2 = \frac{1}{2}(\sigma'_3 - \sigma'_2) + \frac{1}{2}(\sigma'_3 + \sigma'_2)\cdot\sin\varphi - c\cdot\cos\varphi \le 0 \qquad \textbf{Equation 4-5}$$
$$f_3 = \frac{1}{2}(\sigma'_1 - \sigma'_2) + \frac{1}{2}(\sigma'_1 + \sigma'_2)\cdot\sin\varphi - c\cdot\cos\varphi \le 0$$

To avoid tensile stresses when the cohesion $c<0$, which is allowed in the standard MC model, the tension cut-off option included in Plaxis 3D will set allowable tensile stresses equal to zero, by default, if no other value was specified.

The MC model requires five main input material parameters:

E – Young's modulus;

φ - Angle of internal friction;

v – Poison's ratio;

c – Cohesion;

ψ - Dilatancy angle.

4.4.3. Hardening Soil Model

The Hardening Soil (HS) material model is an advanced stress dependent analytical model for both soft and stiff soils (Schanz 1998). The Hardening Soil model in contrast to

the Mohr Coulomb model does not have fixed yield surfaces to principal stresses and can be expanded due to plastic straining (Figure 4-7). Shear hardening due to deviatoric loading and compression hardening due to isotropic loading are incorporated in this model (Plaxis bv 2015c).

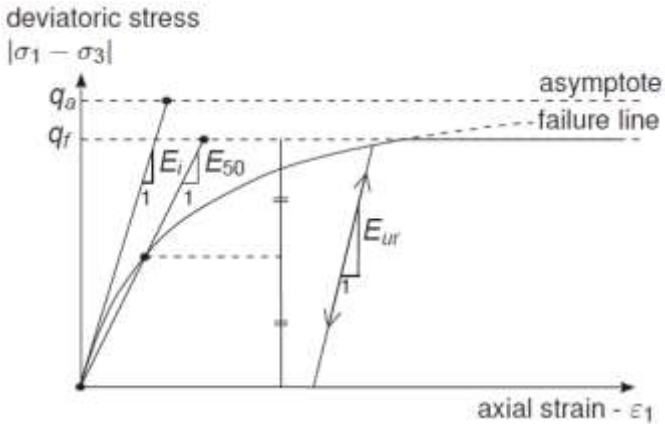

Figure 4-7. Hyperbolic stress-strain relation (Plaxis bv 2015c)

The Hardening Soil model is based on the relationship between irreversible strain development and decreasing stiffness under deviatoric loading. First, this relationship between axial strain and deviatoric stress was observed by (Kondner 1963) in the drained triaxial test. Later this observation was described with the hyperbolic model (Duncan and Chang 1970). However, the HC model supersedes this approach by applying the theory of plasticity instead of the theory of elasticity, including soil dilatancy and by adding yield cap. Additionally, the failure occurs accordingly to the Mohr Coulomb failure criterion.

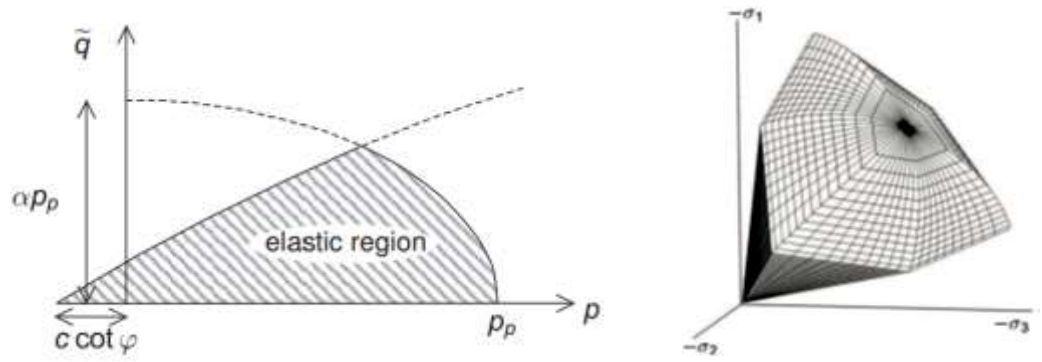

a **b**

Figure 4-8. Yield surfaces of Hardening Soil model: a) in p – q plane; b) in principal stress space (Plaxis bv 2015c)

The failure surfaces of the Hardening Soil model have the same shape as the classical Mohr Coulomb failure criterion, though the HS model introduces a yield cap to enclose the elastic region (Figure 4-8). The shear hardening yield surface shape, shown in Figure 4-8a, depends on hardening parameter γ^p which implies the position of yield loci between the horizontal axis and MC failure line. A second type of yield surface (Figure 4-8b) is introduced to enclose the elastic region for compressive stresses. This formulation defines a model with the independent input of E_{50}^{ref} and E_{oed}^{ref}. The triaxial modulus E_{50}^{ref} controls the magnitude of the plastic strains that are associated with the shear yield surface. Similarly, the oedometer modulus E_{oed}^{ref} controls the magnitude of the plastic strains that come from the yield surface (Plaxis bv 2015c).

The cap yield surface can be expressed by the following equation:

$$f_c = \frac{q^2}{M^2} + (p')^2 - p_p^2 \qquad \textbf{Equation 4-6}$$

where:

M – slope of critical state line in p' – q space.

p' – effective pressure.

p_p – isotropic pre-consolidation pressure.

q – deviatoric stress

The Hardening Soil model requires seven main input material parameters (Plaxis bv 2015c):

E_{oed}^{ref} – Tangent stiffness for primary oedometer;

E_{50}^{ref} - Secant stiffness in a standard drained triaxial test;

E_{ur}^{ref} – Unloading/ reloading stiffness;

ν_{ur} – Poison's ratio for unloading/ reloading;

φ – Angle of internal friction;

ψ – Angle of Dilatancy;

c – Cohesion;

4.5. Material Properties

Three types of materials were considered in this study: soil, concrete, and filling material. The subgrade and backfill soil was modeled using the Mohr-Coulomb material model with the properties correlated to the results of standard penetration tests (SPT). Concrete was modeled using a linear elastic material model, which required only the modulus of elasticity and Poisson's ratio. The filling material (Bitumen Impregnated Fiberboard) modeled with the Hardening Soil model that was dependent on three different elastic moduli to capture the most realistic behavior of the material. These properties are summarized in Table 4-3.

Table 4-3. Material parameters

Layers	Unit weight unsat/sat (lb/in^3)	Modulus of elasticity, (ksi)				Poison ratio, ν		Friction angle, φ (°)	Dilatacy angle,	Cohesion,
		E	E_{50}^{ref}	E_{oed}^{ref}	E_{ur}^{ref}	ν	ν_{ur}		ψ (°)	c (psi)
Mohr-Coulomb										
Backfill	0.070	10.0	-	-	-	0.3	-	30	0	1
1st layer (0-5 ft)	0.062/ 0.074	2.9	-	-	-	0.3	-	34	4	1
2nd layer (5-15 ft)	0.062/ 0.074	5.9	-	-	-	0.3	-	34	4	1
3rd layer (15-25 ft)	0.062/ 0.074	8.1	-	-	-	0.3	-	34	4	1
Hardening Soil										
Filling material, Saturated	-	-	0.03	0.056	0.24	-	-	34	-	-
Filling material, unsaturated	-	-	0.23	0.21	0.65	-	-	34	-	-
Linear-elastic										
Concrete	0.08842	3307	-	-	-	0.2	-	-	-	-

4.5.1. Soil

Of the three built culverts, at the only provided subsurface data was for County Road 258 in Chambers County, where SPT borings were investigated up to 30-ft depth. The raw data for three boring logs are contained in Appendix B.

The measured N values from SPTs were corrected to N_{60} (Equation 4-7) following (Skempton 1986) procedure. In all cases, hammer energy (E_m) was assumed to be equal to 80%, since the borings were tested using an automatic hammer system. Correction factor C_R was taken equal to 0.95, as the depth of borings were up to 30-ft. As there was no information whether the tests were conducted using liners, the value of C_S was assumed to

be equal to 1.0 for the rods without liners. With no available information about the borehole diameter, the factor C_B was taken equal to 1.0.

$$N_{60} = \frac{E_m \cdot C_B \cdot C_S \cdot C_R \cdot N}{0.6} \qquad \textbf{Equation 4-7}$$

where:

N – recorded SPT value in the field;

E_m – Hammer energy efficiency;

C_B – Borehole diameter correction factor;

C_S – Sample barrel correction factor;

C_R – Rod length correction factor;

Based on the calculated value of N_{60}, the soil was divided into three layers (Figure 4-9):

1. Very soft, dark grey, fine sandy CLAY.
2. Medium dense, light grey, fine to coarse SAND.
3. Very dense, tan and light grey, fine to coarse SAND.

The required soil parameters for the analysis were (Figure 4-9**,** Figure 4-10) obtained in accordance with Meyerhof (1956) and Kulhawy et al. (1985).

The fourth soil layer represents the backfill. The characteristics of this layer were based on recommendations in (ASTM D1557-12e1 2012) for typical non-cohesive compacted soil.

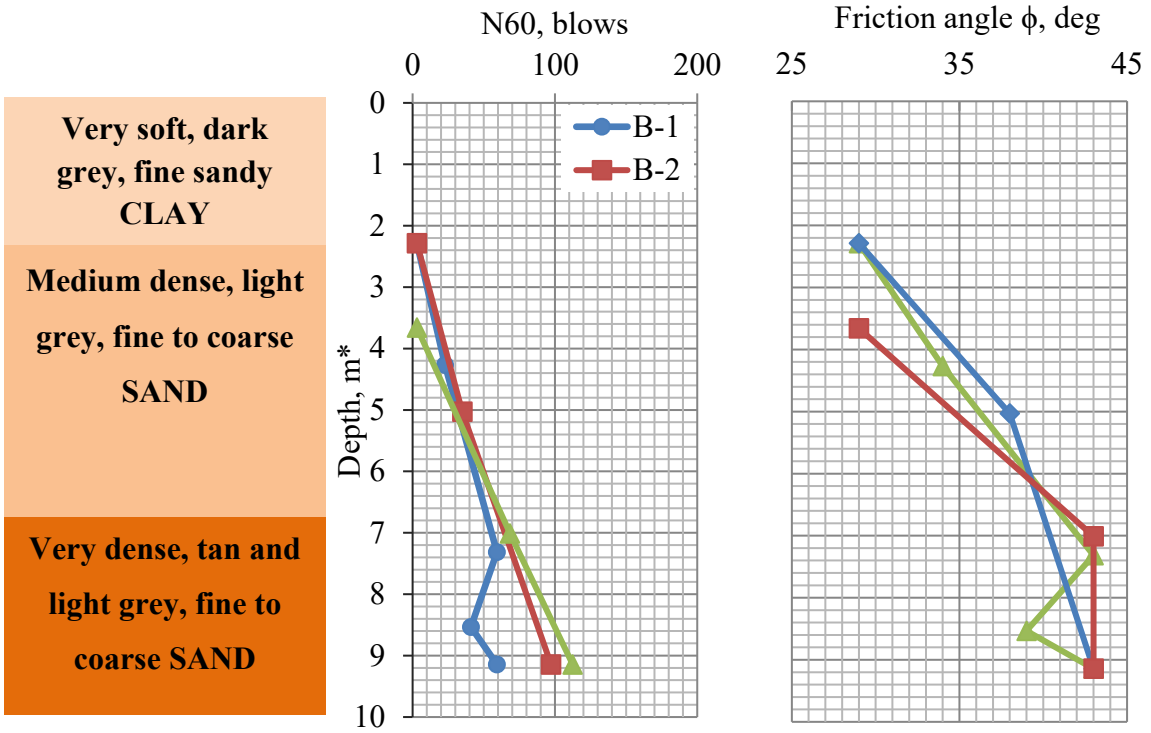

Figure 4-9. Friction angle for Chambers County borings.

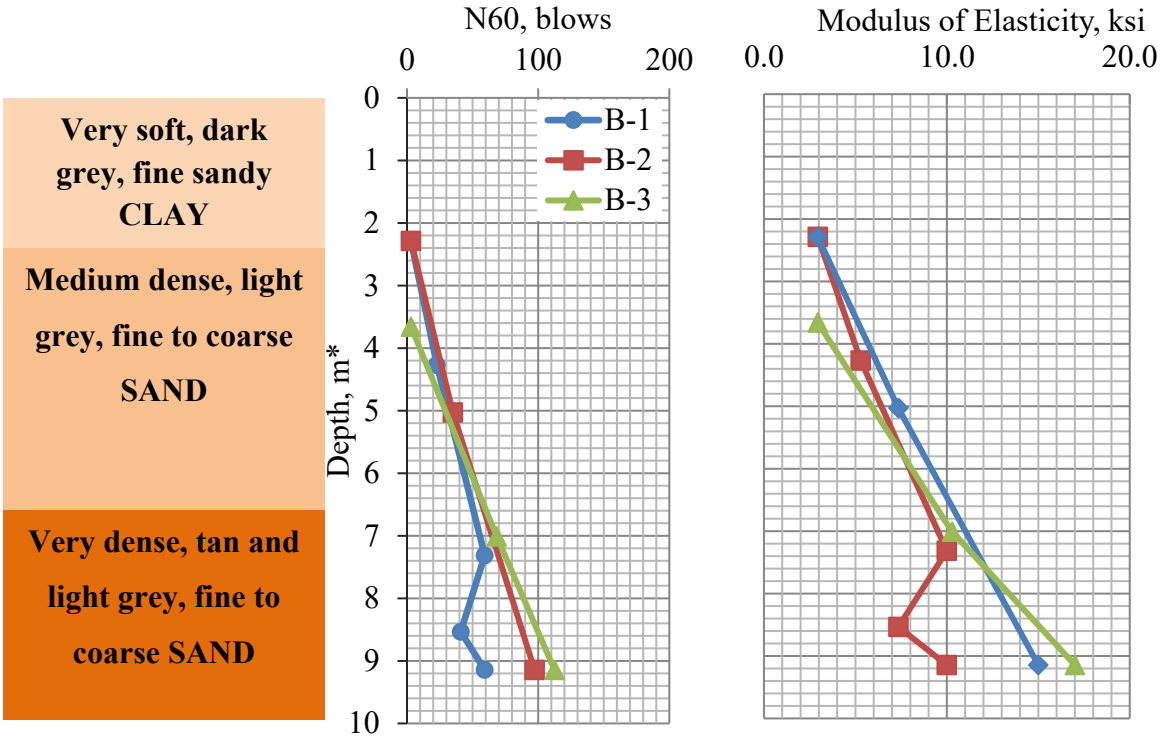

Figure 4-10. Modulus of Elasticity for Chambers County borings.

4.4.2. Filling Material

The joint between the culvert tab and the wing wall was filled with a 1/2-in thick Southern Pine Asphalt Impregnated Fiberboard (Figure 4-11b). Since the data on this material was limited, one-dimensional compression tests were conducted to obtain the stress-strain relationship. An instrumented load frame was utilized to conduct a set of tests (Geotac 2017) (Figure 4-11a).

The actual installed conditions of the filling material were not well defined. Therefore, the cases of saturated and unsaturated along with confined and unconfined boundary conditions. Saturated specimens were less stiff and more compressible. Thus, in the FE model, this filling material causes more deflection. However, when the material is considered unsaturated, it is less compressible but transfers more stresses. The confined specimens were trimmed to fit the confining ring with a diameter of 2½-in. The unconfined test was performed on specimens that were 0.1-in smaller than the ring.

The HS material model used in Plaxis requires the secant modulus E_{50}^{ref}, odometer modulus E_{oed}^{ref}, friction angle φ, *the* value of normal consolidation K_0^{nc} and unloading modulus E_{ur}^{ref} (Plaxis bv 2015c). Thus, this model was calibrated to represent the behavior of tested material adequately. The stress-strain curves obtained from conducted oedometer test scenarios are presented in Figure 4-12. The parameters required for the analysis were taken as follows (Figure 4-12): for saturated conditions, E_{50}^{ref} = 29.97 psi, and E_{oed}^{ref} = 56.01 psi; for unsaturated E_{50}^{ref} = 230 psi and E_{oed}^{ref}= 210 psi. The unloading modulus was calculated as $E_{ur}^{ref} = 3E_{50}^{ref}$, friction angle φ=34°, and the value of normal consolidation $K_0^{nc} = (1-\sin\varphi)$. Other material properties had the same magnitude for all considered cases.

The results of compression tests performed in Plaxis 3D for saturated and unsaturated conditions are shown in Figure 4-12.

a b

Figure 4-11. Assembled GeoJac loading frame (a). Southern pine asphalt impregnated board specimen (b)

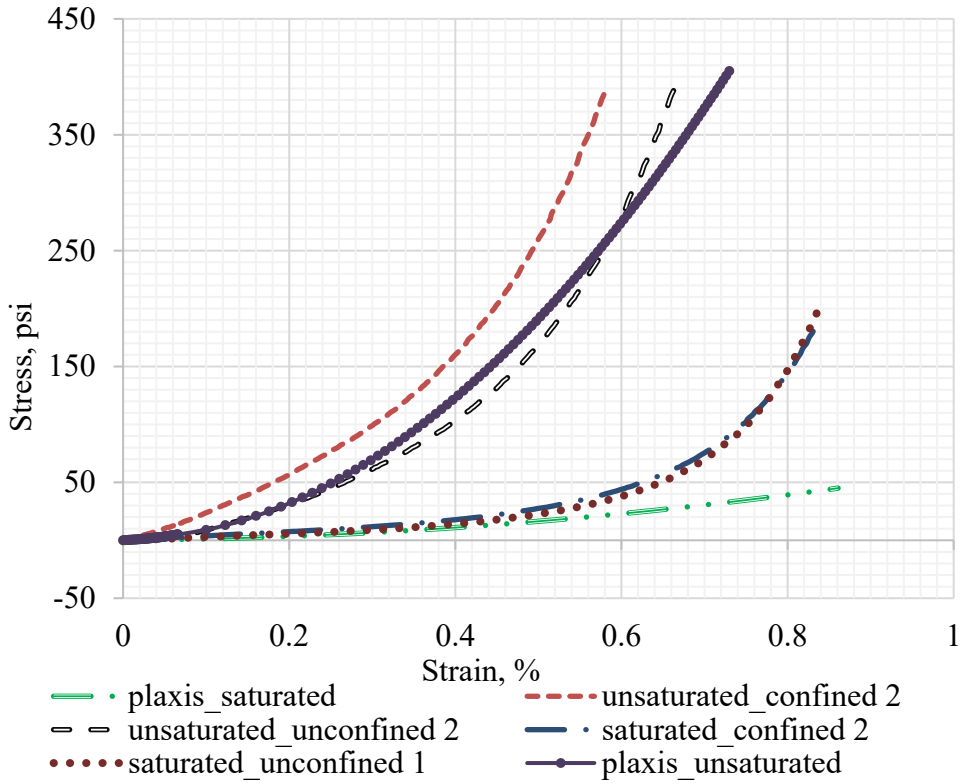

Figure 4-12. Stress-strain diagram of bitumen impregnated board

4.4.3. Concrete

Properties of the concrete were determined by testing concrete cylinders, formed during construction in accordance with (*ASTM C31/C31M* 2015) and (*ASTM C39 / C39M* 2017). Altogether, 14 samples were tested for the Chambers County culvert, six for the Lee County culvert, and eight for the Coosa County culvert. The distribution of determined moduli of elasticity is shown in Figure 4-13. The variation of concrete strength for the Lee County specimens was 10%, while it was 5% for Chambers and Coosa Counties. In the FE models, the conservative lowest value of modulus of elasticity was 3307-ksi, with Poisson's ratio of 0.2.

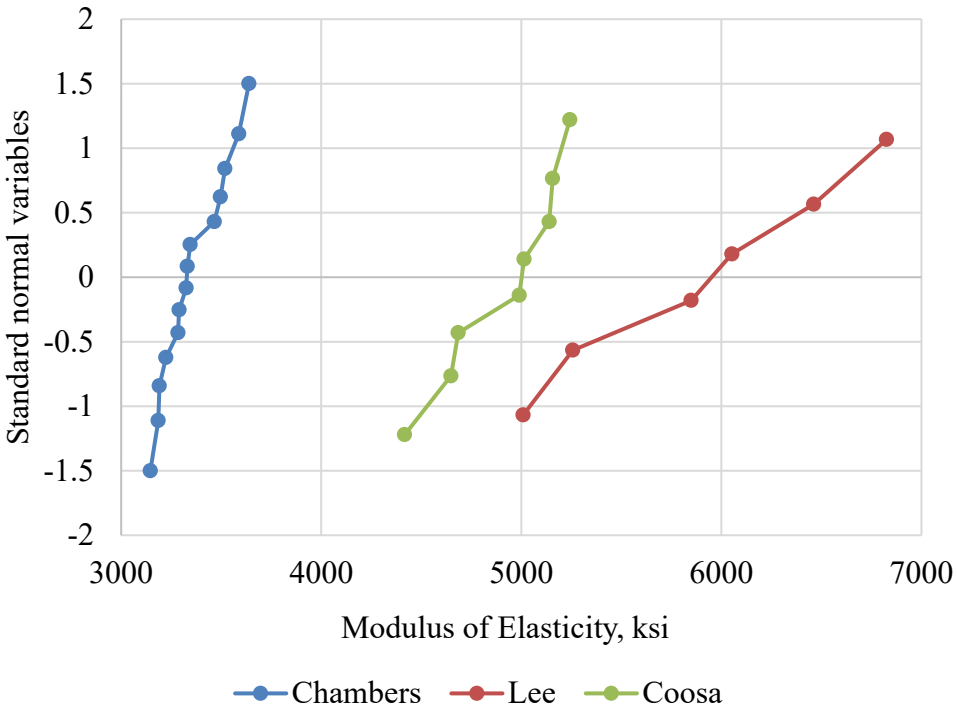

Figure 4-13. Variation of determined moduli of elasticity

4.6. Development of the Model

Plaxis 3D was specially developed to simulate various problems in geotechnical engineering. Structural elements or a whole structure can be embedded into the soil to analyze the behavior of the soil and structure under different impacts, as well as the soil-structure interaction. The available tools in Plaxis 3D allow the user to simulate the problem with relatively simple geometry, such as tunnels, slab foundations, piles, retaining walls, etc. However, creating more sophisticated structural forms with Plaxis, such as in the current study, has the following challenges:

- There is a lack of basic 3D geometrical objects (parallelepiped, pyramid, prism, etc.).
- Disproportional size and shape of structural elements. The meshing is complicated due to a significant difference in element size and sharp edges of the structure.
- There is no option for manual adjustment of meshed elements in Plaxis 3D.

To develop the model in Plaxis, the following steps are required:

- Soil modeling
- Modeling loads and structures
- Mesh generation
- Calculation phases and analysis

4.6.1. Modeling of the Soil

The working space geometry is specified prior to the other steps in order to provide the information for the future meshing. The dimensions of this volume are used to determine the finite element size (Equation 4-2). Also, elements outside this space are not subjected to meshing. In other words, they are completely eliminated from the analysis. In

the current project, the dimensions of working space were set to 747.5 x 520.1 x 695-in in X, Y, Z direction, respectively (Figure 4-14).

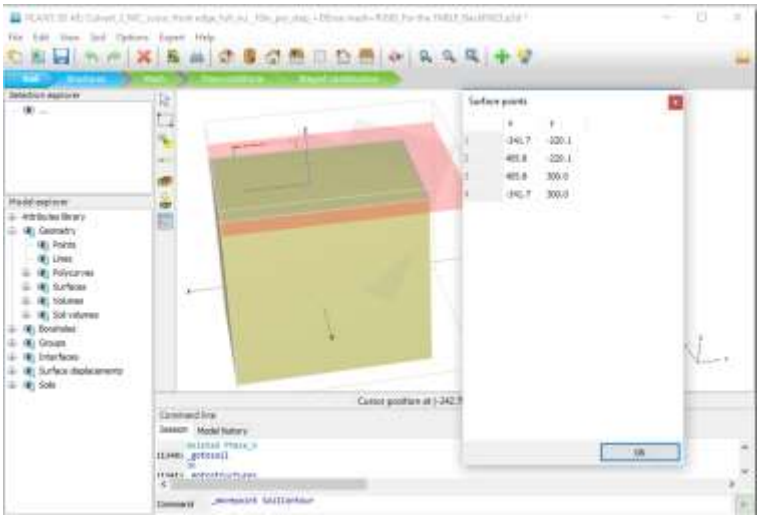

Figure 4-14. View of Plaxis 3D soil input interface

4.6.2. Modeling of Structures

To model the structure, Plaxis provides two options: import the structure shape directly from AutoCAD drawings or create the geometry using special tools. Plaxis 3D tolerate few errors during the import. It is therefore suggested to avoid importing the geometry from other software (Plaxis bv 2015b), since the importing can lead to the structural discontinuity. Thus, the culvert with the wing wall was modeled manually within Plaxis 3D (Figure 4-15). For this study, the models were developed using the geometry of the constructed culverts presented in Chapter 3. To minimize the time for analysis, only a quarter of the structure was modeled with symmetrical boundary conditions to account for the continuity. The only available option to create 3D culvert elements is to specify the geometry using 3D shell or surface elements and extrude them to the proper thickness with

further merging of the separate parts into the solid structure. To cover such a complex geometry, the number of surfaces varied between 20 and 50 for the different models.

The applied boundary conditions in both horizontal directions restrict only the corresponding transition and allow free movement in others. The vertical movement is restricted only at the bottom surface. The dimensions of the model were set to 43 x 62-ft in the plane and 25-ft deep. The depth was set large enough to develop the static failure modes and eliminate boundary effects.

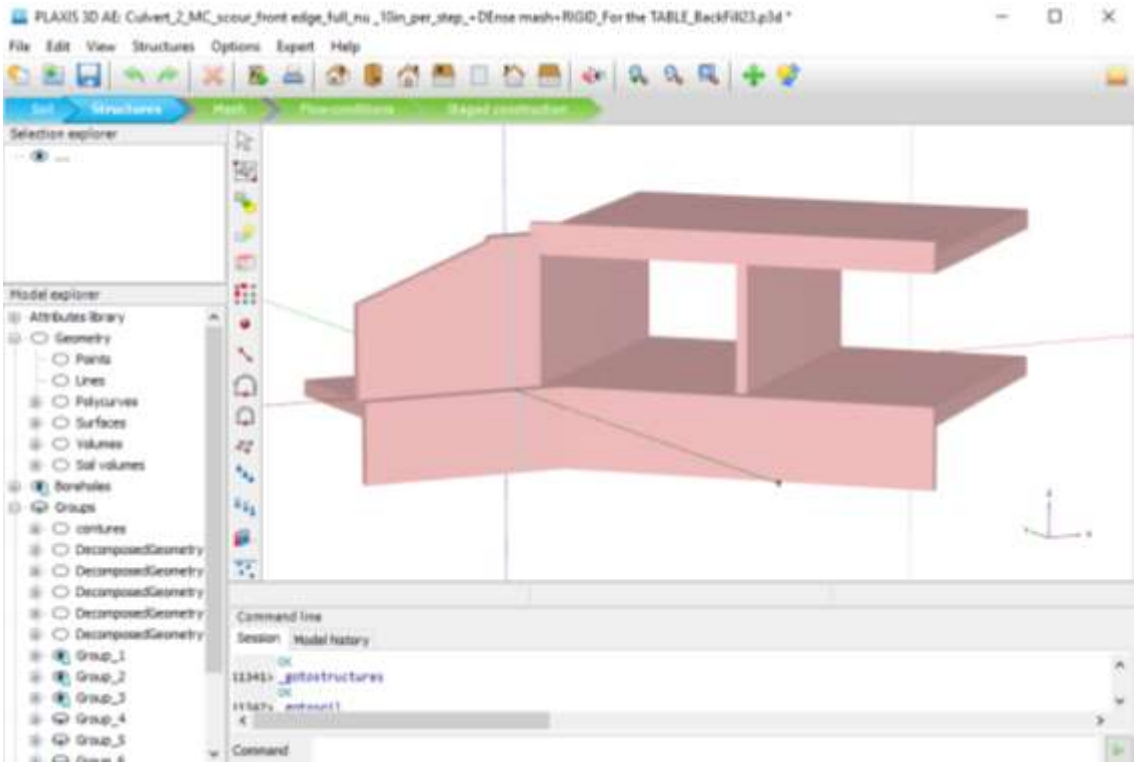

Figure 4-15. View of Plaxis 3D structural input interface

To understand the features of a new tab design, all models were duplicated with the same size but with wing walls rigidly connected to the barrel. The dimensions of the walls were taken the same as with a disconnected joint. The footing width was reduced accordingly similar to conventional monolithic design and the key wall was removed.

4.6.3. Modeling of Loads

In this study only static loads were considered. The main source of the load was the weight of the backfill soil. In FE models, it was specified as the unit weight for each material (Table 4-3) and distributed automatically. Other loads, such as surcharge and traffic, were applied as distributed over the area. The surcharge load included the 3-in paving layer that was applied over the one-foot soil layer on top of the culvert (Figure 4-16). Based on the unit density of the asphalt wearing surface of 0.140-ksf, the applied redistributed load was 0.035-ksf (0.000243-ksi). The traffic load was applied according to AASHTO (2014). Two load components were considered simultaneously: lane load and HL-93 tandem load. AASHTO LRFD (2014) specified the value of lane load is equal to 0.64-klf. As the analysis is performed in 3D space, the lane load needed to be redistributed over the area of the road width. In accordance with Section 3.6.1.2.4 of AASHTO LRFD (2014), lane load was assumed to be uniformly distributed over a 10-ft width. Thus, it was taken equal to 0.064-ksf (0.000444-ksi).

Since the maximum truck load effect on the wing wall was considered, the design tandem load was chosen as governing one of the design live load combinations. This load was applied in the closest possible position to the wing wall, where the truck can be located. It was estimated to be 3-ft away from the headwall and 1-ft from the barrel wall (Figure 4-16). The axle load was applied as uniformly distributed over the wheel area 20x10-in (Figure 4-17) with the magnitude of 4.52-ksf (0.03125-ksi).

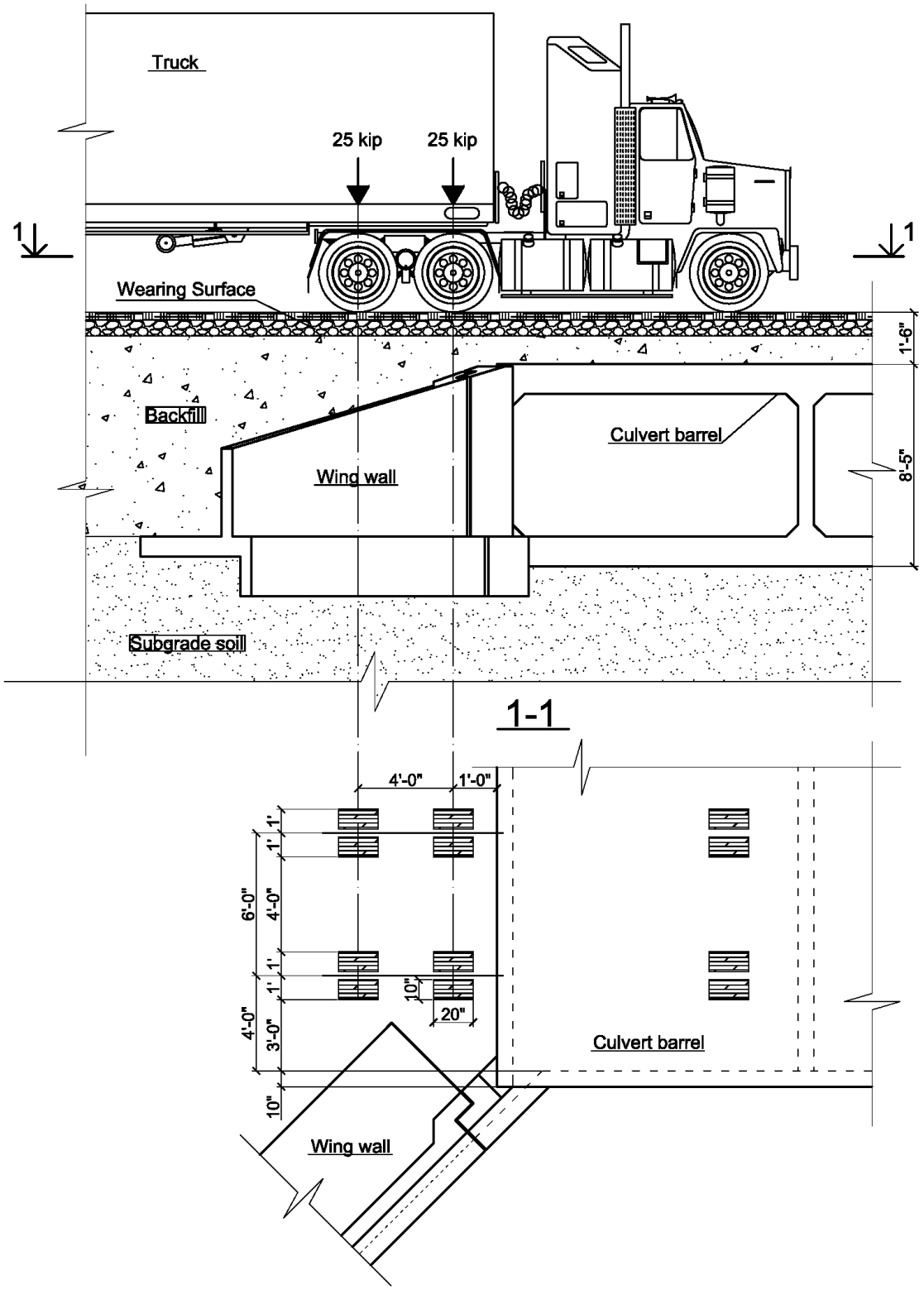

Figure 4-16. Design tandem load

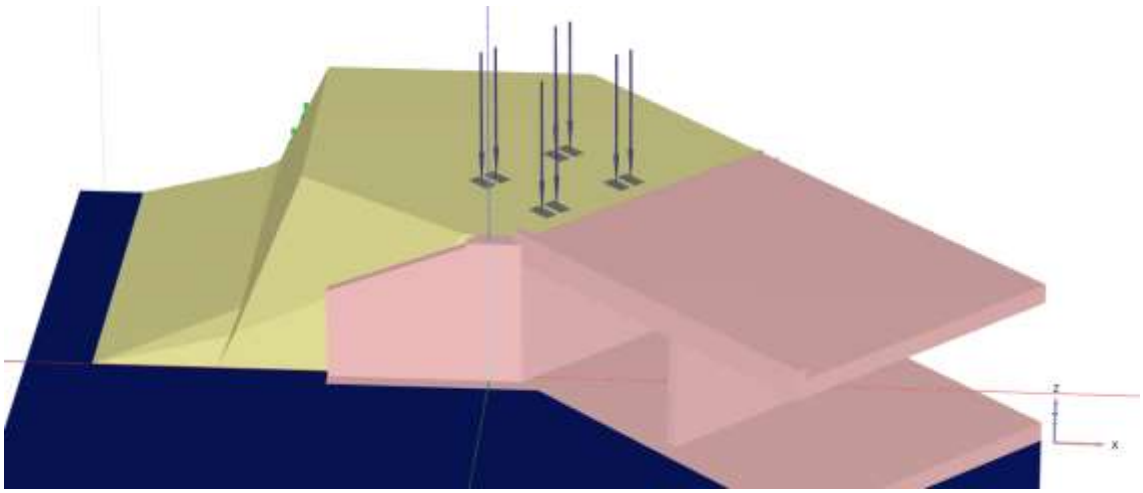

Figure 4-17. Tandem load in Plaxis 3D

4.6.4. Mesh Generation

This research study investigated the stresses transferred from the culvert barrel to the wing wall through the tab surfaces. Thus, the FE analysis was mainly focused on the contact zone of the wing wall. Plaxis 3D is an implicit FE program, which requires an iterative procedure to establish equilibrium within a certain tolerance on each step. Since their number directly affects the time of computation, the number of finite elements plays an important role in the analysis, especially in the parametric study.

To have comparable results, the mesh should be the same for each model. Without the option to manually generate it, the only alternative to controlling mesh coarseness is through relative element size factor. Thus, it was decided to divide the model into three regions based on element size (Table 4-4Table 4-4. Mesh statistics). The first group represents subgrade and backfill soil with relatively large element size. The second group, with medium element coarseness, includes the structural elements of the culvert barrel and the free end with the footing of the wing wall. Tab extensions with the filling material

between them were meshed with a very small element size (Figure 4-18, 19). This was done to have at least two elements within the filing material thickness and the width of the tab.

Table 4-4. Mesh statistics

	Relative element size factor	Element size, in	Element volume, in^3	Number of nodes	Number of elements
Soil	2.0	25.0-60.0	15.0 - 200000.0	251090	25109
Culvert	0.7	13.3	145.0 - 2400.0	41990	4199
Wing wall	0.0875	4.0-5.3	15.0 - 400.0	39450	3945
Gap	0.04	0.5-4.5	0.04 - 6.0	13270	1327
Interfaces	0.04-0.7	0.5-13.3	-	31290	5215
Total	-	-	-	377090	39795

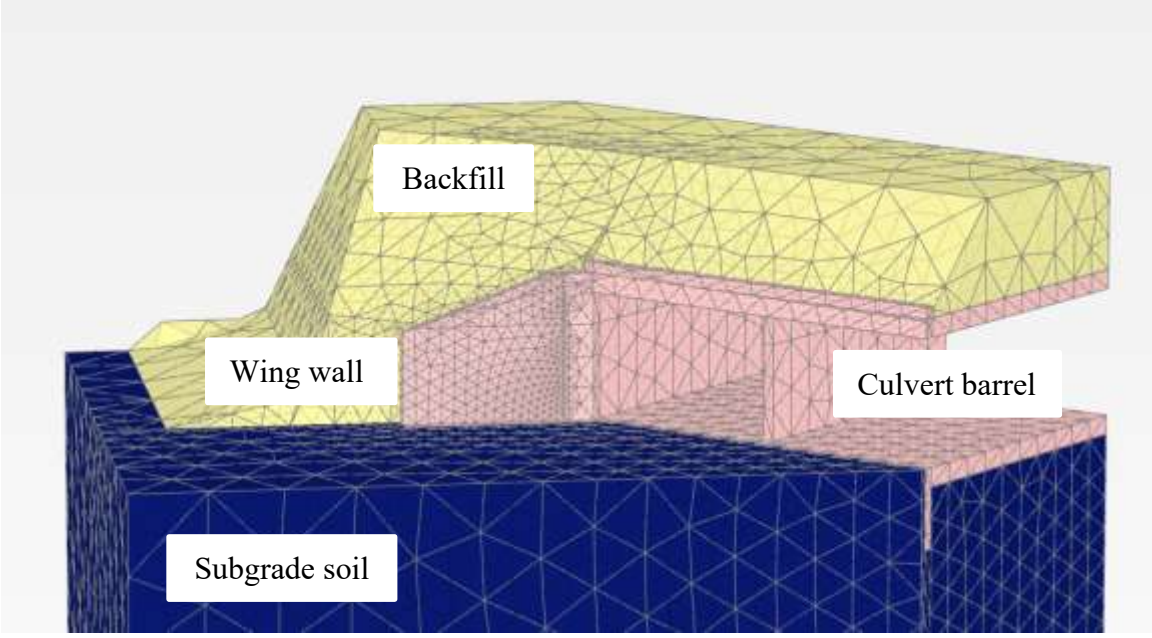

Figure 4-18. Scheme of the meshing of the culvert model.

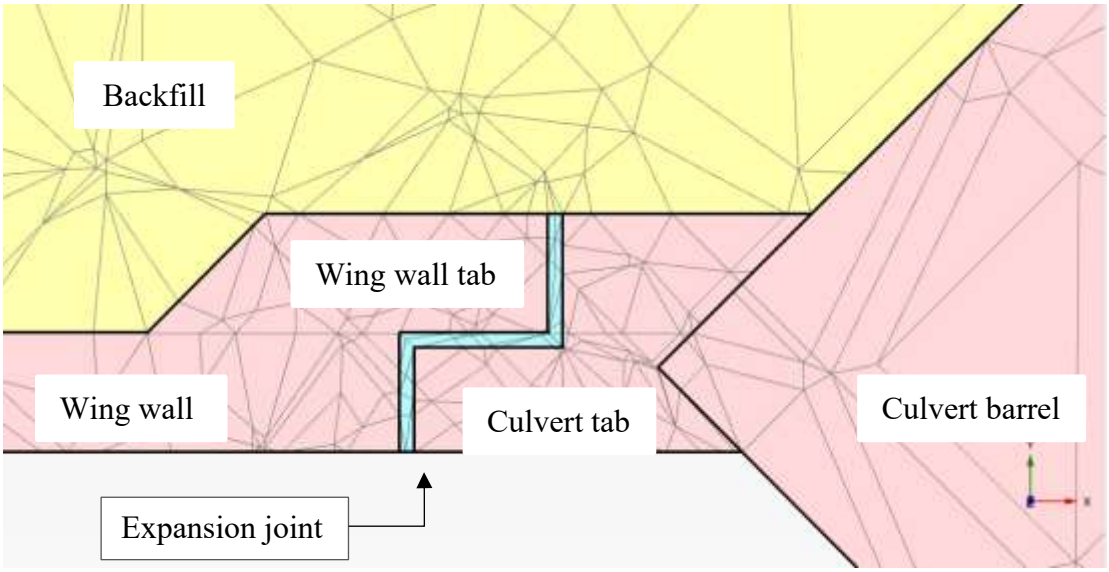

Figure 4-19. Meshing of the joint cross section

4.6.5. Calculation Phases and Analysis

The construction process consists of several sequential stages. Typically for retaining structures, the stages are as follows: excavation of soil, erection of the structure and backfilling. Each stage is characterized by the development of specific stresses and displacement. Except for design conditions, the structures can also experience erosion processes and other extreme events. Thus, to analyze the actual behavior of the structure, different stages of construction along with different load scenarios were included in the analysis.

For the culverts considered in this research, the stage analysis was divided into six primary phases with design loads. Scour development was modeled with using 15 to 20 additional phases.

The considered stages are:

0. Initial stage or K_0 procedure. The soil is a stress-dependent material, so the stress conditions of the undisturbed soil mass must be determined. At this stage, the model represents the site conditions before the construction (Figure 4-20). As the stream bed level was not defined, the initial phase represents the condition before construction. The excavation phase was not considered.

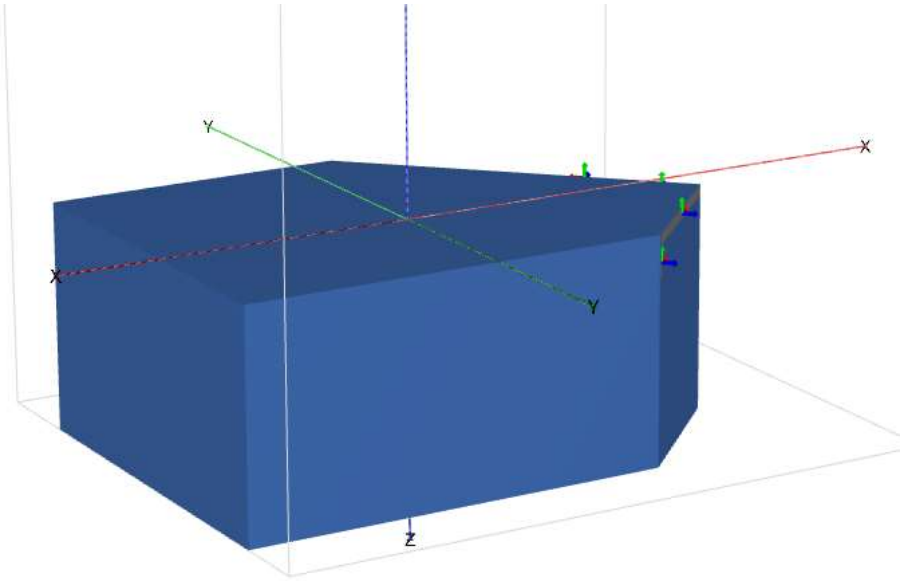

Figure 4-20. The initial stage of the analysis.

1. Placement of the culvert along with the wing wall (Figure 4-21). During this phase, the culvert barrel with the wing wall were activated/erected. No additional load except the self-weight of the structure was considered. The whole culvert was simulated instantly, excluding concrete pouring. The relative movement of both components along with interaction between them was recorded separately due to their independent settlement.

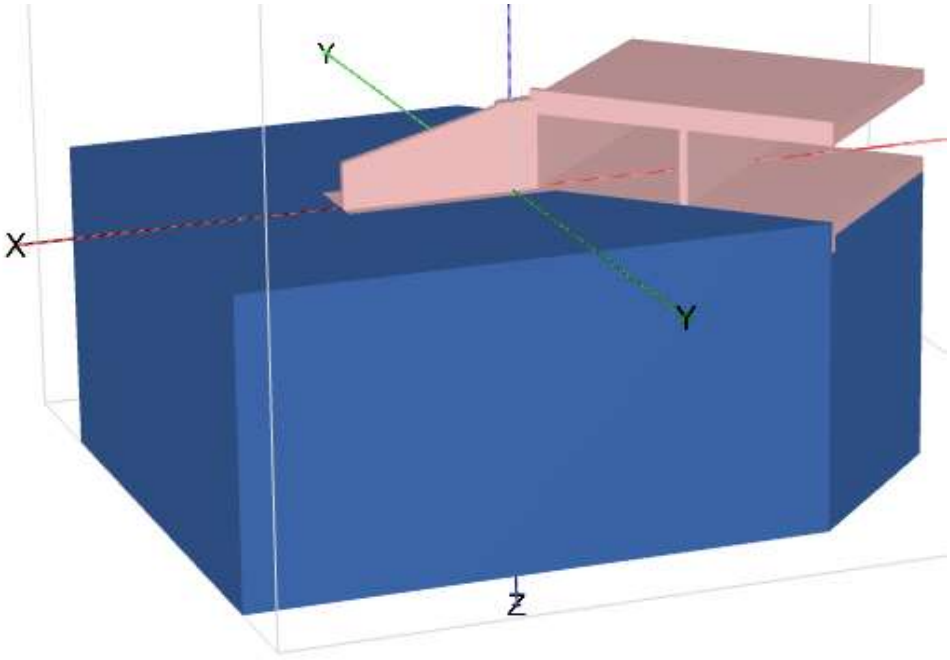

Figure 4-21. Placing the culvert with a wing wall

2. Backfilling to the level of the culvert (Figure 4-22). As it was observed on the field, the backfill was placed and compacted within one day to the same level with the culvert barrel. Thus, it was simulated within one phase for the culverts up to 10-ft deep. For deeper culverts, this stage was divided into two steps: filling backfill to the mid-height of the culvert, and then from the mid-level to the top. The dynamic effect of compaction was not considered. The obtained stresses and displacements of the wall and the tab recorded during this stage will be further compared with the field test results.

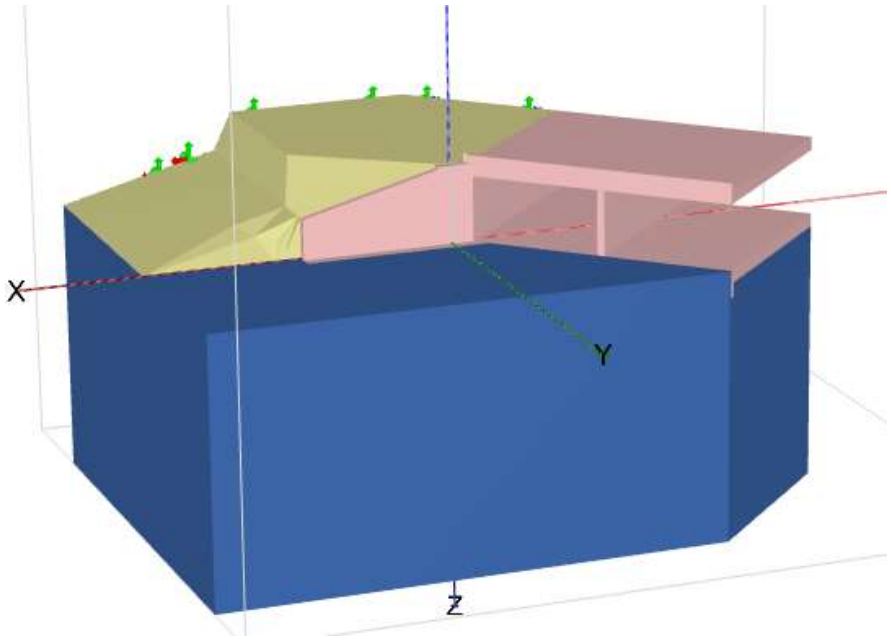

Figure 4-22. Backfill to the level of the culvert

3, 4, and 5. Backfilling gradually raised up to 23-ft (Figure 4-23). During these stages, the effect of deep backfill on the development of stress along the tab surface was studied, as well as the behavior of the wing wall.

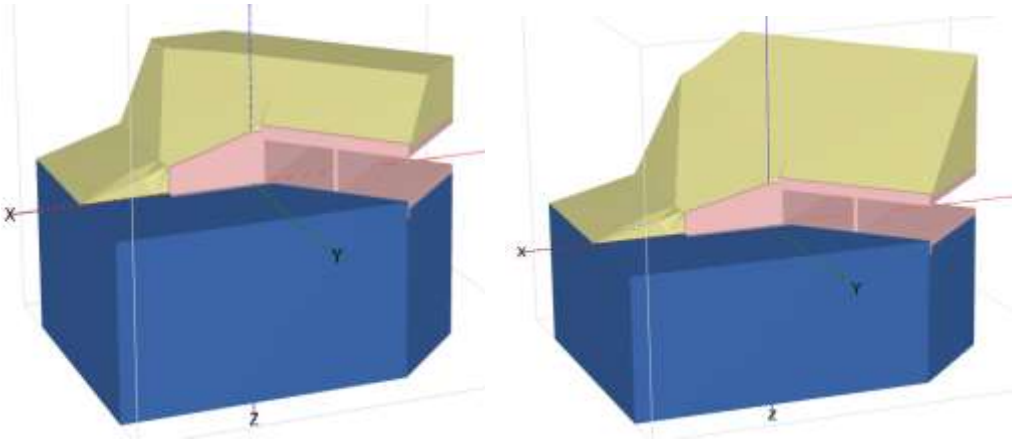

Figure 4-23. Backfilling 6-ft above the culvert (left picture), and 23-ft above (right picture)

6. The traffic load was modeled with a 1-ft soil layer at the top of the culvert similar to the constructed culverts. This phase was divided into two stages. First, the surcharge load was modeled only with the lane load. The second case included a combination of lane and tandem loads applied in the position described in Section 4.6.3 (Figure 4-24).

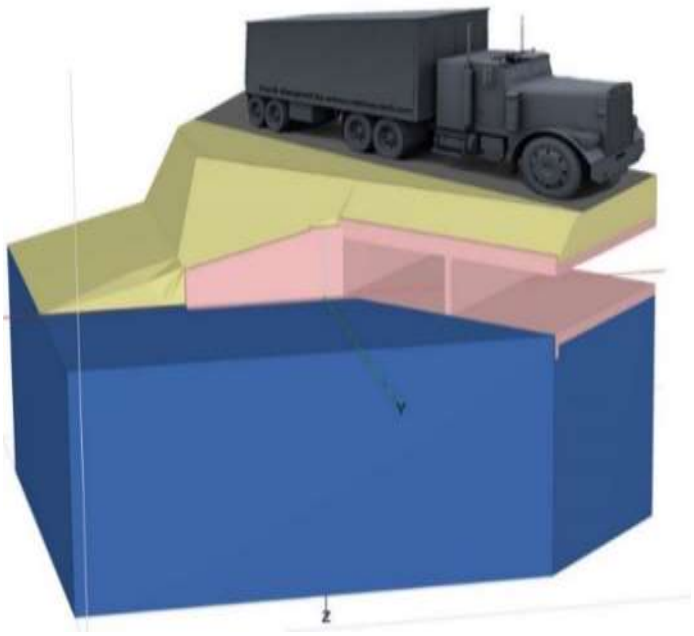

Figure 4-24. Visualization of traffic load

7. Scour effect. The series of phases between 15 and 20 were developed to consider the effect of an extreme event, such as scour, on the wing wall behavior. Erosion due to scour was model by removing 5-10-in of soil per stage as shown in Figure 4-25 for rigidly connected and disconnected wing wall to culvert joint.

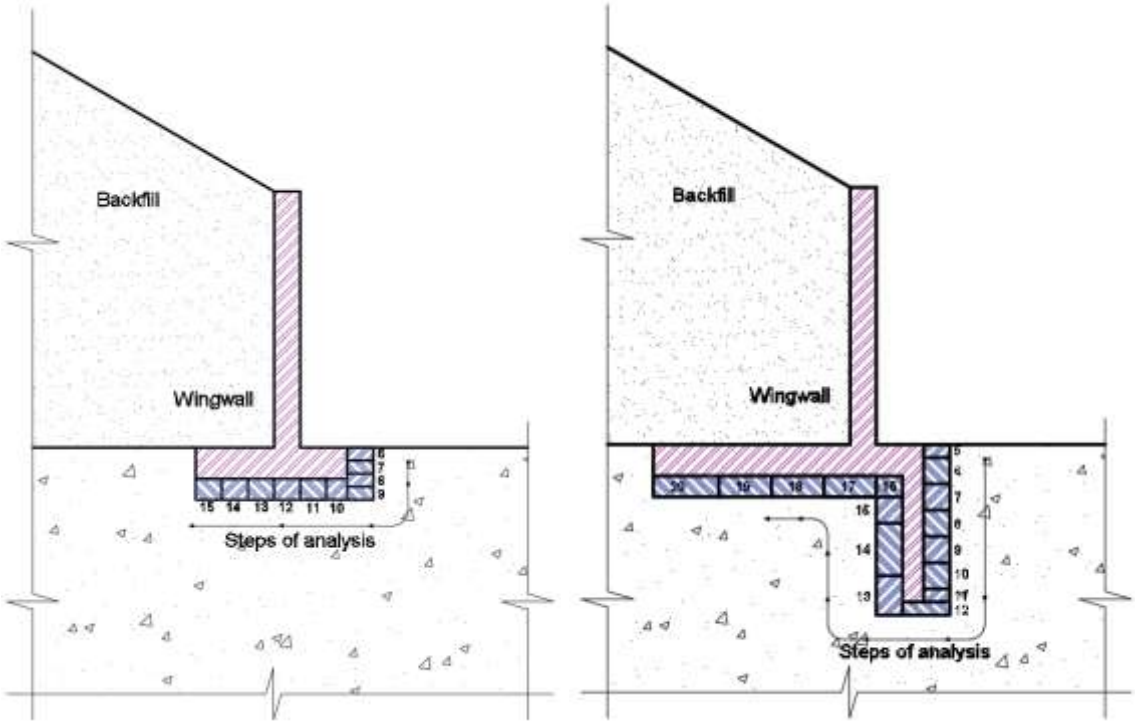

Figure 4-25. Development of the scour in the analysis for rigid connection (left picture) and disconnected joint (right pictures)

4.6.6. Sign Convention

For convenience, the directions of displacements and compression stresses normal to the joint surface were set the same for all models (Figure 4-26). Unlike typical geotechnical convention, Plaxis 3D has the following sign convention:

8. Compression stresses –"-".
9. Tensile stresses – "+".
10. Displacement in axes direction – "+".

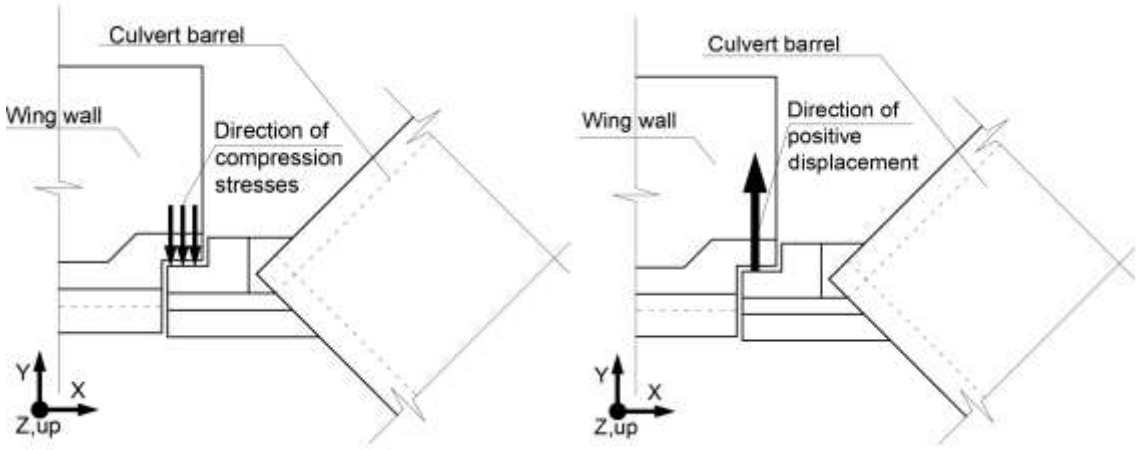

Figure 4-26. Directions of compression stresses (left picture) and positive displacement (right picture)

4.7. Verification

4.7.1. Sign Convention

Verification of the correctness of a soil pressure distribution in a 3D model with a soft foundation is a complicated problem. Therefore, a classical retaining wall with fixed base conditions was created. The height of the wall was taken 9.1-ft (Figure 4-27a). Soil and concrete properties were used as described in Section 4.5. The lateral earth pressure distribution on the wall surface was calculated using active earth pressure coefficient K_a calculated in accordance with Rankine theory. The comparison of theoretical pressure distribution and obtained from Plaxis 3D are shown in Figure 4-27b. The difference between two methods are within 5%.

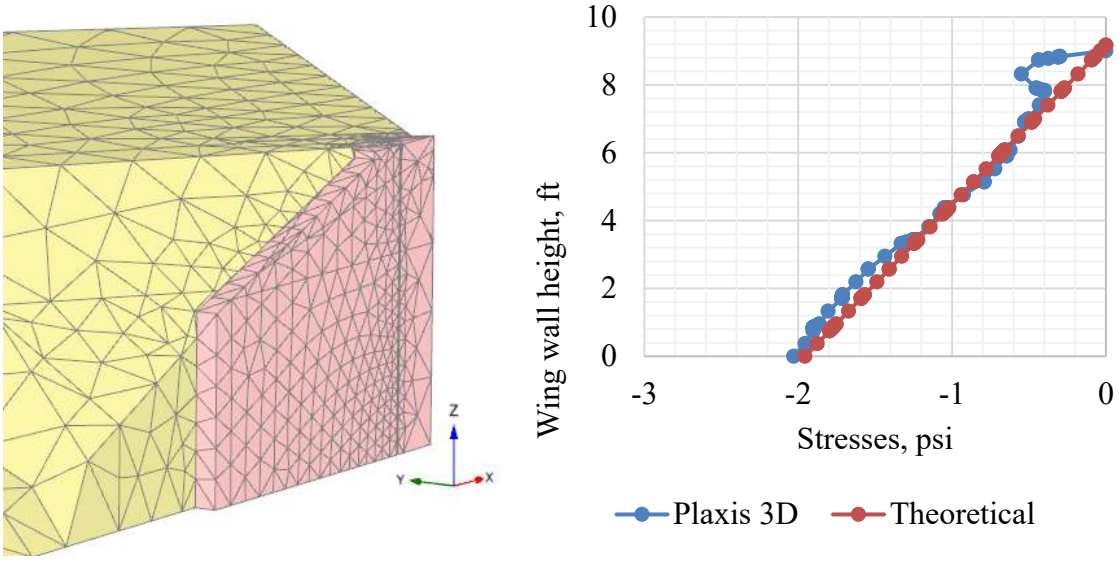

a b

Figure 4-27. a) 3D FE model; b) Earth pressure distribution on the wall surface

4.7.2. Interface Elements

One of the most important parts in simulation and analyzing the behavior of soil structure interaction is proper modeling of the contact surface between them. To model the contact surface, Plaxis 3D has a special interface element. This element simulates the interconnection between two different materials involving their physical properties. The behavior of surface interface element is explained in detail in Chapter 4.2.

Since it is complex to understand and verify the behavior of interface element using a full-scale 3D model, a simplified model was created. This test model was created in accordance with a theoretical example provided by Plaxis (2010). It consists of two linear solid blocks with a non-linear interface between them (Figure 4-28). The blocks were modeled as a stiff linear elastic material with a modulus of elasticity E=4351-ksi and Poisson's Ratio ν=0.

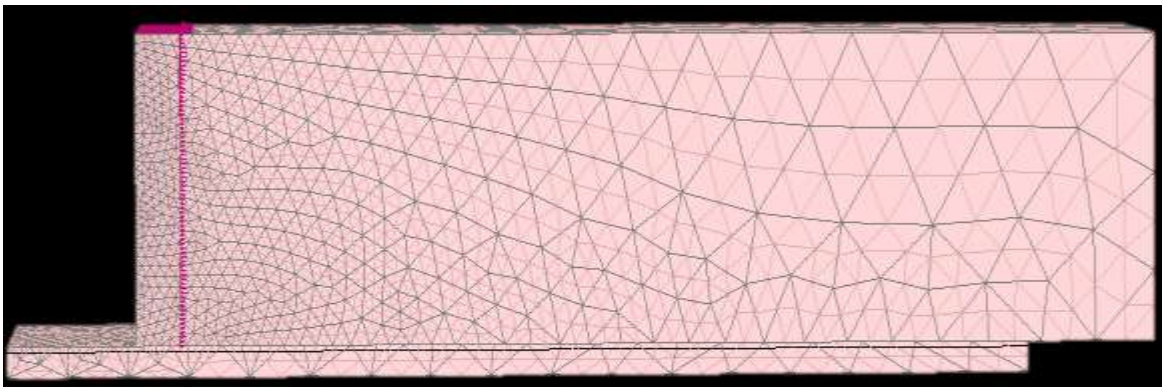

Figure 4-28. Deformed shape of the sliding block

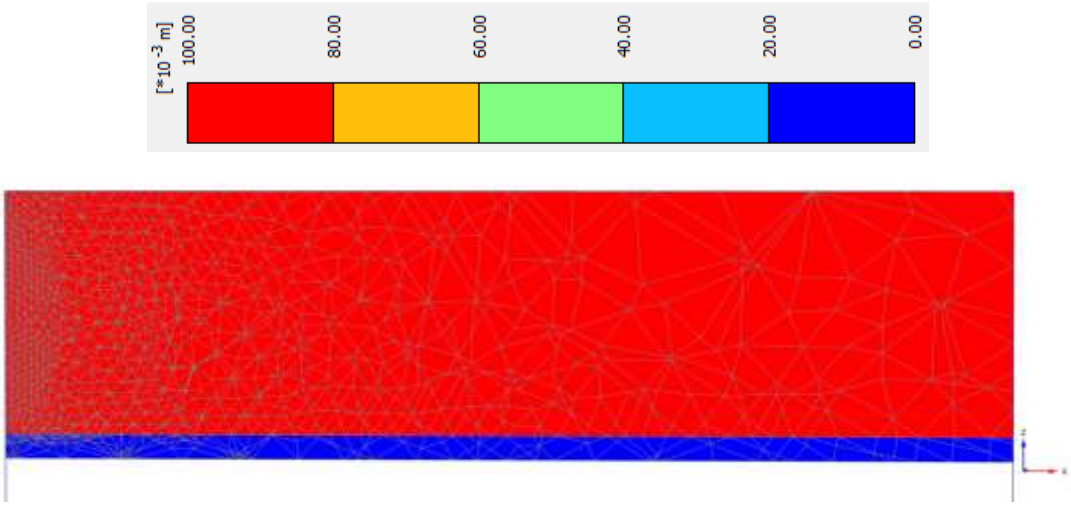

Figure 4-29. Contours of deformation along the block.

The interface was simulated with the Mohr-Coulomb material model defined by a modulus of elasticity ten times lower them the block material (E= 435.1-ksi), Poisson's Ratio ν=0.45, friction angle φ=26.6° and cohesion c=0.363-psi. The unit weight of the box was 0.092-pci. The load was applied in the form of a horizontal prescribed displacement of 3.94-in (0.1-m) to one side of the solid block. All nodes of the bottom block were fully restrained, and all nodes of the top block were free to move.

There was no significant deformation of the rigid body under applied load. However, large movement was observed along the contact surface, and equal to the applied prescribed displacement (Figure 4-30). The distribution of shear stresses along the interface

is shown in Figure 4-30. The maximum shear stress at failure was 8.89-psi (61.31-kN/m^2) which appeared on the right side of the model due to the development of rotational moments (Figure 4-30).

As no exact theoretical solution exists for verifying the internal stress distribution, the maximum shear stress can be calculated as:

$$\tau_{max} = width * c + \gamma \cdot tan\varphi = 4m * 2.5\frac{kN}{m^2} + \frac{25kN}{m^3}\tan(26.6) * 4m$$

$$= 8.72psi(60.1\frac{kN}{m^2})$$

The results of numerical and theoretical solution were within 2%.

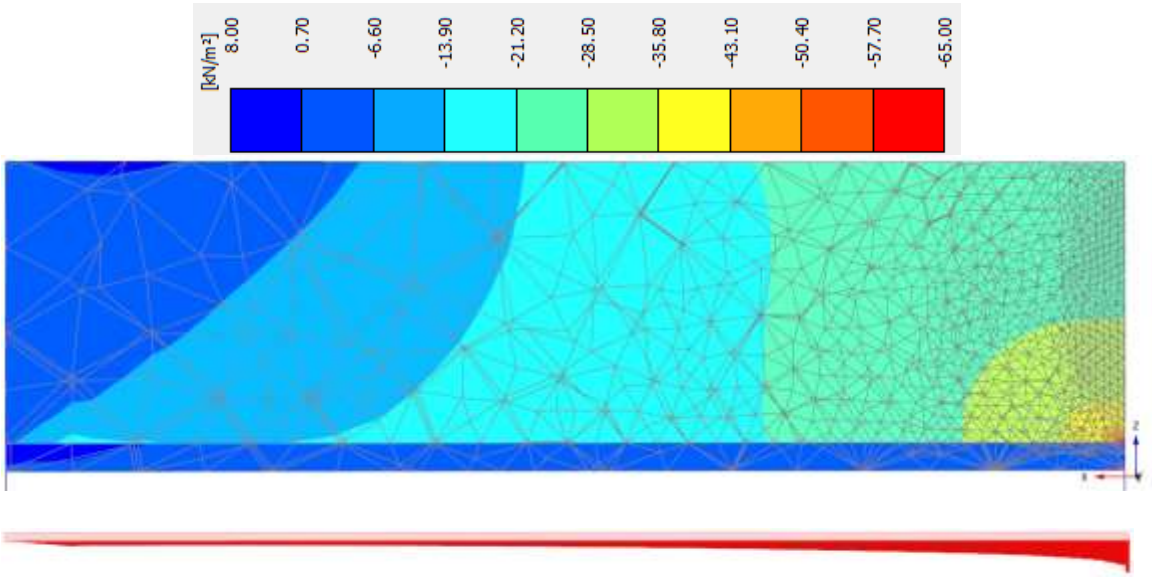

Figure 4-30. Shear stress distribution along the contact surface.

Chapter 5. Field Measurement of Culvert Tab Loading

5.1. Introduction

One the objectives purposes of this project was to estimate the magnitude of force or pressure that transfers between tab extensions. To fulfill this goal, pressure sensors were installed in the wing tabs of three culverts constructed for the project. In addition, relative movements of the top of the walls were recorded. This section summarizes the selection and installation of the instrumentation along with the measured results. The complete, step-by-step, description of sensor installation, equipment calibration and field measurements was detailed in Lee (2017).

5.2. Field Measurement of Lateral Earth Pressure

Model GK-4810 vibrating wire earth pressure cells manufactured by Geokon, Inc were used to measure the magnitude of the pressure between tabs, (Figure 5-1). These sensors were selected because of several factors. First, they are specially designed to measure the earth pressure under a spread footing foundation, or similar structure. Second, the magnitude of stress predicted by numerical modeling fell within the available stress range (0 to 50 psi) of the sensor. The third reason was the dimensions of the cell were such that they could be easily installed in the tab. The outer diameter of the sensor was 9-in and thickness was ½-in, which is smaller than tab width of 12-in.

The sensors consist of two thin plates welded together along their circumference and the gap between them filled with hydraulic fluid. This specific model had a rigid plate

on one side that was made for attachment to hard surface like concrete. In this case, the rigid plate side was attached to the structure and flexible side faced the tab gap with the intent that it would deform under applied pressure if the gap were to close (Figure 5-1).

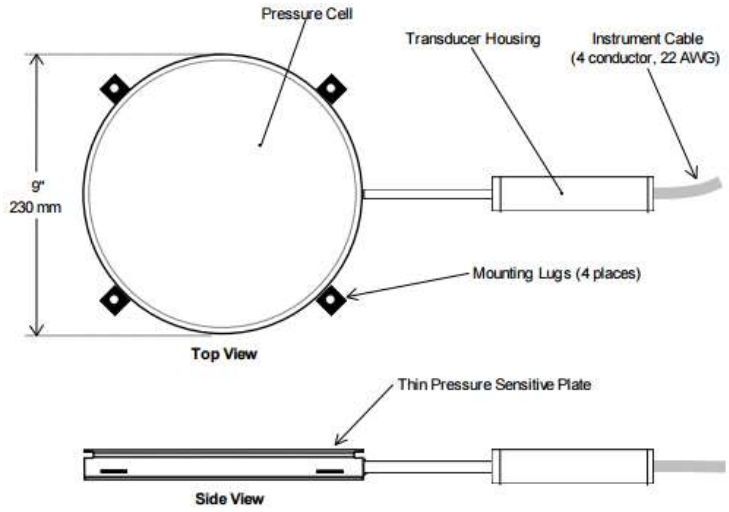

Figure 5-1. Contact pressure cell (Geokon, Inc. 2011)

Each instrumented tab contained three pressure cells uniformly distributed along the height. One placed 1-in from the bottom of the tab, one placed 2-in below the top of the tab, and another placed at the center (Figure 5-2). The cells were installed on the culvert side of the tab in a recess formed in the concrete. The wing walls were constructed, so that, the surface of the wing tab and sensors were in a full contact through the gap filling material. The cables were attached to the tab surface so that they would not pass in front of the cells (Figure 5-3).

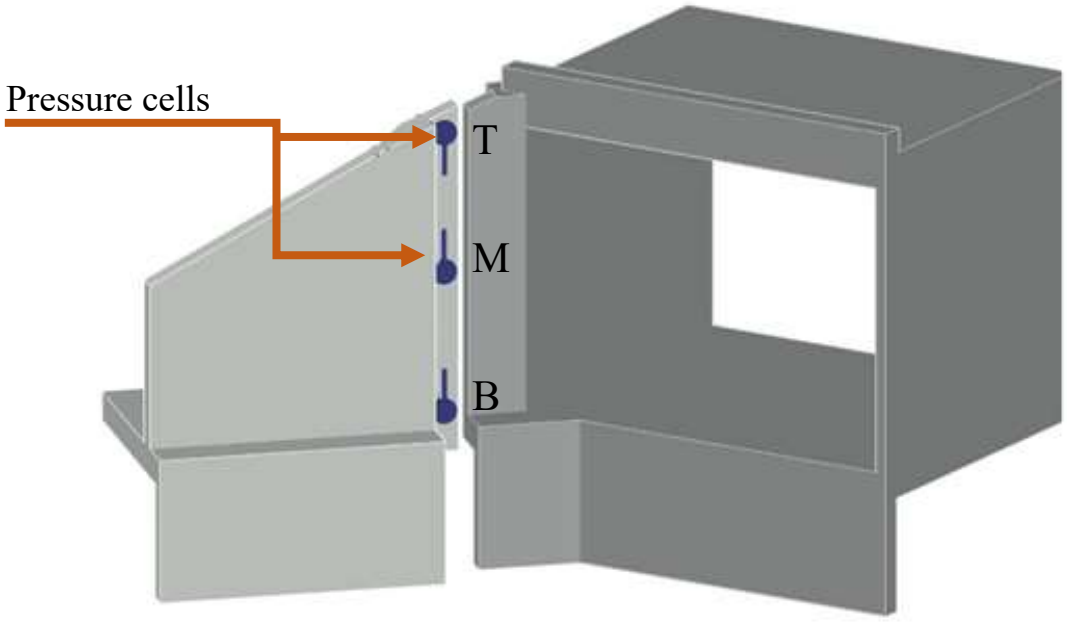

Figure 5-2. Location of the pressure cells

Figure 5-3. Post installed pressure cells (Lee 2017)

5.3. Tab Pressure

The pressure cells were monitored from the day sensors were installed until the last month of monitoring, which was December 2017. The data was recorded on a monthly basis for the three constructed culverts. The monitoring of the Chambers County culvert started on July 6, 2015, and contained 27 readings for each tab. The construction of the Lee County culvert was finished on March 3, 2016, and has 38 readings for each tab. In the case of the Coosa County culvert, sensors were installed only in two tabs due to an error with a formwork during construction. The monitoring of this culvert started on May 5, 2016, and only 15 readings were taken due to travel distance. The data recorded before March 14, 2017, was recorded by Lee (2017) and after this date, by the author.

The readings from pressure cells are presented in this section. The distribution of recorded pressure in the tabs from all three culverts shows the same trend. After backfill was placed, pressure increased almost to its maximum value and over time gradually reduced to almost zero. However, fluctuations of pressure occurred within the monitoring period due to environmental factors - predominantly rain. The maximum observed pressure typically occurred at the bottom of the tab.

5.3.1. Chambers County Culvert

The normal pressure in all tabs was less than 1-psi after construction was finished and until the backfill was placed. The pressure was t recorded immediately after the backfilling due to miscommunication with the construction crew. The maximum recorded pressure in the tab after the backfilling observed in tab #1 was 2.9-psi (Figure 5-4). Also, pressure peaks up to 5.7-psi were recorded in tab #1 due to significant rain. These peaks gradually reduced to 2-psi at the bottom and zero at the middle and top sensors. Stresses

recorded at tab #2 (Figure 5-5) after backfilling were 0.7-psi and 0.8-psi following rain. During the remainder of the monitoring period, they oscillate around zero. In tabs #3 and #4 maximum recorded pressure of 6.7-psi was during culvert construction (Figure 5-6,7). During the remaining monitoring, pressures in these tabs oscillated between 0 and 1-psi.

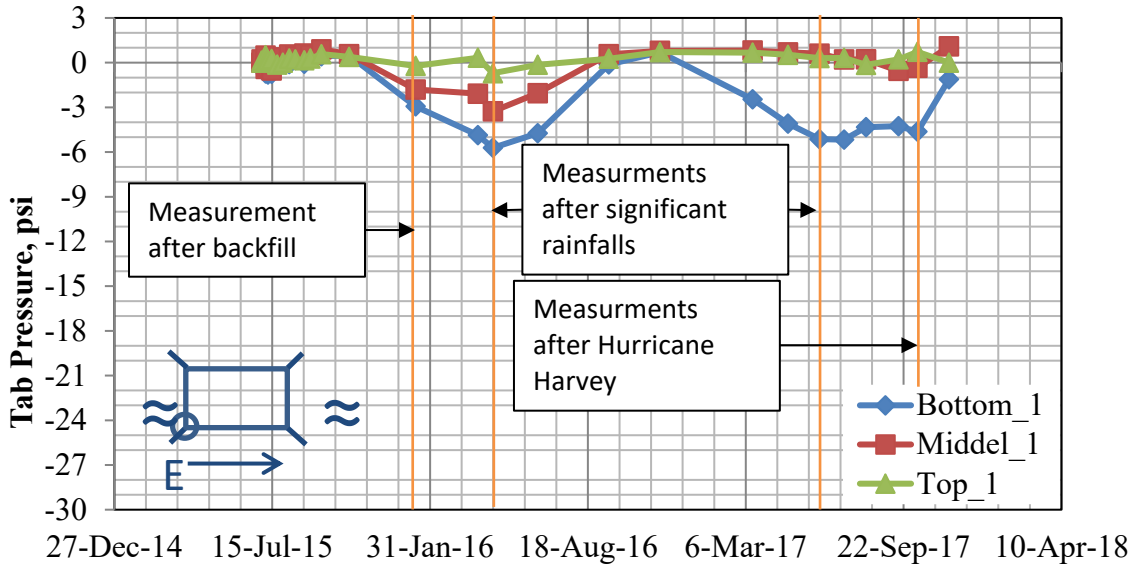

Figure 5-4. Chambers County tab #1

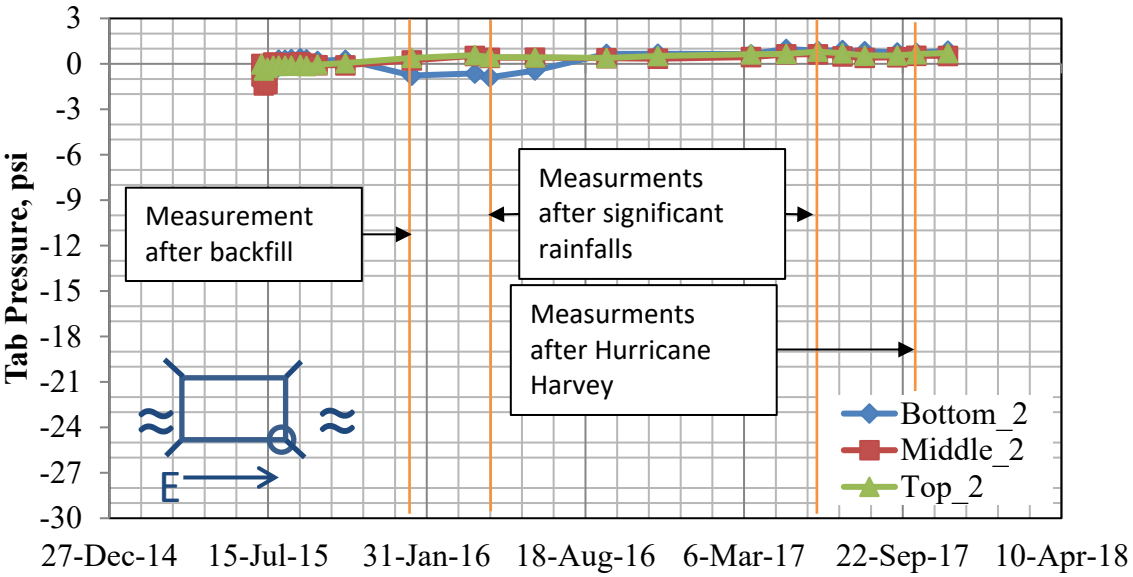

Figure 5-5. Chambers County tab #2

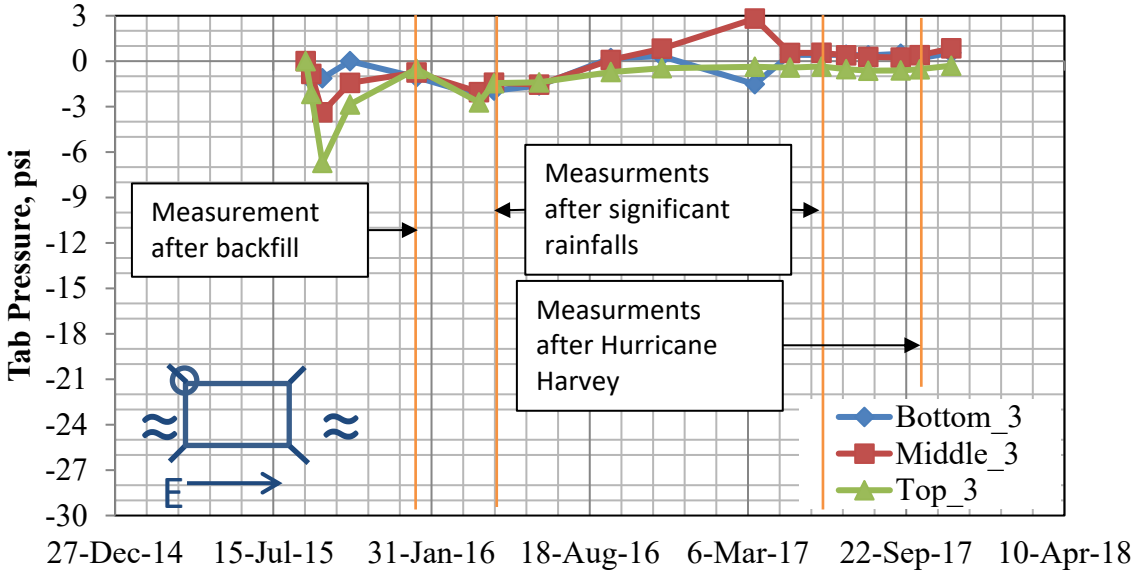

Figure 5-6. Chambers County tab #3

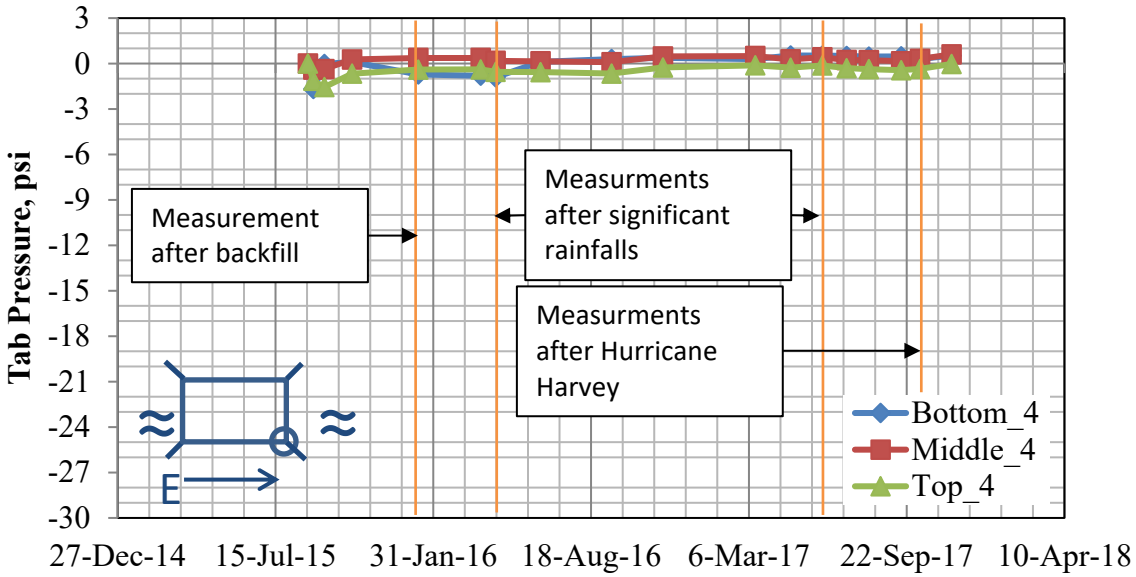

Figure 5-7. Chambers County tab #4

5.3.2. Lee County Culvert

Unlike the Chambers County culvert, the maximum pressure in Lee County culvert was recorded on August 29, 2016, immediately after the backfill was placed and compacted. In addition to backfill, these measurements include the effect of an

approximately 80-kip truck parked as close to each tab as possible. The maximum pressure in tab #1 after the backfill was 26.6-psi at the bottom, 3.6-psi in the middle and zero at the top sensors. Within a short period of time, the pressure magnitude decreased to 14.6-psi at the bottom and 1.8-psi in the middle (Figure 5-8). Also, the stresses in tab #1 were the maximum observed among all instrumented tabs. The pressure in tab #2 after the backfilling was 17.6-psi, 11.7-psi, and 4.5-psi at the bottom, middle and top sensors, respectively (Figure 5-9). Similar to tab #1, the pressure magnitude decreased to 9.3-psi at the bottom, 5.5-psi in the middle, and 1-psi at the top, which remains the same for the recorded period. Pressure recorded in sensors installed in tab #3 remained constant during the monitoring period. The average pressure 2-psi was recorded by the bottom sensor, 0.3-psi by the middle and zero by the top (Figure 5-10). Unlike other tabs, the pressures detected by sensors in tab #4 did not decrease with time after placing backfill. The average value at the bottom was 10-psi during the monitoring period and around 1-psi at the middle and top sensors (Figure 5-11).

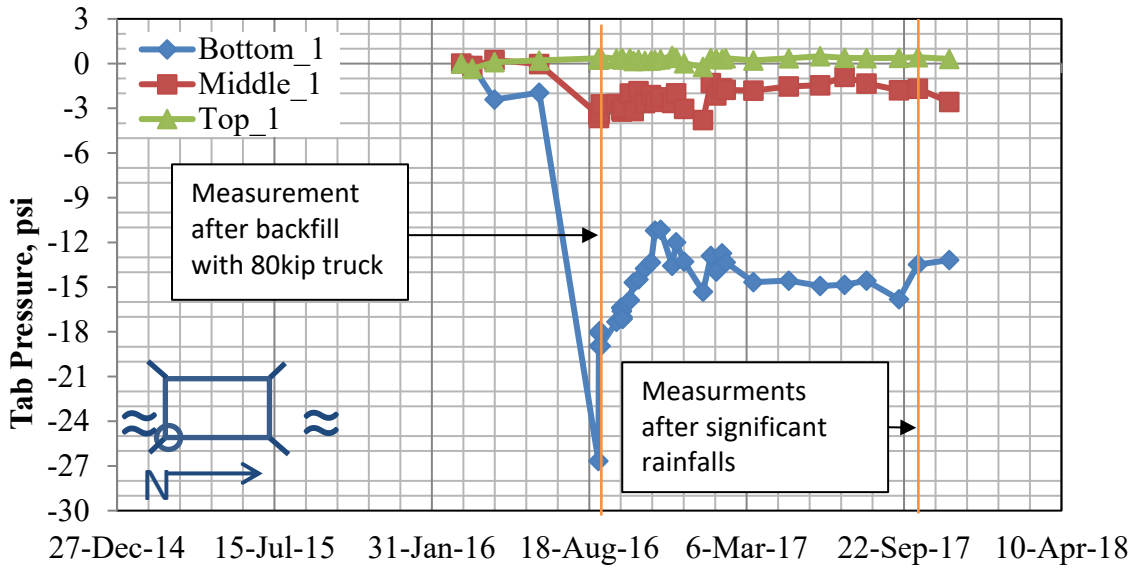

Figure 5-8. Lee County tab #1

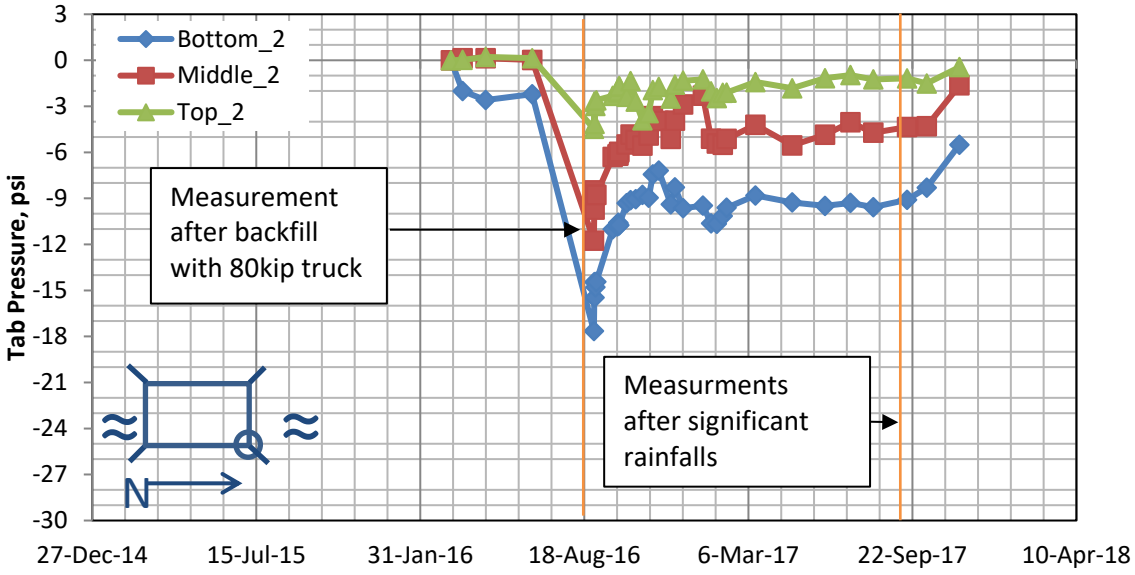

Figure 5-9. Lee County tab #2

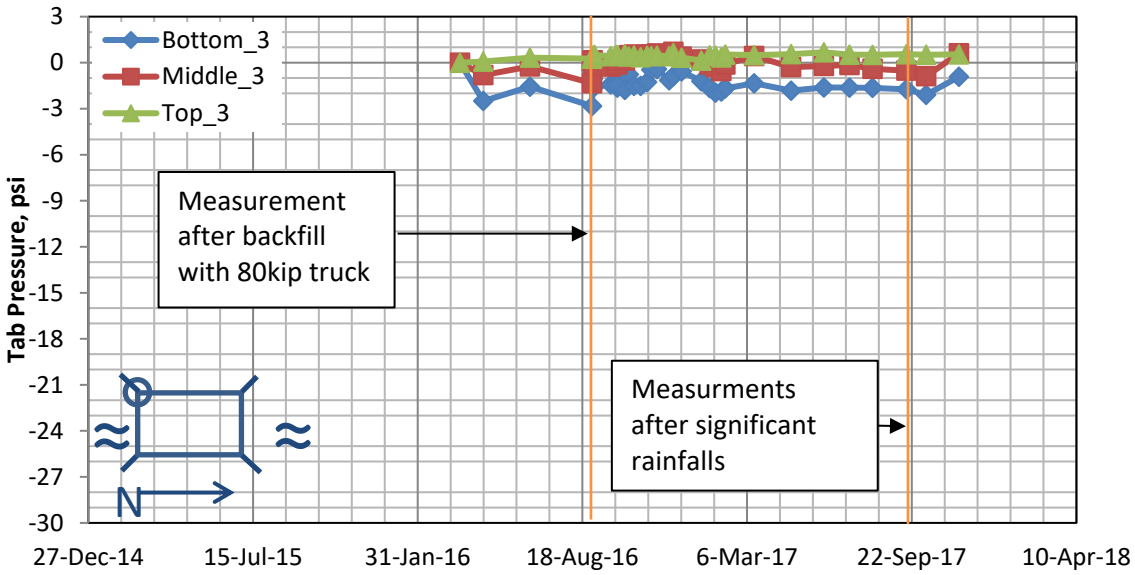

Figure 5-10. Lee County tab #3

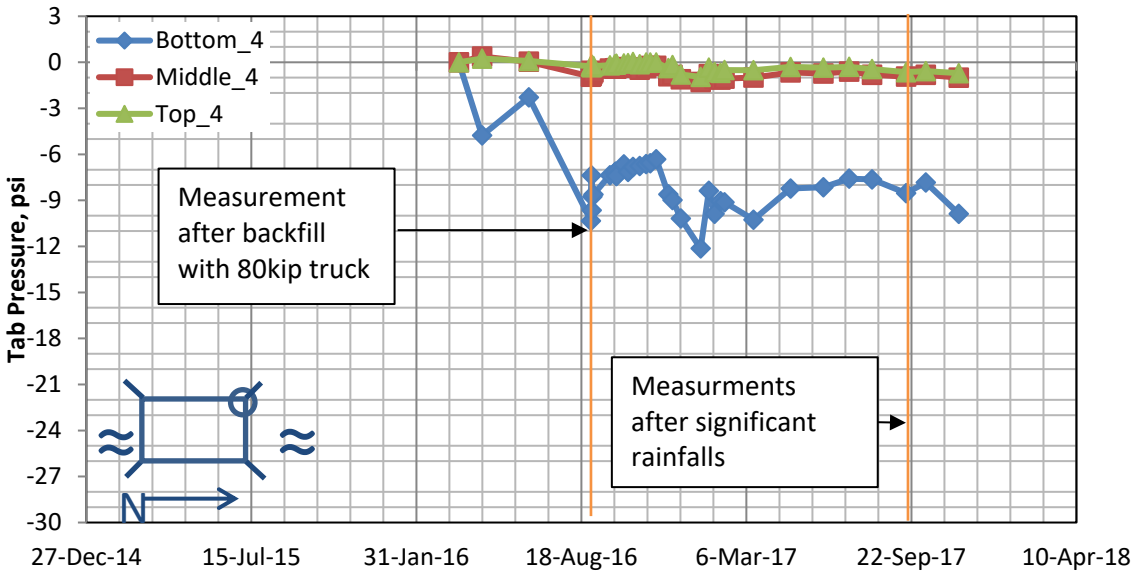

Figure 5-11. Lee County tab #4

5.3.3. Coosa County Culvert

The pressure recorded in tab #1 at the Coosa County culvert had a uniform distribution with highest recorded pressure of 6.8-psi at the top. The pressures in the middle and at the bottom were 2.4 and 3.0-psi, respectively. This suggested simultaneous rotation of the wing wall and sliding of the wing wall away from the backfill (Figure 5-12). The pressure distribution in tab #2 showed an unforeseen type of behavior for the wing wall. Due to possible bending of the wall, the center cells recorded the highest compression pressure of 2.1-psi while pressure at the bottom was 1-psi (Figure 5-13). The top cell did not record any pressure during the monitoring period.

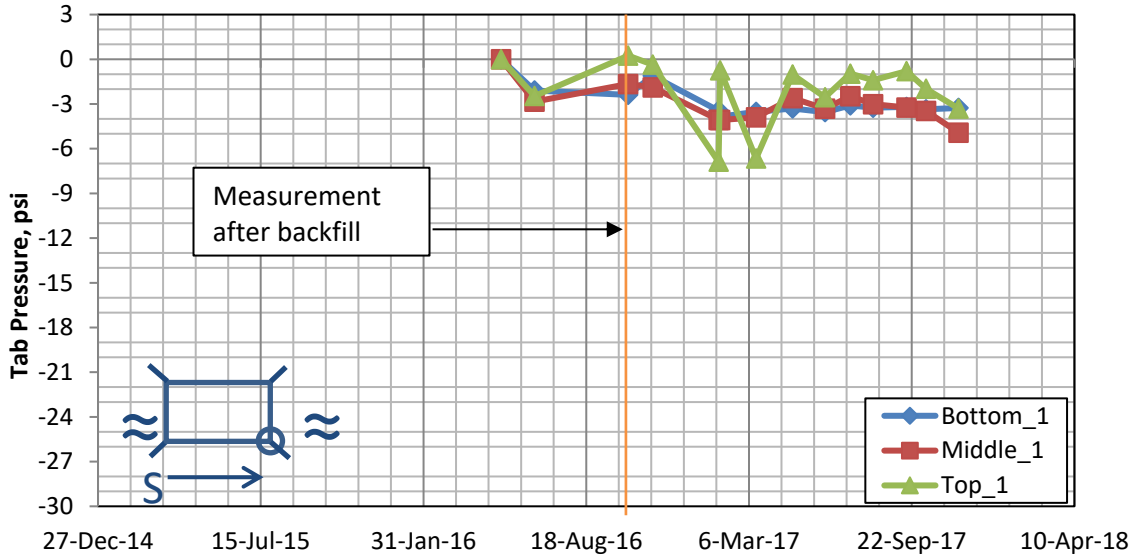

Figure 5-12. Coosa County tab #1

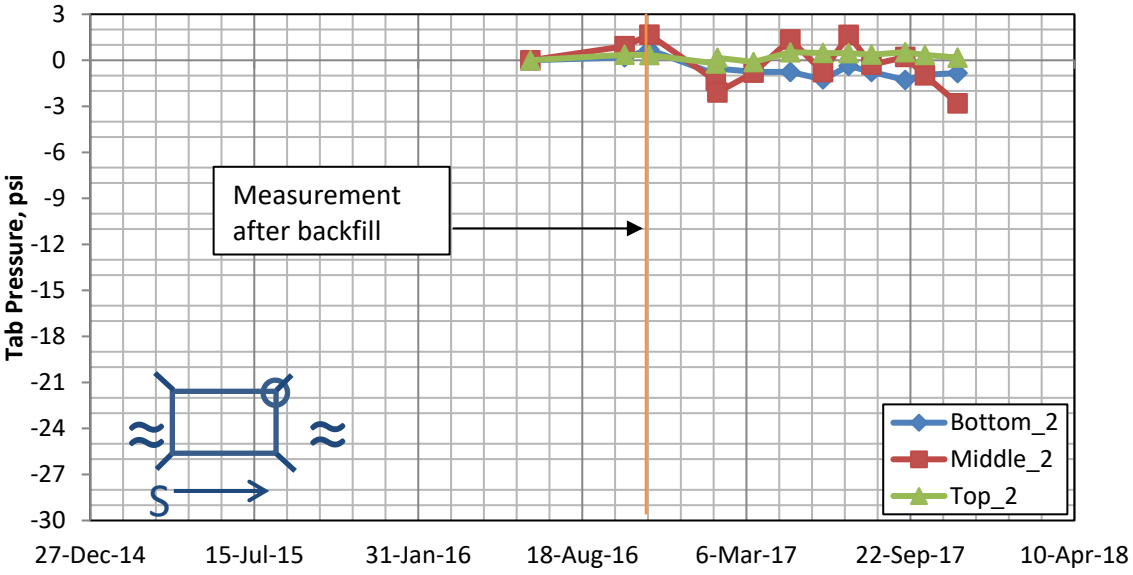

Figure 5-13. Coosa County tab #2

Chapter 6. Numerical Modeling Results

6.1. Introduction

In order to analyze the behavior of the newly designed and constructed culverts under a set of expected loads, three finite element model sets were developed as described in Chapter 4. The applied geometry was based on the new designs in Coosa, Lee and Chambers counties described Chapter 3. Two different load scenarios were applied to each simulated structure: design load, including backfilling and traffic load, and an extreme event, such as scour (Chapter 4.6.3). In addition, monolithically connected and disconnected joints were considered to evaluate the difference between the new and traditional design of the wing wall-to-tab connection.

6.2. Displacement

Upon the applied load, the movement trends of free standing wing wall and barrel are the same for each set of models. The maximum/dominating displacement occurs in the vertical direction under both sets of loads, while the values of horizontal displacement are much smaller. However, the horizontal translation is of interest in this study, since the transfer of stresses in a tabbed connection occurs in this direction.

When the design set of loads was applied, the top of the wing wall tended to rotate towards the backfill, regardless of the culvert depth. At the same time, the bottom part slid away from the backfill. The displacement of the other end of the wall followed the same with a higher magnitude. The uneven translation and rotation of the wall depended on the

footing width, wall geometry and restraint at the tab connection. The wing wall monolithically connected to the culvert barrel deflected as a cantilever element under the earths pressure.

With scour development (Figure 4-25), the direction of the free-standing wing wall displacement reversed. While soil erosion progressed in front of the key wall, the wing wall changed the direction of rotation and starts moving towards the barrel. The magnitude was relatively small and linearly increased through all stages of scour propagation along the key wall. While scour gradually grew under the footing, the horizontal displacement increased significantly at every stage. The soil erosion under the footing caused vertical settlement of the wing wall to fill the formed cavity. In the case of a fully connected wing wall, the horizontal earth pressure from backfill created a severe effect on the wing wall. The scour cannot cause substantial movement of a rigidly connected wall.

6.3.1 Chambers County Culvert

The wing wall displacements under the design loads are shown in Figure 6-1, Figure 6-2, Figure 6-3 and Figure 6-4 for all stages of construction. The direction and intensity of displacements in the Y direction are shown in terms of vectors of displacement (Figure 6-1), while the contours (Figure 6-2) show the magnitude of displacement in every node of the meshed structure. In addition, summarized displacements along the tab are shown in Figure 6-3 for the main stages of construction and in Figure 6-4 for the stages modeling scour propagation. The applied sign convention was described in Chapter 4.6.6.

At the first stage of construction, once the structure was placed, the top of the wing wall moved towards the barrel by 0.02-in (Figure 6-1a and Figure 6-2a). With backfilling to the same level with a culvert (Stage 2), which corresponds to the design height of the

backfill, the wing wall rotated clockwise or away from the barrel (Figure 6-1b). With the increase of the backfilling from 6-ft to the design height (Stages 3-5), the footing slid towards the culvert by 0.04-in from the original position, while the top part moved to the backfill (Figure 6-2c-Figure 6-2e and Figure 6-3). This occurred due to higher vertical earth pressure acting on the footing. Further increasing the backfill height to 16-ft and 23-ft above the culvert (Stages 4-5) caused the wing wall to continue moving toward the culvert without changing its rotation (Figure 6-1-2d, e). The traffic load (Figure 6-2) created an equivalent effect as the 6-ft backfilling (Stage 3 - Figure 6-1f) for the culvert constructed in Chambers County.

With the scour development, the whole wing wall slid towards the opening as the soil eroded in front of the key wall (Figure 6-4). This lead to the redistribution of applied pressure on the wall. Horizontal displacement of the top of the wall in Y direction slightly increased from 0 to 0.02-in with scour propagation down to the bottom of the key wall (Stages 5-11) and behind it (Stages 12-16) (Figure 6-4). Therefore, the depth of the key wall did not create a significant effect on the wing wall displacement in the case of scour. Further, scour development under the footing (Stages 17-20) caused more substantial horizontal displacement of the top of the wing wall (from 0.02 to 0.16-in) for each increment of soil removal (Figure 6-4). When the scour reached 50% of footing width, the FE analysis experienced converging difficulties due to large wall displacements.

The displacements of the wall for backfill levels of 6-ft, 16-ft, and 23-ft over the culvert are summarized in Appendix C. For the design conditions, the lateral earth pressure distribution had a triangular shape with almost zero stresses at the top of the wall. Under high backfill, the stress distribution on the wall had a more trapezoidal shape with

significant pressure at the top. This increase of lateral earth pressure resulted in additional lateral movement of the wing wall (Figure C-1,2,3). Also, due to the bending of the wall, the angle of rotation changed and this caused an additional displacement.

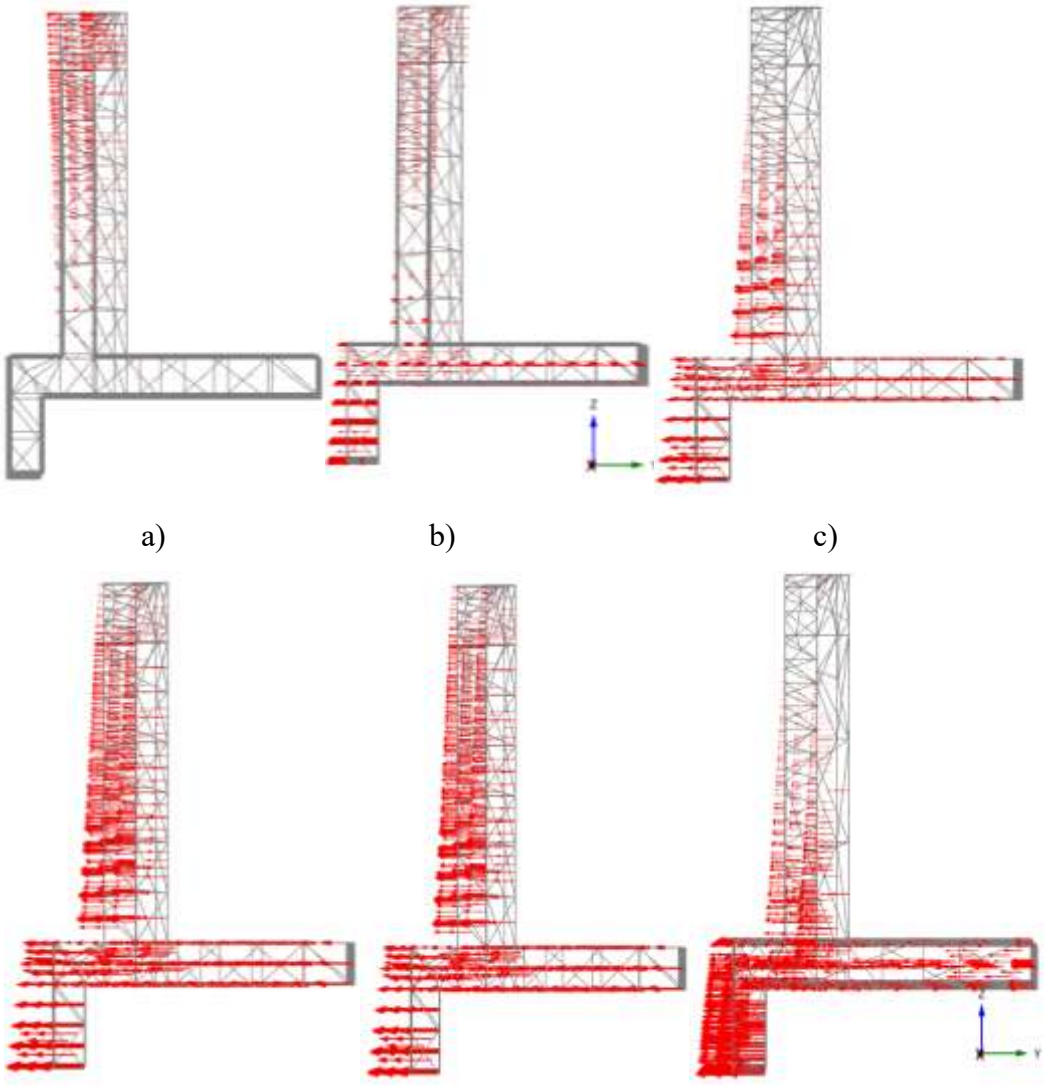

a) b) c)

d) e) f)

Figure 6-1. Vectors of displacement of the wing wall for six stages of the design load in Y direction for Chambers County culvert

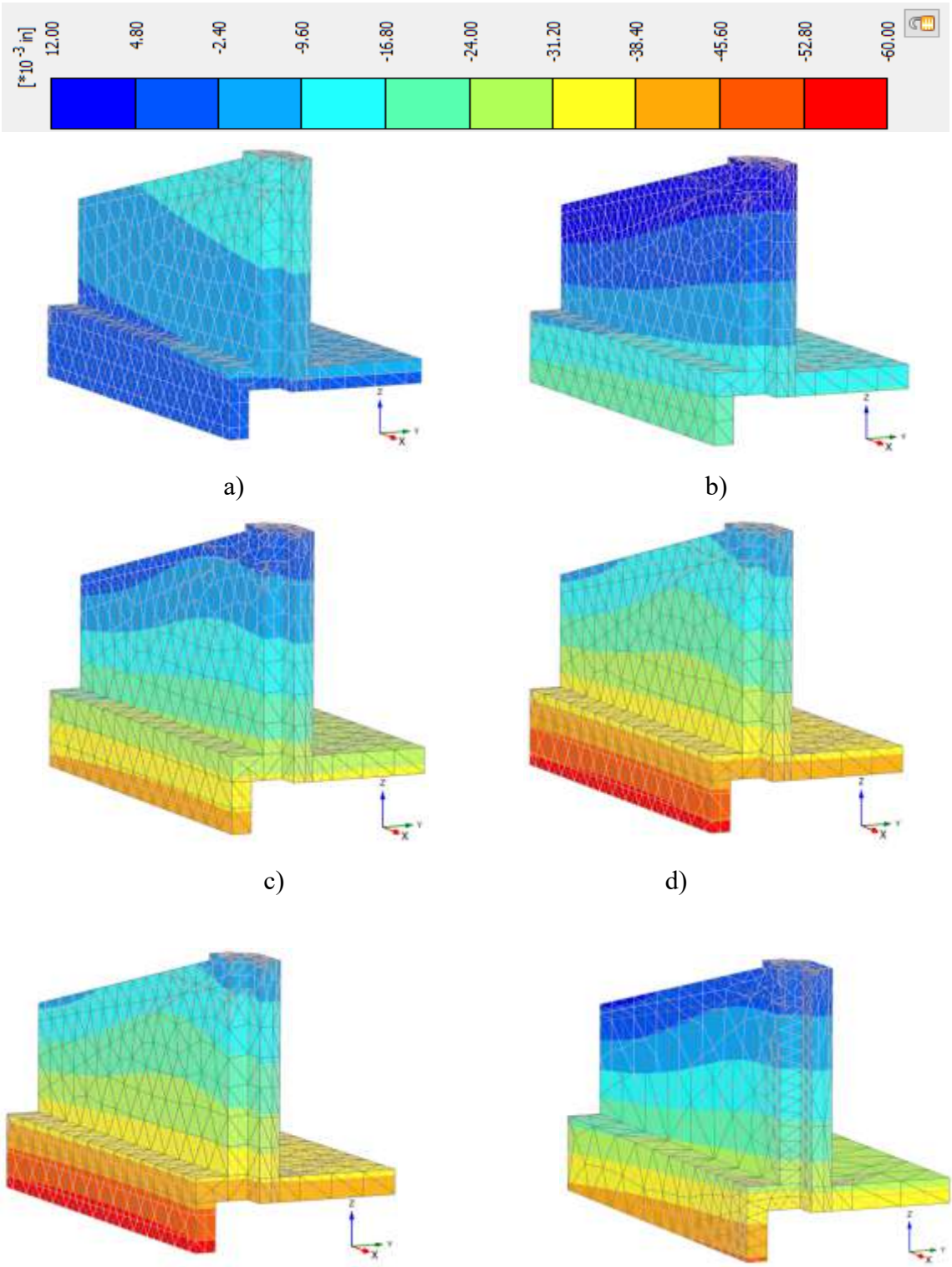

Figure 6-2. Contours of the wing wall displacements for six stages of design load in Y direction for Chambers County culvert

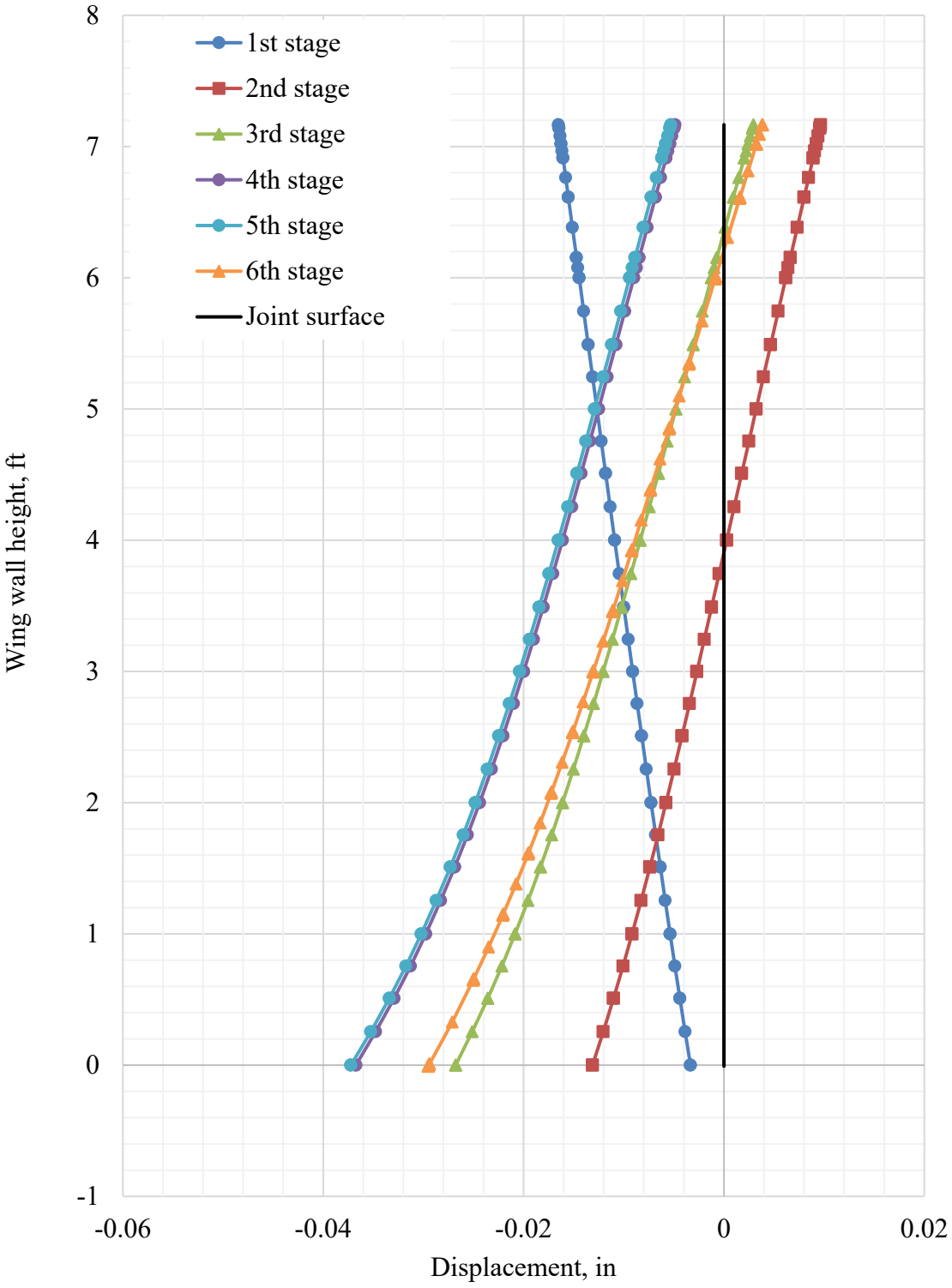

Figure 6-3. Summarized displacement of the wing wall along the tab extension under design loads for the Chambers County culvert

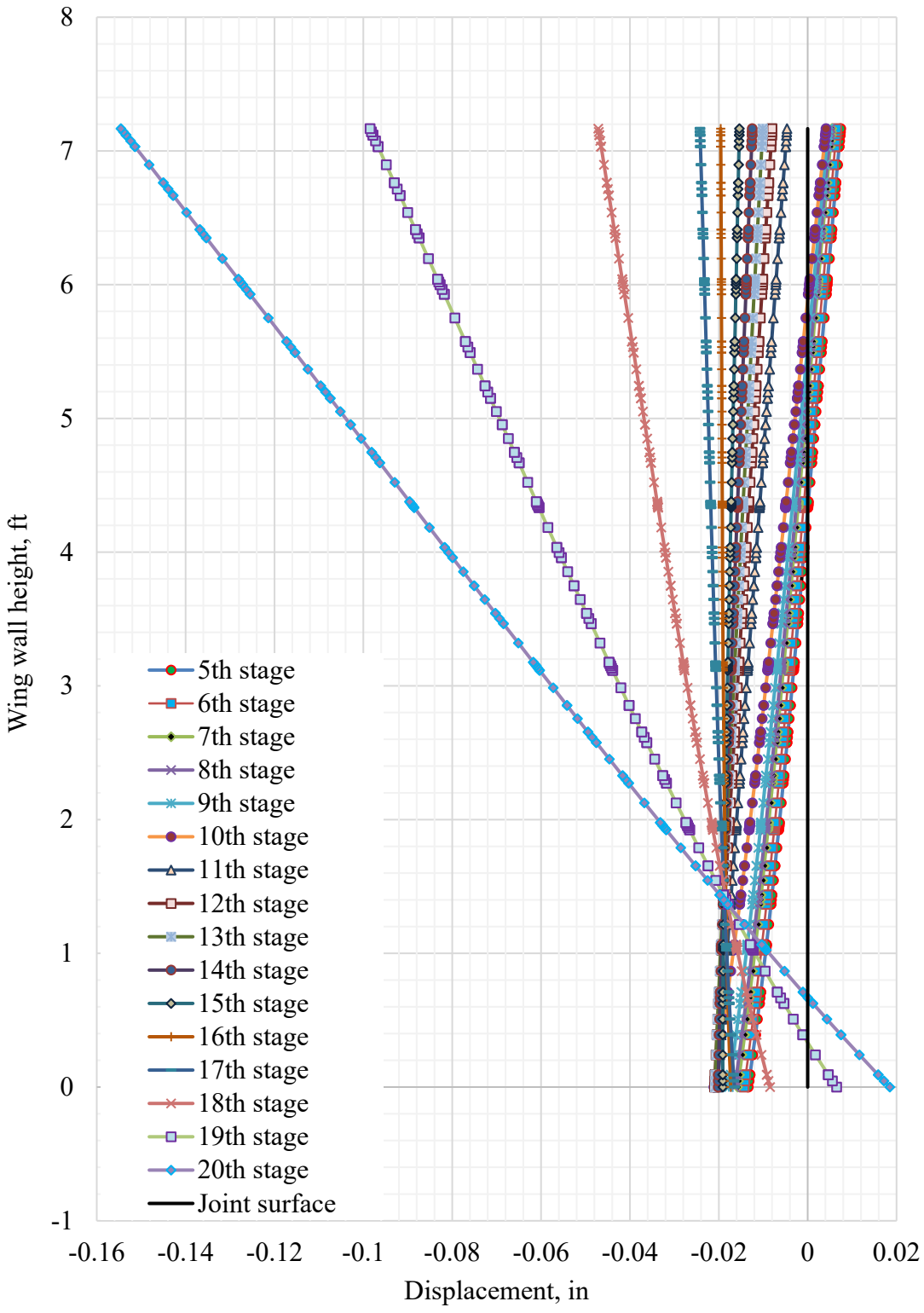

Figure 6-4. Summarized displacement of the wing wall with scour development in Chambers County culvert

6.3.2 Lee County Culvert

The resultant displacements of the culvert built in Lee County are similar to the Chambers County culvert (Chapter 6.3.1). The direction and magnitude of displacement of the structure under all stages of construction and scour propagation are shown in Figure 6-5, Figure **6-6**, Figure 6-7 and Figure 6-8. Vectors and contours of displacements, representing the direction and magnitude of movement of the structure, are shown in Figure 6-5 and Figure **6-6**, respectively. The summarized displacements along the tab surface are plotted in Figure 6-7 and Figure 6-8 for the design load and scour, respectively. The same sign convention is applied (Chapter 4.6.6).

The behavior of the wing wall constructed in Lee County under design loads and scour behaved similarly to the one in Chambers County (Figure 6-7 and Figure 6-8) due to similar geometry. The depth of the wing wall in Lee County was 2-ft greater than in Chambers County (Figure 3-5 and Figure 3-7). During Stage 1, under the self-weight only, the wing wall tended to rotate towards the barrel around the base (Figure 6-5a, Figure 6-6a). Once the height of the backfill reached the design level, equal to the height of the barrel (Stage 2), the wing wall started moving in the opposite direction. The displacement of the top of the wall in Y direction went up to 0.03-in compared to the position at Stage 1 (Figure 6-5b, Figure 6-6b). The wing wall continued sliding towards the barrel (Figure 6-5c-e) as the backfill height increased (Stages 3-5). The magnitude of the displacement incrementally increased up to 0.02-in at Stage 5, which corresponded to the backfill height of 23-ft (Figure 6-6c and e). At Stage 6, once the traffic load was applied, the bottom part of the wall translated towards the barrel compressing the filling material, whereas the top of the wall did not move (Figure 6-5f, Figure 6-6f). This occurred because of the tandem

wheel load that caused high vertical stress on the footing. The effect of the tandem load directly depended on the distance of the applied load to the wall. A summary of out-of-plane displacements in the Y direction along the tab surface for six main stages of construction is shown in Figure 6-7.

The simulated soil erosion due to scour caused the same displacement of the wing wall as in case of the design loads. The scour propagation at the front edge of the key wall reversed the direction of movement. The top of the wall moved more towards the excavation, while the bottom stayed at the same position. The scour propagation along the key wall at Stages 5 to 12 did not have a significant effect on the structure (Figure 6-8). However, with the soil removal under the key wall and behind it (Stages 13 - 15), the wing wall rotated back to its original vertical position (Figure 6-8). The magnitude of wall displacement at the top and bottom were equal. At the final stages (Stages 16-20) the soil under the footing was removed incrementally, and this caused the largest displacement of the wall in comparison to the other impacts (Figure 6-8). Once the scour propagated to more than 1/3 of footing width, the horizontal displacement grew geometrically (Figure 6-8).

The contours of displacement of the wing wall at the joint surface at the level of backfill equal to 6-ft, 16-ft, and 23-ft and with scour propagation are summarized in Appendix C. The higher vertical earth pressure on the footing (due to the high backfill – Stages 3-5) caused lower horizontal displacement than in the actual conditions, when the backfill height was equal to the height of the barrel (Figure C-4,5,6). Also, with higher backfills, additional lateral movement was occurred due to bending of the wing wall.

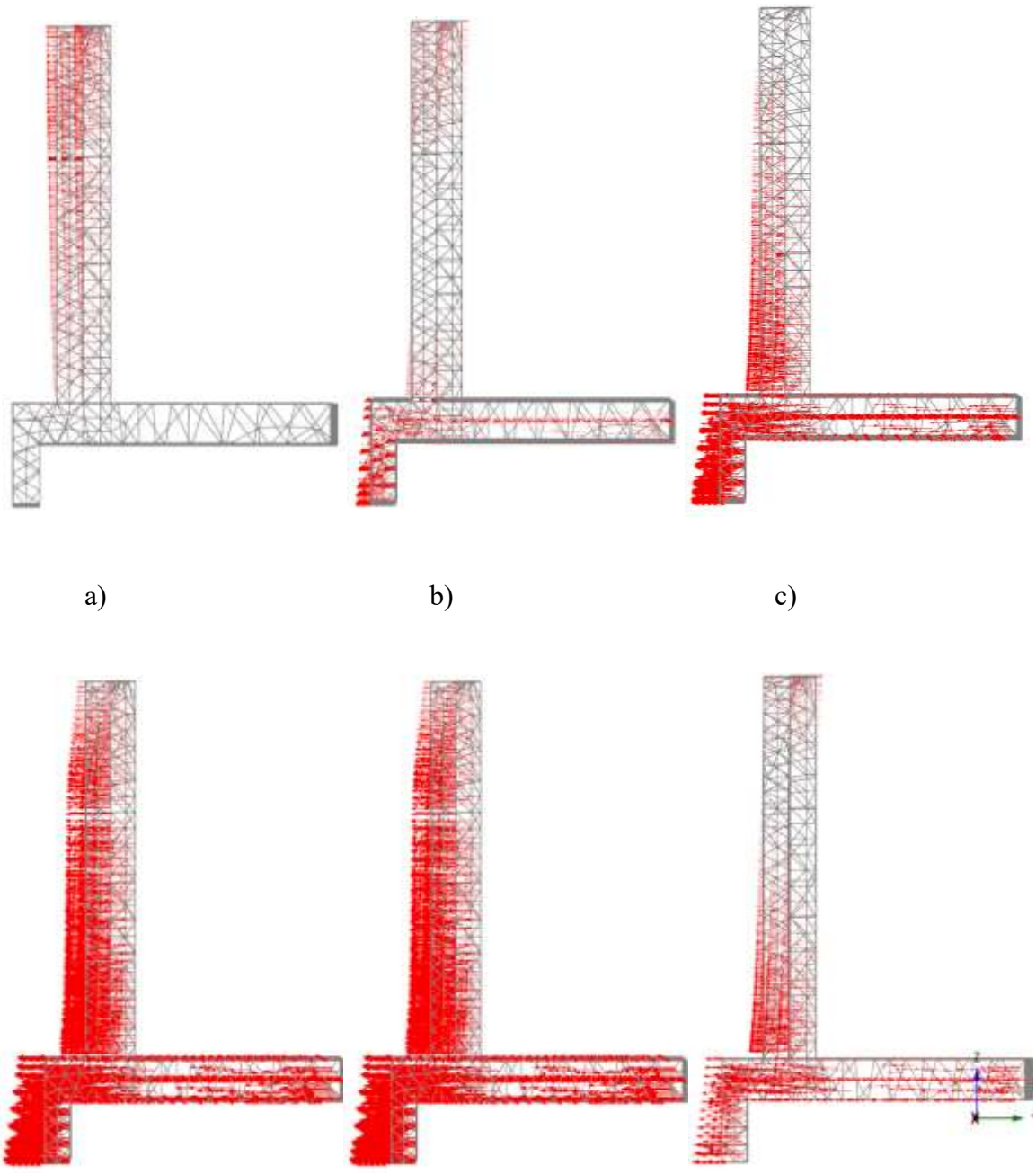

a) b) c)

d) e) f)

Figure 6-5. Vectors of displacement of the wing wall for six stages of the design load in Y direction for Lee County culvert

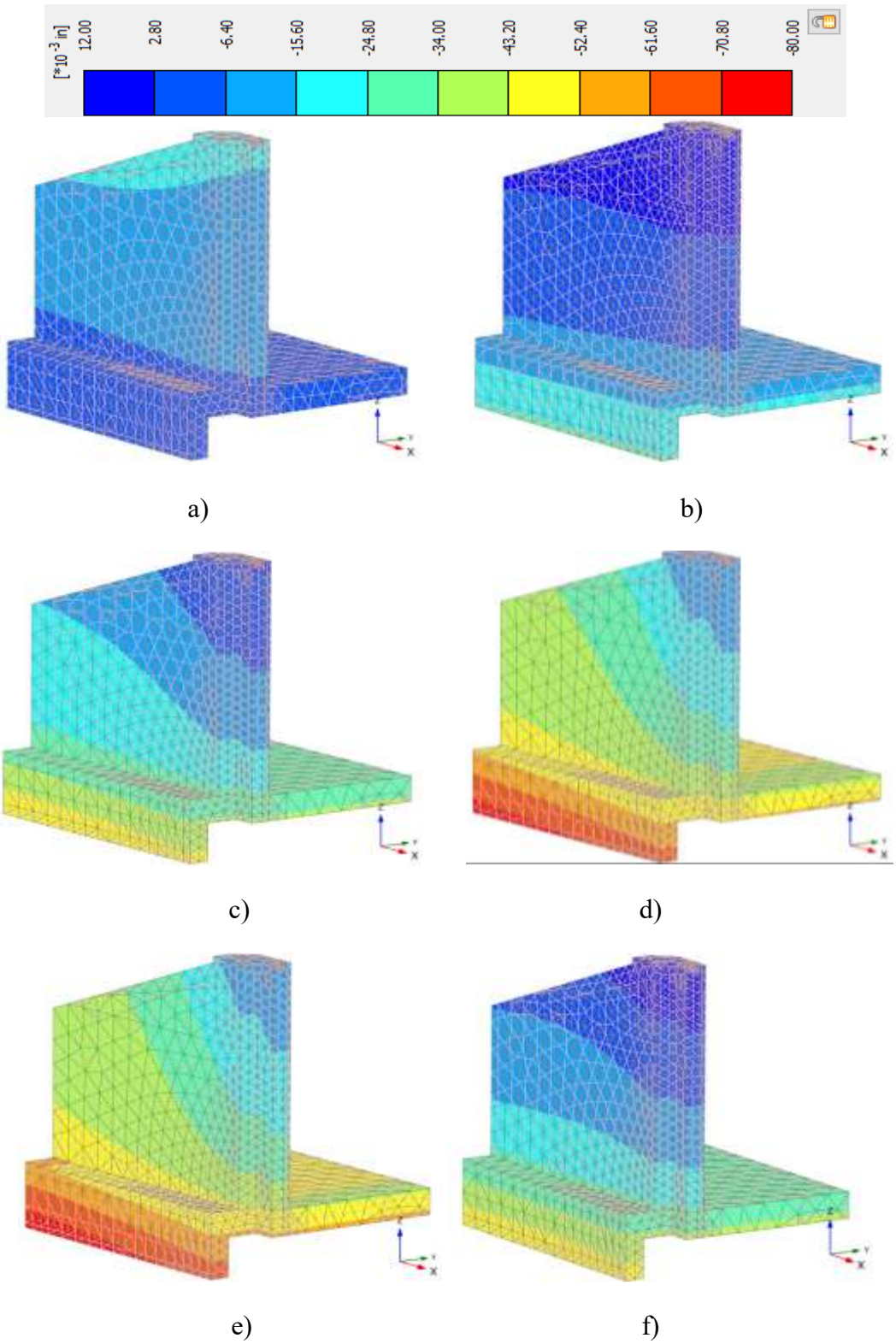

Figure 6-6. Contours of the wing wall displacements for six stages of design load in Y direction for Lee County culvert

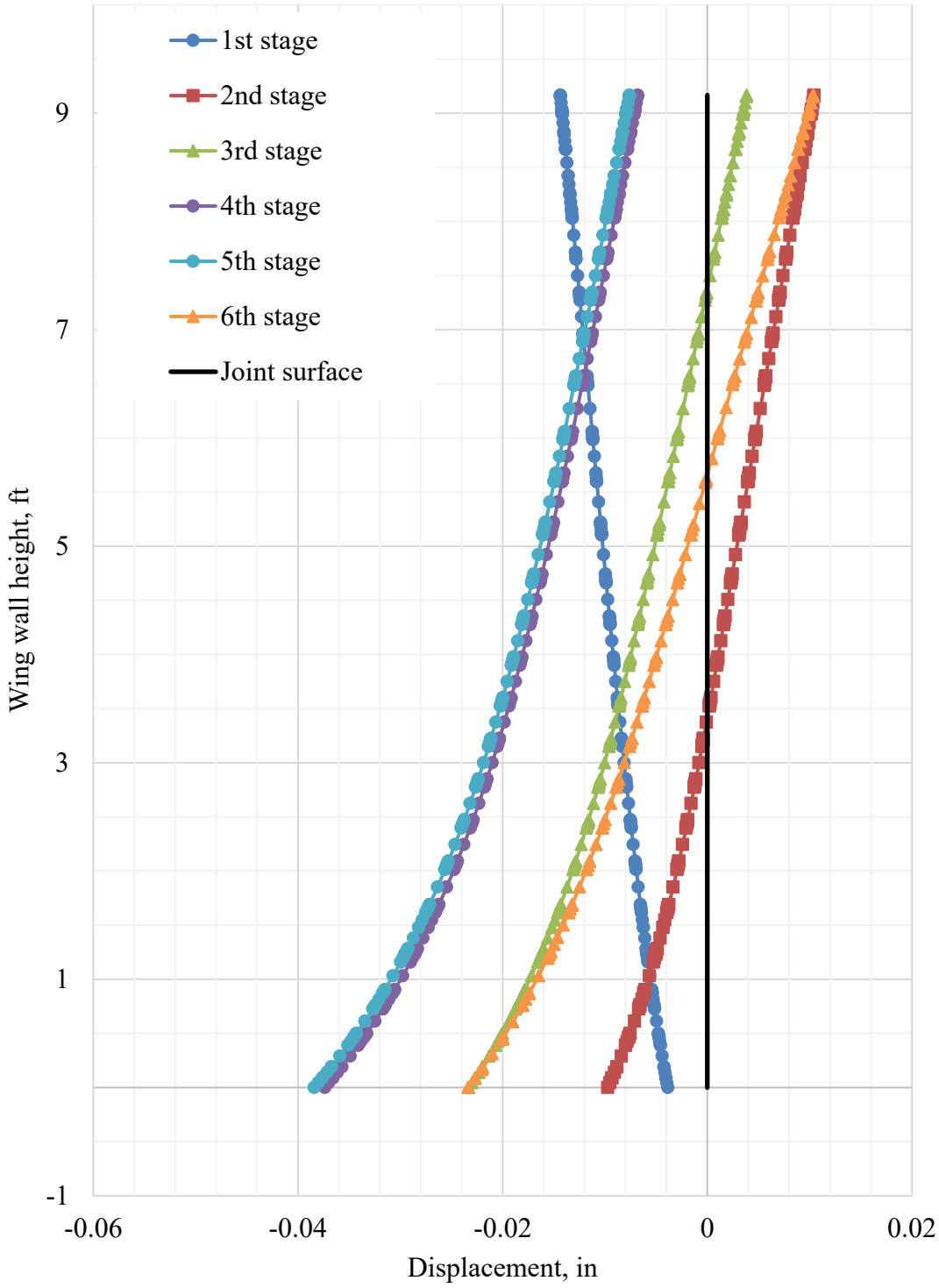

Figure 6-7. Summarized displacement of the wing wall along the tab extension under design loads for the wing wall in Lee County culvert

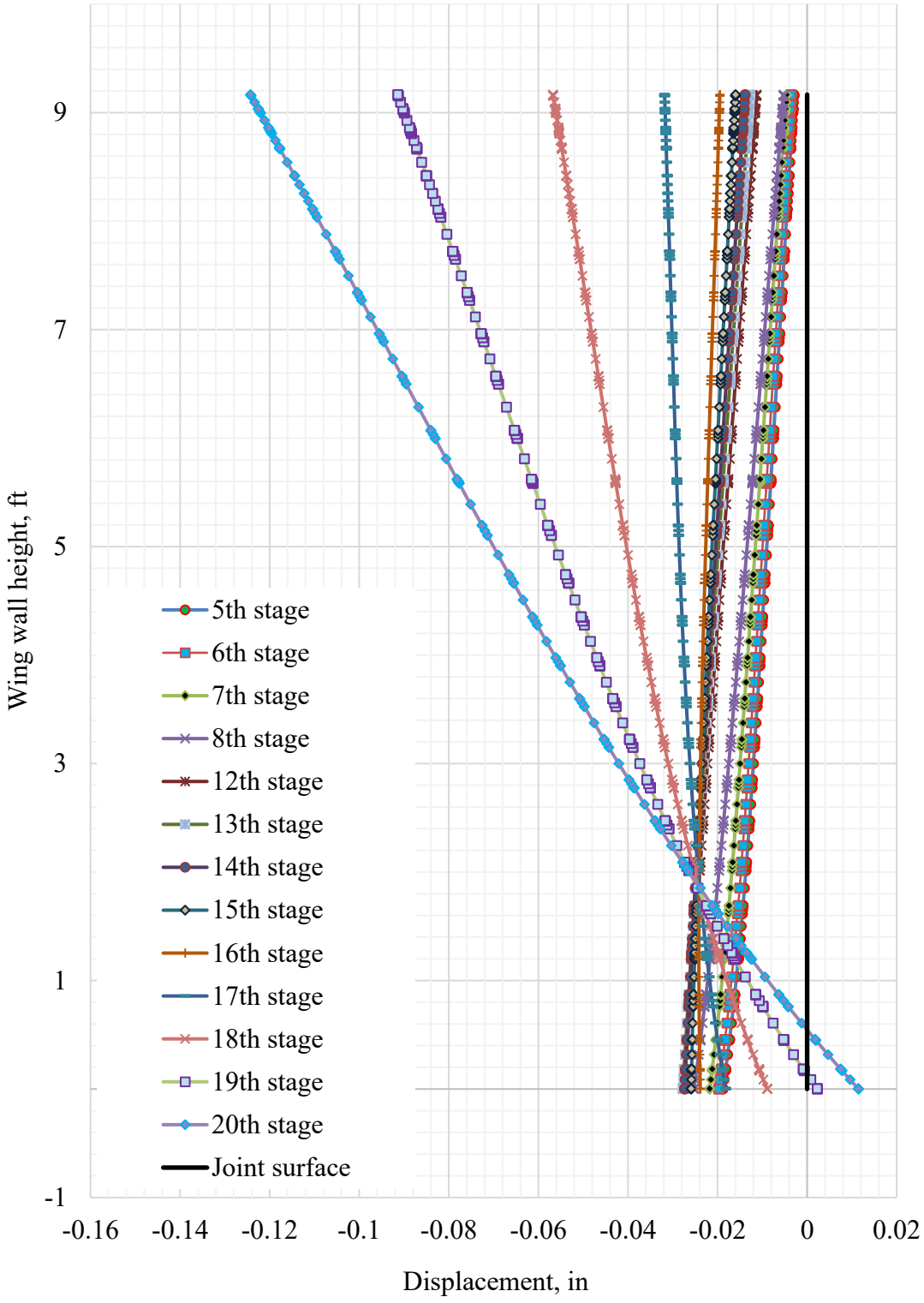

Figure 6-8. Summarized displacements of the wing wall along the tab with scour development in Lee County culvert

6.3.3 Coosa County Culvert

Vectors and contours of displacement of the wing wall in Y direction for six main stages are shown in Figure 6-10 and Figure 6-11. Although the culvert built in Coosa County was the deepest one, the behavior of the wing wall through the stages with the design loads and the extreme event was similar to the other constructed culverts. As in the previous cases, the top of the wing wall moved toward the barrel by 0.02-in at Stage 1 (Figure 6-10a). The magnitude was similar to the other cases since it primarily depended on the compressibility of filling material (Figure 6-11a). At Stage 2, the backfill reached the same height with the barrel, and the wing wall moved away from the culvert opening the gap between tab extensions at the top part of joint (Figure 6-10b, Figure 6-11b). Increasing the height of the backfill to 23-ft resulted in incremental sliding of the wing wall (Figure 6-10c,d,e) with the magnitude similar to the other cases (Figure 6-11c,d,e).

In Coosa County, the pavement was placed directly on the culvert. Thus, the effect of the traffic load was negligible (Figure 6-10f Figure 6-11f). The higher lateral earth pressure significantly affected the curvature of the tab surface and, as a result, the bending moments in the wall.

While scour propagated along the front surface of the key wall (Stages 5 – 12), the wing wall incrementally slid towards the excavation without changing the deformed shape (Figure 6-12). Further development of scour around the key wall and under the footing (Stages 13 – 20) affected the displacement of the wall by changing its direction (Figure 6-12). The top of the wall started moving towards the barrel creating a stress concentration in the top part of the connection. At the same time, the bottom part of the wall slid toward the backfill, opening the gap and removing compression stresses.

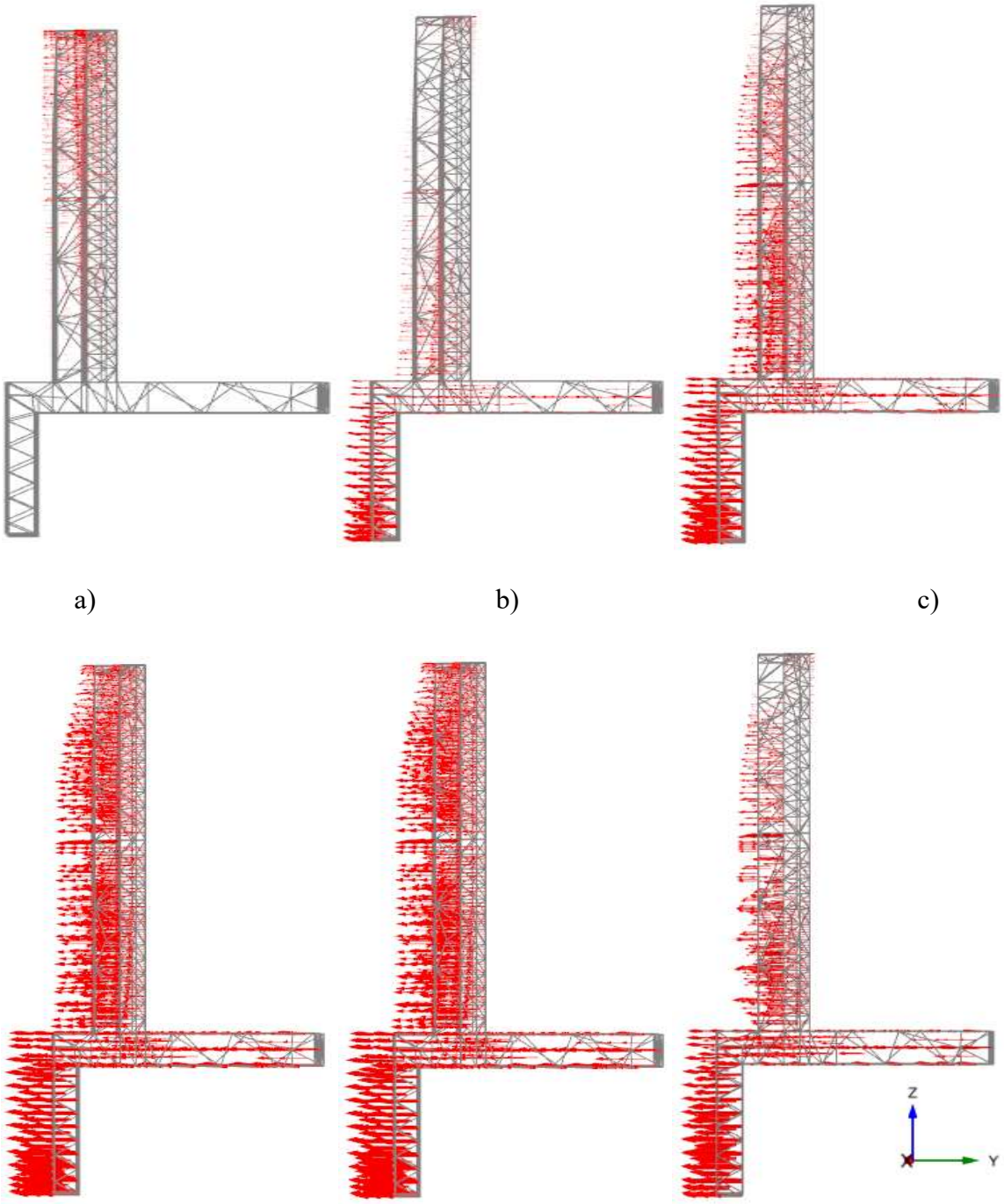

Figure 6-9. Displacement shapes of the wing wall for six stages of the design load in Y direction for Coosa County culvert

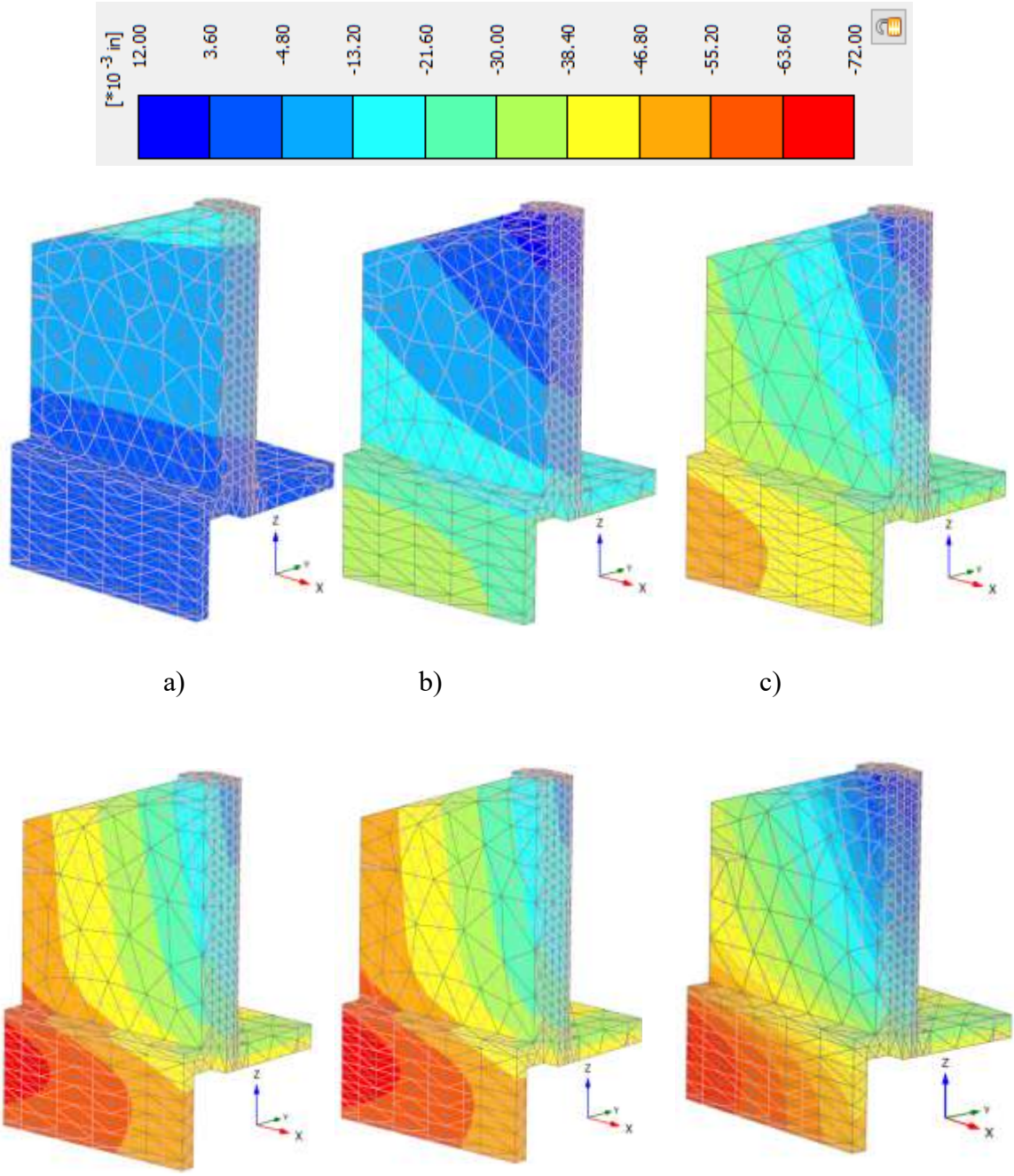

Figure 6-10. Contours of the wing wall displacements for six stages of design load in Y direction for Coosa County culvert

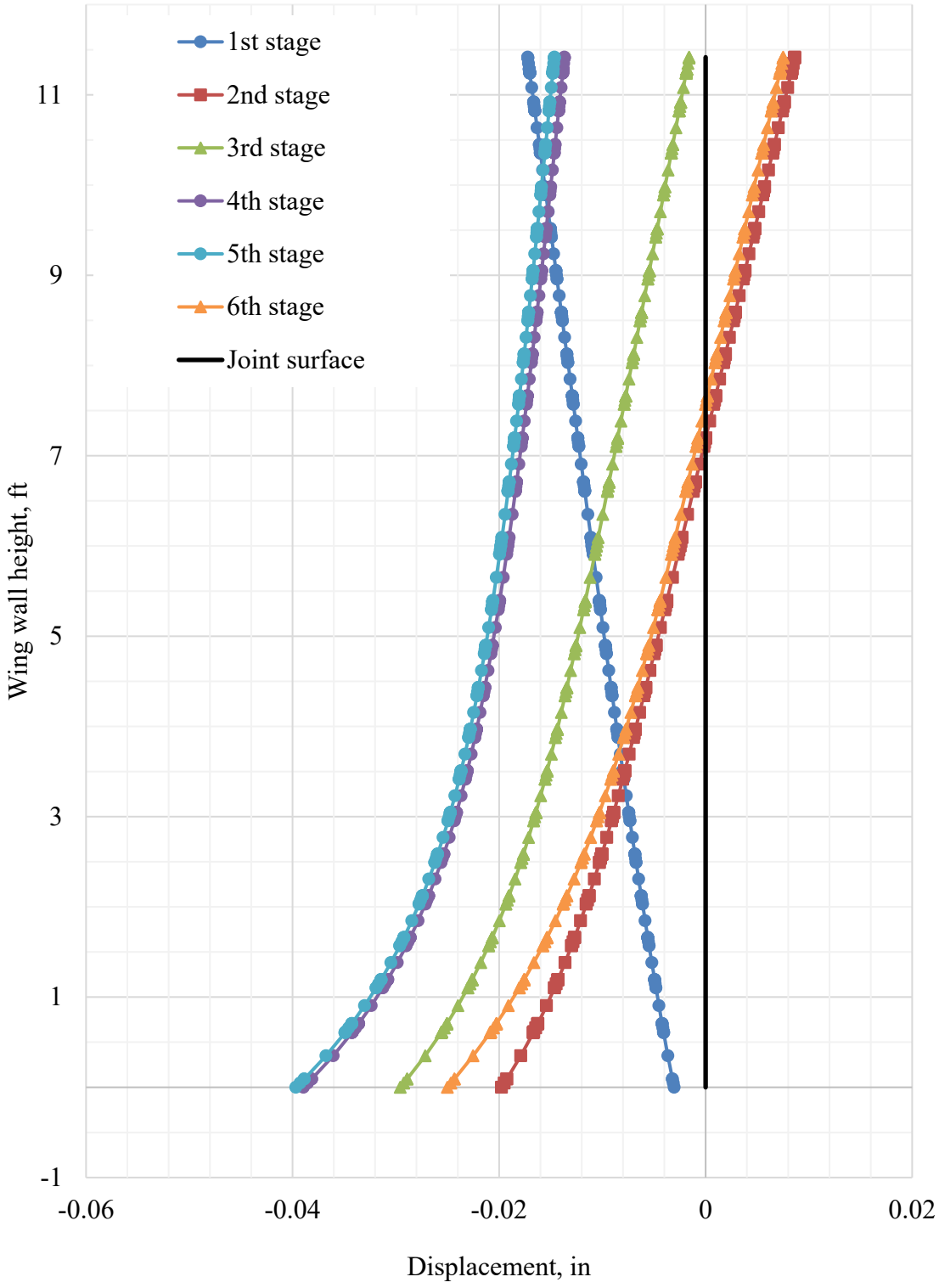

Figure 6-11. Summarized displacement of the wing wall along the tab extension under design loads for Coosa County culvert

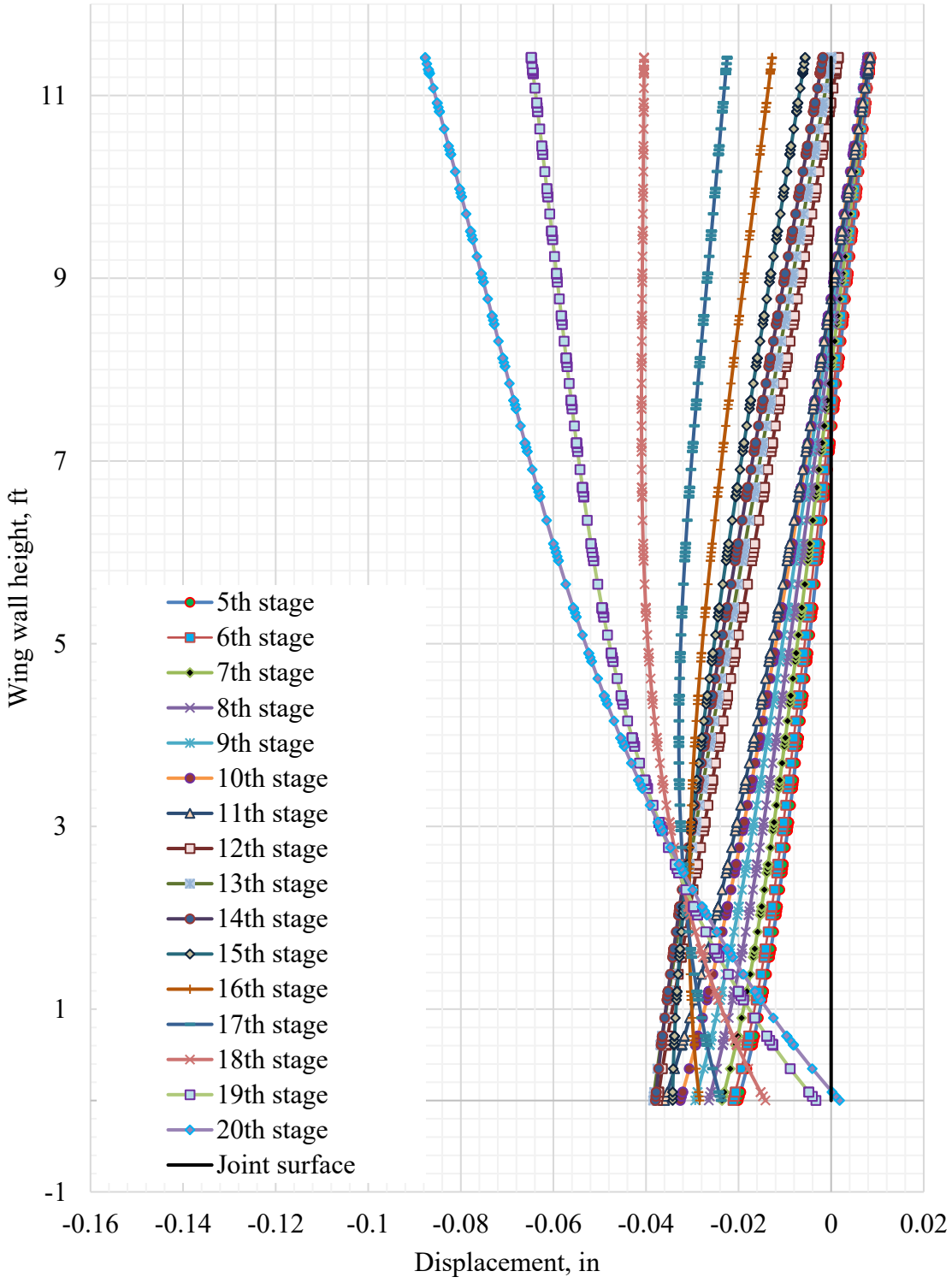

Figure 6-12. Summarized displacements of the wing wall along the tab with scour development in Coosa County culvert

Displacement due to scour for other backfill heights is summarized in Appendix C. For all cases, the behavior was the same except for the starting point, which corresponded to the results under the design load only (Figure C-7,8,9). The results shown in Figure 6-11 were used as a starting stage for corresponding backfill height. Due to higher vertical earth pressure on the footing, the lateral movement of the wing wall along the tab surface was smaller than in other culverts.

6.3.4. Culvert with Monolithically Connected Wing Wall

The contours of displacements of the wing wall for the six stages of design loads are shown in Figure 6-13. The deflections of a monolithically connected wing wall along the connection surface occurred only due to bending of the wall and did not vary with increasing loads. The displacement due to horizontal earth pressure was possible only at the free end since the wing wall behaved like a cantilever element. During the first two stages, the free end displaced away from the backfill by 0.005-in (Figure 6-13 and Figure 6-14 a, b). With applied traffic load and deeper backfills, the free end changed the direction of rotation towards the backfill (Figure 6-13c, d, e, f). The displacement of the tab surface had the same pattern as in the case of a disconnected joint with a backfill height up to the level of the culvert (Figure 6-14). The top part of the wing wall tended to bend toward the backfill up to 0.0003-in, while the bottom part bent away from it by 0.0017-in. Once the traffic load was applied, the position of the top part of the wall remained the same, but the bottom part was displaced by 0.008-in. Under deeper backfills, the deflection due to bending linearly increased up to 0.07-in at the top and 0.013-in at the bottom of the tab surface.

The resultant distributions of deflection of the wall along the joint surface are shown in Figure 6-14 for scour propagation and different backfills. In the case of scour propagation, the deflection oscillated between -0.02-in and 0.02-in for all stages of construction. Despite the small deflection, the deformed shapes of the joint changed with scour propagation through the stages due to bending of the wall.

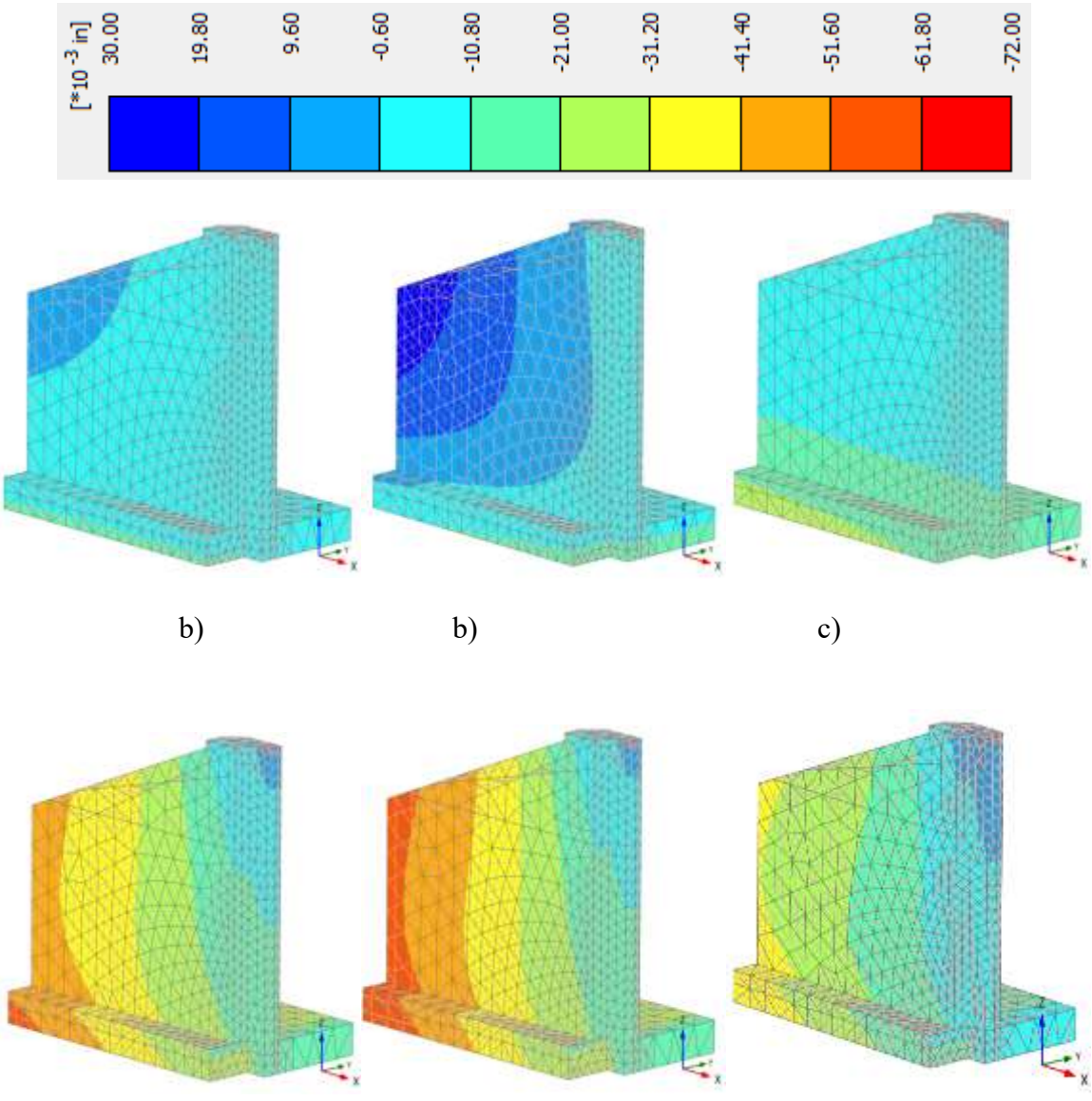

Figure 6-13. Contours of the wing wall displacements for six stages of design load in Y direction for monolithically connected wing wall

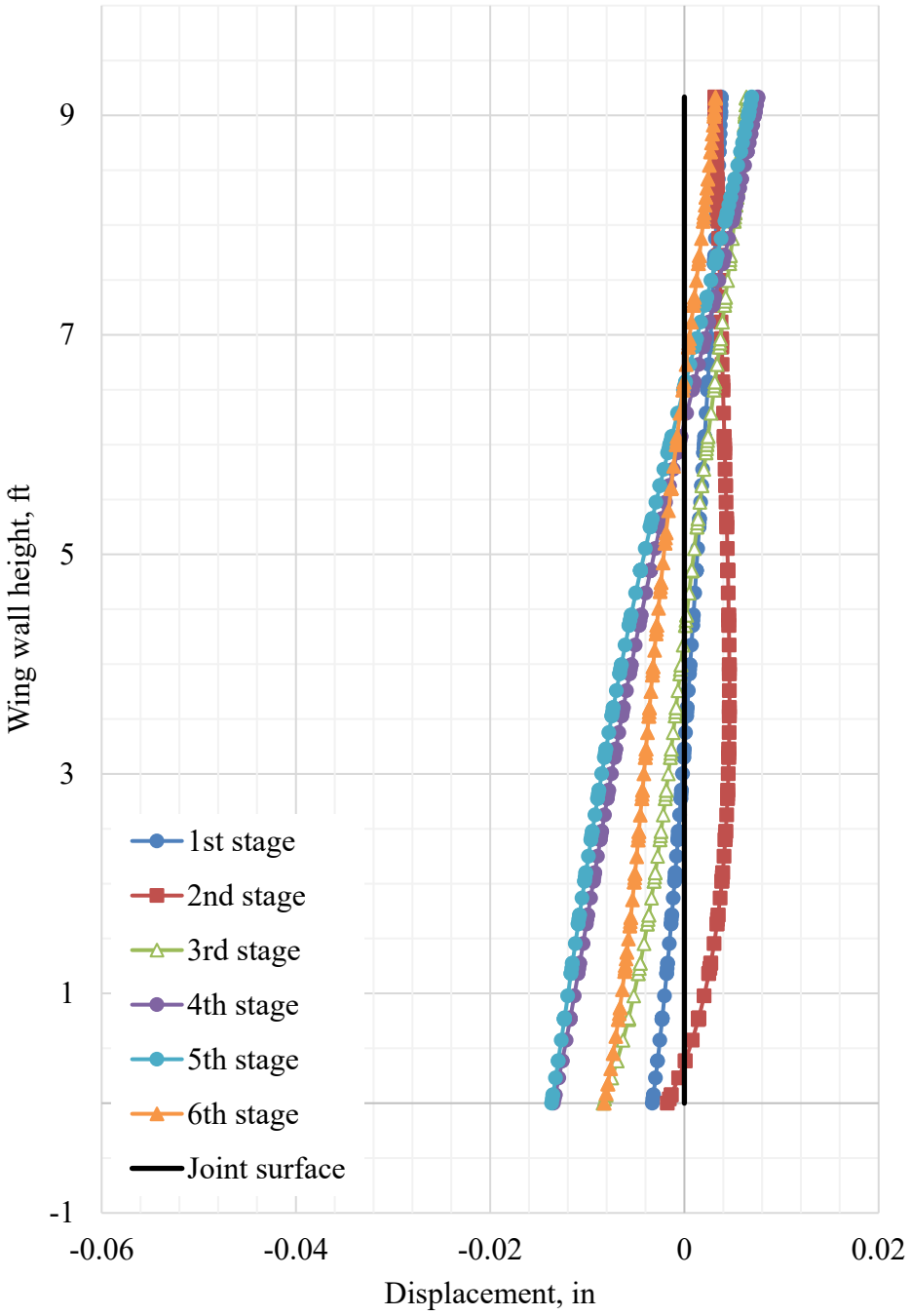

Figure 6-14. Summarized displacement of the wing wall along the tab extension under design loads for monolithically connected wing wall

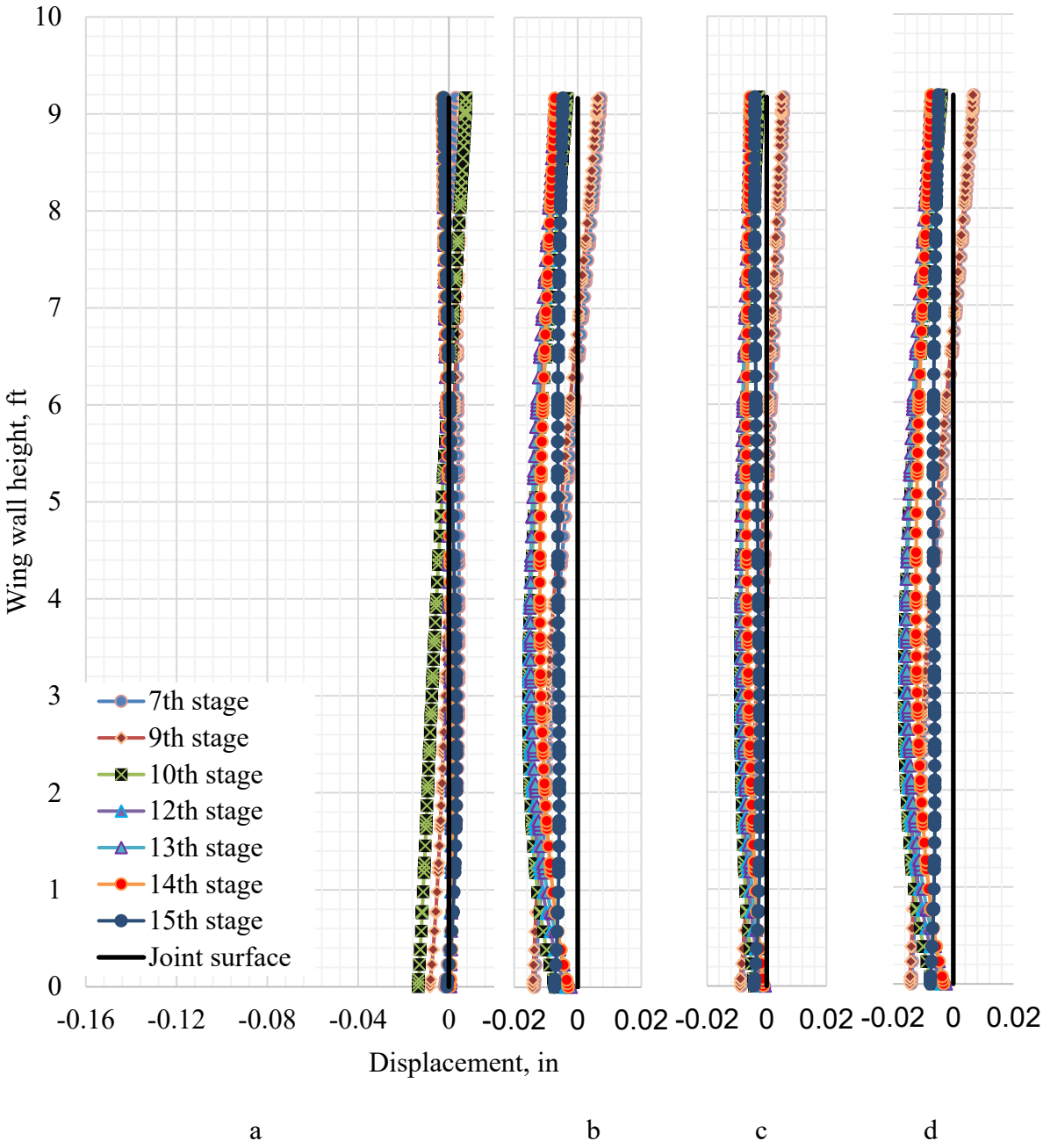

Figure 6-15. Summarized displacements of the wing wall along the tab with scour development in monolithically connected wing wall:

a) 0-ft backfill; b) 6-ft backfill; c) 16-ft backfill; d) 23-ft backfill

6.4. Development of Stresses

Similar to displacements discussed in the previous section, stresses from the FE models were recorded at the same location where the actual sensors were installed – in the middle of the tab. The compression stresses acting along the tab surface (Figure 4-26) were analyzed for each constructed culvert and load (Chapter 4.6). The stress distribution correlates with the displacement of the tab surface presented in the previous chapter.

Under the design set of loads (backfill and traffic load), the maximum compression stresses occurred at the bottom of the tab and gradually decreased toward the top. The magnitude of these stresses was relatively small (up to 20-psi). The height of the wall and backfill depth were the most sensitive factors. For comparison, in the case when the wing wall is monolithically connected to the culvert barrel, stresses were recorded in the same location as in models with a disconnected joint. In case of a rigidly connected joint, stresses along the tab surface were much higher and localized at the bottom part of the wing wall. However, the maximum stresses observed in the models with the rigid connection were located along the corner of the barrel, where the wing wall was attached.

The pattern of stress distribution was different under scour propagation. According to the displaced shape (Figure 6-15), the wing wall rotated toward the barrel creating the compression stress concentration zone at the top part of the connection, which dissipated to the bottom. The magnitude of these stresses was much higher (up to 50-psi) than in the case of design loads. For a wing wall rigidly connected to the barrel, the scour effect did not increase the magnitude of stresses, since it could not create a substantial movement of a cantilever wall.

An additional set of models was developed to analyze the theoretical scenario of two tab extensions being in full lock. This scenario may occur when the filling material is entirely squeezed, and the wing wall cannot move at the tab side, creating a high stress concentration on the tip of the tab. The maximum stresses located within the top 5-in of the tab surface rapidly decrease to the average magnitude for the rest of the joint.

6.4.1. Chambers County culvert

At the first stage, the wing wall moved toward the barrel (Figure 6-3), creating a uniform compression of 1-psi along the height of the joint (Figure 6-16). At stage two, which represents the design height of the backfill, compression stresses were developed at the bottom of the joint with the magnitude of 5-psi and dissipated toward the mid-height of the wall (Figure 6-16). The top half of the wall did not experience any compression stresses as the wall moved toward the backfill. Increasing the backfill during the next three stages to 6-ft, 16-ft, and 23-ft lead to a rise in the maximum compression stresses up to 9.3-psi, 10.9-psi, and 11.2-psi, respectively (Figure 6-16). The compression stresses dissipated toward the top of the wall to 0-psi for 6-ft backfill and to 1-psi for 23-ft backfill. At stage six, the magnitude of maximum stresses was 10.3-psi with applied traffic load, which was twice as high as with the backfill load at stage two. This increase of stress with the traffic load corresponded with results observed during the field instrumentation.

Compression stresses decreased with the scour development at the front of the key wall and with a backfill height at the level of the culvert (Figure 6-17). As mentioned previously, the vertical settlement was greater than the horizontal displacement, and the direction of its displacement vector was diagonally downwards. Thus, the magnitude of compression stresses decreased due to the additional displacement of the wing wall into

the formed cavity. The development of the scour under the footing caused a change in the direction of displacement of the wing wall, thus the maximum compression stresses were located at the top of the tab surface. During the propagation under the footing, the magnitude of these stresses increased from 5-psi to 40-psi.

In the scenario with a near rigid lock between two tab extensions, design loads and scour propagation around the key wall did not affect the stresses. Scour propagation under the footing and backfill to the level of the culvert caused compression stresses to increase to 155-psi within the top 5-in of the tab height.

Development of compression stresses along the tab height for the backfill levels of 6-ft, 16-ft, and 23-ft over the culvert are summarized in Appendix D. Under high backfill, the stress distribution on the tab surface had the same shape as when the backfill height was equal to the level of the culvert. As backfill height increased from 6-ft to 23-ft, the average value of compression stresses increased from 5-psi to 10-psi, while the maximum value decreased from 40-psi to 25-psi (Figure D-1, 2, 3).

The compression stresses with locked tabs and scour propagation for other backfill levels (6-ft, 16-ft, and 23-ft) are shown in Appendix D. The magnitude of maximum compression stresses increased from 80-psi to 110-psi with increasing backfill height from 6-ft to 23-ft. Similar to the other models, stresses under higher backfill were smaller than in the model with a backfill up to the level of the culvert.

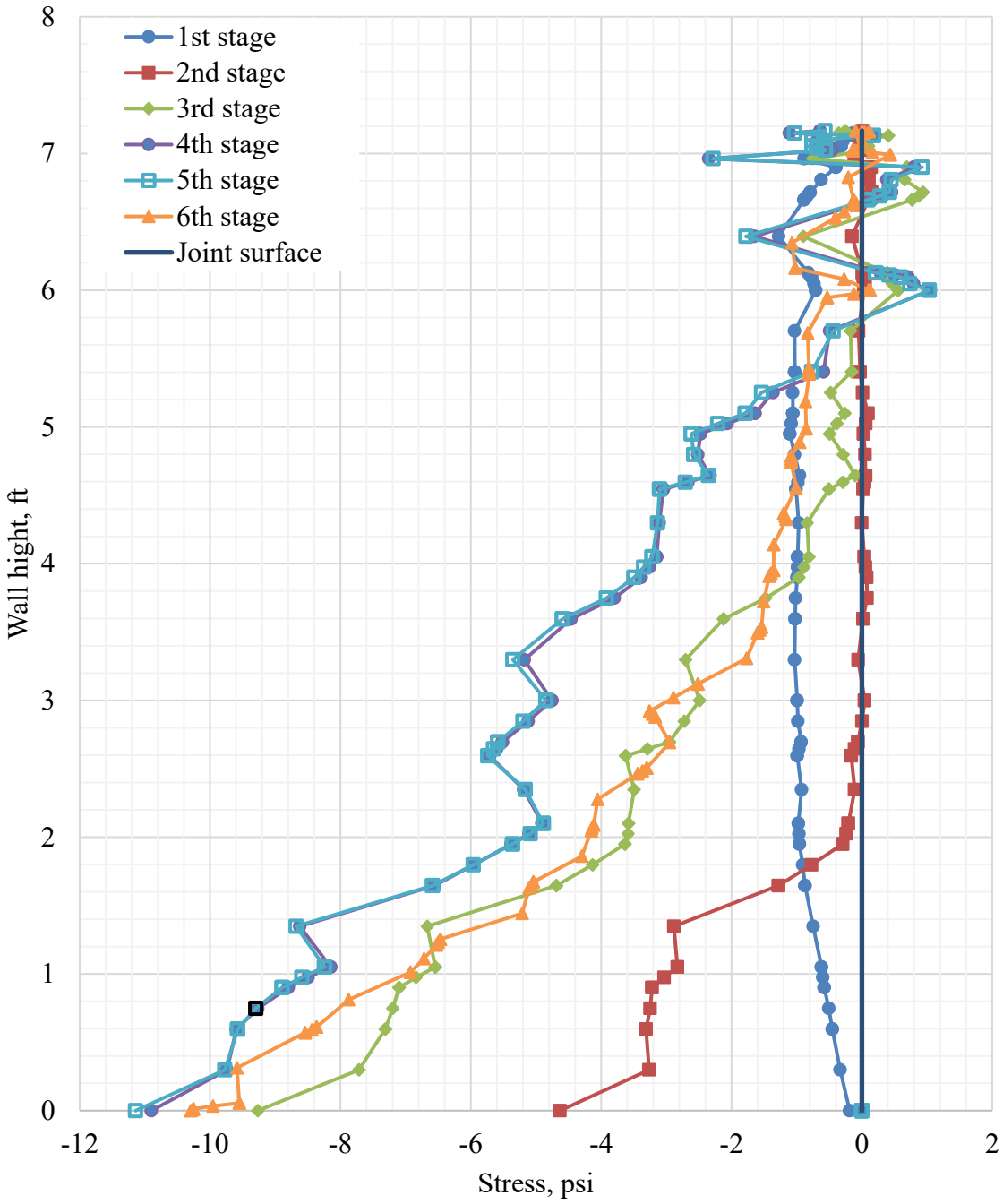

Figure 6-16. Development of stresses along the tab extension under design loads for the Chambers County culvert.

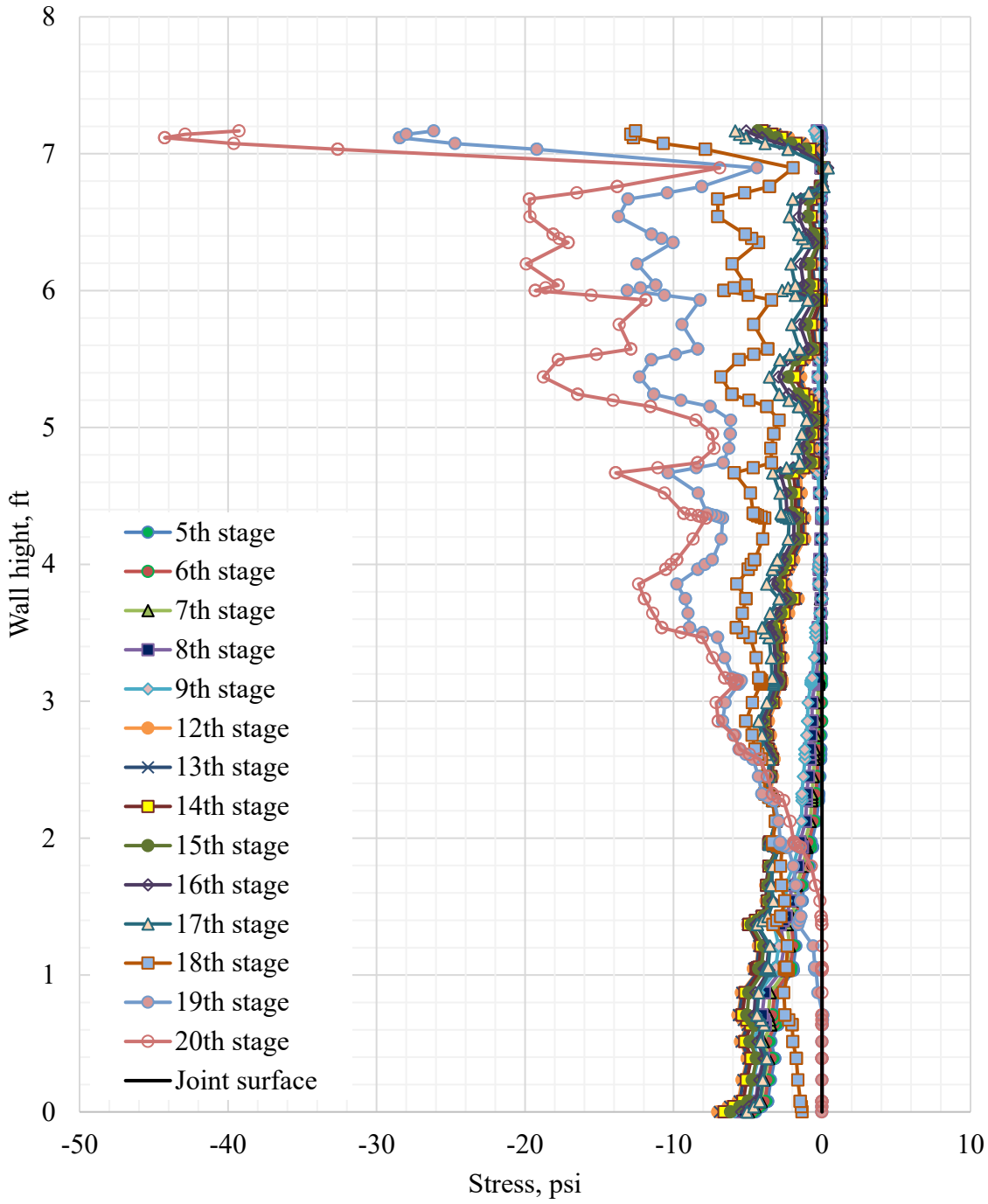

Figure 6-17. Development of stresses along the tab extension with scour propagation in Chambers County culvert.

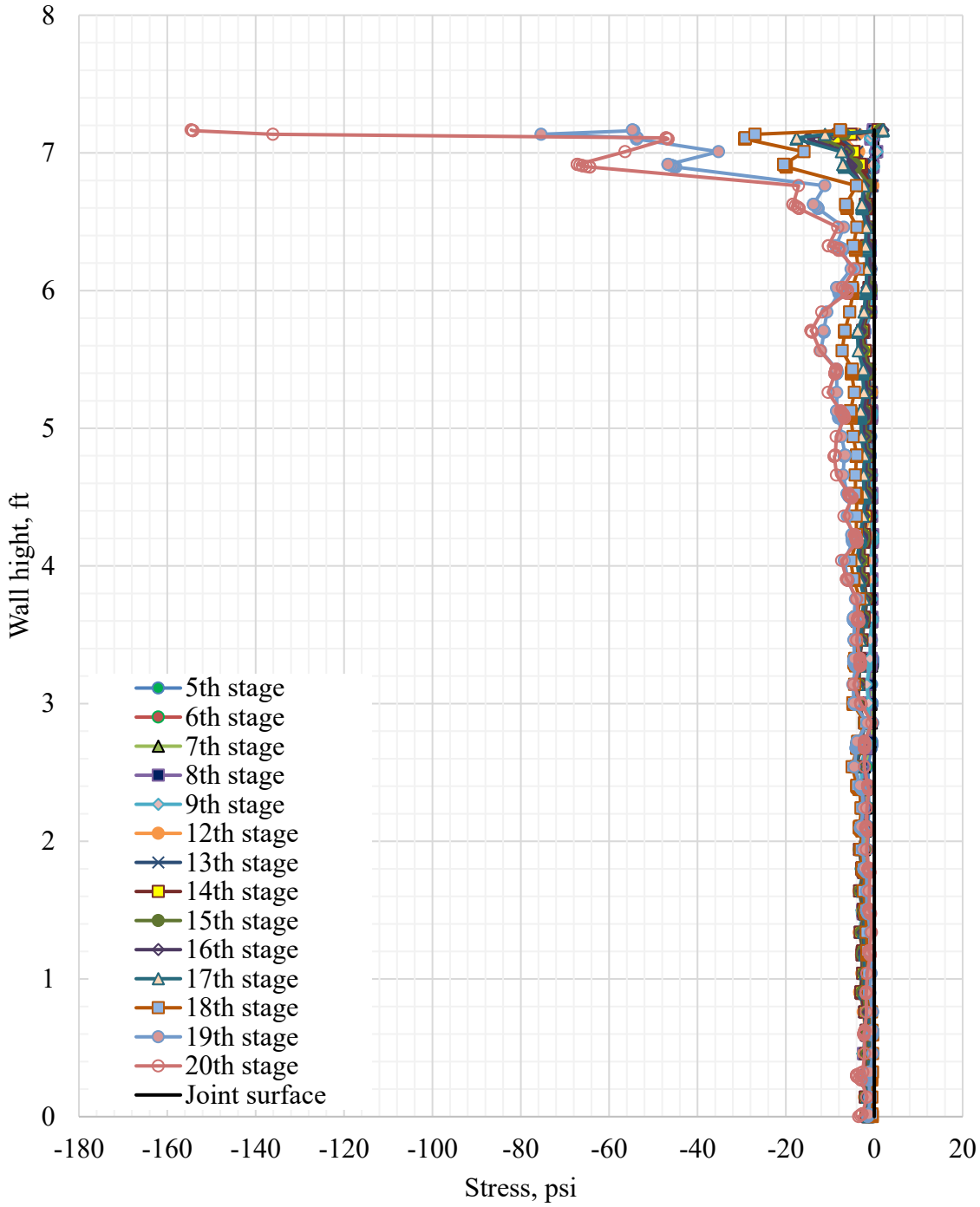

Figure 6-18. Development of stresses along the tab extension with the locked tabs in Chambers County culvert.

6.4.2. Lee County Culvert

Similar to the stress development in the tab for the Chambers County culvert, the stress development was uniform at magnitude 1-psi after constructing the culvert and before backfilling (Figure 6-19). At stage two, with the height of the backfill equal to the height of the barrel, the maximum compression stresses were 6-psi at the bottom of the tab (Figure 6-19). These stresses decrease to zero at one-third of the wall height. The compression stresses at the bottom increased as the backfill height went up to 23-ft through stages three to five (Figure 6-19). For the 6-ft deep backfill, the magnitude of the compression stress is 11-psi, which dissipated towards the mid-height of the wall. With the backfill height of 16-ft and 23-ft over the culvert, the compression stresses at the bottom were 14.9-psi and 15.7-psi, respectively. Stresses during stages four and five went up to 1.5-psi at the top of the tab surface due to bending of the wall. Under applied traffic load, compression stresses were doubled (12.6-psi) (Figure 6-19).

The distribution of compression stress with modeled soil erosion due to scour followed the same trend as in the previous case. With the scour propagation at the front edge of the key wall, the stresses at the bottom increased linearly up to 11-psi from an initial magnitude of 6-psi at stage two (Figure 6-20). During the final stages (16 to 20), the erosion of soil propagated under the footing and caused the largest displacement in the opposite direction, which created maximum stresses at the top of the wall (Figure 6-20). The magnitude of these compression stresses increased from 2.6-psi to 30.8-psi for corresponding stages.

In the theoretical simulation of the near rigid lock between two tabs, the maximum compression stresses at the top went up to 109-psi with the scour development under the

footing. The compression stresses along the rest of the height were distributed uniformly around 10-psi (Figure 6-21).

Appendix D contains the results of compression stress distributions with scour propagation for other backfill heights. Also, the results of locked tabs are summarized in Appendix D. Under higher backfill, the distribution of stresses had different shapes than with design backfill level. The maximum compression stresses remained in the lower part of the tab height with magnitudes of 23-psi, 24-psi, and 32-psi for 6-ft, 16-ft, and 23-ft backfill depth, respectively (Figure D-7,8,9). The compression stresses ranged from 5 to 10-psi over the remainder of the joint height. At stages 16 to 20, the magnitude of stress increased up to 15 to 20-psi at the top of the joint due to wall movement in the opposite direction as described in Chapter 6.3. Similar to the previous case with the locked tabs, the magnitude of stresses increased up to 70-psi for all backfill levels. The rest of the height of the wall experienced the compression stress with an average magnitude of 5-psi (Figure D-10,11,12).

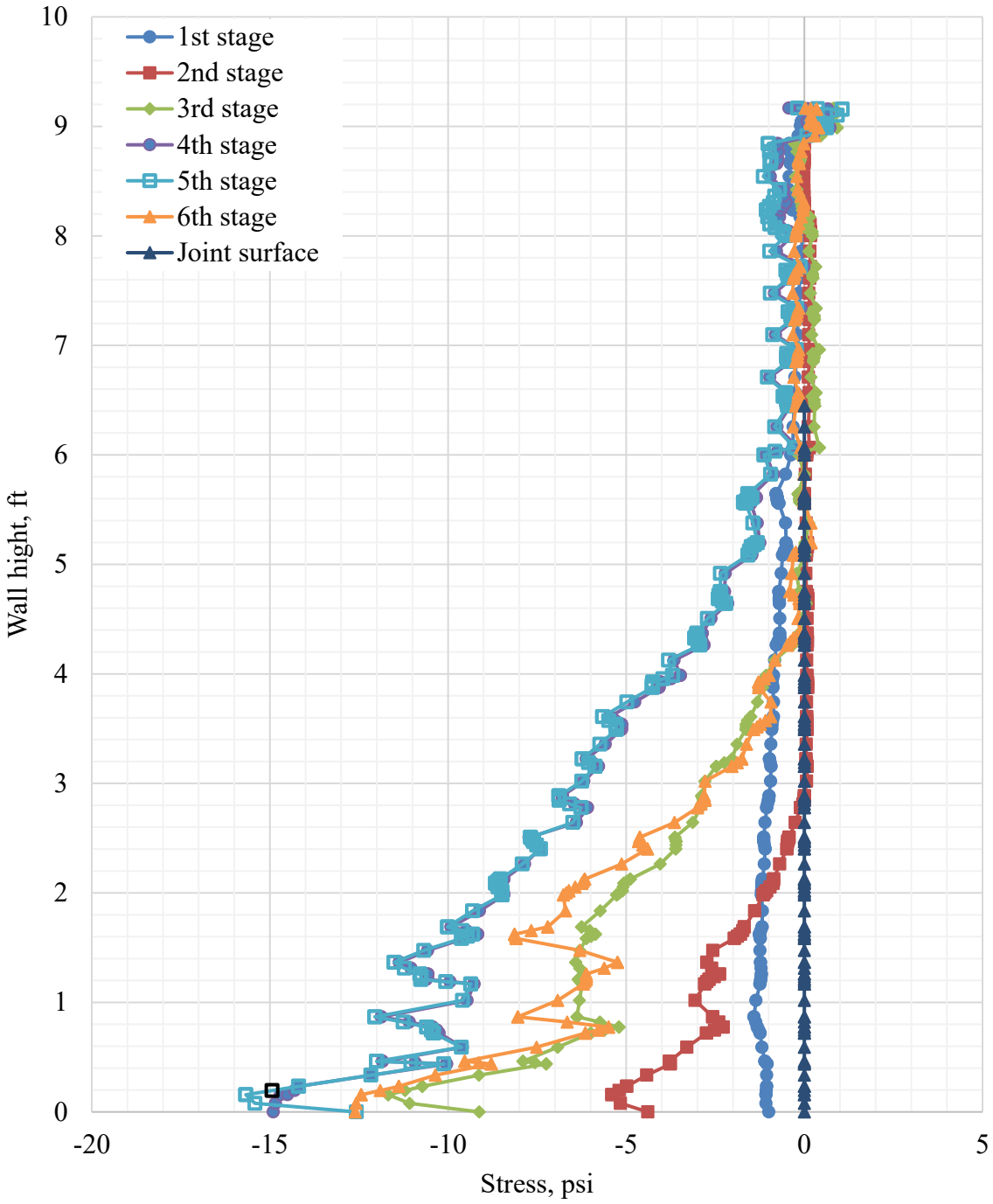

Figure 6-19. Development of stresses along the tab extension under design loads for the Lee County culvert

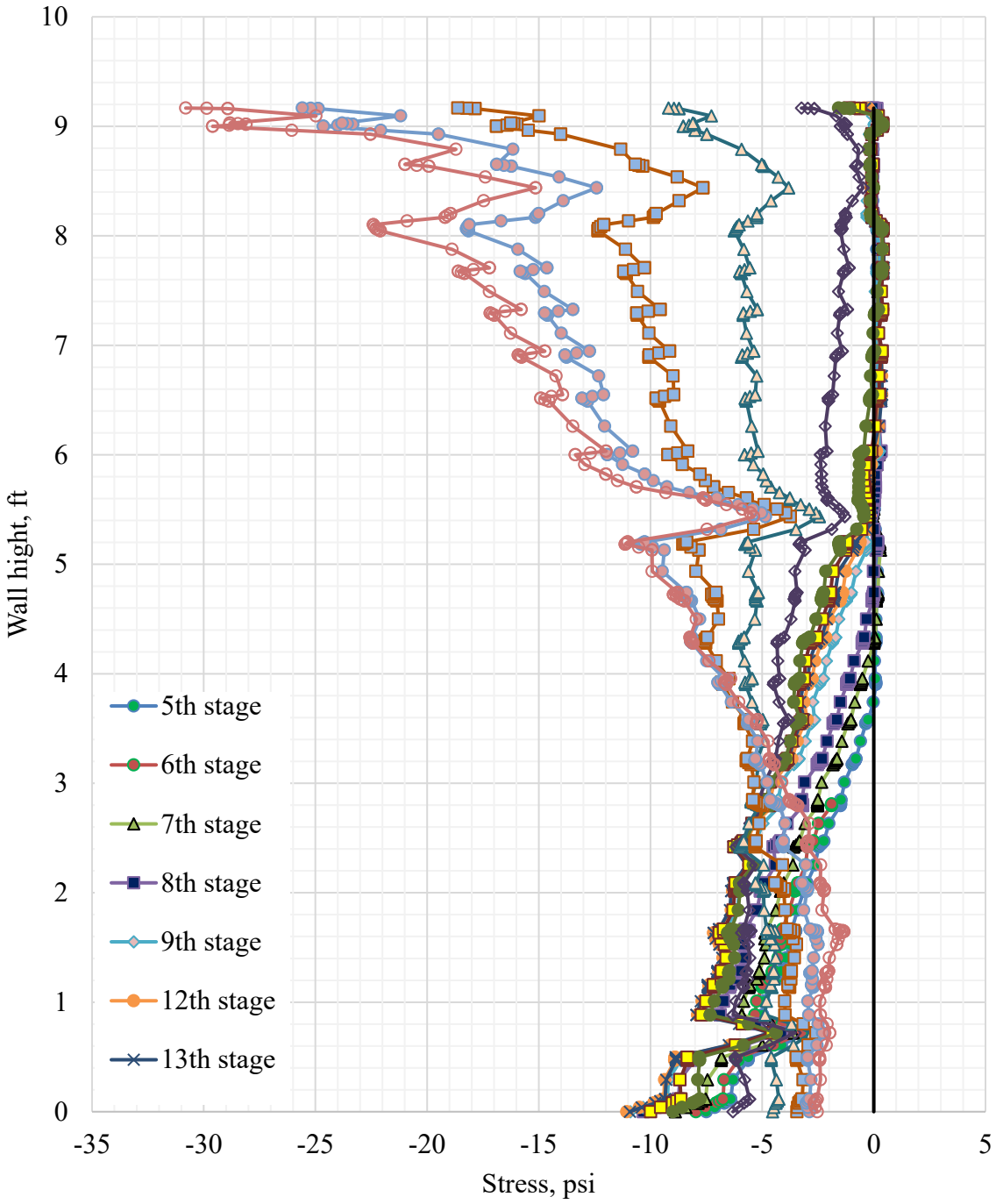

Figure 6-20. Development of stresses along the tab extension with scour propagation in Lee County culvert

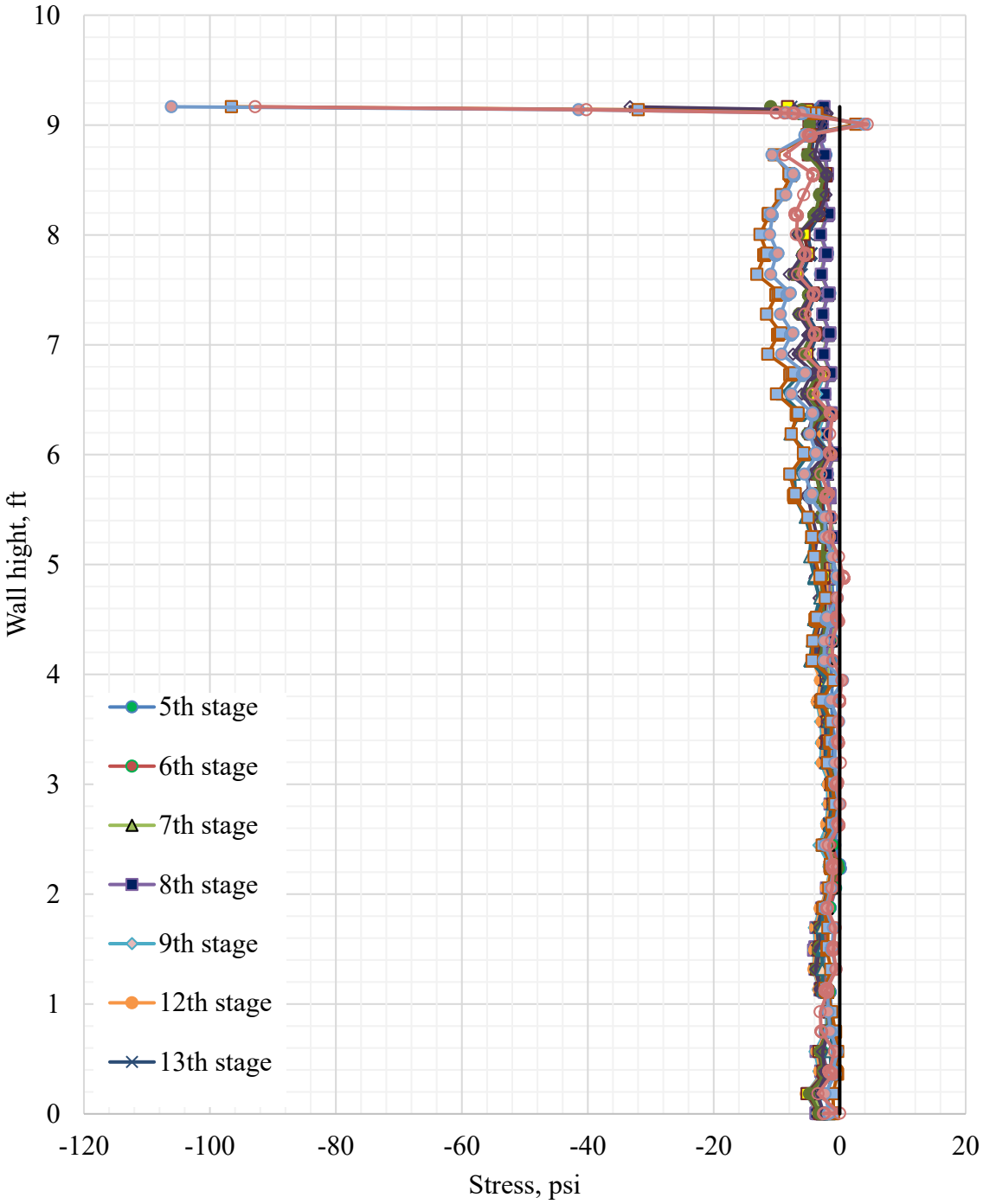

Figure 6-21. Development of stresses along the tab extension with the locked tabs in Lee County culvert

6.4.3. Coosa County Culvert

The distribution of compression stresses along the tab surface developed under the design loads is shown in Figure 6-22 for the culvert built in Coosa County. Similar to the other cases, the stresses along the tab surface were uniformly distributed at Stage 1 and reach 1-psi. Once the backfill wass leveled with the culvert barrel at Stage 2, the compression stresses at the bottom increased to 8.7-psi, and linearly decreased to 0 within the bottom third of the wall height. The increase of the backfill height to 6-ft above the barrel created the compression stresses at the bottom of the wall with a maximum magnitude of 11.6-psi. These stresses dissipated at the mid-height of the wall. When the height of the backfill was equal to 16 and 23-ft, the maximum compression stresses were 19 and 19.8-psi, respectively (Figure 6-22). The compression stresses propagated along the joint surface became zero at the top. Under applied traffic load, the magnitude of compression stresses becomes equal to 15.7-psi, which was twice as high as the design load conditions.

The distribution of the compression stresses when scour propagated under the footing and the backfill height reached the top of the culvert barrel is shown in Figure 6-23. Compared to the design load case, the development of scour does not create a severe effect on the stress distribution and magnitude (overall the stresses are lower than in the two culverts discussed in previous chapters). At Stage 13, when scour propagated behind the key wall, the maximum compression stresses reached 15-psi. With further soil erosion under the footing, the wing wall changed its direction of rotation. Similar to the other cases, the stress concentration zone with the magnitude of 11-psi was formed at the top.

If the tab extensions are locked, the peak stresses were smaller than for the other culverts (up to 37-psi - Figure 6-24). However, the stresses along the rest of the tab height were uniformly distributed with magnitude 5-psi.

Stress distributions for other considered backfill heights under the design load, scour, and when the tab extensions were locked are summarized in Appendix D. Similar, to the other models with backfill leveled to the height of the barrel, the stress distribution pattern was consistent with the other cases for all stages (Figure D-13, Figure D-15, Figure D-16, D-17 and D-18).

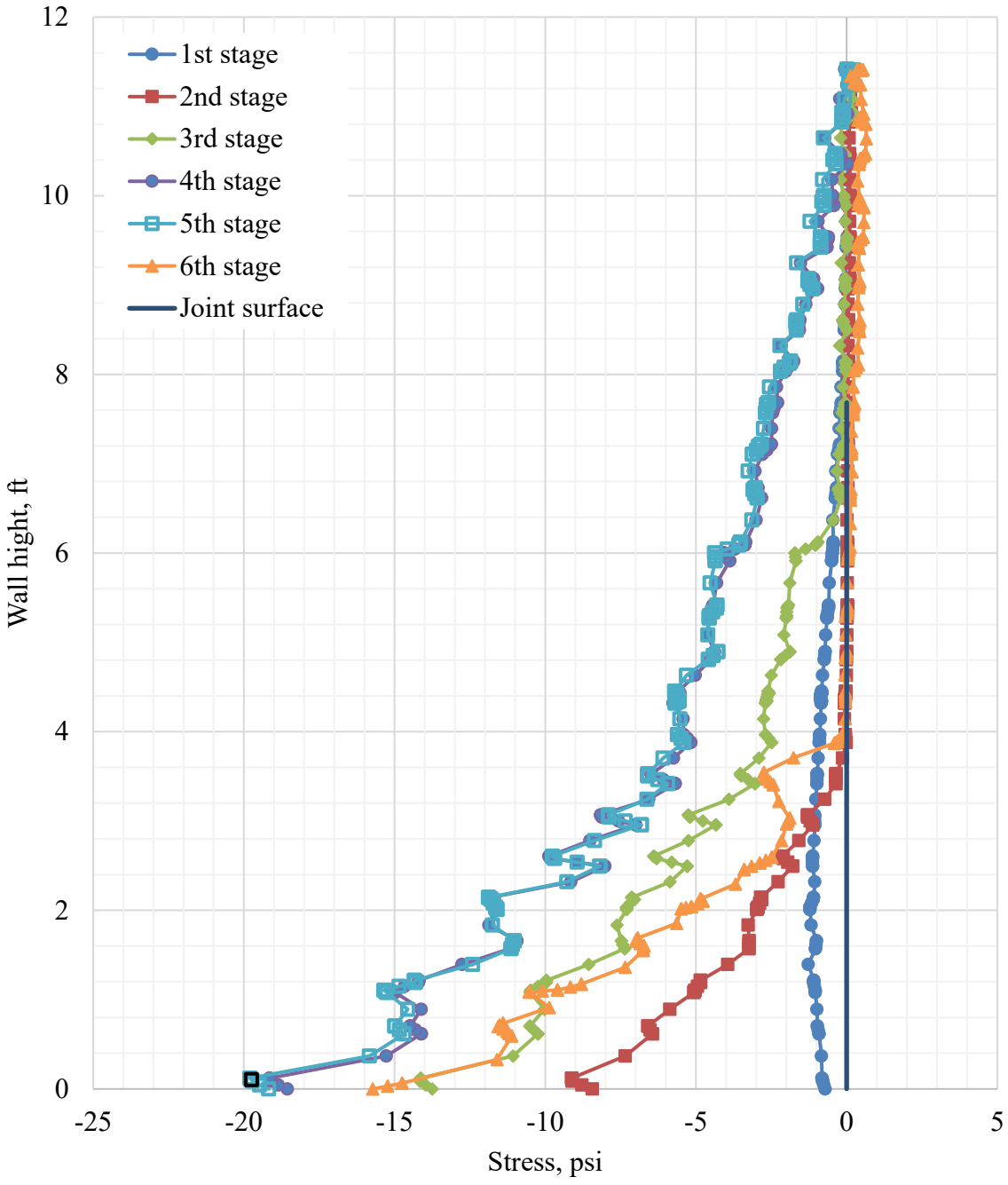

Figure 6-22. Development of stresses along the tab extension under design loads for the Coosa County culvert

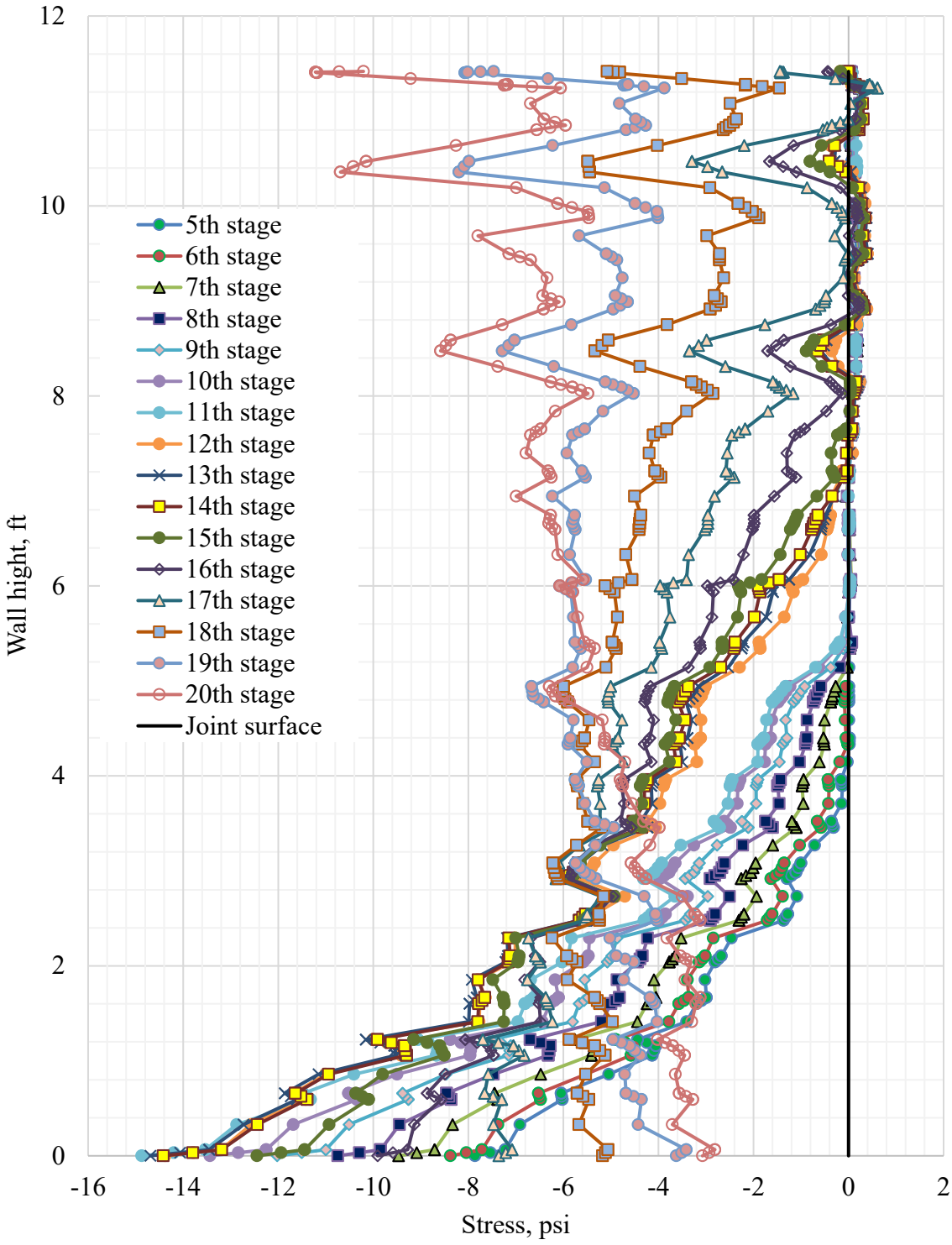

Figure 6-23. Development of stresses along the tab extension with scour propagation in Coosa County culvert

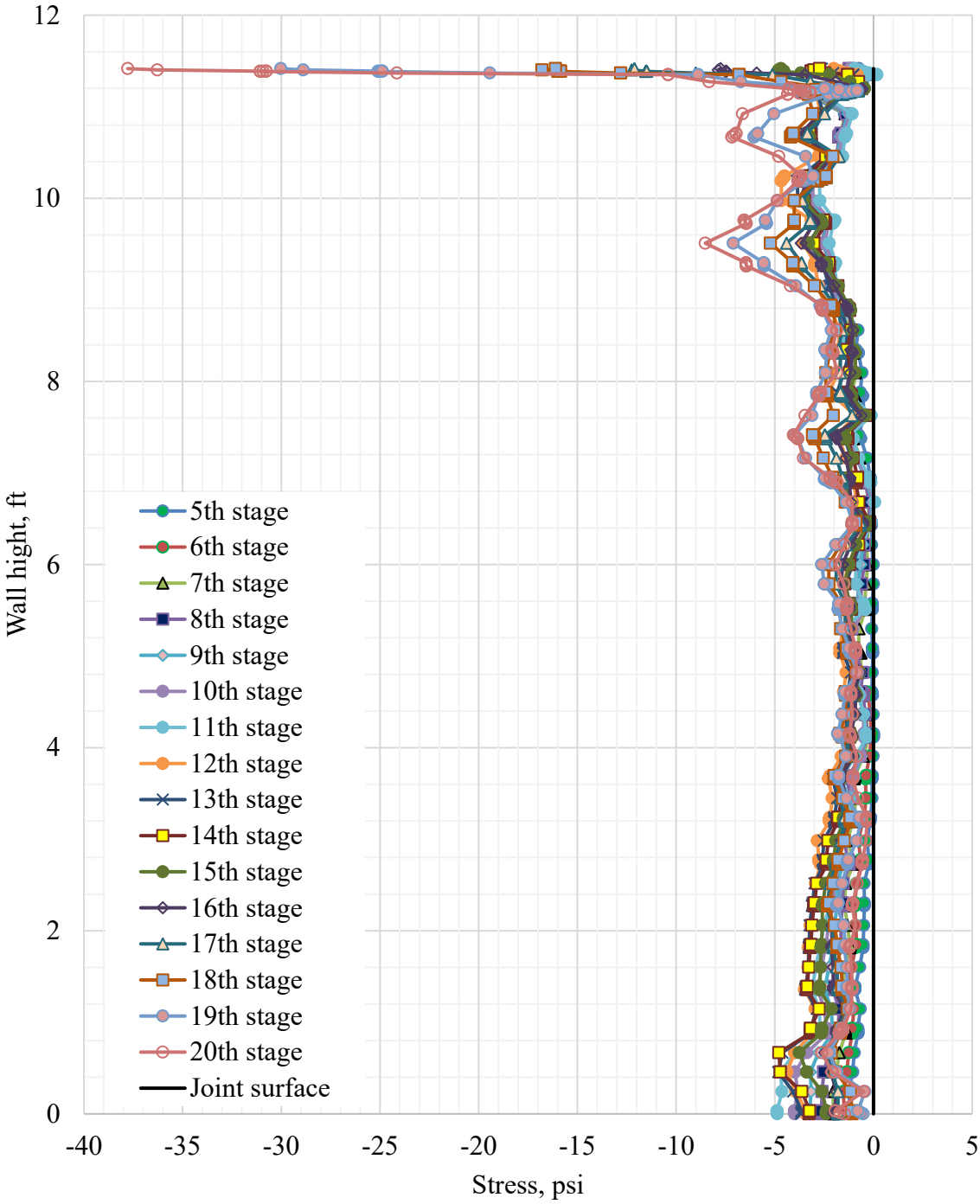

Figure 6-24. Development of stresses along the tab extension with the locked tab extensions in Coosa County culvert

6.4.4. Culvert with Monolithically Connected Wing Wall

The stress analysis for a monolithically connected wing wall of the 9-ft deep culvert barrel was performed in this study. The distribution of stresses was similar with regard to the shape for all stages of construction and considered structures. The resultant stress measured at the same location, as for the tabbed connection, are shown in Figure 6-25. The maximum compression stresses, which range from 120 to 174-psi for different heights of the backfill, were located at the bottom of the wall. These stresses decreased almost to zero within the next 6-in of the wall height. At Stage 1, before the backfill was placed, the compression stresses at the bottom reached 14-psi. With the backfill filled to the level of the barrel, the stresses increased up to 140-psi. Applied traffic load reduced the magnitude to 120-psi. Further increasing the backfill height to 6-ft, 16-ft and 23-ft produced the development of compression stresses equal to 174-psi, 154-psi and 137-psi, respectively.

Scour propagation did not create a significant impact on stress distribution in the case of a monolithically connected wing wall. The resultant stresses developed along the tab are shown in Figure 6-26 for the backfill height equal to the height of the barrel and scour propagation. The shape of the stress distribution remained the same, as for design loads, with the maximum magnitude of 187-psi. Therefore, the stresses developed due to scour exceeded the stresses from backfilling load only by 30%. Once the scour propagated under the bottom of the wing wall, the stresses dropped to 146-psi.

A high stress concentration zone was noticed in all models with the rigid joint. The compression stresses with a magnitude up to 1600-psi were localized at the top 5-in of the wall when 23-ft high backfill is placed (Figure 6-27**Error! Reference source not found.**). This location corresponded to a position of crack formation in existing culverts (Figure

1-1). From Figure 6-28, the maximum stresses in this location were smaller in case of soil erosion due to scour.

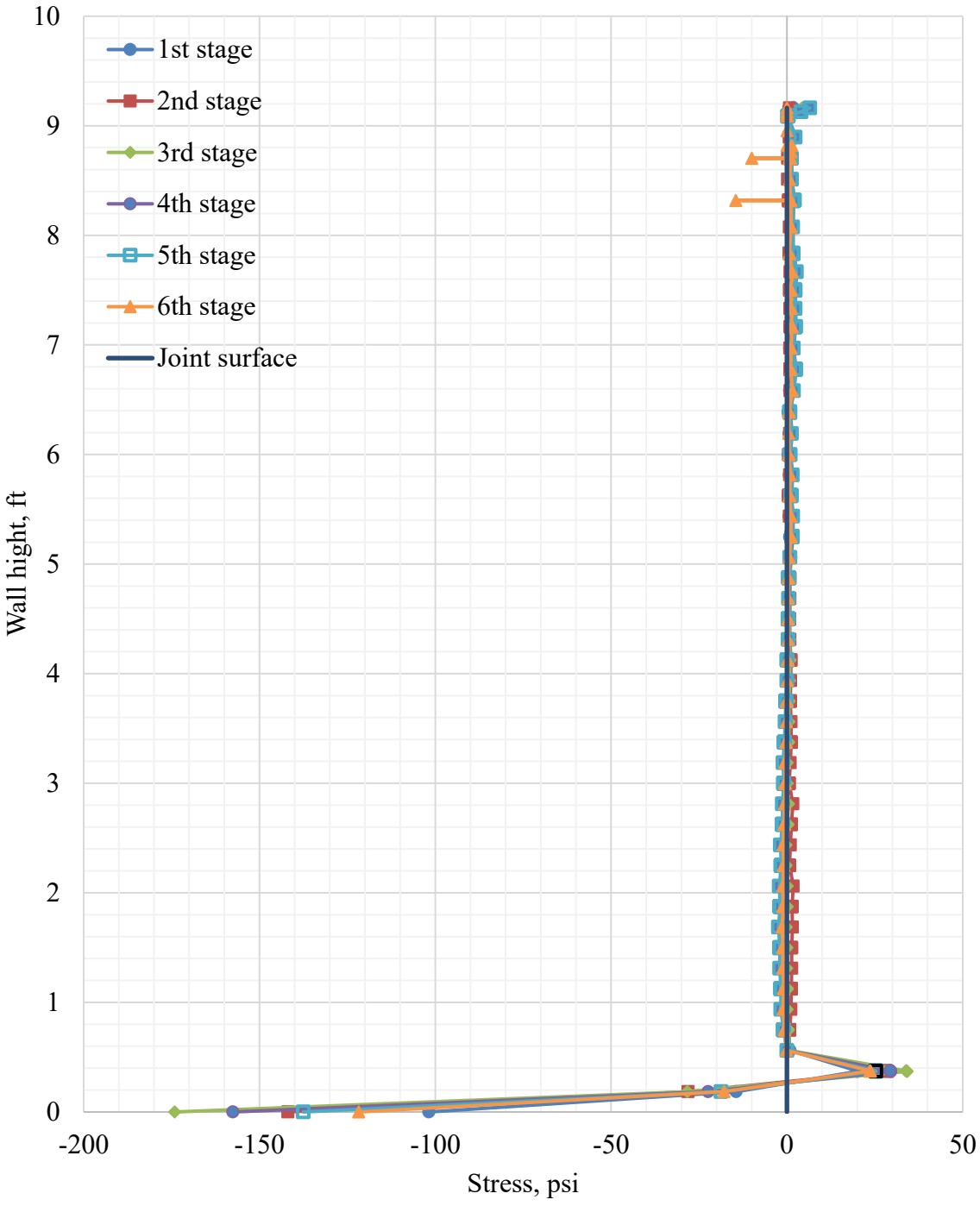

Figure 6-25. Development of stresses in the monolithic connection under design loads

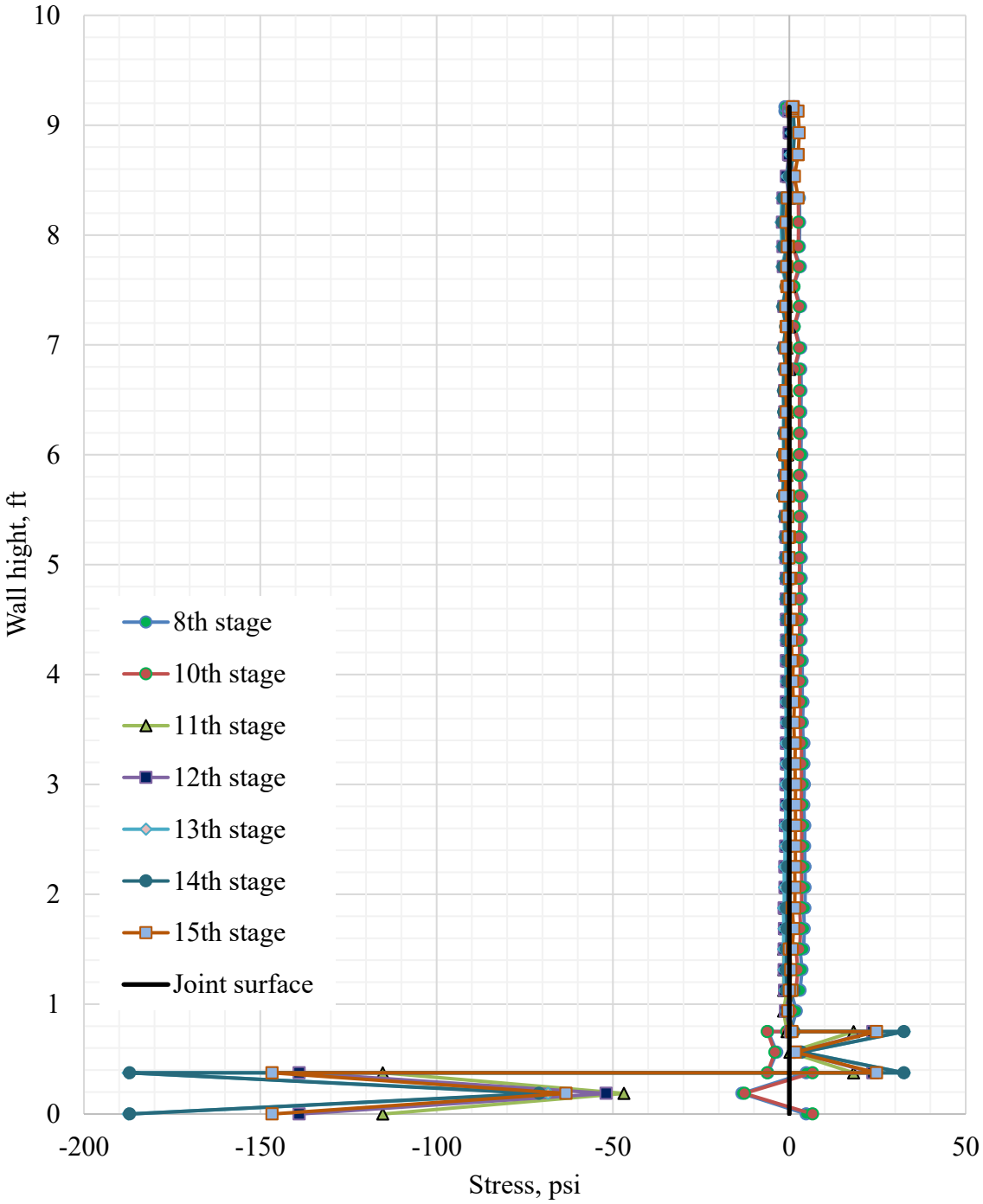

Figure 6-26. Development of stresses in the monolithic connection with scour propagation and backfill to the level with scour

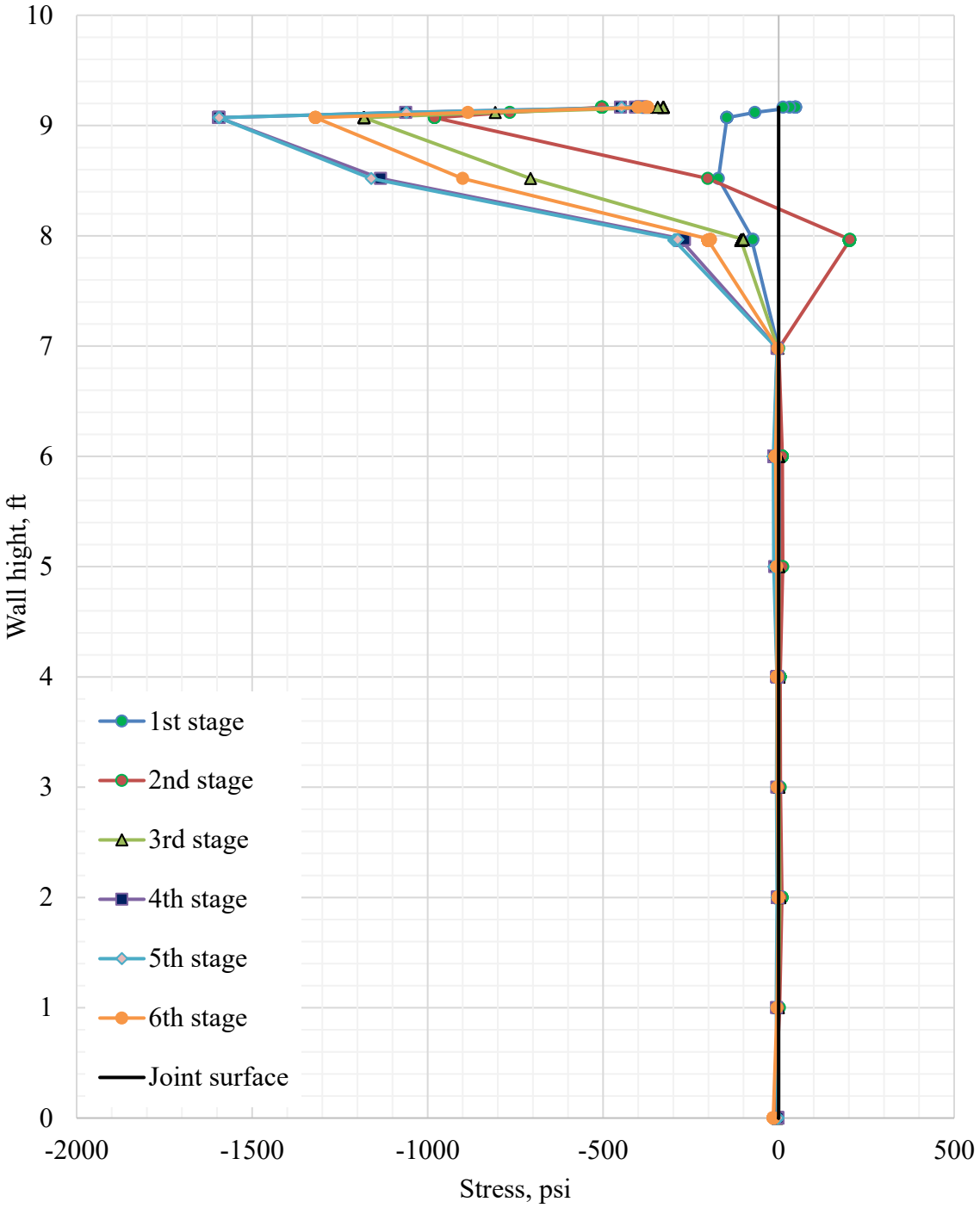

Figure 6-27. Development of stresses in the monolithic connection at critical location for under design loads

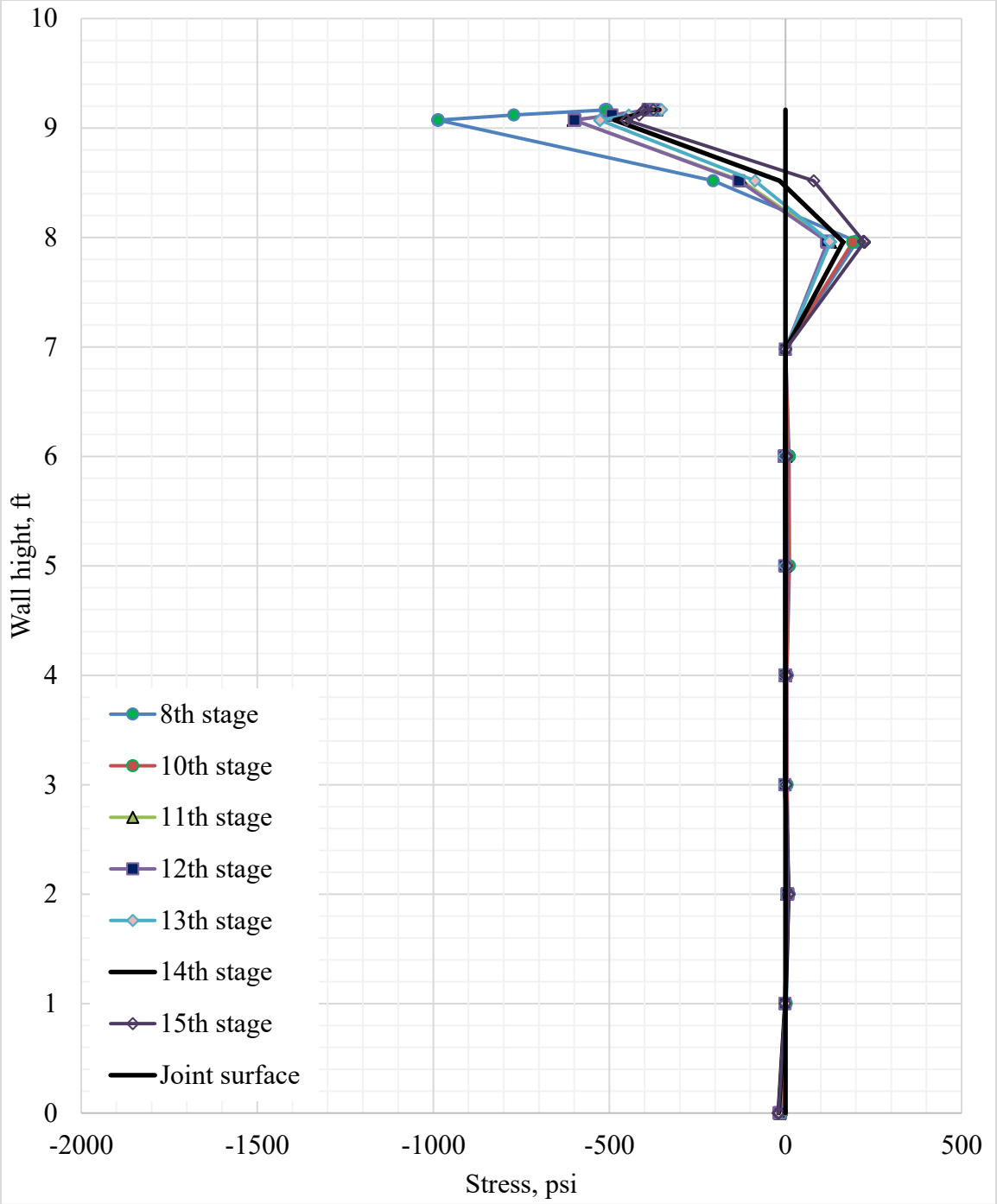

Figure 6-28. Development of stresses in the monolithic connection at critical location with scour propagation for 0-ft backfill

6.5. Comparison of Numerical and Measured Results

The charts in this section present the comparison between stress distribution along the tab height obtained from numerical analysis and the stress distribution measured in the field. The stress distribution from numerical results was calculated for the design height of the backfill (Stage 2), which is in the level with culvert for all considered cases. The measured pressure distribution represents the maximum and average set of recorded data in constructed culvert from each cell within the tab.

The pressure distribution after placing the backfill showed a similar trend as the numerical solution for the Chambers County culvert. The maximum compression occurred at the bottom and decreased to the top of the wall (Figure 6-29). The magnitude of maximum compression stresses was similar but it was more likely a coincidence than a trend. The field measurements were recorded in the uncontrollable environment, which involved a number of uncertainties. As it was mentioned in Chapter 5, after placing the backfill, the maximum recorded pressure gradually reduced to an average value of 2-psi in all three cells along the height.

The bottom pressure cells in the Lee County culvert experienced the greatest pressure among the constructed culverts. Unlike the previous case, the trend of pressure distribution showed evidence of nonlinearity similar to the numerical results. Despite the lower magnitude, the shape of average pressure distribution follows the shape of maximum distribution. The magnitude of the recorded stresses was three times higher than the numerical results after placing the backfill (Figure 6-30). This may be explained by the dynamic effect during compaction, which was not considered in the numerical analysis.

The pressure distribution along the tab in the Coosa County culvert shows evidence of uniform translation and rotation of the wall away from the backfill. This resulted in maximum compression stresses at the top of the tab (Figure 6-31). This behavior was completely different from predicted by the numerical model when the maximum pressure was located at the bottom of the wall. Also, unforeseen type of behavior was observed for most of the readings where the maximum pressure was greater at the central cell and smaller or near zero in other two locations.

Overall, different types of movement were recorded. Most of the tabs, where the maximum pressure at the bottom, exhibited evidence of wing wall rotation so that the top of the wall moved towards the backfill and the bottom away from it. This type of behavior corresponded with that predicted by numerical modeling. The rest of the tabs experienced comparatively small pressures due to sliding or bending of the wall.

Despite the difference in magnitude of compression stresses, the total behavior of the wing wall had the same trend as obtained in the numerical simulation with maximum compression at the bottom. These results were important and were used to develop the procedure of estimating the magnitude of the maximum force acting on the tab surface for the design, which will be explained in the following chapter.

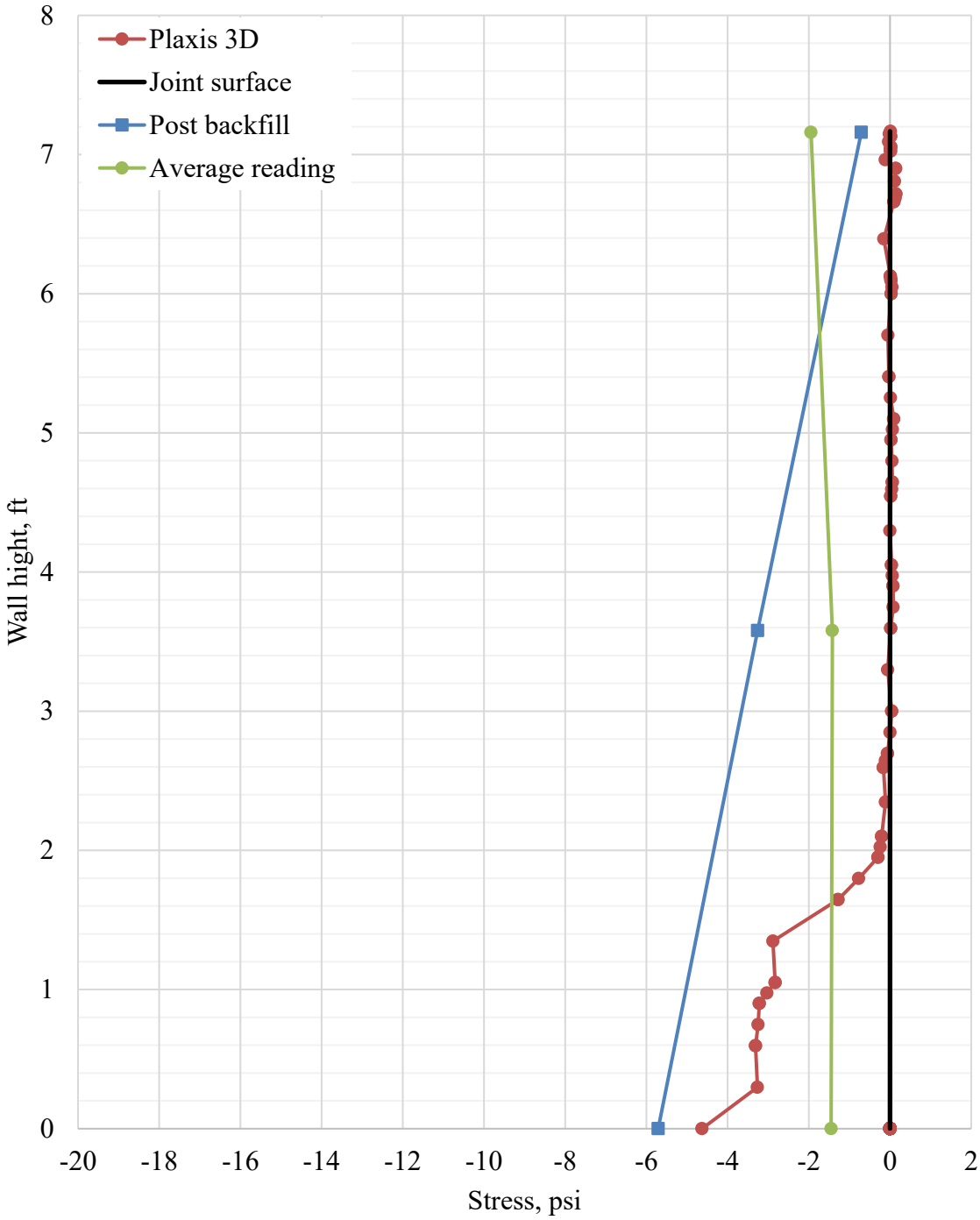

Figure 6-29. Pressure comparison for Chambers County culvert

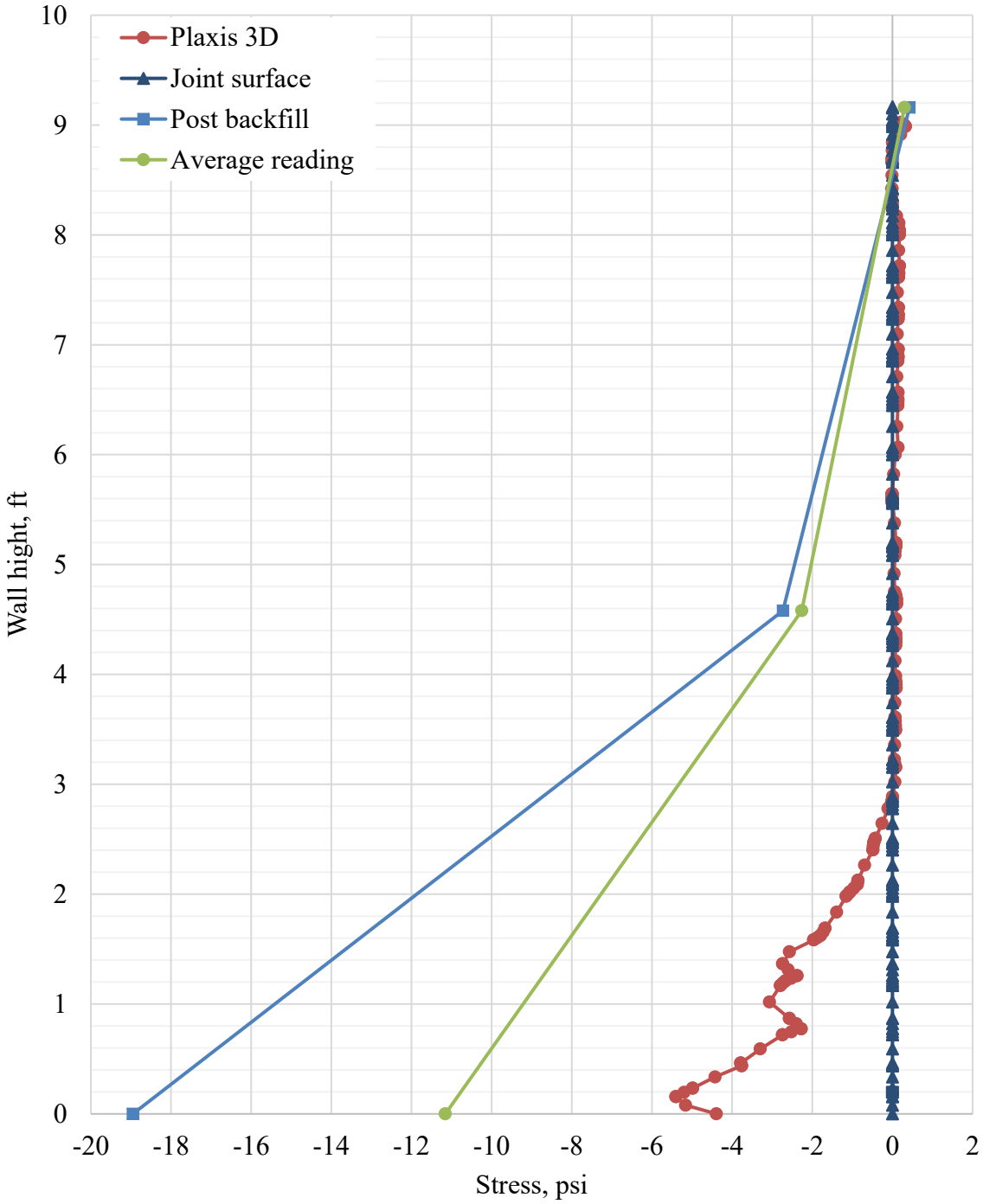

Figure 6-30. Pressure comparison for Lee County culvert

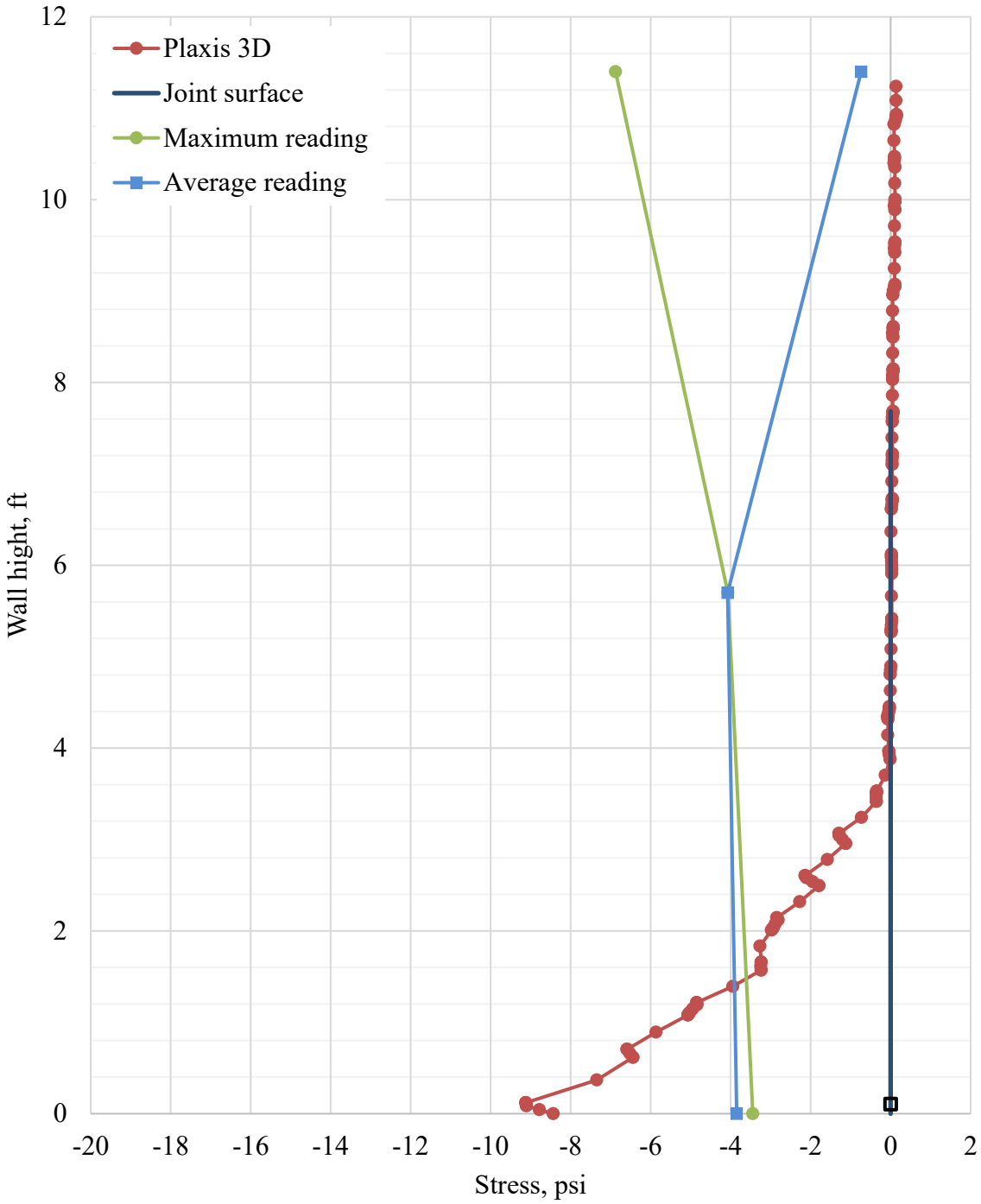

Figure 6-31. Pressure comparison for Coosa County culvert

6.6. Summarized Maximum Pressure in the Tab

This section presents the summarized results of compressive pressure calculated and measured within the tab that was presented in previous chapters. The maximum compressive stress magnitude was selected from all developed and analyzed models for Chambers, Lee, and Coosa counties culverts. The position of these stresses along the height of the wall varies between models. Only field measurements of pressure at stages that correspond with the numerical analysis were shown. For Chambers and Coosa counties culverts, the Stage 2 represents the design backfill level. For the Lee County culvert, the recorded data was available not only for the stage with backfill load but with the traffic load as well. The presented data contain only the maximum recorded pressure within all four tabs for each culvert.

Maximum measured and calculated pressure in the tab for three constructed culverts are summarized in Appendix E. The distribution of compressive stresses through different stages of analysis for Chambers, Lee and Coosa counties culverts are presented on Figure 6-32, 33, 34. Dispersion of these results indicates that the pressure developed in the tab primarily depends on the applied load from the backfill. When only applying backfill and traffic load, the increase of pressure magnitude is almost linear. As it was mentioned in the previous section, the scour propagation in front and around the key wall does not cause significant increase of the compressive pressure for the constant backfill height. The substantial rise of the stresses occurs with scour propagation under the footing. However, the adverse effect of the scour propagation on the compression stresses in the tab decreases with the height of the wing wall. Despite the lack of variety of backfill-to-

culvert height ratios, the magnitude of measured pressure in the tab was similar to the results obtained from numerical analysis.

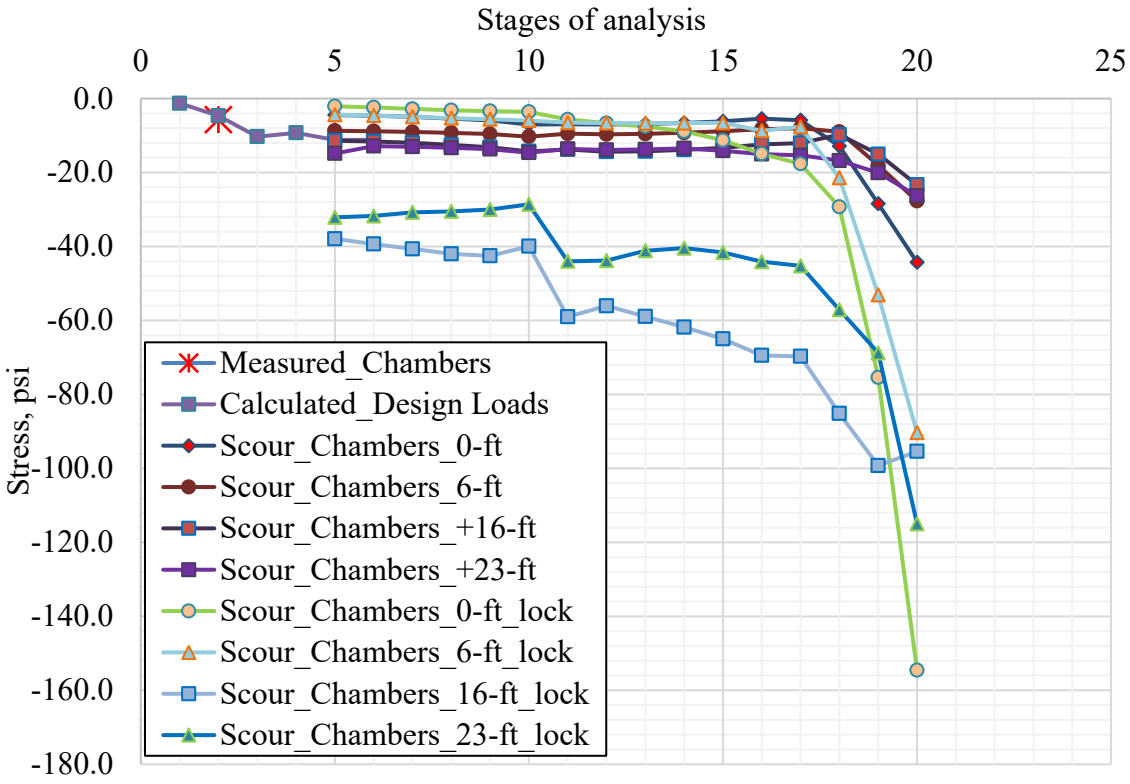

Figure 6-32. Maximum pressure in the tab in Chambers County culvert

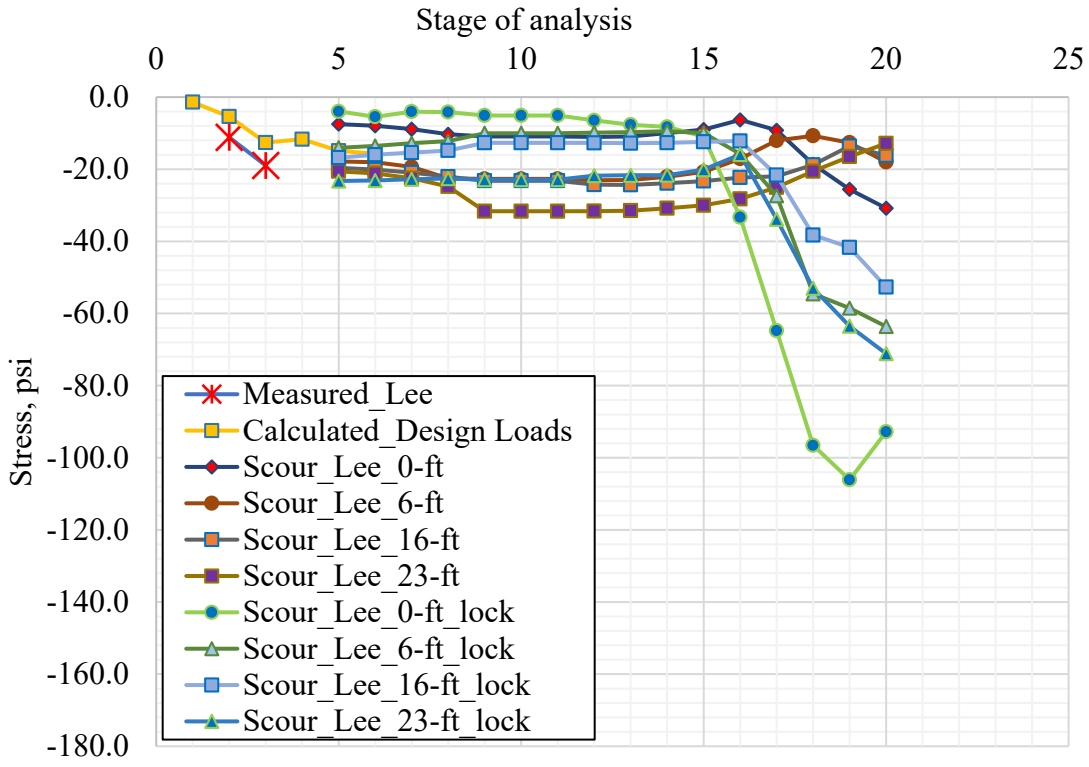

Figure 6-33. Maximum pressure in the tab in Lee County culvert

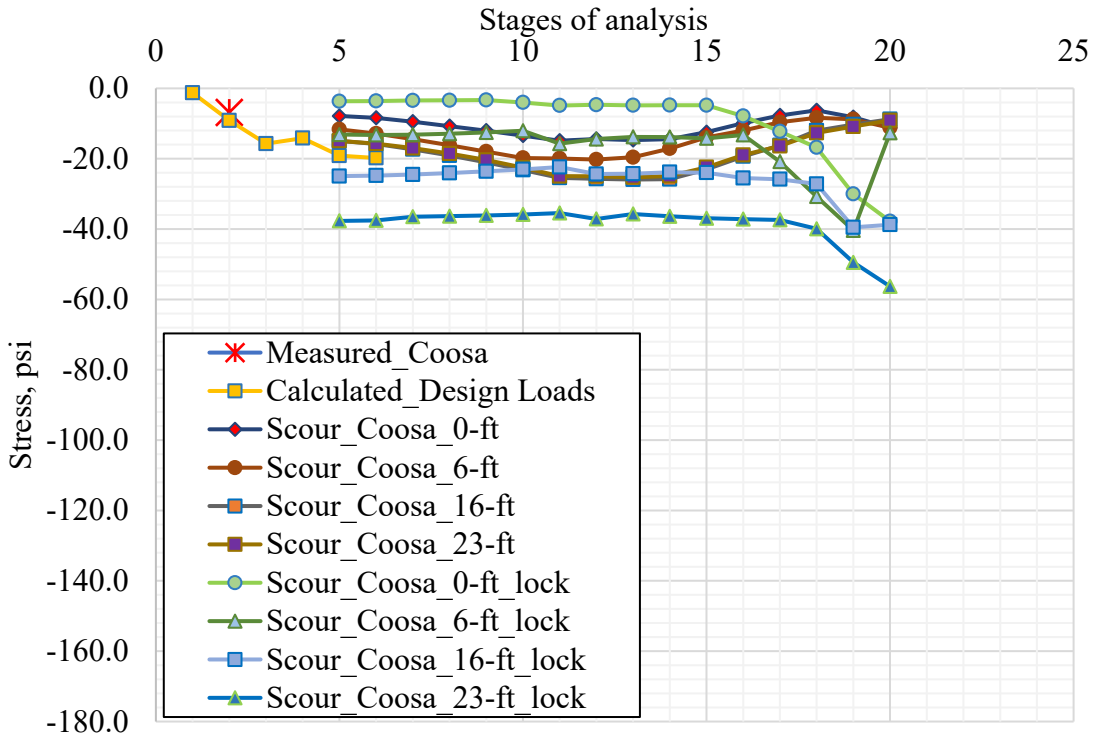

Figure 6-34. Maximum pressure in the tab in Coosa County culvert

6.7. Forces in the Tab

The design procedure of tab extension will be discussed in Chapter 7. This procedure considers the design of a one-foot strip of the tab height. The only input load considered in the design is the shear force acting on the tab surface. As this is a new design, there is no established procedure to calculate the magnitude of this force. Finite element analysis was therefore used to estimate the magnitude of the shear force. For each model developed within this project, the maximum resultant force per one linear foot of the tab height was recorded. The position of the one-foot strips varies with the height of the wing wall for different culvert configurations and applied load combinations. This location matches the area that experiences maximum compression stresses. This approach provides conservative estimates of the maximum value of the shear force normal to the tab surface.

The resultant forces on the one-foot strips of the tab height for different backfill heights and traffic loads are shown in Figure 6-35. The vertical axis corresponds to the stages of analysis discussed in Section 4.6. The backfill heights on the graph in Figure 6-35 refer to the backfill over the culvert. Thus, 0-ft backfill means the backfill height equal to the level of the culvert (Stage 2). The magnitude of transferring force directly depends on the backfill height and culvert depth.

The amount of force that may be generated/developed between two tabs directly depends on the lateral active earth pressure, which acts on the wing wall. Since the tab design considers forces that act on one-foot strips, it is essential to estimate the magnitude of this force based on the maximum magnitude of the lateral earth pressure $\sigma_{ah}^{'} = K_A \cdot \gamma \cdot H$ at the bottom of the wall (Figure 6-36a). The maximum magnitude of the

lateral earth pressure was assumed to be uniformly distributed over the 1-ft height. Therefore, the equivalent force is calculated as (Figure 6-36b):

$$P_{ah\_1ft} = \sigma'_{ah} \cdot 1ft \qquad \textbf{Equation 6-1}$$

Where:

P_{ah_1ft} – force acting per foot long strip

σ'_{ha} - lateral earth pressure.

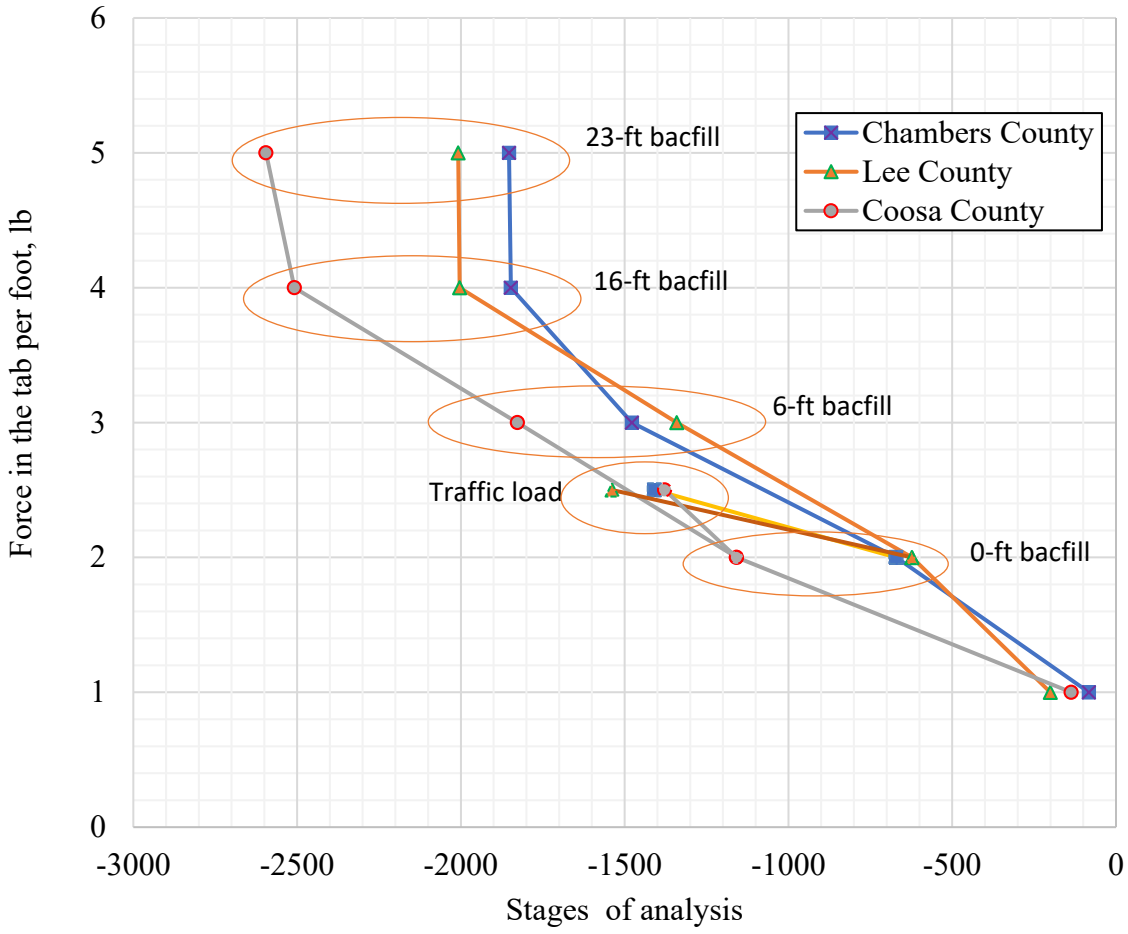

Figure 6-35. Force in the tab under design loads

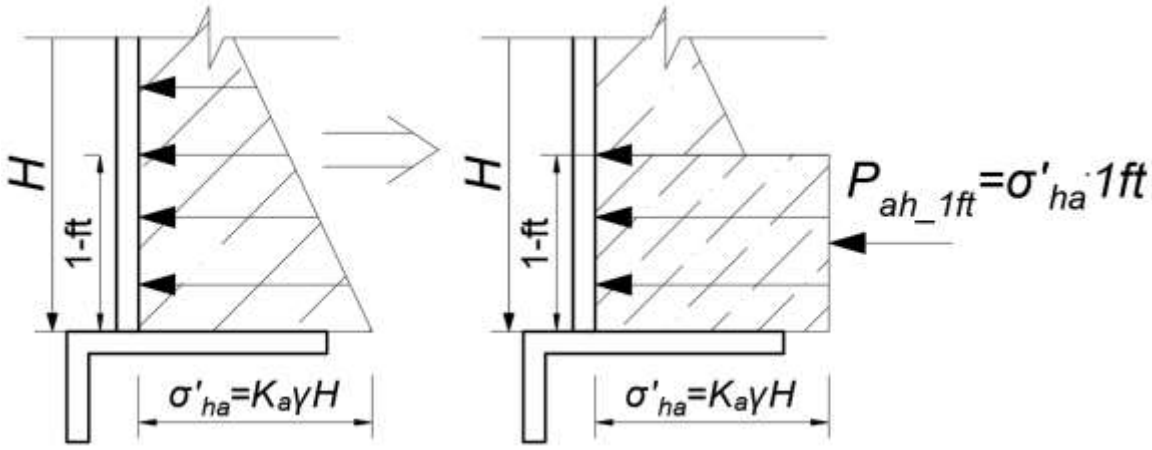

a) b)

Figure 6-36. Distribution of lateral earth pressure: a) theoretical; b) idealized

The comparison between the resultant active lateral earth force P_{ah_1ft} on the one-foot strips and the maximum force in the tab for the three constructed culverts are shown in Figure 6-37. The horizontal axis represents the magnitude of the transferring force, while the corresponding wing wall height is on the vertical axis (7.1-ft in Chambers County culvert, 9.1-ft in Lee county culvert, and 11.4-ft in Coosa County culvert). The forces obtained from finite element models are shown for 0-ft and 23-ft backfills. The lateral earth pressure was calculated using Rankine theory to estimate the value of active earth pressure coefficient K_a. The soil properties as discussed in Section 4.5. were applied to calculate the earth pressure. A soil unit weight of 120-pcf (0.062-pci) and a friction angle of the soil of 30° were used for all models. To compare the forces with 23-ft backfill, the active earth pressure coefficient was calculated using a slope of backfill angle equal to 25°, which corresponds to the one used in the numerical model. For the backfill up to the level of culvert, the backfill slope angle was set to 0°.

The maximum lateral earth force acting on the wing wall is shown as 1.0 x P_{ah_1ft} for corresponding culvert depth (Figure 6-37). The magnitude of this force was lower than the stresses that are transferred between the two tabs under design loads. Increase in the magnitude of the theoretical force by 4.5 was well-correlated with the numerical results for the backfill slope angle of 25°. In case of flat backfill (0-ft over the culvert), the magnitude of the theoretical force acting on the wing wall with 0° backfill slope angle needed to be increase by 2.5 (Figure 6-37).

To determine the maximum tab force developed due to backfilling a 30-ft deep culvert was simulated. For the considered material properties, 4.5 and 2.5 of the magnitude of the theoretical force acting on the one-foot width of the wing wall is highly correlated with the numerical results for the wing wall heights from 7-ft to 30-ft depth (Figure 6-38). In the case of no backfill over the culvert, the force in the tab was between 1.5 and 2.5 of the theoretical force P_{ah_1ft} for considered backfill heights. With the 23-ft backfill, the results for the culvert depth below 15-ft were between 3.5 and 4.5 of the theoretical force P_{ah_1ft}. For the culverts deeper than 15-ft, the force transferring in the tab was decreasing in comparison to shallower culverts.

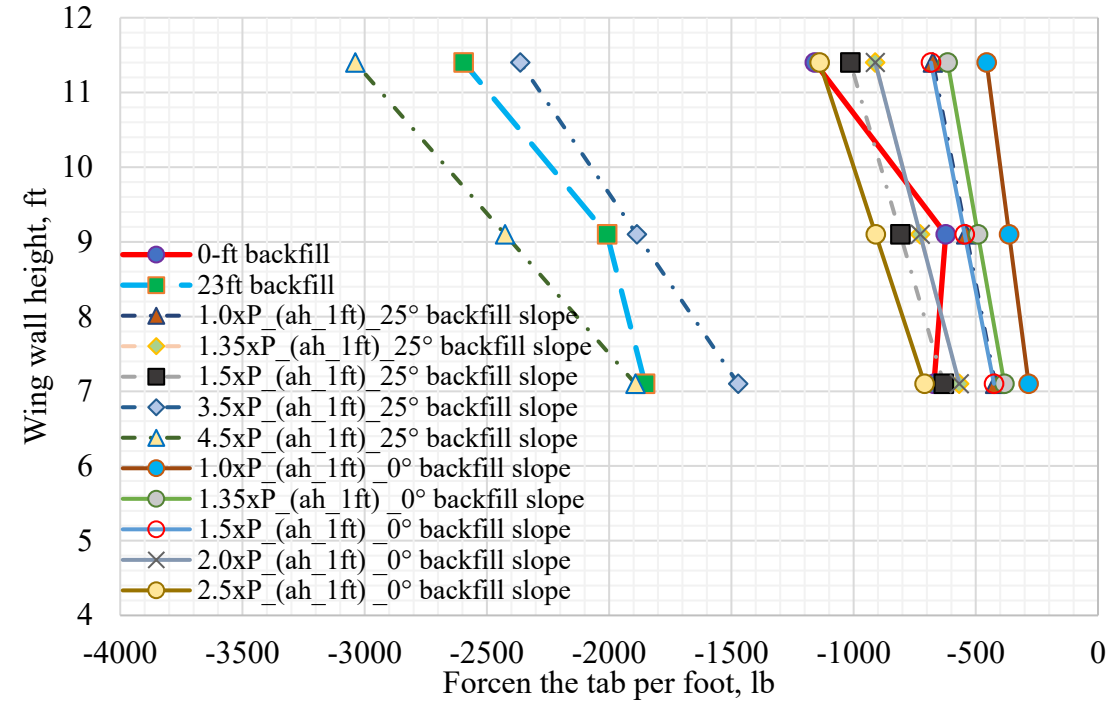

Figure 6-37. Comparison of calculated and theoretical forces in the tab for different backfills

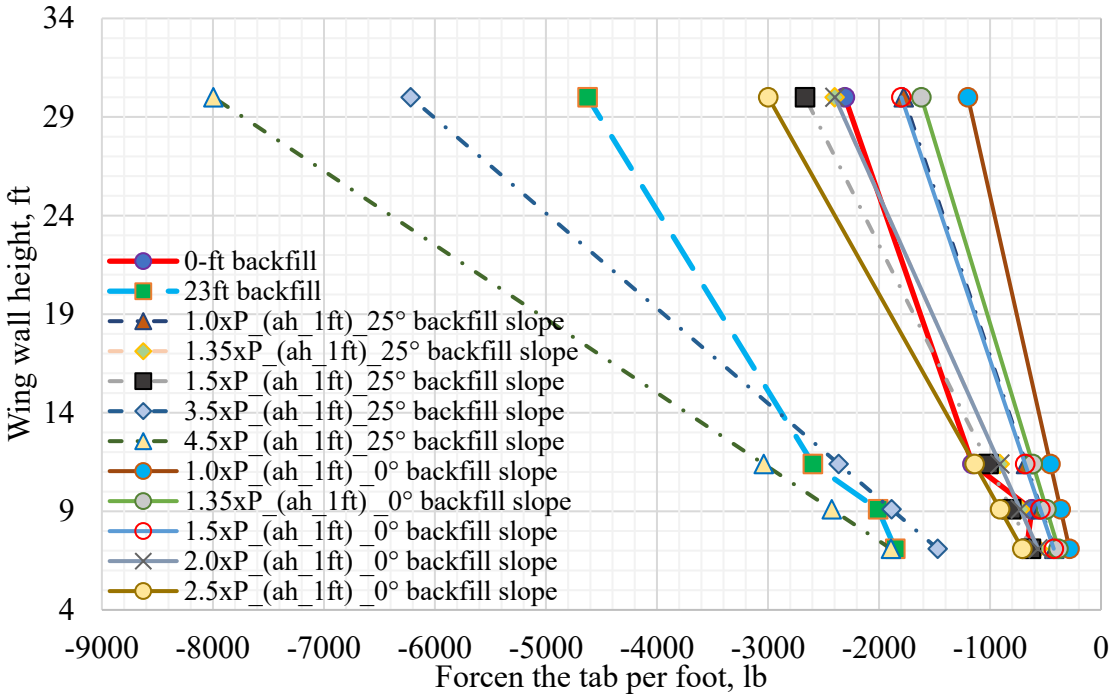

Figure 6-38. Comparison of calculated and theoretical forces in the tab for different backfills

In case an extreme event, such as scour, the maximum analyzed force in the tab per linear foot is shown in Figure 6-39 for constructed culverts. The horizontal axis represents the stages of scouring described in Section 4.6. For the tabs installed in the Chambers County culvert, the maximum force due to scour, obtained from numerical results, was 2000-lb (Figure 6-39a). This value falls within a range from 2700-lb to 900-lb, based on the theoretical lateral force with and without backfill over the culvert, respectively. For the Lee County culvert, the magnitude of forces in the tab was the highest among the constructed culverts with a magnitude up to 4000-lb (Figure 6-39b). The theoretical forces for 9.1-ft wing wall height were 1300-lb and 3500-lb with and without incline backfill, respectively. In the Coosa County culvert, the maximum calculated force in the tab was 3800-lb (Figure 6-39c), which was much smaller than the lateral earth pressure, which was 1450-lb and 4400-lb with and without inclined backfill, respectively.

The resultant forces in the high stress concentration zone which develops in the top corner of the tab when the tabs are in full lock under the theoretical scenario are shown in Figure 6-40. The maximum force of 6000-lb was developed in the tab in the Chambers County culvert. For the Lee and Coosa counties culverts, the maximum analyzed forces were 2500-lb and 4500-lb, respectively. These force magnitudes were smaller than the theoretical lateral earth pressure force discussed in the previous paragraph.

Based on these results, the following equation can be used to conservatively estimate the magnitude of the force that can occur in between two tabs due to lateral earth pressure:

$$V_h = k \cdot K_A \cdot \gamma \cdot H \cdot of \qquad \textbf{Equation 6-2}$$

where,

V_h – force acting on the tab surface;

κ – applied load coefficient (Table 6-1);

K_a – active earth pressure coefficient;

γ – unit weight of backfill soil;

H – height of the wall;

of – one-foot portion of the tab height (1-ft).

Table 6-1. Load coefficient

Influence factors	κ
No sloping backfill	2.5
Sloping backfill	4.5
High possibility of scour with flat backfill	3.2
High possibility of scour with sloping backfill	6.5

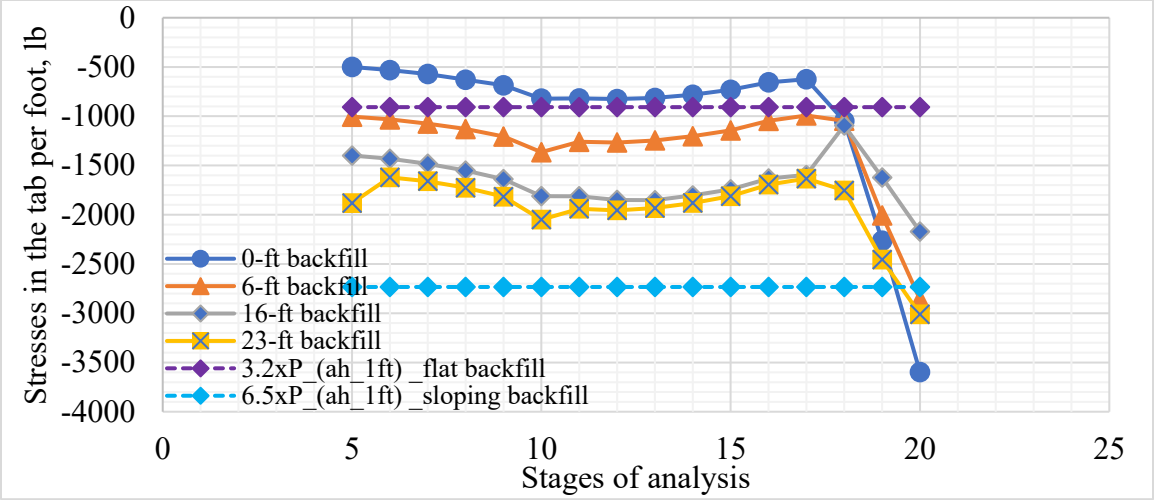

a)

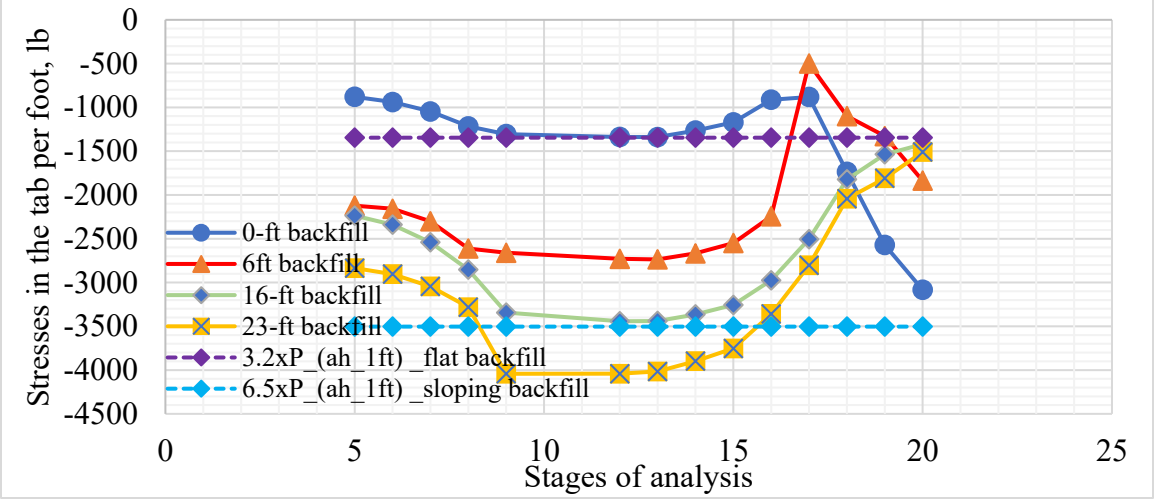

b)

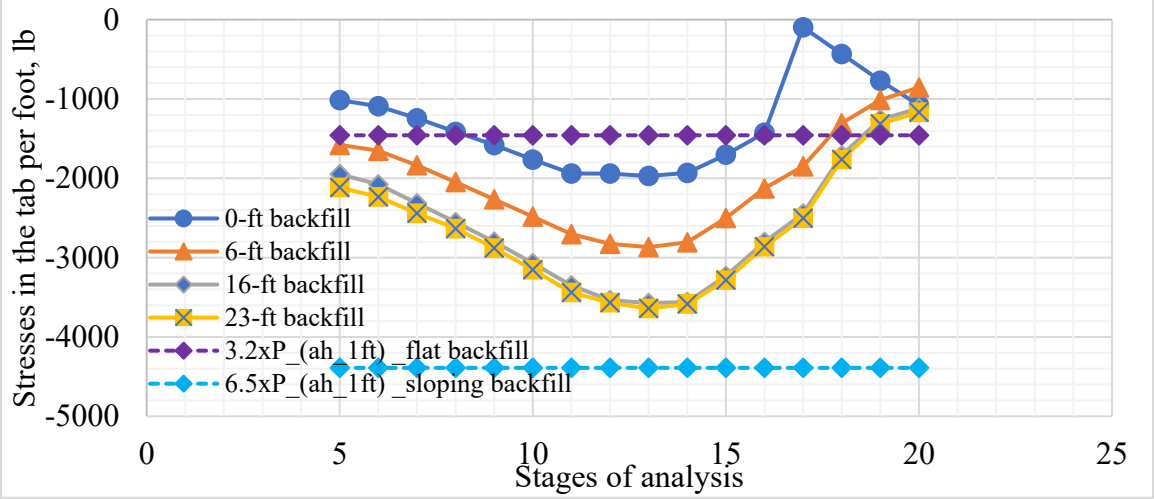

c)

Figure 6-39. Force in the tab with scour: a) Chambers County culvert; b) Lee County culvert; c) Coosa County culvert

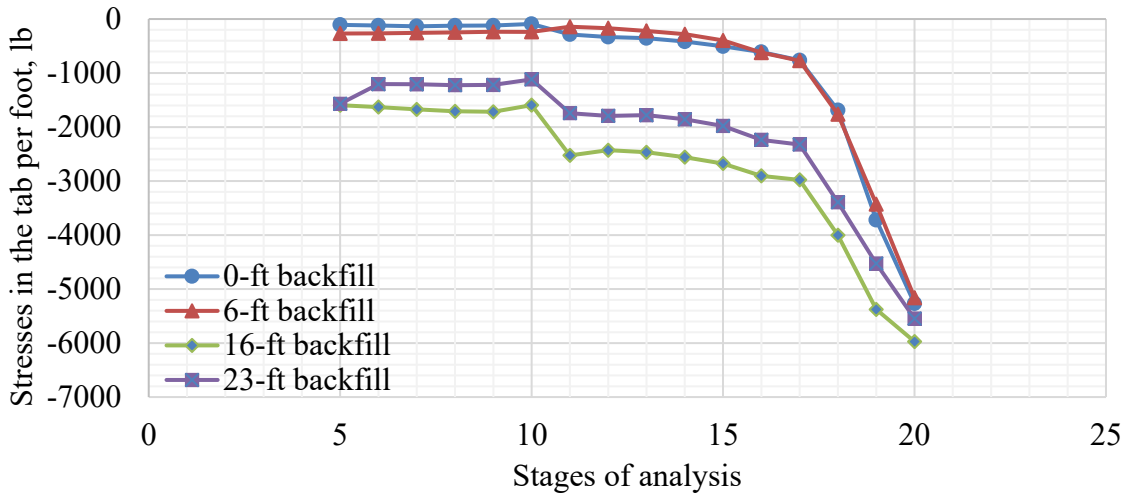

a)

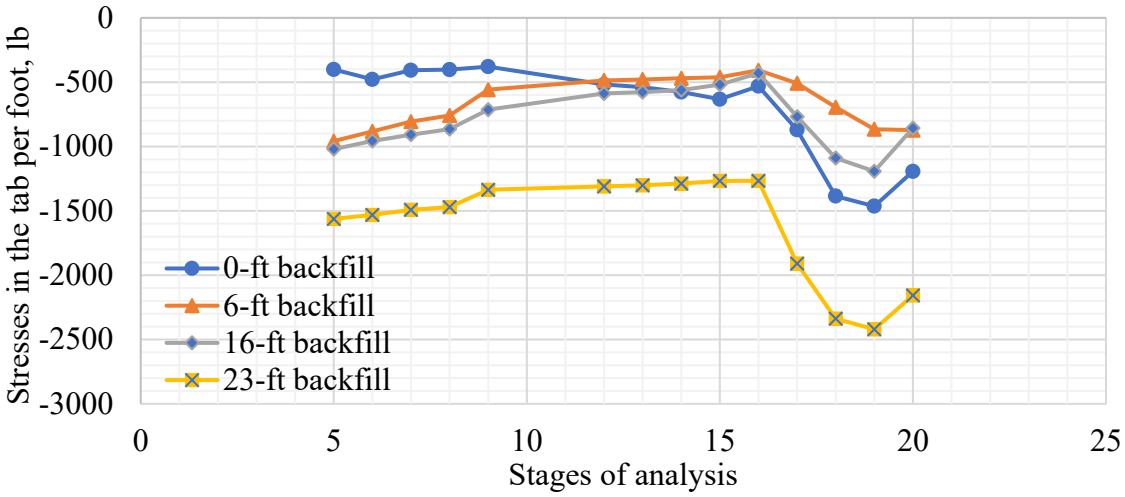

b)

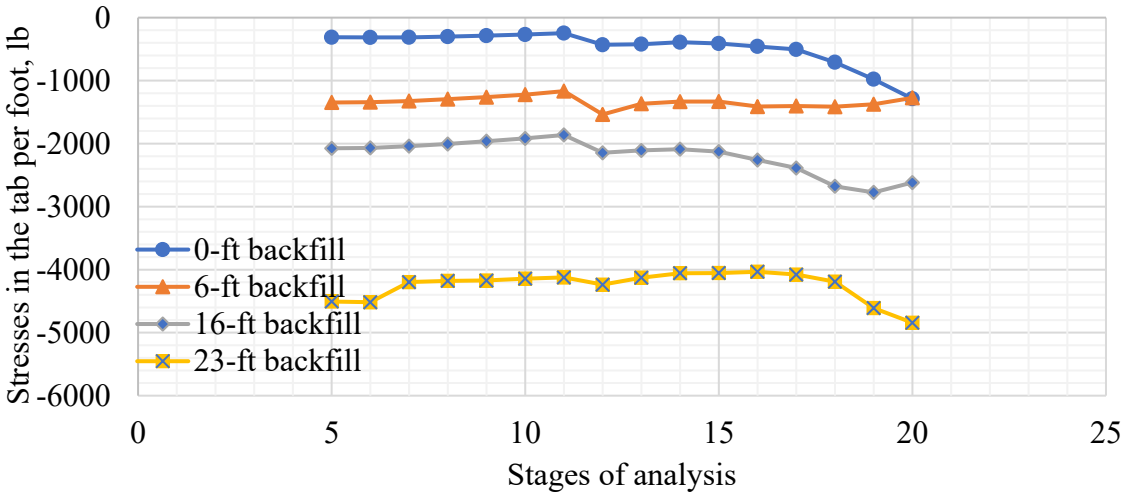

c)

Figure 6-40. Force in the tab with locked in tabs and scour: a) Chambers County culvert; b) Lee County culvert; c) Coosa County culvert.

Chapter 7. Tab Design

7.1. Introduction

The tab extension (Figure 7-1. Tab extension with typical reinforcement), overlapping the wing wall and culvert barrel, is a short cantilever reinforced concrete element employed to transfer the horizontal earth pressure acting on the wing wall to the barrel. The width of tab extension is comparable to its depth. Also, it can be assumed that transferred force is acting on the limited area of its width. Therefore, the potential failure modes of the tab extension are similar to those of a corbel. Thus, the behavior of these two items are quite similar, and the provisions of AASHTO LRFD (2014) for corbel design can be applied to the tab extension design.

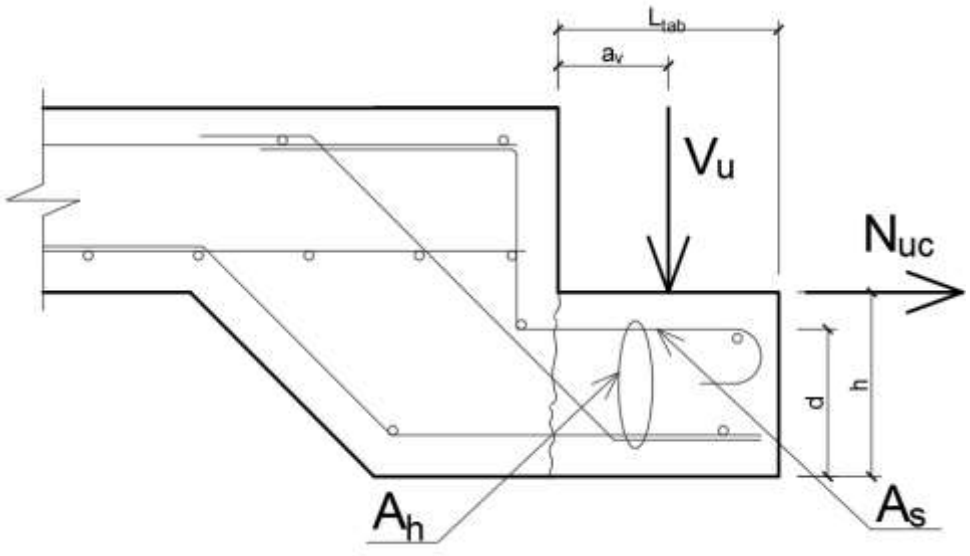

Figure 7-1. Tab extension with typical reinforcement

7.2. Behavior and Failure Modes

The shear crack occurs near the point of application of the concentrated force and propagates to the bottom corner of the structure-tab interface (Figure 7-2a). It can also start forming at the upper corner of the tab proceeding vertically to the bottom fiber (Figure 7-2b). Failure due to the splitting of the concrete around the tensile reinforcement may occur if the anchorage length is insufficient (Figure 7-2c). Inadequate proportions of the tab can result in failure due crushing of the concrete under concentrated load (Figure 7-2d).

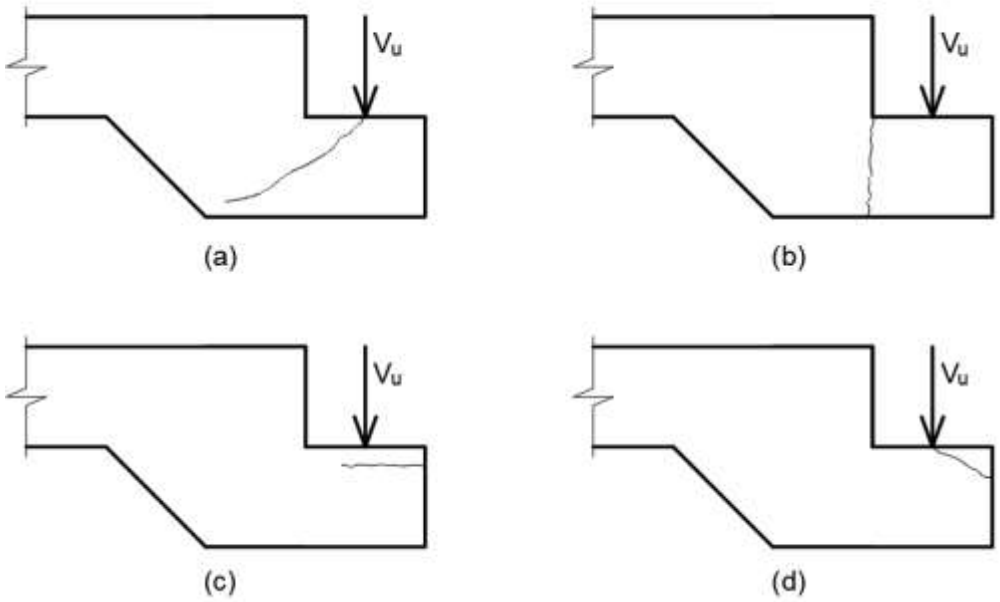

Figure 7-2. Failure patterns: a) diagonal shear; b) shear friction; c) anchorage splitting; d) vertical splitting

Shear friction reinforcement must be provided to prevent crack propagation using the shear friction provisions 5.8 of AASHTO LRFD (2014). The horizontal resisting force in the anchored closed tie transforms into the transverse nominal resisting force through the friction coefficient μ (Figure 7-3). This transverse resistance must be larger than the external factored shear load (Mattock 1976).

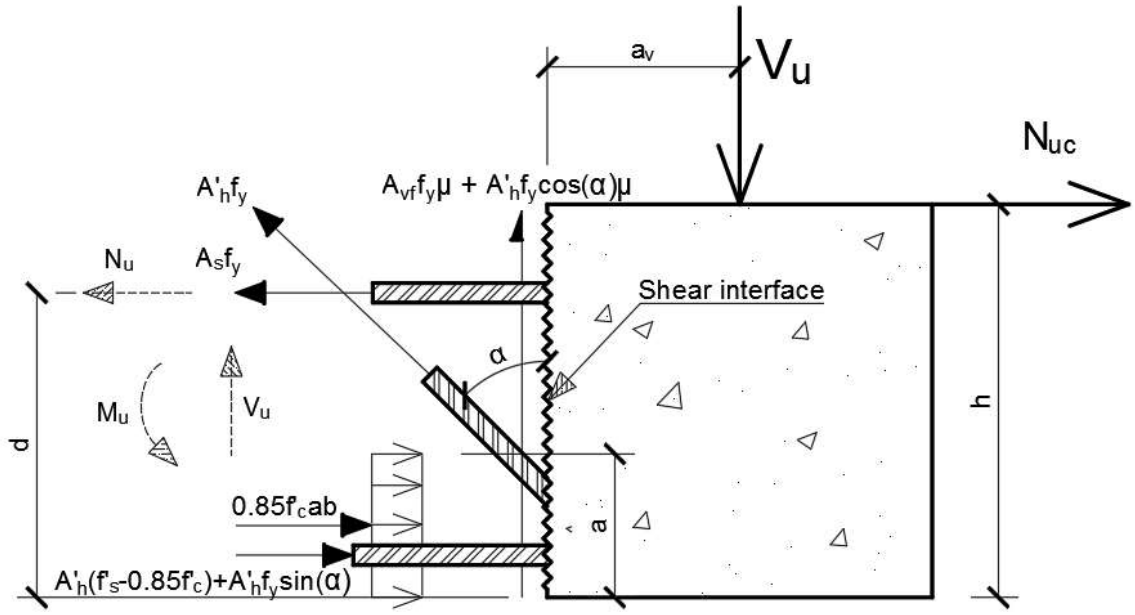

Figure 7-3. Tab extension free body diagram

The horizontal tensile force N_{uc} (Figure 7-3) is added to avoid tension force due to shrinkage and creep, and it shall be considered as a live load (Mattock 1976). To resist the horizontal tensile force, additional tensile reinforcement with yielding stress equal to N_{uc} shall be provided (*AASHTO LRFD* 2014).

To prevent diagonal failure of the tab extension the total yielding strength of closed stirrups shall be greater or equal to one-half of yielding strength of reinforcement required to resist factored moment A_h or a sum of two-thirds of the required shear reinforcement A_{vf} and tensile reinforcement A_n, whichever is greater.

7.3. Design Procedure

Estimation of the tab dimensions:

- Length of the tab L_{tab} shall not be smaller than the outer end of the tensile reinforcement hook development length l_{hb} plus a concrete cover layer of 2-in.
- The thickness of the tab h shall not be smaller than the thickness of the wing wall.

- The position a_v of ultimate shear force V_u from the inner edge of the tab shell be taken not greater than $0.5\ L_{tab.}$

Design procedure:

1. Calculate the ultimate shear force V_u (Figure 7-3) using Equation 6-2 and recommendation from Section 6.6.
2. The ultimate shear force for normal weight concrete shall satisfy $\phi \cdot V_n \geq V_u$

$$V_n = 0.2 \cdot f_c^{'} \cdot b_w \cdot d \qquad \textbf{Equation 7-1}$$

$$V_n = 0.8 \cdot b_w \cdot d \qquad \textbf{Equation 7-2}$$

where:

f_c' - specified 28-day compressive strength of the weaker concrete on either side of the interface, ksi;

b_w – tab width, in;

d – depth of the center of gravity of steel, in (Figure 7-3);

ϕ – strength reduction factor (ϕ=0.9 for normal weight concrete) as specified in AASHTO (5.5.4.2.1);

3. Calculate the minimum area of shear friction reinforcement A_{vf}.

$$A_{vf} \geq \frac{0.05 \cdot A_{cv}}{f_y} \qquad \textbf{Equation 7-3}$$

where:

A_{cv} - area of concrete considered to be engaged in interface shear transfer, in^2;

$$A_{cv} = b_{vi} \cdot L_{vi}$$ **Equation 7-4**

b_{vi} – interface width considered to be engaged in shear transfer, in;

L_{vi} – interface length considered to be engaged in shear transfer, in;

f_y – yield strength of the flexure reinforcement, ksi;

4. Check the nominal interface shear resistance V_{ni}

$$V_{ni} = c \cdot A_{cv} + \mu \cdot (A_{vf} \cdot f_y + P_c)$$ **Equation 7-5**

where:

c – cohesion factor specified in AASHTO (5.8.4.3), ksi;

μ – friction factor specified in AASHTO (5.8.4.3), dim.;

P_c – permanent net compressive force normal to the shear plane; if force is tensile, $P_c=0.0$, ksi;

The nominal shear resistance V_{ni} shall not be greater than the lesser of:

$$V_{ni} \le K_1 \cdot f_c^{'} \cdot A_{cv}$$ **Equation 7-6**

$$V_{ni} \le K_2 \cdot A_{cv}$$ **Equation 7-7**

where:

K_1 – fraction of concrete strength available to resist interface shear, as specified in AASHTO (5.8.4.3);

K_2 – limiting interface shear resistance specified in AASHTO (5.8.4.3), ksi;

5. Calculate the minimum area of tension reinforcement A_n.

$$A_n \ge \frac{N_{uc}}{\phi \cdot f_y}$$ **Equation 7-8**

where:

ϕ – strength reduction factor (ϕ=0.9 for normal weight concrete) as specified in AASHTO (5.5.4.2.1) for tension control members.

6. Calculate the area of flexural reinforcement A_f.

$$A_f = \frac{M_u}{\phi \cdot f_y \cdot (d - \frac{a}{2})} \quad \textbf{Equation 7-9}$$

where:

M_u – ultimate flexure moment (Figure 7-3), kip-in.

$$M_u = V_u \cdot (a_v) + N_{uc} \cdot (h - d) \quad \textbf{Equation 7-10}$$

h – height of the tab (Figure 7-3), in;

d – effective depth of corbel, in;

a – depth of the stress block.

ϕ – strength reduction factor (ϕ=0.9 for normal weight concrete) as specified in AASHTO (5.5.4.2.1) for tension control members.

At the first trial step the value *(d-a/2)* sell be assumed equal *0.9d*:

$$A_f = \frac{M_u}{0.9 \cdot \phi \cdot f_y \cdot d} \quad \textbf{Equation 7-11}$$

7. As the value of *(d-a/2)* is based on an assumption, the value of ***a*** shell be computed and recomputed A_f:

$$a = \frac{A_f \cdot f_y}{0.85 \cdot f_c^{'} \cdot b} \quad \textbf{Equation 7-12}$$

8. Area of primary tension reinforcement A_s shall be not smaller than:

$$A_s \geq \frac{2A_{vf}}{3} + A_n \qquad \textbf{Equation 7-13}$$

and $$A_s \geq A_f + A_n \qquad \textbf{Equation 7-14}$$

9. Calculate the minimum total area of closed stirrups or ties A_h parallel to A_s.

$$A_h \geq \frac{1}{2}(A_s - A_n) \qquad \textbf{Equation 7-15}$$

10. The limits of primary steel reinforcement at he the face of support shall satisfy:

$$\rho = \frac{A_s}{b_w \cdot d} \geq 0.04 \cdot \frac{f_c^{'}}{f_y} \qquad \textbf{Equation 7-16}$$

11. The anchorage of the outer end of the tensile reinforcement l_{hb} (Figure 7-4).

The outer end of the bar must be anchored in accordance with Article 5.11.2.4. *AASHTO LRFD* (2014)

Development length for a hooked-bar with yield strength $f_y \leq 60\ ksi$ shell be taken as:

$$l_{hb} = \frac{38.0 \cdot d_b}{\sqrt{f_c^{'}}} \qquad \textbf{Equation 7-17}$$

where:

d_b – diameter of the tensile reinforcement, in;

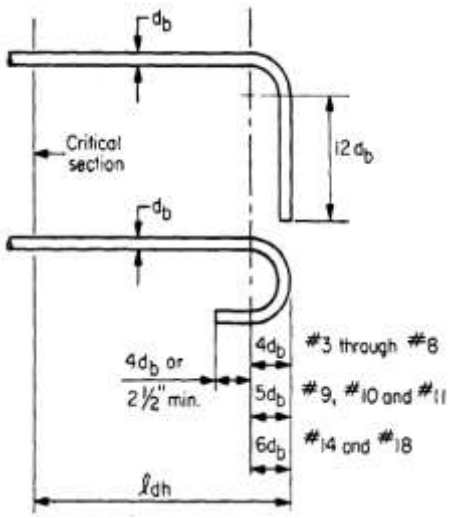

Figure 7-4. Hooked-bar details for development of standard hook (*AASHTO LRFD* 2014)

Chapter 8. Reliability Analysis

8.1. Introduction

The need for including the inherent variability of design parameters in geotechnical engineering was discussed in Chapter 2.4. Reliability theory considers most of the load and resistance parameters, as random variables instead of deterministic quantities. This allows evaluation theoretical/hypothetical probability of failure for considered geotechnical or structural system. This is especially important for experimental design, which does not have a sufficient history of structural performance.

The concepts of reliability-based analysis can be applied to new designs or evaluation of existing methods. The load and resistance factors for new designs can be developed using various techniques and target reliability index to achieve the desired safety level.

The impact of variable design parameters, as well as possible consequences of errors, can also be estimated in terms of the structural reliability (reliability index). The sensitivity analysis identifies the most important parameters that affect the structural safety and defines the criteria/parameters for the optimum design.

Human errors substantially contribute to inherent variabilities of considered design parameters. This effect is analyzed by evaluating the reliability index for selected error scenario. The sensitivity functions developed for each scenario can demonstrate the

consequential effect on the level of safety for the considered structural system. Thus, the effect of frequency of the particular error can be reduced by eliminating its cause.

8.2. Reliability Index

The safety level of any structural system can be expressed/evaluated in terms of reliability index, β, (Hasofer and Lind 1974). This term is commonly used since there is not always a closed form solution to assess the probability of failure, P_f. It is especially complex once the performance function is non-linear and incorporates a number of variables. The concept of probability of failure, P_f, was previously introduced in Section 2.2.5. Mathematically, the value of the reliability index is a standard normal variable of P_f:

$$\beta = -\Phi^{-1}(P_f) \qquad \textbf{Equation 8-1}$$

where: Φ^{-1} – the inverse standard normal distribution function;

As an example, the numerical values of reliability indices versus corresponding values of probability of failure are summarized in Table 8-1.

Table 8-1. Reliability index versus corresponding probability of failure

Reliability index, β	$\Phi(-\beta)$
0.0	0.5
1.0	0.158655254
2.0	0.022750132
3.0	0.001349898
4.0	3.16712E-05
5.0	2.86652E-07
6.0	9.86588E-10
7.0	1.27981E-12
8.0	6.22096E-16
9.0	1.12859E-19
10.0	7.61985E-24

To determine the reliability index for a practical problem, the first-order second moment method is applied (Nowak and Collins 2012):

$$\beta = \frac{\mu_R - \mu_Q}{\sqrt{\sigma_R^2 + \sigma_Q^2}} \qquad \textbf{Equation 8-2}$$

where:

μ_R – mean value of R

σ_R – standard deviation of R

μ_Q – mean value of Q

σ_Q – standard deviation of Q

For n components of the performance function, expressed with the fundamental (Equation 2-16) the mean μ_{Qi} and standard deviation σ_{Qi} the resultant parameters are calculated using Equation 8-3 and Equation 8-4:

$$\mu_Q = \sum_{i=1}^{n} (\mu_{Q1}..., \mu_{Qn}) \qquad \textbf{Equation 8-3}$$

$$\sigma_Q = \sqrt{\sum (\sigma_i)^2 ..., (\sigma_n)^2} \qquad \textbf{Equation 8-4}$$

where:

μ_{Qi} – mean value of Q_i

n – number of load components in the design formula

σ_{Qi} – standard deviation of Q_i

The second moment method is a powerful tool used to solve a wide range of practical problems, which requires the knowledge of just two parameters for each random variable in performance function: mean and standard deviation. However, if these random

variables are not distributed normally or log-normally, the second moment method gives just an approximate value of reliability index. There are other methods to determine the reliability index, including the non-linearity of performance function, the coefficient of correlation between random variables and type of distribution of the random variables (Hasofer and Lind 1974; Nowak and Collins 2012; Wisniewski et al. 2016).

8.3. Considered Limit States for Wing Wall Design

The main objective of this subchapter is to evaluate the AASHTO LRFD (2014) provisions related to retaining wall design. There are two categories of limit states describing the possible failure scenarios for such structures: structural and stability (geotechnical) limit states (Figure 8-1). The stability limit states were briefly described in Section 8.3. In literature, the sliding and overturning limit states are considered critical for the stability design (Fenton et al. 2005; Low 2007; Phoon et al. 2003; Sivakumar and Basha 2008). In particular, the lowest reliability was calculated for sliding limit state (Fenton et al. 2005).

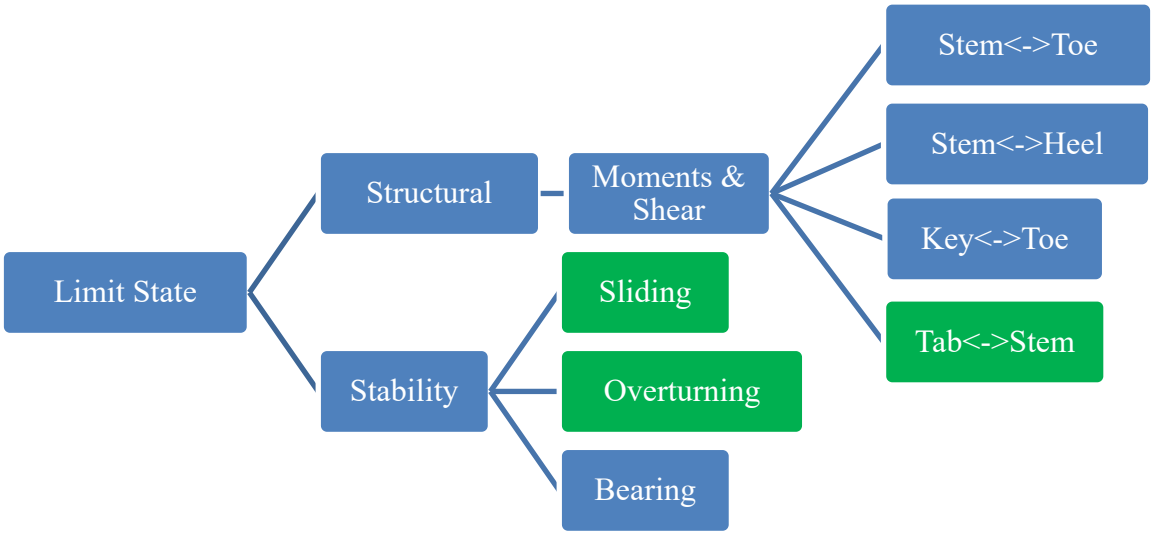

Figure 8-1. Limit states for retaining wall design

The sliding and overturning failure modes were chosen in order to evaluate the safety of newly designed CIP reinforced concrete wing walls. The statistical parameters for the reliability analysis were selected based on literature (Table 2-4), (Nowak and Collins 2012) and soil properties derived from in-situ tests conducted for the current study as it is shown in Table 8-2.

Table 8-2. Statistical parameters of soil and concrete for sliding and overturning limit states

Random variable	Mean Value	COV	Type of distribution	Reference
Unit weight of backfill soil, γ_{bs}, kN/m^3	18	0.07	Normal	(Sivakumar and Basha 2008), (Castillo et al. 2004)
Unit weight of underline soil, γ_{us}, kN/m^3	19	0.07	Normal	(Sivakumar and Basha 2008)
Angle of internal soil friction for backfill, φ_b, degrees	30	0.10	Lognormal	(Castillo et al. 2004)
Angle of internal soil friction for underline soil, φ_{un}, degrees	20	0.05	Lognormal	(Sivakumar and Basha 2008)
Friction angle between structure and soil, φ, degrees	20	0.10	Lognormal	(Sivakumar and Basha 2008)
Cohesion of soil base, c, kN/m^2	30	0.2	Lognormal	(Harr 1987)
Unit weight of concrete, γ_c, kN/m^3	24	0.16	Normal	(Nowak and Collins 2012)
Coefficient of friction, μ	0.5	0.15	Normal	(Castillo et al. 2004)

8.3.1. Sliding

According to AASHTO LRFD (2014), the sliding structural failure occurs due to an excessive horizontal force and insufficient soil shear resistance. The basic equation for sliding resistance is shown in Equation 2-1. In terms of a fundamental design equation, the nominal resistance (R) component can be rewritten as follows:

$$R_n = \varphi_\tau \cdot R_\tau + \varphi_{ep} \cdot R_{ep} \qquad \textbf{Equation 8-5}$$

where:

φ_τ – resistance factor for sliding (Table 10.5.5.2.2.1 of *AASHTO LRFD* (2014)

R_τ – sliding resistance

φ_{ep} - resistance factor for passive earth pressure (Table 10.5.5.2.2.1 *AASHTO LRFD* (2014)

R_{ep} – passive resistance at the key wall. The passive pressure component is calculated:

$$\mathrm{R}_{ep} = \frac{1}{2} \cdot \gamma_{un} \cdot l_{kw}^2 \cdot K_P \qquad \textbf{Equation 8-6}$$

where:

γ_{un} – unit weight of underlying soil (Table 8-2)

l_{kw} – length of the key wall, (Figure 3-5, Figure 3-7 and Figure 3-9).

K_P – coefficient of the passive earth pressure that computed using Equation 2-6.

The code does not recommend including the passive pressure component in retaining wall design, since it requires ten times more movement of the wall in order to

activate it, in comparison to the active earth pressure. However, for the sensitivity analysis performed within this study, two cases were considered: including the R_{ep} and without it.

The total vertical load providing the sliding resistance (Figure 2-8) includes the load due to the weight of the structure V_c and backfill soil V_{soil}:

$$\sum V = V_c + V_{soil} \qquad \textbf{Equation 8-7}$$

The nominal load component, Q_n, rewritten for the sliding limit state as follows:

$$Q_n = \varphi_{EH} \cdot P_a \cdot \cos(\delta_b) \qquad \textbf{Equation 8-8}$$

where:

φ_{EH} – horizontal active earth pressure factor (for Strength Ia - Table 2-3).

δ_b – friction angle between stem and backfill ($\delta_b = 0.7\varphi$)

P_a - horizontal active earth pressure force, which determined as:

$$P_a = \frac{1}{2}\gamma_b \cdot K_A \cdot H^2 \qquad \textbf{Equation 8-9}$$

where:

γ_b – unit weight of the backfill soil (Table 8-2)

K_A – coefficient of active earth pressure (Equation 2-5)

H – height of the wing wall (Figure 3-5, Figure 3-7 and Figure 3-9).

The statistical parameters for considered random variables are summarized in Table 2-4.

8.3.2. Overturning

AASHTO LRFD (2014) defines the overturning structural failure due to a loss of the wall stability. The capacity of the structure to remain stable and resist the overturning moment can be evaluated in terms of moments or eccentricities of the resultant forces acting on the structure. The general formulation of the eccentricity equation was presented in Section 2.2.5.2 (Equation 2-19). The forces acting on the wall are shown in Figure 2-8.

The limit state function for overturning can be rewritten in terms of load (Q) and resistance components(R).

$$g(R,Q) = R - Q = e_{\max} - e \qquad \textbf{Equation 8-10}$$

where:

e_{max} – the maximum eccentricity of the resultant force acting on the retaining wall footing.

The resistance component is expressed as a maximum allowed eccentricity depending on the footing dimensions (*AASHTO LRFD* 2014):

$$R = e_{\max} = \frac{1}{3} B_f \qquad \textbf{Equation 8-11}$$

where: B_f– width of the footing, as it is shown in Figure 3-5, Figure 3-7 and Figure 3-9 for Chambers, Lee and Coosa respectively.

The load component (L), can be expressed as an eccentricity of the actual forces acting on the structure (Equation 8-12):

$$Q = e = \frac{1}{3} B_f - \frac{\sum M_R - \sum M_O}{\sum V} \qquad \textbf{Equation 8-12}$$

where:

ΣM_R – sum of resisting moments produced by the vertical forces due to:

- weight of the structure
- weight of backfill
- vertical component of active earth pressure

ΣM_O – sum of moments produced by horizontal forces due to:

- horizontal component of active earth pressure
- reaction force in the tab

8.4. Limit State Function for Tab Design

According to (*AASHTO LRFD* 2014) the tab extension design should satisfy the requirements of the moment as a shear limit state, as it was stated in Chapter 7. The evaluation of the new tabbed connection design with the acceptance to the following criteria was verified:

- The limit state for flexure:

$$\phi M_n > \gamma M_u \qquad \textbf{Equation 8-13}$$

where:

ϕ – resistance factor for flexure

γ – load factor for flexure

The maximum nominal bending moment is calculated using the following:

$$M_n = A_f \cdot F_y \cdot (d - \frac{a}{2})$$ **Equation 8-14**

where:

M_n – nominal flexure resistance of the tab

A_f – area of flexure reinforcement

F_y – yield strength of reinforcement steel

d – effective depth of corbel

a – depth of the stress block

The ultimate moment is:

$$M_u = V_u \cdot a_v$$ **Equation 8-15**

where:

V_u – ultimate shear force acting on the tab

a_v – position of shear force

The limit state for shear:

$$\phi V_n > \gamma V_u$$ **Equation 8-16**

where:

ϕ – resistance factor for flexure

γ – load factor for shear

V_u – based on FE results using random generation of the main variables.

V_n – nominal shear resistance of the tab calculated using the following:

$$V_n = c \cdot A_{cv} + \mu \cdot (A_{vf} \cdot f_y + P_c)$$ **Equation 8-17**

where:

c – cohesion factor for concrete specified in AASHTO (5.8.4.3), ksi;

μ – friction factor for concrete specified in AASHTO (5.8.4.3), dim.;

P_c – permanent net compressive force normal to the shear plane; if force is tensile, $P_c=0.0$, ksi.

8.5. Sensitivity Analysis

A reliability-based sensitivity analysis was performed in order to evaluate the tabbed design of the wing wall for sliding and overturning failure modes. Geometrical parameters, such as the height of the wing wall, depth of the key wall and length of the footing were considered variable to understand the effect on the structure performance. These parameters were chosen as the most influential on the design. The sensitivity functions were developed for all random variables to investigate how sensitive the reliability index was to the changes in statistical parameters of the load and resistance components.

8.5.1. Effect of Design Parameters

First of all, the statistical parameters for load and resistance variables and the type of distributions were defined for considered limit states. The statistics were obtained by reviewing the literature on this topic (Allen et al. 2005; Castillo et al. 2004; Harr 1987; Kulhawy 1992; Ranganathan 1999; Sivakumar and Basha 2008). The statistical parameters such as mean values (μ_x), the coefficient of variation (V_x) and approximate type of distribution for each random variable are summarized in Table 2-4. The structural safety of the current design was measured in terms of reliability index, β. According to (Fenton et al. 2005), considering the uncorrelated variables, it was more conservative. Thus, it was decided not to include the correlation between the variables. Since both sliding and

overturning limit state functions are non-linear and complex the Monte Carlo simulation was utilized to access the reliability index for each considered design combination.

The reliability index was calculated for the actual design parameters of the Coosa County culvert (Figure 3-9). The nominal load and resistance components were taken from the design. According to the limit state function, the failure criterion is the exceedance of the sliding shear resistance by the acting lateral force (Equation 8-5, Equation 8-8). One million design cases were simulated in order to determine the theoretical probability of failure, P_f, as a ratio of the number of cases, n, when the failure occurred and the total number of simulations, *N (N=1,000,000)*:

$$\boldsymbol{P_f = \frac{n}{N} = \frac{total\ number\ of\ cases\ when\ g<0}{total\ number\ of\ simmulated\ cases}} \qquad \textbf{Equation 8-18}$$

The reliability index can be determined using Equation 8-1. Graphically the location of the reliability index is shown in Figure 8-2 as an intersection of the resultant function and vertical axis in standard variable scale. Similarly, the resultant reliability indices were determined for all three culverts constructed in Alabama and summarized in Table 8-3.

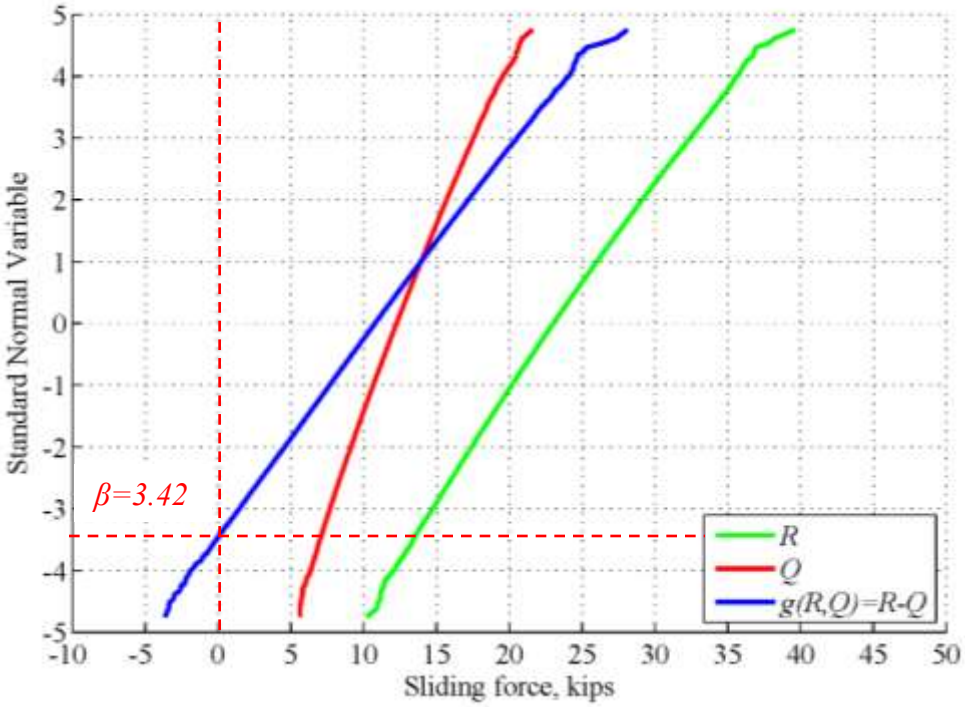

Figure 8-2. Reliability index calculated for sliding stability for the Coosa County culvert.

The other culverts have different dimensions and load conditions. In order to investigate the effect of geometrical parameters on the structural safety of the built structures. The reliability index was calculated for different proportions of the key wall depth (H_{kw}), wing wall height (H_{ww}) and footing length (L_f). The results are shown in Figure 8-3Figure 8-4.

The sensitivity analysis demonstrates the dependence of structural reliability on the footing length. Thus, the optimum level of structural safety that corresponds to $\beta=3.5$ could be obtained for the ratio of L_f to H_{ww} equal to 1.0 without a key wall. The results are especially important in terms of scour (Figure 8-4). For example, for the H_{kw}/H_{ww} ratio 0.3 (Coosa County - Figure 3-9) the optimum footing length is 6.25-ft that corresponds to β=3.5. However, the development of scour may reduce the footing length, which provides

the effective resisting friction force against sliding. Therefore, the decrease of the L_f from 6.25 to 2.0-ft may result in the increase of P_f from 0.023% to 50% respectively.

Table 8-3. Reliability index for newly constructed culverts - sliding limit state

Location	Variable dimensions of the wing wall			Reliability index, β	
	Height, wing wall, H_{ww}, *ft*	Depth of the key wall, H_{kw}, *ft*	Length of the footing, L_f, *ft*	Actual design	Code specified, β_T
Chambers County	7.1	1.5	4.8	3.76	3.00-3.20
Lee County	9.5	1.5	6.25	3.25	3.00-3.20
Coosa County	12.5	4	6.25	3.43	3.00-3.20

The reliability index calculated for the tabbed wing wall connection vary from 3.25 to 3.75 for different locations Table 8-3. This confirms the adequate safety of the tabbed design for sliding limit state.

The impact of the key wall on the performance of the structural system for the sliding limit state was investigated by calculating the reliability index for the current and theoretical design of H_{ww} varying from 5 to 30-ft (Figure 8-5, Figure 8-6). Two cases were considered: $H_{kw}=(0.2\text{-}0.3)H_{ww}$ (Figure 8-5) and $H_{kw}=0$ (Figure 8-6). The effect was significant only for cases with short footing $(L_f/H_{ww}=0\text{-}0.5)$, while for long footing the reliability indices were similar for both cases.

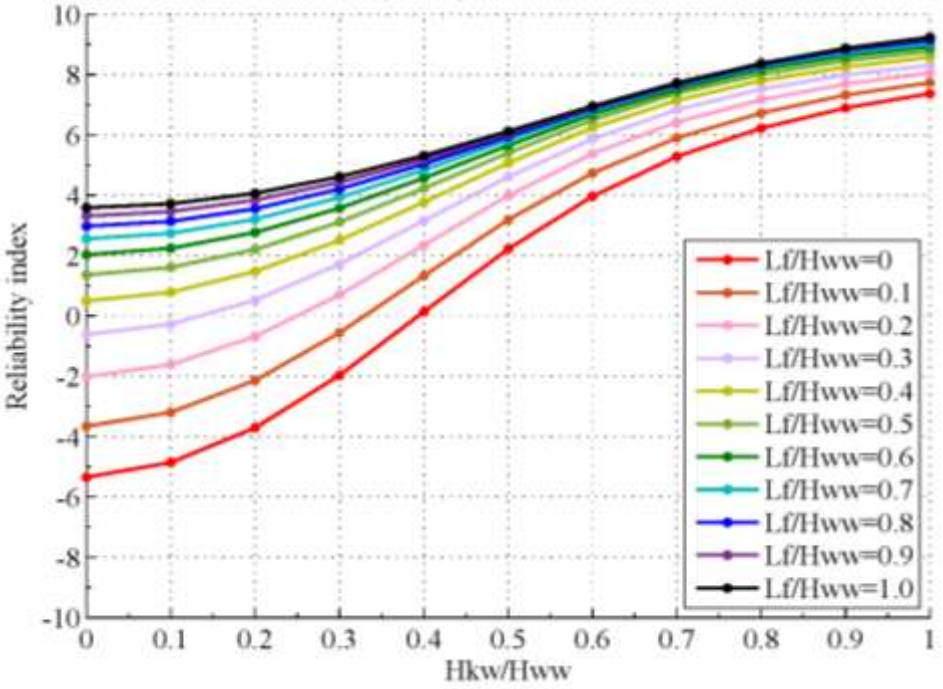

Figure 8-3. Reliability index calculated for sliding stability for different proportions of H_{kw}/H_{ww}

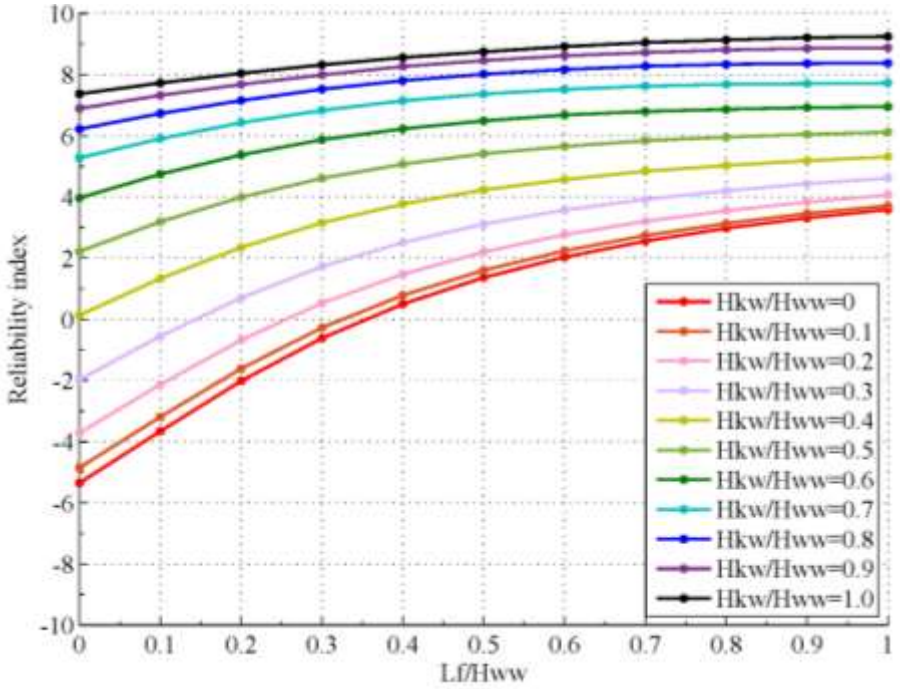

Figure 8-4. Reliability index calculated for sliding stability for different proportions of L_f/H_{ww}

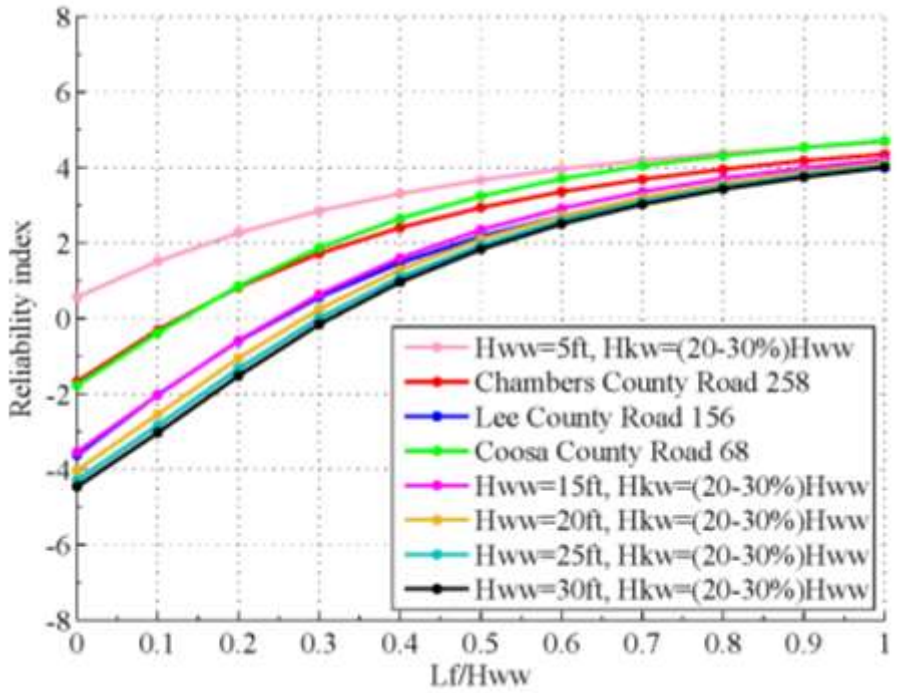

Figure 8-5. Reliability index calculated for sliding stability for different proportions of L_f/H_{ww} of current design

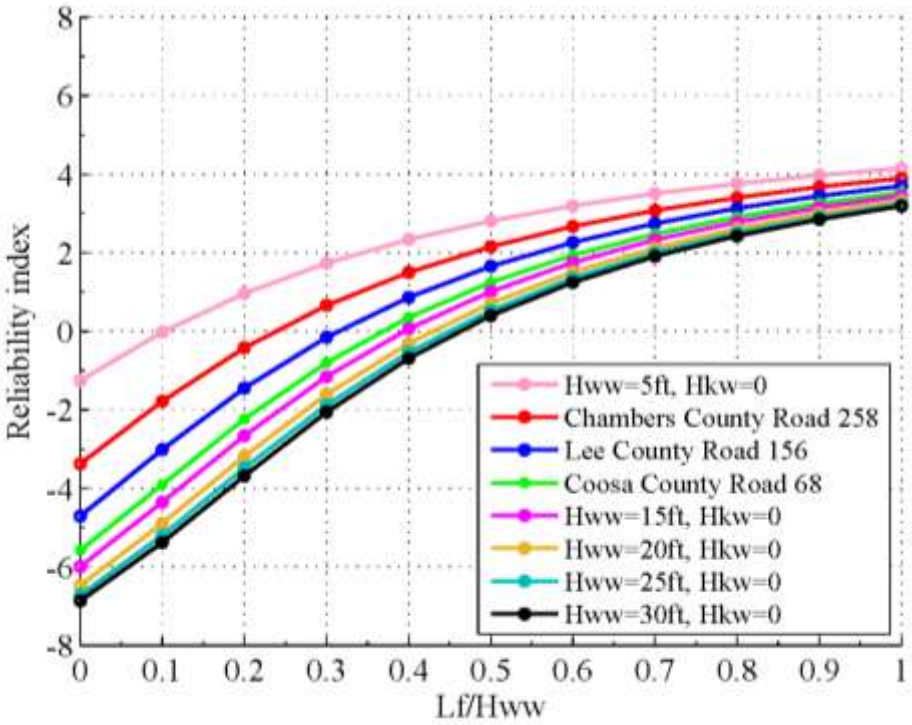

Figure 8-6. Reliability index calculated for sliding stability for different proportions of L_f/H_{ww} of current design ($H_{kw}=0$)

A similar approach was applied for the overturning limit state (Chapter 8.3.2). The reliability index was computed for the performance function expressed with the Equation 8-10. The reliability index was determined using the same Monte Carlo simulation procedure, as for the sliding limit state (Figure 8-2). The graphical representation of the applied procedure is shown in Figure 8-7 for the culvert designed for Coosa County. The resistance component (R) is deterministic and, thus, distributed vertically without variation. The same number of simulated design cases, as in case of sliding, was developed ($N=1,000,000$). Since overturning does not control the retaining wall design ($\beta_{overturning} > \beta_{sliding}$) this number of simulations was not sufficient to intersect the vertical axis ($g(R, Q)=0$), linear first-order fitting was applied. The reliability indices calculated for the other locations are summarized in Table 8-4.

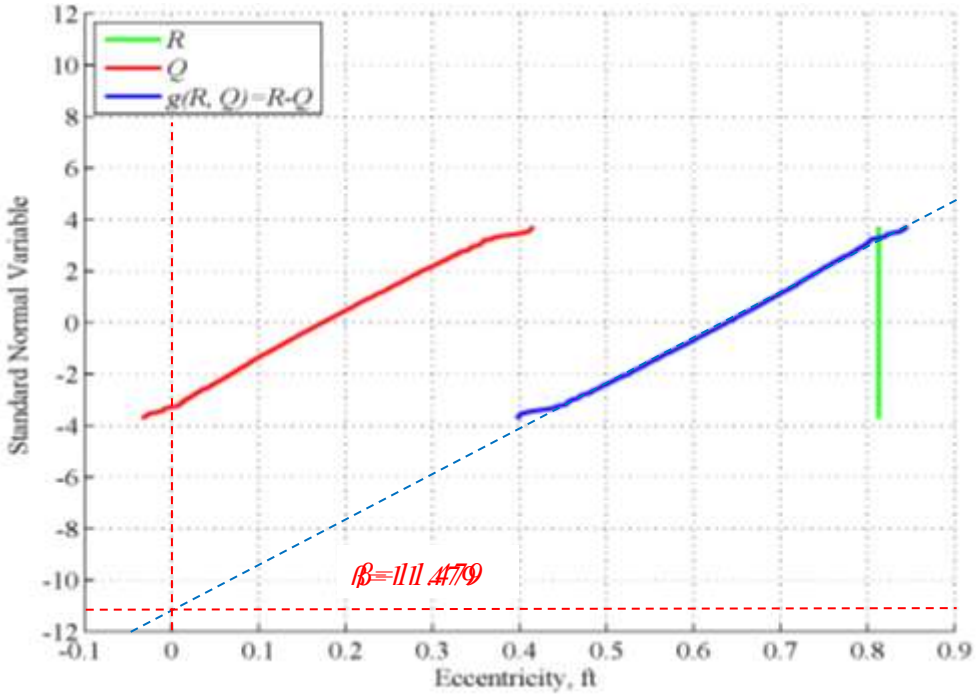

Figure 8-7. Reliability index calculated for overturning stability for Coosa County culvert

Table 8-4. Reliability index for newly constructed culverts - overturning limit state

Location	Variable dimensions of the wing wall			Reliability index, β	
	Height, wing wall, $H_{ww,}$ *ft*	Depth of the key wall, $H_{kw,}$ *ft*	Length of the footing, $L_{f,}$ *ft*	Actual design	Code specified, β_T
Chambers County	7.1	1.5	4.8	25.28	3.00-3.20
Lee County	9.5	1.5	6.25	22.02	3.00-3.20
Coosa County	12.5	4	6.25	11.479	3.00-3.20

The reliability indices calculated for culverts in Chambers, Lee and Coosa counties vary from 25.282 to 11.479 respectively. The results correspond to the study performed by (Mandali et al. 2011) for the retaining walls for sliding and overturning. The structural reliability for overturning is significantly higher than $\beta_T=3.00,$ targeted in the literature. It confirms that the overturning is not a controlling limit state for retaining structures of this type.

To evaluate the effect of different geometry on the stability of the wing walls the reliability indices were calculated for different proportions of the key wall depth (H_{kw}), wing wall height (H_{ww}) and footing length (L_f). The results are shown in Figure 8-8 and Figure 8-9 for the culvert constructed in Coosa County. The results of the sensitivity analysis show that the longer footing creates a positive impact on structure performance (Figure 8-9). The reliability index varies from -5.0 to 37 for the L_f/H_{ww} ratio from 0 to 1.0 respectively, while $H_{kw}=0$. However, the acceptable level of safety for overturning can be assessed with the L_f/H_{ww} ratio from 0.3 to 0.7 for any H_{kw} (from 0 to H_{ww}).

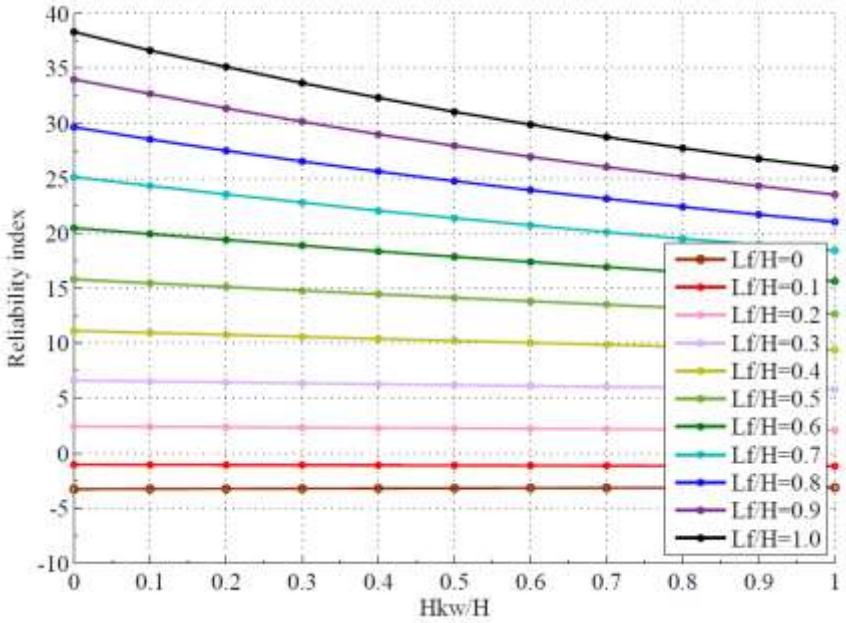

Figure 8-8.Reliability index calculated for overturning stability for different proportions of H_{kw}/H_{ww} for Coosa County culvert

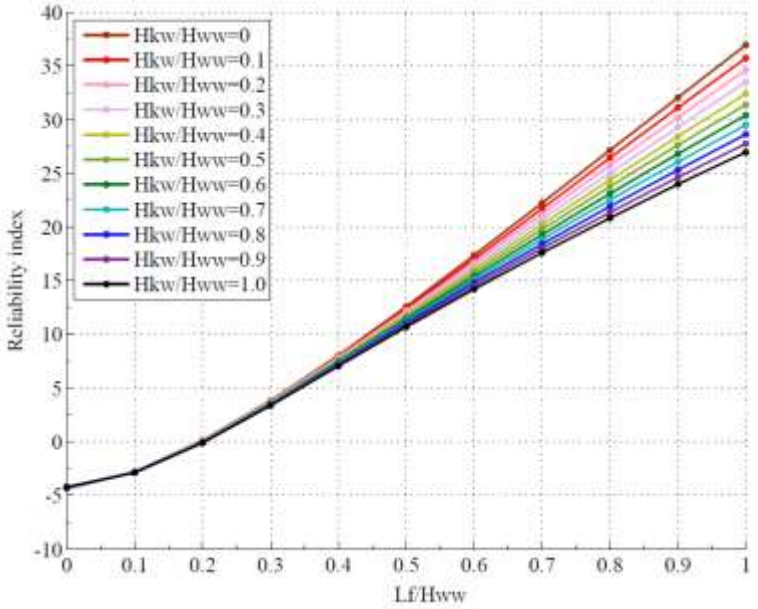

Figure 8-9. Reliability index calculated for overturning stability for different proportions of L_f/H_{ww} for Lee County culvert

The effect of the key wall on the structural performance against overturning was further analyzed as shown in Figure 8-10 and Figure 8-11. The reliability indices were

calculated for the designed culverts with and without a key wall. The presence of the key wall has a negative effect on the behavior of the wing wall the moment from its weight increase the overturning moment. The reliability index decreases from 40 ($H_{kw}=0$) to 35 ($H_{kw}=0.2H_{ww}$) for all considered cases. The taller wing walls were not sensitive to the changes in key wall and footing dimensions (Figure 8-10, 11).

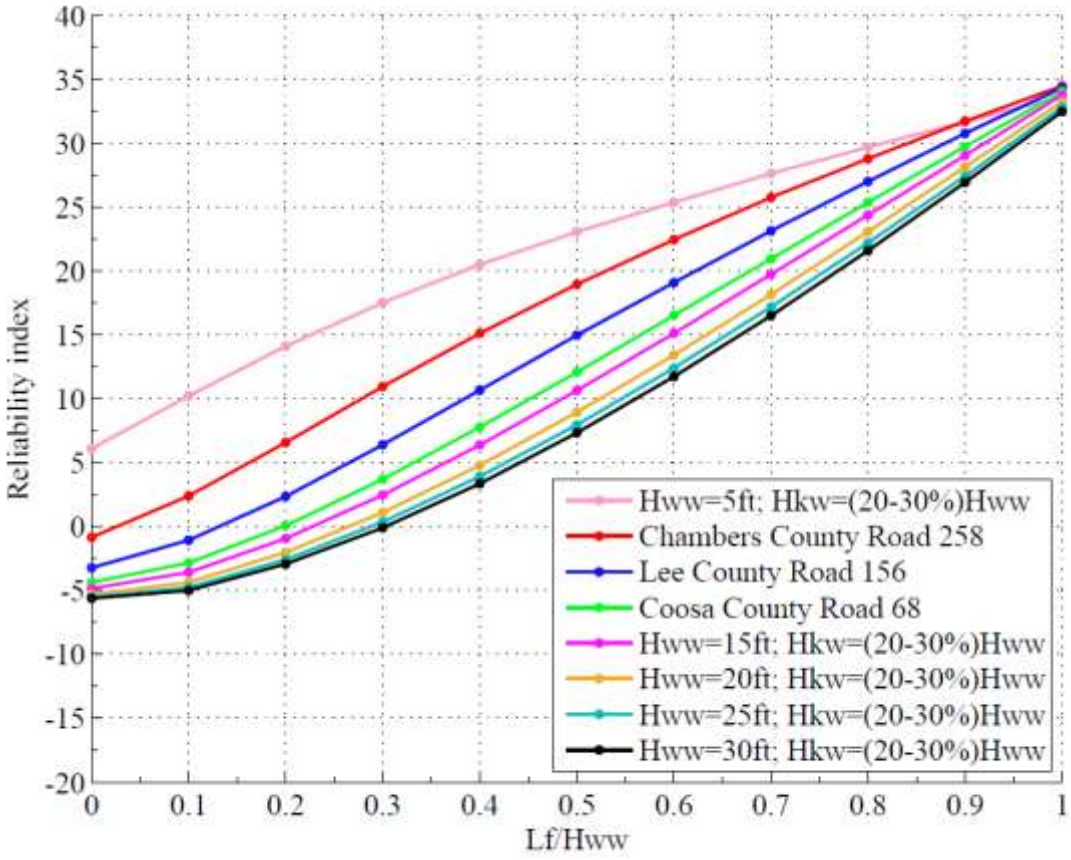

Figure 8-10. Reliability index calculated for different proportions of L_f/H_{ww}

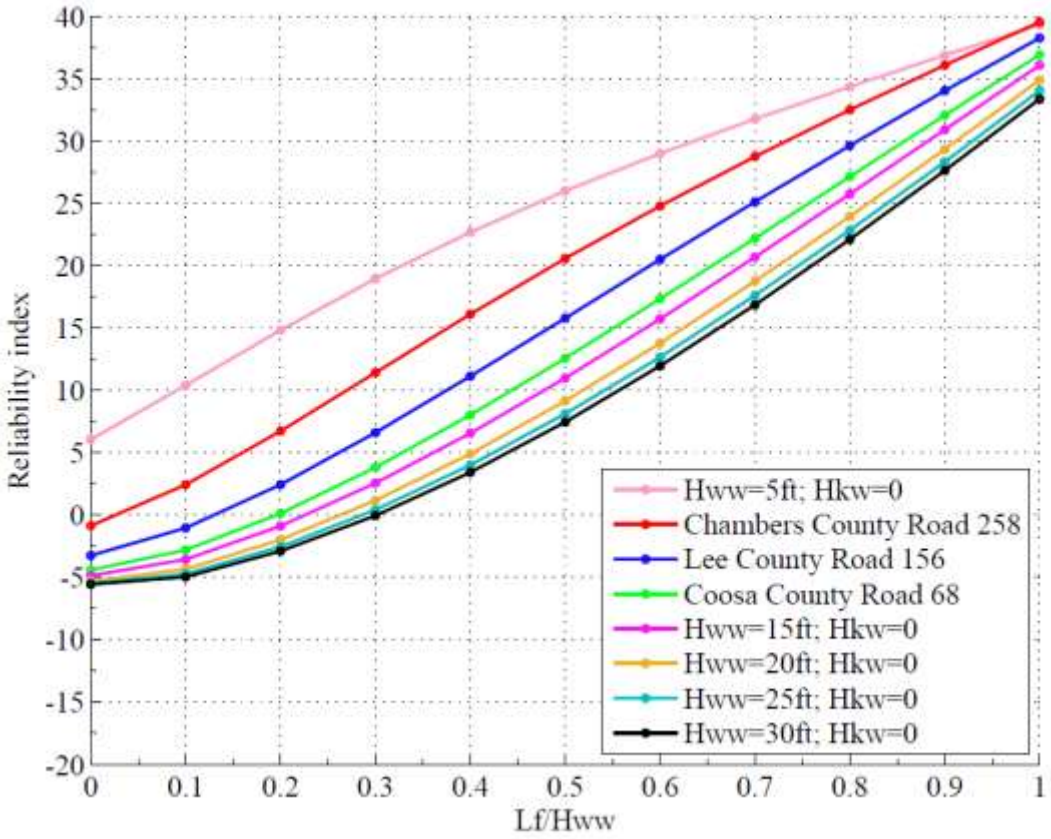

Figure 8-11. Reliability index calculated for different proportions of L_f/H_{ww} ($H_{kw}=0$)

8.5.2. Effect of Uncertainties in Statistical Parameters

This type of sensitivity analysis is utilized to detect the most important structural and geotechnical parameters affecting the safety of the considered system. Adequate structural analysis and design require knowledge about possible errors in defining the main design parameters. This knowledge often controls the frequency of error occurrences and reduces the possible impact on structural safety.

The uncertainties in nominal or statistical parameters may come from different sources: human errors, incorrect calibration of measuring equipment (man-made hazard), sensor malfunction and insufficient amount of measurements (natural hazard) (Nowak and

Collins 2012). The design of geotechnical structures often involves the errors related to complex load conditions, incomplete understanding of the behavior of the structure and an insufficient amount of measurements. These errors can be divided into conceptual, executional and intentional, according to the cause and consequences. The conceptual errors cover the range of incorrect measurements due to the lack of information. The errors of execution and intention are an unintentional and intentional departure from acceptable practice respectively.

The consequences of different types of errors can be identified through a sensitivity analysis that involves the following steps:

- Definition of the variable parameters that can affect the structural performance
- Selection of the possible error scenarios
- Computation of the reliability index for each case
- Identification of the most sensitive parameters.

In order to establish the critical variables that affect the reliability of a free-standing wing wall, the sensitivity analysis, described above, was applied. The design parameters (γ_s, φ, μ, γ_c, c), recognized in the literature as random variables (Table 2-4), were selected as potentially affected by the errors. The statistics for these variables, reported in the literature by Castillo et al. (2004), Harr (1987a), Ranganathan (1999), and Sivakumar and Basha (2008) were consistent. Thus, it is assumed, that the only nominal values that can be affected due to limited accessibility to the field test values or equipment malfunction. The reliability indices were computed using the First-order second-moment method

(Equation 8-2), with load (Q) and resistance (R) parameters determined using (Equation 8-5 and Equation 8-8). Since the load and resistance side are simultaneously affected by the same parameters, the positive and negative deviation was considered for such parameters as the unit weight of the backfill soil and friction angle between the concrete and soil surface. The resultant sensitivity functions are shown in Figure 8-12.

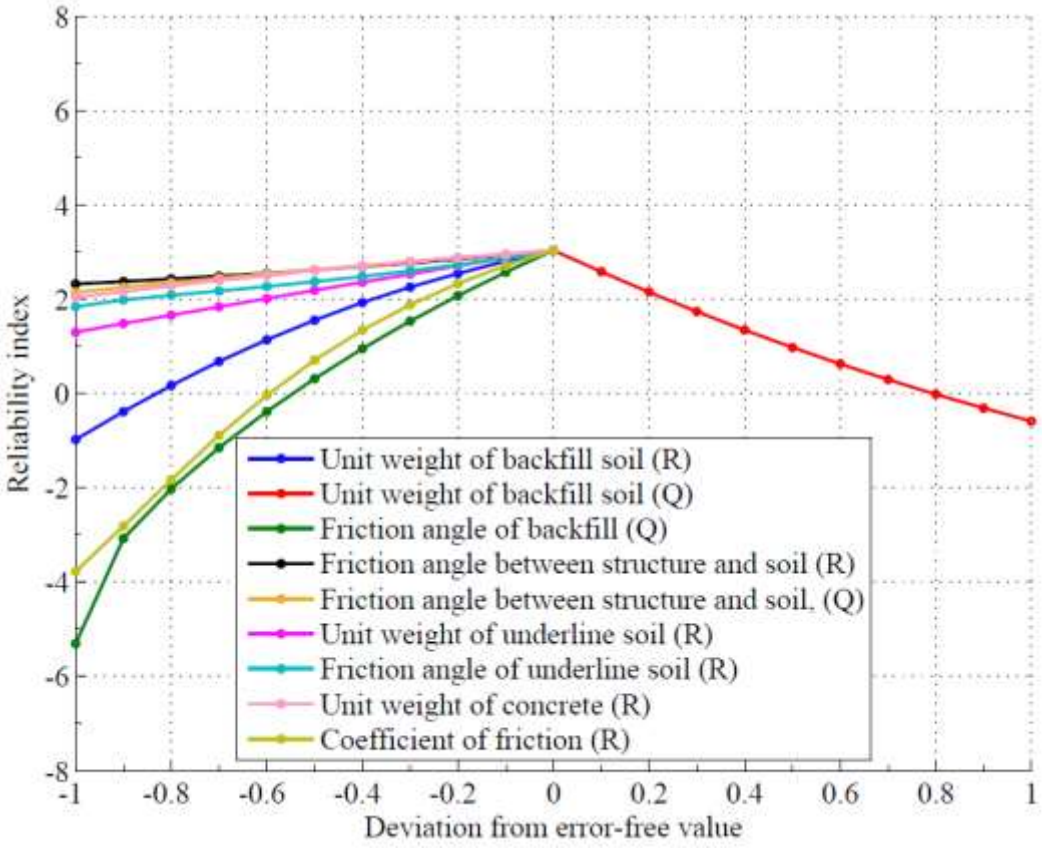

Figure 8-12. Sensitivity function for sliding limit state of wing wall design

From Figure 8-12 it is clear that the coefficient of friction (μ), friction angle and unit weight of backfill soil (φ_b and γ_b) are the most sensitive geotechnical parameters in this design. Plus, or minus 20% error in measurements result in a reliability index below the acceptable limit (β_T=*3.0-2.3*). Error greater than 50% corresponds to a theoretical

probability of failure P_f=0.5. However, the remaining parameters do not have a significant impact on the overall sliding stability of wing wall.

Similarly, sensitivity functions were developed for the basic parameters of overturning the limit state, previously discussed in Chapter 8.3.2. Although, the resistance component is deterministic (Equation 8-11), both positive and negative deviation was simulated for considered random variables.

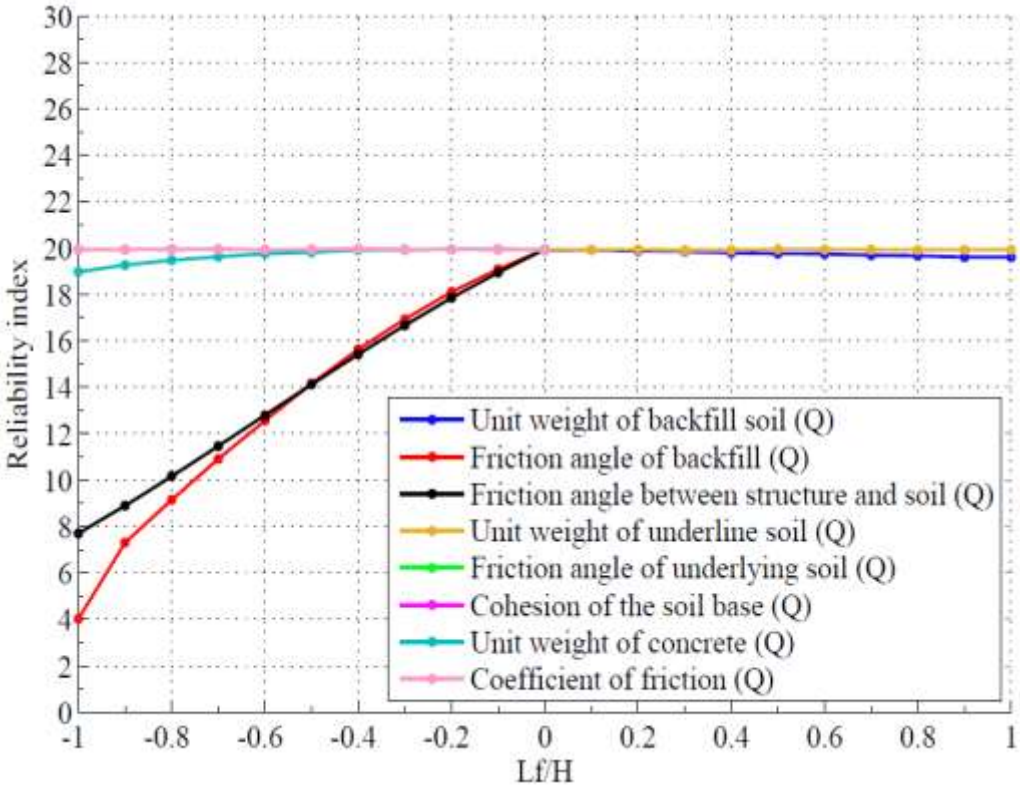

Figure 8-13. Sensitivity function for overturning limit state of wing wall design

The overturning limit state does not control for the free-standing wing wall design. However, the most sensitive design parameters were determined: friction angle of the backfill soil and friction angle between the structure and soil base. Underestimation of these parameters may lead to a significant level of conservatism in the design of the wing wall for stability.

Overall, the results of sensitivity analysis correspond to the observation made by (Sivakumar and Basha 2008) that the geometrical parameters used in the design of the retaining wall have a greater impact on sliding stability that the statistics of the soil properties for considered limit states.

8.6. Selection of Target Reliability Index for Tab Design

One of the main objectives of this study was to develop the design procedure for the novel wing wall-to-tab connection. The reliability-based design employs the concept of target reliability index as a measure of the minimum required level of structural safety. This term was previously discussed in Chapter 2.2.5.1. The targeted safety level is meant to be a minimum to provide an adequate balance of acceptable consequences in case of failure and costs for construction of a particular system. While there are design codes involving full reliability analysis to define the theoretical failure for a different scenario, the tabbed design provision was decided to develop based on closeness to the target reliability.

To select the target reliability index, the following factors are taken into account:

- The desired probability if failure (P_f), for the structure or structural component.
- The required service life of the structure. Therefore, the targeted reliability index for the structural component can be accepted lower than one for the whole structure if the component is designed for shorter service period than the whole structure.
- The desired utility of the structure, which is the ratio of costs to the consequences of theoretical failure.

- Past practice on the design and construction of similar structures.

In order to select the benchmark reliability, an extensive literature review was performed along with the evaluation of the current design provisions for retaining wall design. As it was mentioned before there are many uncertainties involved in the design of geotechnical structures, as well as the desired safety level. According to the current *AASHTO LRFD* (2014), the target reliability index for structural components is $\beta_T = 3.5$. However, based on past geotechnical practice the desired probability of failure and reliability index for geotechnical structures are $\beta_T = 3.0$ and $P_f = 0.001$, respectively (Sivakumar and Basha 2008; Withiam et al. 1998). Phoon et al. (2003), in their study considered the acceptable reliability index, β_T in the range from 3.0 to 3.2 as optimum for all limit states for the design of retaining walls. Authors have also chosen the same target reliability for the flexure and shear design of the stem, heel and toe of the wall. Goh et al. (2009) evaluated the traditional design approach for the target reliability index β_T=2.5 which corresponds to the P_{fT} =0.01.

The problem of redundancy of components of geotechnical structures was also discussed before (Chapter 2.2.5.1). In other words, the retaining structure is able to remain stable after failure of the main barrel due to the ability of the soil to redistribute the pressure. A reduced target reliability 2.33-2.5 was recommended by Allen et al. (2005) and Bathurst et al. (2009, 2012) for retaining structures due to their inherent redundancy. This was also taken into account while selecting the target level of structural safety for a new design of tabbed connection. Since this design has never been implemented, no history of the successful practice of the design and performance of similar structures exists. Therefore, it

was decided to derive the load and resistance factors for the new design based on a range of reliability indices, β_T from 2.0 to 3.5.

8.7. Code calibration procedure

The design procedure for the tabbed culvert wing wall connection was presented in Chapter 7. Reliability analysis was conducted to develop the load and resistance factors corresponding to the targeted level of reliability.

The development of the new design consists of the following steps: determining the safety demand of the design and developing the design formulas including the load and resistance factors. The basic format of an LRFD design formula requires multiplying the load and resistance components by corresponding load factors and resistance factors respectively, as it is shown in Equation 8-19.

$$\phi R_n \geq \sum \gamma_i \cdot Q_i \qquad \textbf{Equation 8-19}$$

where:

ϕ – resistance factor

R_n – nominal resistance

Q_i – ith load component

γ_i – load factor for ith load component

The load (γ) and resistance (ϕ) factors provide the safety margin embedded in the design. Therefore, the load effects are overestimated, and resistance are underestimated. There is still a certain probability of failure which is not covered by developed factors. However, it is substantially limited to the desired level.

As it was mentioned above, both load and resistance components are random in nature and can be defined with the specific statistical parameters (bias factor λ and

coefficient of variation *V)*. Using the defined statistics for load and resistance, as well as target reliability index β_T, the optimum values of factored load (Q^*_i) and resistance(R^*) calculated as (Nowak and Collins 2012):

$$R^* = \mu_R - \frac{\beta_T \cdot \sigma_R^2}{\sqrt{\sigma_R^2 + \sigma_Q^2}} \quad \textbf{Equation 8-20}$$

$$Q_i^* = \mu_Q - \frac{\beta_T \cdot \sigma_Q^2}{\sqrt{\sigma_R^2 + \sigma_Q^2}} \quad \textbf{Equation 8-21}$$

where:

μ_R – mean value of resistance

σ_R – standard deviation of resistance

μ_Q – mean value of load

σ_Q – standard deviation of resistance

β_T – reliability index

The corresponding load and resistance factors calculates as follow:

$$\gamma_i = \frac{\lambda_{Qi} \cdot Q_i^*}{\mu_{Qi}} \quad \textbf{Equation 8-22}$$

$$\phi = \frac{\lambda_R \cdot R^*}{\mu_R} \quad \textbf{Equation 8-23}$$

The type of distribution for each variable is important in the actual calibration of the new design factors. Since the distribution type for both sides of $\phi R_n \geq \sum \gamma_i \cdot Q_i$

Equation 8-19 are unknown for the new connection design, they are assumed to be normal.

8.8. Development of Load and Resistance factors for Tab Design

The fundamental equation in structural reliability consists of two components: load (Q) and resistance (R). The limit state functions for moment and shear design are previously discussed in Section 8.4. In both cases, the resistance component is defined as

$$M_n = A_f \cdot F_y \cdot (d - \frac{a}{2})$$ Equation 8-14. The statistical parameters, such as bias factor, the coefficient of variation and type of distribution, for the selected random variables in resistance component were collected from literature and summarized in Table 8-5. The nominal values are shown in Table 4-3.

Table 8-5. Statistical parameters for tab extension design

Random variable	Bias factor	COV	Type of distribution	References
Compressive strength of concrete, f'_c	1.27	0.16	Normal	(Andrzej S. Nowak, Rakoczy, & Szeliga, 2012)
Area of reinforcing rebar #4	1.13	0.03	Normal	(Andrzej S. Nowak et al., 2012)
Yield strength of reinforcing steel, F_y	1.05	0.11	Normal	(Ellingwood, 1980)

The formulation of the load component for both: moment and shear limit state require the knowledge of the actual shear force acting on a tab extension (Equation 8-15 and Equation 8-16). This shear force directly depends on the properties of the backfill soil,

which are highly variable (Table 8-2). Thus, it cannot be considered as a deterministic random variable.

At the same time, since the tabbed design is new, the magnitude of the shear force can only be assessed through FE modeling. The main steps of simulation and interpretation of results are discussed in detail in Chapter 4.

In order to determine the variability of the shear force acting on a tab extension, a Monte Carlo simulation was utilized. A set of FE models were analyzed for random combinations of the soil properties. This combination was generated using the Monte Carlo method and statistical parameters of the soil, previously defined in Table 8-2. The resultant values of the shear force are shown in Figure 8-14 as a cumulative distribution function (CDF) plotted on probability paper. The bias factor and coefficient of variation for the shear force are 0.77 and 0.26 respectively.

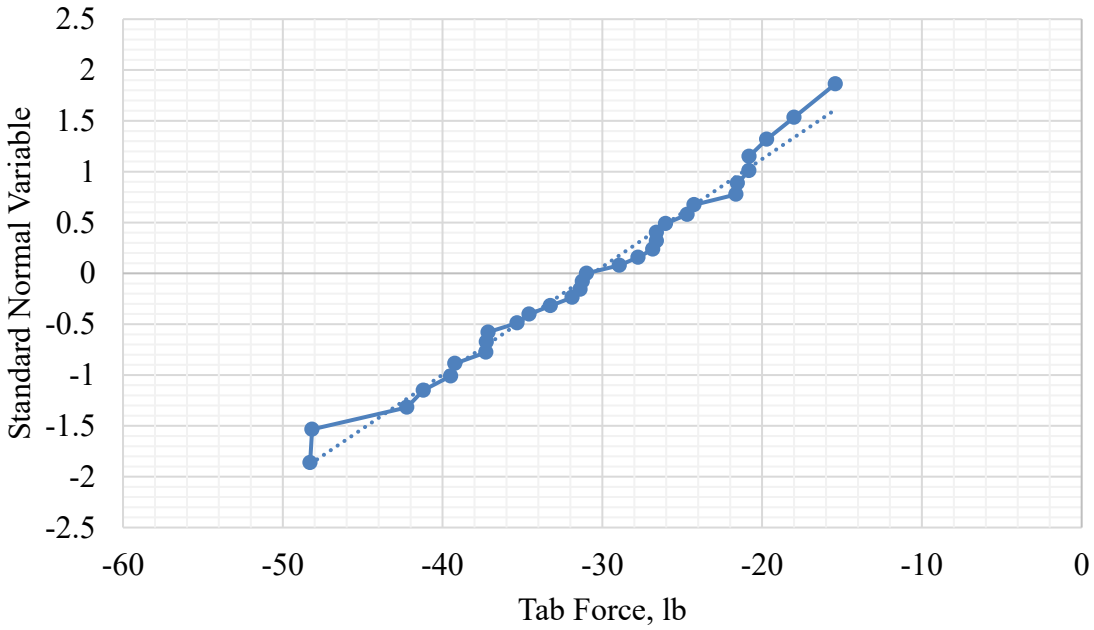

Figure 8-14. Cumulative distribution function of the tab force

Using the obtained statistical parameters for load and resistance the corresponding factors were calculated following the calibration procedure, described in Chapter 8.7. The load and resistance factors were determined for the different target reliability indices 2.0, 2.5, 3.0 and 3.5 for moment and shear limit states as it is shown in Table 8-6 and

Table 8-7.

Table 8-6. Load and resistance factors for tab design - flexure

β_T, / Factors	β_T=2.0	β_T=2.5	β_T=3.0	β_T=3.5
Load factor, γ	1.106	1.200	1.274	1.358
Resistance factor, φ	1.046	1.011	0.976	0.941

Table 8-7. Load and resistance factors for tab design - shear

β_T, / Factors	β_T=2.0	β_T=2.5	β_T=3.0	β_T=3.5
Load factor, γ	1.102	1.185	1.269	1.352
Resistance factor, φ	1.035	0.998	0.961	0.923

The calculated factors take into account the natural variability of the components involved in the design.

Chapter 9. Summary, Conclusions, and Recommendations

The objective of this research was to evaluate the possible mechanism that causes cracking along the culvert to wing wall connection. To prevent the crack formation along the contraction joint, this study examined the proposed design of new tabbed wing wall-to culvert connection, which allows the wing wall to deflect separately from the barrel. This causes the wing wall to behave similarly to the cantilever retaining wall with a pin support along one side. To evaluate the behavior of the proposed design, three culverts with different depths were constructed in Alabama. The four tabs in each culvert were equipped with three pressure sensors equidistantly installed along tab height. However, it was not possible to simulate the behavior of the structure under different load conditions, except the culvert designs used in this study. Thus, the numerical simulation was chosen as an equivalent method to simulate different load combinations and extreme event such as scour. The different backfill heights and traffic load were used to generate different potential load on the culverts. The combined results of numerical analyses and field measurements were used to develop the analytical approach of estimating possible loads on the tab surface. This load estimate approach addresses the missing component (Load) of the developed tab design procedure which can be applied to future CIP culvert-like structures with disconnected wing walls.

9.1. Summary

A numerical study was performed in order to investigate the new tabbed wing wall-to-culvert connection. Finite element simulations were conducted using Plaxis 3D. Three sets of models were developed to simulate the behavior of constructed culverts with tabbed wing wall connection. Separate models were developed to investigate the behavior of the structure under the design loads, and extreme events, such as scour. A culvert with traditional monolithically connected wing walls was modeled to study the scenario of crack formation in existing structures. An LRFD design procedure for the tab extension was developed based on existing design algorithm for corbels. Reliability based sensitivity analysis was performed for the controlling limit states for the wing wall design as a free standing retaining wall: sliding and overturning. The effects of variability of material parameters and dimensions of the structure were considered. Load and resistance factors were developed for the new design of the tab extension using reliability based calibration procedure.

9.2. Conclusions

Conclusions of this study are:

1. Possible reasons of crack formation are: increase of stresses while the backfilling, displacement of the top part of the wing wall toward the backfill, and high stress concentration at the top part of the wing wall-to-culvert connection.
2. The maximum stresses on the culvert wing tab surface located at the bottom of the tab and reduces till the top. Also, high stress level was recorded in the top corner of tab extension which is locked with tab extension from the barrel due to complex

rotation of the wing wall. The methodology how to estimate the force acting on the tab surface was developed.

3. An approved design procedure for tab extension was developed to determine the dimensions and reinforcing steel details that articulates with the AASHTO LRFD (2014).
4. The suggested reliability factors were calculated for the target reliability indexes of 2.0, 2.5, 3.0, 3.5. The resultant load factors vary from 1.106 to 1.358 for flexure and from 1.102 to 1.352 for shear. The resultant resistance factors vary from 1.046 to 0.941 for flexure and from 1.035 to 0.923 for shear.

9.3. Discussion

Plaxis 3D was suitable to simulate such complicated problems which involved soil-structure interaction. This software is equipped with advanced material models that closely simulate the behavior of the soil. Features, such as interface elements, an automated mesh generator and the embedded inaccuracy and error check allow recreating a fairly realistic behavior of the structure.

The results of the numerical simulations show a similar behavior of all constructed culverts in terms of stress distribution and displacement. Under backfill loading, the wing wall tends to rotate towards the backfill creating a stress concentration at the base. The magnitude, of these stresses decrease toward the top of the wall. With increasing backfill height, the wing wall gradually slides toward the barrel and this causes an increase of the magnitude of the stress. With applied traffic load, the magnitude of compression stresses increased as well. Scour propagation under the wing wall causes settlement and rotation changing the stress distribution. The maximum compression stresses are at the top of the

tab and dissipate toward the bottom. If the joint filling material is fully compressed the top part of the tab can be locked in the joint and this leads to formation of high stress concentration zone. Taking into account the actual distribution of stresses along the tab surface this scenario is only theoretically possible.

The data collected during field instrumentation of the culvert shows that compression stresses were recorded only in three tabs out of ten. In the rest of the cases, stresses oscillated around zero which indicate that the wing wall did not move or move toward the backfill. The largest pressure was recorded during the backfill portion of the construction and gradually reduced over time. The recorded compression stresses were in good agreement with numerical results. However, a stronger correlation between numerical and field results cannot be established due to limited field data.

Several observations were made during the study that may explain reasons of crack formation along the wing wall-to-culvert connection. All of the models show the same trend of the wing wall rotating toward the backfill. Therefore, a tensile zone is created at the top of the connection. In case of monolithically connected wing wall, the maximum compression stresses within top 5-in of the joint sharply increased up to the magnitude equal the compressive strength of concrete. Each of these factors is sufficient to cause crack formation in the top part of the connection. The location of these stress concentration zones corresponds to crack locations observed in existing culverts.

The design parameters, which affect the structural performance of newly designed culverts were identified based on the sensitivity analysis. In terms of sliding stability, the new design is the most sensitive to the footing length, especially if scour propagation is considered. Therefore, an acceptable reliability index ($\beta=3.5$) can still be reached with a

L_f/H_{ww} ratio equal to 1.0 without a key wall. In the design for the overturning the limit state, the negative impact of the key wall on structural performance was demonstrated. At the same time, a longer footing substantially contributes to the overturning stability of the structure. From the developed sensitivity functions, the errors in defining the coefficient of friction, friction angle, unit weight of backfill and friction angle between the structure and soil are the most critical for the culvert design for sliding and overturning. The remaining of parameters do not have a significant impact on sliding stability of the free-standing wing wall.

The load and resistance factors for flexure and shear limit states were developed for the new design procedure for the wing wall-to-tab connection. The target reliability index was assumed to be in the range from 2.5 to 3.5, according to the literature review. The resultant factors are consistent and can be applied in the design procedure depending on the desired level of safety.

References

AASHTO LRFD Bridge Design Specifications, 7th Edition. (2014a). Washington, D.C.

Abuhajar, O., Newson, T., and Naggar, H. E. (2017). "The Effect of Soil Depth and Box Culvert Geometry on the Static Soil-Culvert Interaction." *Geotechnical Frontiers*, Proceedings.

ACPA. (1983). *BOXCAR. Box Culvert Analysis and Reinforcing Design.* American Concrete Pipe Association, Irving, TX.

Ahmed, B., Amanat, K.M., Saflullah, A.M.M., and Choudhury, J. R. (2003). "Causes of cracking of culverts on filled soil and their performance after repair." *Journal of Civil Engineering*, CE 30(1).

ALDOT. (2012a). "Bureau of Research & Development Research Need Problem Statement: Culvert Wing Tab Design Loads." Alabama Department of Transportation.

ALDOT. (2008). "Roadway Plans Preparation Manual: Plans Preparation and Assembly." Alabama Department of Transportation.

Alkhrdaji, T., and Nanni, A. (2001). "Design, Construction, and Field-Testing of an RC Box Culvert Bridge Reinforced with GFRP Bars." *Non-Metallic Reinforcement for Concrete Structrures*, FRPRCS-5, 1055–1064.

Allen, T. M., Christopher, B. R., and Holtz, R. D. (1992). "Performance of a 12.6 m High Geotextile Wall in Seattle, Washington." 81–100.

Allen, T. M., Nowak, A. S., and Bathurst, R. J. (2005). *Calibration to Determine Load and Resistance Factors for Geotechnical and Structural Design*. Transportation Research Board.

Ang, A. H.-S., and Tang, W. H. (1984). *Probability Concepts in Engineering Planning and Design, Vol. 2: Decision, Risk, and Reliability*. John Wiley & Sons Inc, New York.

Arneson, L. A., Zevenbergen, L. W., Lagasse, P. F., and Clopper, P. E. (2012). "Evaluating scour at bridges."

Ashari, S. (2014). "Ultimate Strength Design Method of Reinforced Concrete Structures."

ASTM C31/C31M-15ae1 Standard Practice for Making and Curing Concrete Test Specimens in the Field. (2015). ASTM International, West Conshohocken, PA.

ASTM C39 / C39M-17a, Standard Test Method for Compressive Strength of Cylindrical Concrete Specimens. (2017). ASTM International, West Conshohocken, PA.

ASTM D1557-12e1, Standard Test Methods for Laboratory Compaction Characteristics of Soil Using Modified Effort (56,000 ft-lbf/ft3 (2,700 kN-m/m3)). (2012). ASTM International, West Conshohocken, PA.

Barker, R. M., Duncan, J. M., Rojiani, K. B., Ooi, P. S. K., Tan, C. K., and Kim, S. G. (1991). "Manuals for the Design of Bridge Foundations: Shallow Foundations, Driven Piles, Retaining Walls and Abutments, Drilled Shafts, Estimating Tolerable Movements, and Load Factor Design Specifications and commentary." *NCHRP Report*, (343).

Bathurst, R. J., Huang, B., and Allen, T. M. (2011). "Analysis of installation damage tests for LRFD calibration of reinforced soil structures." *Geotextiles and Geomembranes*, 29(3), 323–334.

Bathurst, R. J., Huang, B., and Allen, T. M. (2012). "LRFD Calibration of the Ultimate Pullout Limit State for Geogrid Reinforced Soil Retaining Walls." *International Journal of Geomechanics*, 12(4), 399–413.

Bathurst, R. J., Nernheim, A., and Allen, T. M. (2009). "Predicted Loads in Steel Reinforced Soil Walls Using the AASHTO Simplified Method." *Journal of Geotechnical and Geoenvironmental Engineering*, 135(2), 177–184.

Benjamin, J. R., Cornell, C. A. (1970). *Probability, Statistics, and Decisions for Civil Engineers*. McGraw-Hill, New York; Maidenhead.

Bentler, J. G., and Labuz, J. F. (2006). "Performance of a Cantilever Retaining Wall." *Journal of Geotechnical and Geoenvironmental Engineering*, 132(8), 1062–1070.

Boussinesq, M. J. (1885). *Application des potentiels a l'etude de l'equilibre et du mouvement des solides elastiques, principalement au calcul des deformations et des pressions que produisent, dans ces solides, des efforts quelconques exerces sur*

une petite partie de leur surface ou de leur interieur: Memoire suivi de notes etendues sur divers points de physique mathematique et d'analyse. GauthierVillars, Paris.

Bowles, J. E. (1988). *Foundation Analysis and Design, 4lh ed.* McGraw Hill.

Bruner, R. F., Coyle, H. M., and Bartoskewitz, R. E. (1983). "Cantilever retaining wall design." Texas A&M University.

BS 5400-2. (1978). "British standard BS 5400-2: Steel, concrete and composite bridges — Part 2:Specification for loads." Board of BSI.

Campos, M. (2004). "Section 5 - Retaining Walls." *Bridge Design Specification*, California Department of Transportation, Sacramento, CA.

Casagrande, L. (1973). "Comments on Conventional Dessign of Retaining Structures (Discussion)." *Journal of Soil Mechanics & Foundations Div*, 99(sm8).

Castillo, E., Mínguez, R., Terán, A. R., and Fernández-Canteli, A. (2004). "Design and sensitivity analysis using the probability-safety-factor method. An application to retaining walls."

Chalermyanont, T., and Benson, C. (2004). "Reliability-Based Design for Internal Stability of Mechanically Stabilized Earth Walls." *Journal of Geotechnical and Geoenvironmental Engineering*, 130(2), 163–173.

Christian John T., Ladd Charles C., and Baecher Gregory B. (1994). "Reliability Applied to Slope Stability Analysis." *Journal of Geotechnical Engineering*, 120(12), 2180–2207.

Chugh, A. K., Guney, O. C., and Labuz, J. F. (2016). "Soil Structure Interactions of Retaining Walls." *Geotechnical and Structural Engineering Congress 2016*, Proceedings.

Clough, G. W., and Duncan, J. M. (1971). "Finite Element Analyses of Retaining Wall Behavior." *Journal of the Soil Mechanics and Foundations Division*, 97(12), 1657–1673.

Coghlan, B. K. (1916). "Highway bridges and culverts." Agricultural and Mechanical College of Texas.

ConnDOT. (2000). *Drainage Manual*. Connecticut Department of Transportation (ConnDOT).

Coulomb, C. A. (1776a). *Essai sur une application des règles de maximis & minimis à quelques problèmes de statique, relatifs à l'architecture*. De l'Imprimerie Royale, Paris.

Coulomb, C. A. (1776b). *Essai sur une application des règles de maximis & minimis à quelques problèmes de statique, relatifs à l'architecture*. De l'Imprimerie Royale, Paris.

CYBER 180-840A. (1986). Control Data, Saint Paul, MN.

Dasgupta, A., and Sengupta, B. (1991). "Large-Scale Model Test on Square Box Culvert Backfilled with Sand." *Journal of Geotechnical Engineering*, 117(1).

Dunavant, D. A. (1985). "High degree efficient symmetrical Gaussian quadrature rules for the triangle." *International Journal for Numerical Methods in Engineering*, 21(6), 1129–1148.

Duncan, J. M. (2000). "Factors of Safety and Reliability in Geotechnical Engineering." *Journal of Geotechnical and Geoenvironmental Engineering*, 126(4), 307–316.

Duncan, J. M., and Chang, C.-Y. (1970). "Nonlinear Analysis of Stress and Strain in Soils." *Journal of the Soil Mechanics and Foundations Division*, 96(5), 1629–1653.

ETCulvert. (2017). Eriksson Technologies, Lakewood, CO.

FDOT. (1993). *Reinforced Concrete Box Culvert and Wingwall Design and Analysis User's Manual*. Version 2.3, Structures Design Office Florida Department of Transportation.

FDOT. (2011). *Plans Preparation Manual*. Florida Department of Transportation (FDOT).

Fenton, G. A., Griffiths, D. V., and Williams, M. B. (2005). "Reliability of traditional retaining wall design." *No 1.*, (Vol. 55), pp.55-62.

FHWA. (1983). *Structural Design Manual for Improved Inlets & Culverts*. U.S. Department of Transportation.

Garg, A. K., and Abolmaali, A. (2009). "Finite-Element Modeling and Analysis of Reinforced Concrete Box Culverts." *Journal of Transportation Engineering, ASCE*.

Geokon, Inc. (2011). *Models 4800, 4810, 4815, 4820 and 4830 VW Earth Pressure Cells.* Lebanon, NH: Geokon, Inc.

Geotac. (2017). *GEOJAC - Digital Load Actuators*.

Goh A. T., Phoon K. K., and Kulhawy F. H. (2009). "Reliability Analysis of Partial Safety Factor Design Method for Cantilever Retaining Walls in Granular Soils." *Journal of Geotechnical and Geoenvironmental Engineering*, 135(5), 616–622.

Goh, G. A. T. (1993). "Behavior of Cantilever Retaining Walls." *Journal of Geotechnical Engineering*, 119(11), 1751–1770.

"Google Maps." (2017a). 4300 County Road 258. La Fayette, Alabama.

"Google Maps." (2017b). 722 Lee Rd 156. Opelika, Alabama.

"Google Maps." (2017c). County Road 68. Sylacuaga, Alabama.

Harr, M. E. (1987). *Reliability-Based Design in Civil Engineering*. Mcgraw-Hill, New York.

Hasofer, A. M., and Lind, N. (1974). "An Exact and Invariant First Order Reliability Format." *Journal of Engineering Mechanics*, 100.

Hoeg, K., and Murarka, R. P. (1974). "Probabilistic Analysis and Design of a Retaining Wall L." *Journal of Geotechnical and Geoenvironmental Engineering*, 100(GT3).

Huntington, W. C. (1957). *Earth pressures and retaining walls.* Wiley, New York.

Hurd, J. O. (1991). "Field Performance of Precast Reinforced Concrete Box Culverts." *In Transportation Research Record, Transportation Research Board*, (№1315), 53–57.

IES. (2017). *VisualAnalysis*. IES, Bozeman, MT.

INDOT. (2012). “Large Culvert 50-47-51.36 Inspection Report.” Indiana Departmetn of Transportation.

IODOT. (2013). *Culvert Calc, Technical Manual, Automated RCB culvert analysis and design in accordance with the AASHTO LRFD Bridge Design Specifications, 5th Edition*. Iowa Department of Transportation.

Itasca. (2017). *FLACK*. Itasca, Minneapolis, MN.

Jaky, J. (1948). “Pressure in silos.” Vol. 1, 103–107.

Katona, M. G. (2017). *CANDE. Culvert Analysis and Design.* CANDE, Gig Harbor, WA.

Koiter, W. T. (1960). *General Theorems for Elastic-plastic Solids*. North-Holland.

Kondner, R. L. (1963). *A hyperbolic stress-strain formulation for sands*. Northwestern University.

Kulhawy, F. H. (1992). “On the Evaluation of Static Soil Properties.” ASCE, 95–115.

Kulhawy, F. H., Callanan, J. F., and Cornell University. (1985). *Evaluation of procedures for predicting foundation uplift movements*. Electric Power Research Institute, Palo Alto, Calif.

Kulhawy, F. H., and Phoon, K.-K. (2002). “Observations on geotechnical reliability-based design development in North America.” Foundation design codes and soil investigation in view of international harmonization and performance based design.

KYTC. (2011). *Drainage Manual*. Kentucky Transportation Cabinet (KYTC).

Lee, H. I. (2017). “Design of Lateral Support for Non-Integral Wing Walls of Culverts.” Master’s Thesis, Auburn University.

Low, B. K. (2007). “Reliability-based design applied to retaining walls.” *Risk and Variability in Geotechnical Engineering*, Thomas Telford Publishing, 151–163.

Mandali, A. K., Sujith, M. S., Rao, B. N., and Maganti, J. (2011). “Reliability analysis of counterfort retaining walls.” *Electronic Journal of Structural Engineering*, 11(1), 42–56.

Mattock, A. H. (1976). “Design proposals for reinforced concrete corbels.” *Precast/Prestressed Concrete Institute. Journal*, 21(3).

Mayne, P. W., and Kulhawy, F. H. (1982). “K0-OCR relationships in soil.” Vol. 108 (GT6), 851–872.

McGrath, T. J., Selig, E. T., and Beach, T. J. (1996). “Structural Behavior of Three-Sided Arch Span Bridge.” *In Transportation Research Record: Journal of the Transportation Research Board*, (№1541), 112–119.

Meyerhof, G. G. (1956). “Penetration Tests and Bearing Capacity of Cohesionless Soils.” *Journal of the Soil Mechanics and Foundations Division*, 82(1), 1–19.

MNDOT. (2000). *Drainage Manual.* Minnesota Department of Transportation (MNDOT).

Musser, S. C. (1995). “A Synthesis of the Application and Performance of Three-Sided Precast Box Culverts.” *In Transportation Research Record: Journal of the Transportation Research Board*, (№951091).

Nisha, S., Shivashankar, R., and Ravi Shankar, A. U. (2011). “Role of Shear Keys in Cantilever Retaining Wall.” *Scribd*, (Geotechnical Engineering, Chemical Product Engineering).

Nowak, A. S., and Collins, K. R. (2012). *Reliability of Structures, Second Edition*. CRC Press.

Nowak, A. S., and Lind, N. C. (1979). “Practical Bridge Code Calibration.” *ASHRAE Journal*, 105(12).

Nowak, A. S., Szerszen, M. M., Szeliga, E. K., Szwed, A., and Podhorecki, P. J. (2005). *Reliability-Based Calibration for Structural Concrete*. University of Nebraska, Lincoln, NE, 124.

NYSDOT. (2012). *Geotechnical Design Manual*. NYSDOT.

Paikowsky, S. G. (2004). *Load and Resistance Factor Design (LRFD) for Deep Foundations*. Transportation Research Board, Washington, D.C.

Phoon, K. K., Kulhawy, F. H., and Grigoriu, M. D. (1995). *Reliability-Based Design of Foundations for Transmission Line Structures*. Electric Power Research Institute, Palo Alto, 380.

Phoon, K. K., Kulhawy, F. H., and Grigoriu, M. D. (2003). "Development of a Reliability-Based Design Framework for Transmission Line Structure Foundations." *Journal of Geotechnical and Geoenvironmental Engineering*, 129(9), 798–806.

Plaxis bv. (2010). *Plaxis Version 8. Validation manual*. Plaxis.

Plaxis bv. (2015a). *Plaxis 3D AE - Scientific Manual*. Plaxis.

Plaxis bv. (2015b). *Plaxis 3D AE - Reference Manual.* Plaxis.

Plaxis bv. (2015c). *Plaxis 3D AE - Material Models Manual*. Plaxis.

Powell, R. E., and Foster, S. J. (1996). *Experimental Investigation on Rectangular Corbels Cast in High Strength Concrete*. University of New South Wales.

Ranganathan, R. (1999). "Structural reliability and design."

Rankine, W. (1857). *On the Stability of Loose Earth*. Royal Society of London.

Rankine, W. J. M. (1858). *A Manual Of Applied Mechanics*. Hoar Press.

Reinforced concrete box culvert and wing wall design and analysis computer program user's manual. (1993). Florida Department of Transportation (FDOT).

Rhomberg, E. J., and Street, W. M. (1981). "Optimal Design of Retaining Walls." *Journal of the Structural Division*, 107(5), 992–1002.

Sarıbaş Aşkın, and Erbatur Fuat. (1996). "Optimization and Sensitivity of Retaining Structures." *Journal of Geotechnical Engineering*, 122(8), 649–656.

Scanlon, R. F. (2012). "Detailed visual culvert inspection guidelines." Main Roads Western Australia.

Schanz, T. (1998). *Zur Modellierung des mechanischen Verhaltens von Reibungsmaterialien*. Universitat Stuttgart., Mitteilung 45 des Instituts fur GeotechnikUniversit ¨ ¨at Stuttgart.

Senthil, K., Iqbal, M. A., and Kumar, A. (2014). "Behavior of cantilever and counterfort retaining walls subjected to lateral earth pressure." *International Journal of Geotechnical Engineering*, 8(2), 167–181.

Sivakumar, B. G. L., and Basha, B. M. (2008). “Optimum Design of Cantilever Retaining Walls Using Target Reliability Approach.” *International Journal of Geomechanics*, 8(4), 240–252.

Skempton, A. W. (1986). “Standart penetration test procedures and the effects in sands of overburden pressure, relative density, particle size, ageing and overconsolidation.” *Geotechnique*, 36(3).

Spangler, M. G. (1960). “Marston theory for soil pressure on conduits.” *International Text Book Co.*

Smith, I. M., and Griffiths, D. V. (2004). *Programming the finite element method*. Wiley, Hoboken, NJ.

Tang, W. H., Stark, T. D., and Angulo, M. (1999). “Reliability in Back Analysis of Slope Failure.” *SOILS AND FOUNDATIONS*, 39(5), 73–80.

Terzaghi, K. (1934). “Large Retaining Wall Tests. I. Pressure of Dry Sand.” *Engineering News-Record*, 102(20).

Terzaghi, K. (1947). *Theoretical Soil Mechanics*. NY.

Terzaghi, K., Peck, R. B., Mesri, G., and Knovel (Firm). (1996). *Soil mechanics in engineering practice*. Wiley, New York.

Tschebotarioff, G. P. (1973). *Foundations, Retaining and Earth Structures: The Art of Design and Construction and Its Scientific Basis in Soil Mechanics*. Mcgraw-Hill, New York.

Van Langen, H., and Vermeer, P. A. (1990). “Automatic step size correction for non-associated plasticity problems.” *International Journal for Numerical Methods in Engineering*, 29(3), 579–598.

Van Langen, H., and Vermeer, P. A. (1991). “Interface elements for singular plasticity points.” *International Journal for Numerical and Analytical Methods in Geomechanics*, 15(5), 301–315.

Whitman. (2000). “Organizing and Evaluating Uncertainty in Geotechnical Engineering.” *Journal of Geotechnical and Geoenvironmental Engineering*, 126(7), 583–593.

Wisniewski, J., Nowak, A., and Hung, J. (2016). *Recommended AASHTO LRFD Tunnel Design and Construction Specifications*. Transportation Research Board, Washington D.C.

Withiam, J. L., Voytko, E. P., Barker, R. M., Duncan, J. M., Kelly, B. C., Musser, S. C., and Elias, V. (1998). *Load and Resistance Factor Design (LRFD) for Highway Bridge Substructures*. Federal Highway Administration, Washington, D.C.

Wolff, T. F. (1994). *Evaluating the reliability of existing levees*. US Army Engineer Waterways Experiment Station Geotechnical Laboratory, Vicksburg, MS.

Zhang, L., Tang, W. H., and Ng, C. W. W. (2001). "Reliability of Axially Loaded Driven Pile Groups." *Journal of Geotechnical and Geoenvironmental Engineering*, 127(12), 1051–1060.

A. APPENDIX A: Constructed Culvert Design Drawings.

Chambers County Culvert

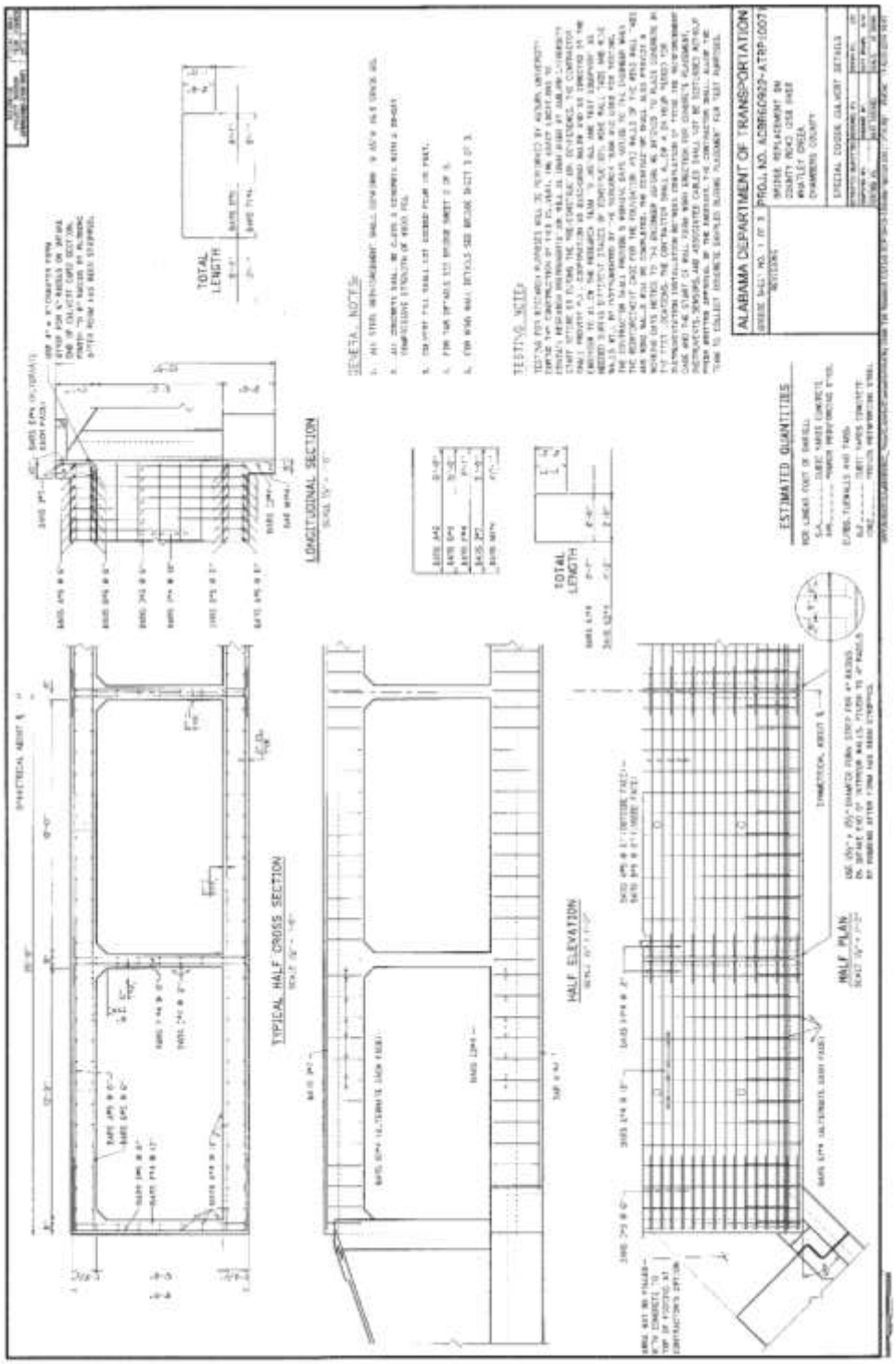

Figure A-1. Chambers County culver detail, sheet #1

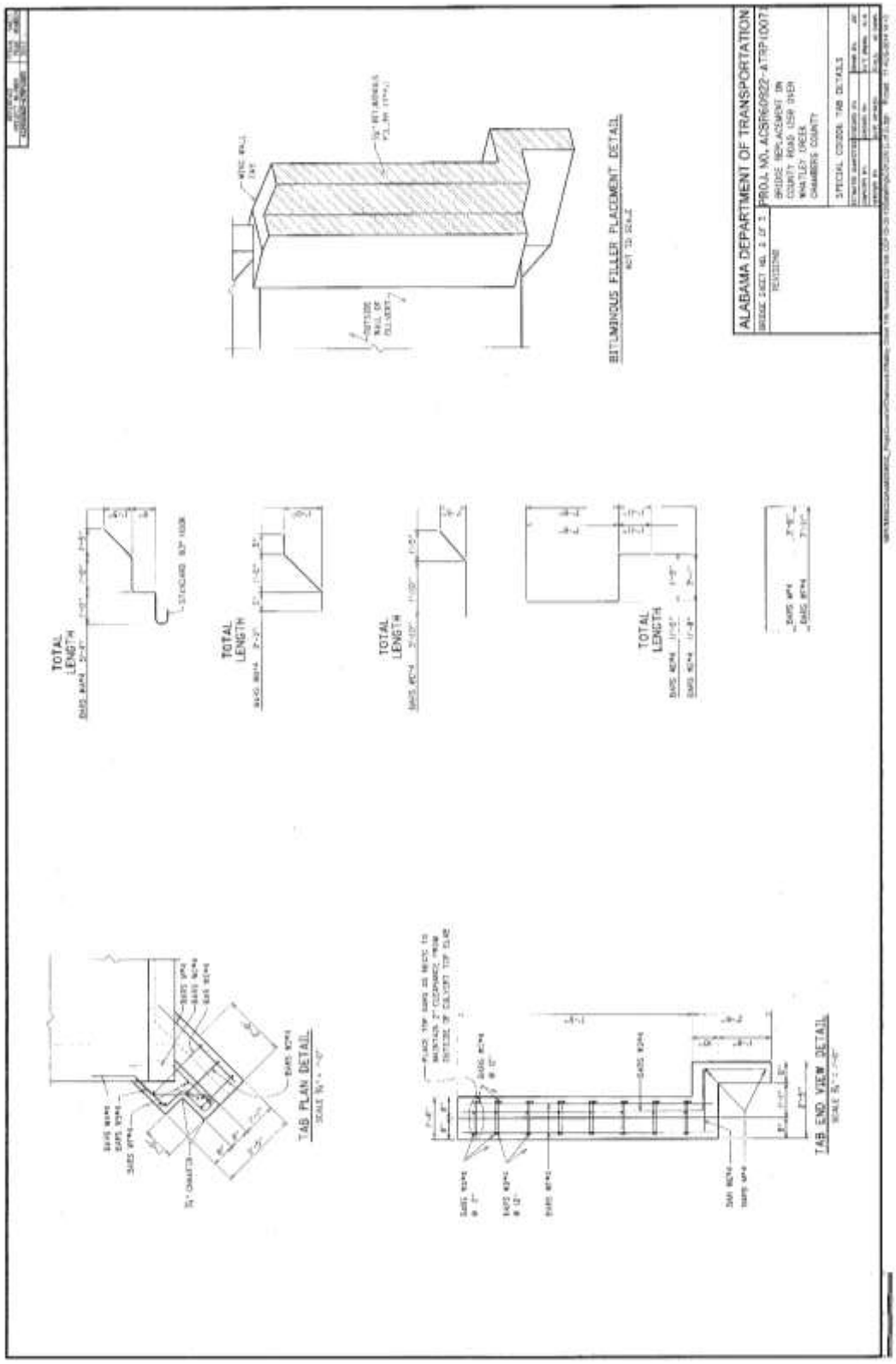

Figure A-2. Chambers County culver detail, sheet #2

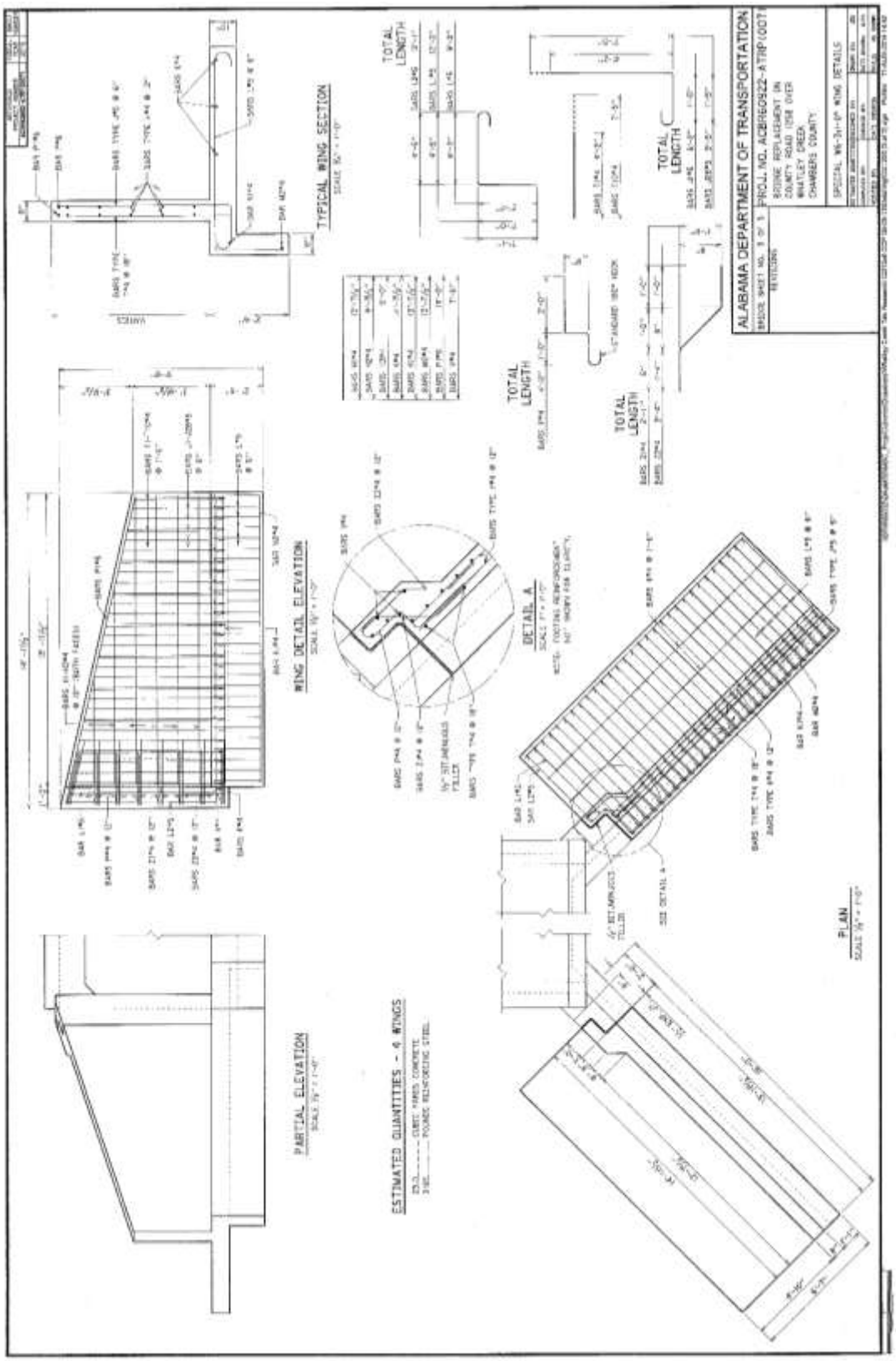

Figure A-3. Chambers County culver detail, sheet #3

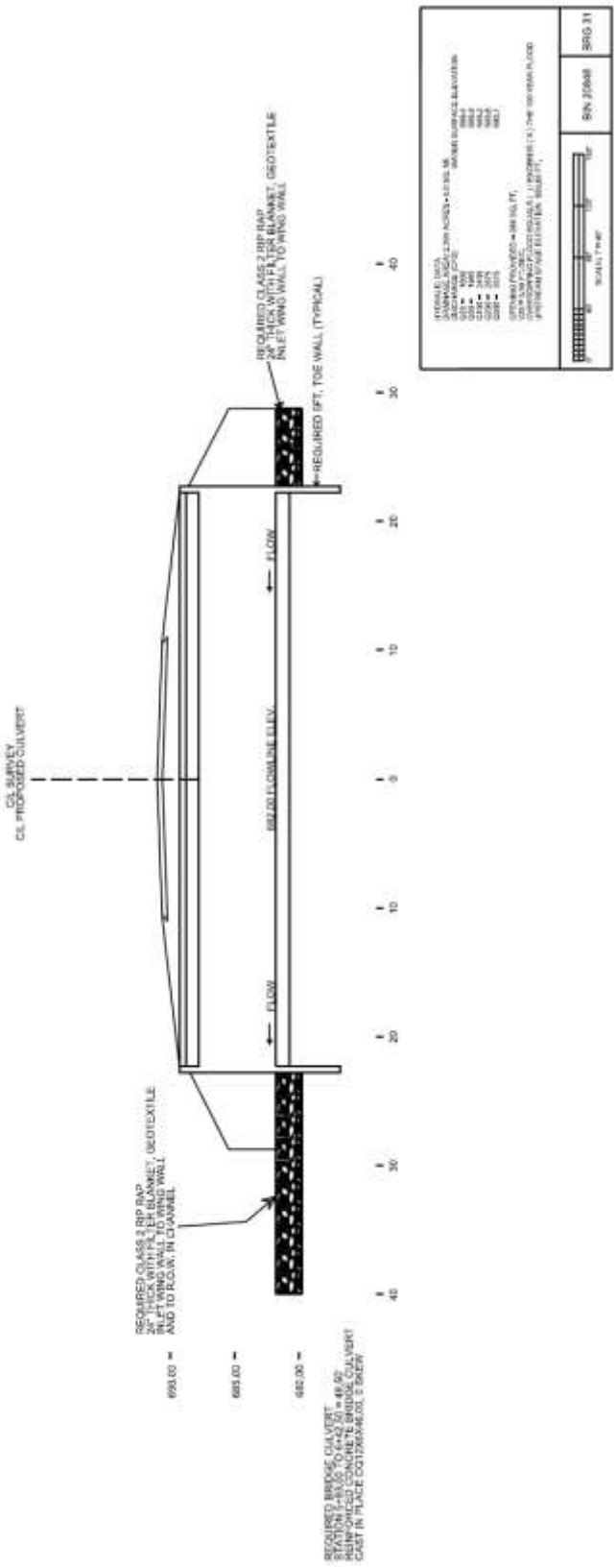

Figure A-4. Chambers County culver drainage section and profile

Lee County Culvert

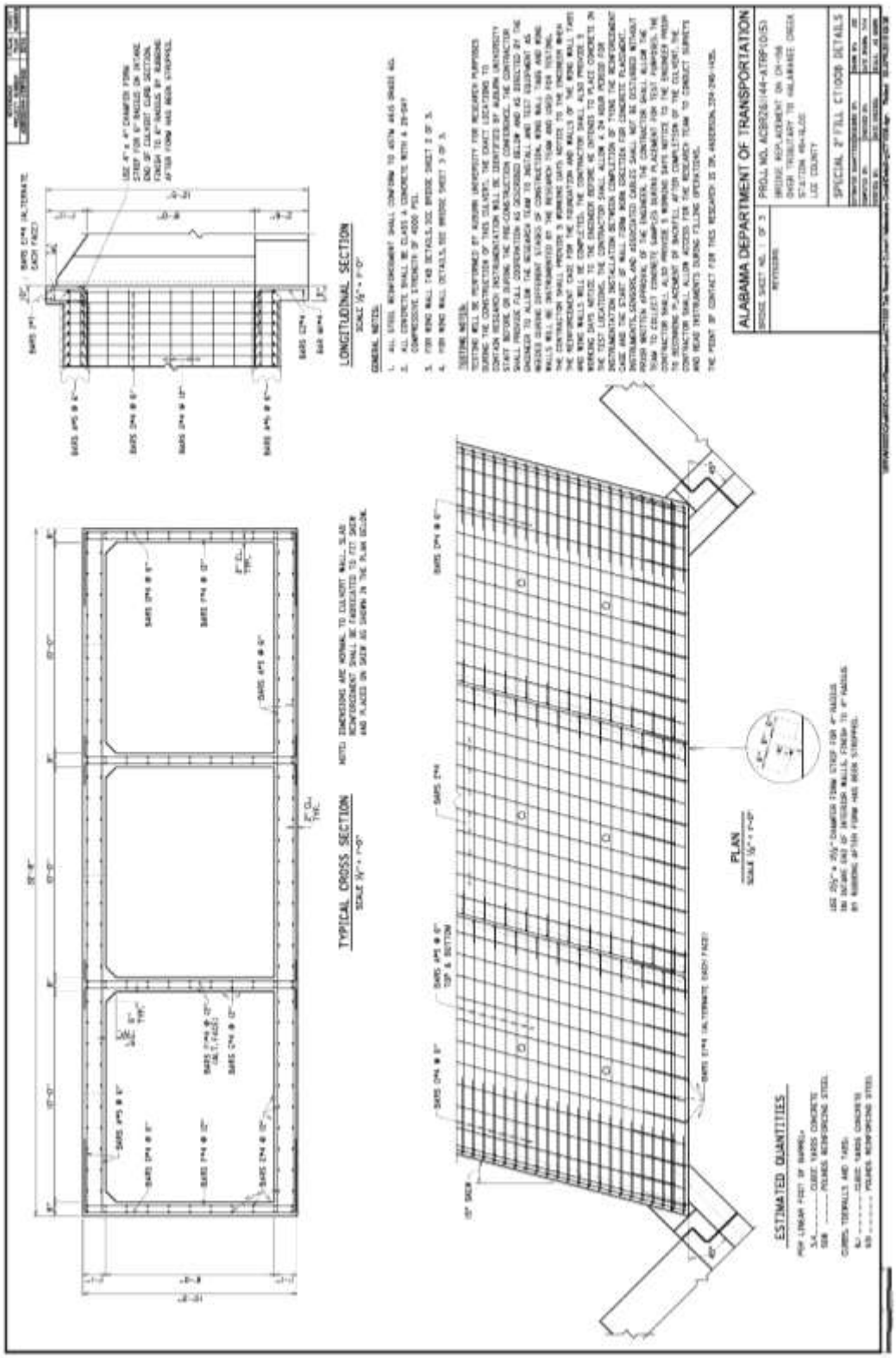

Figure A-5. Lee County culver detail, sheet #1

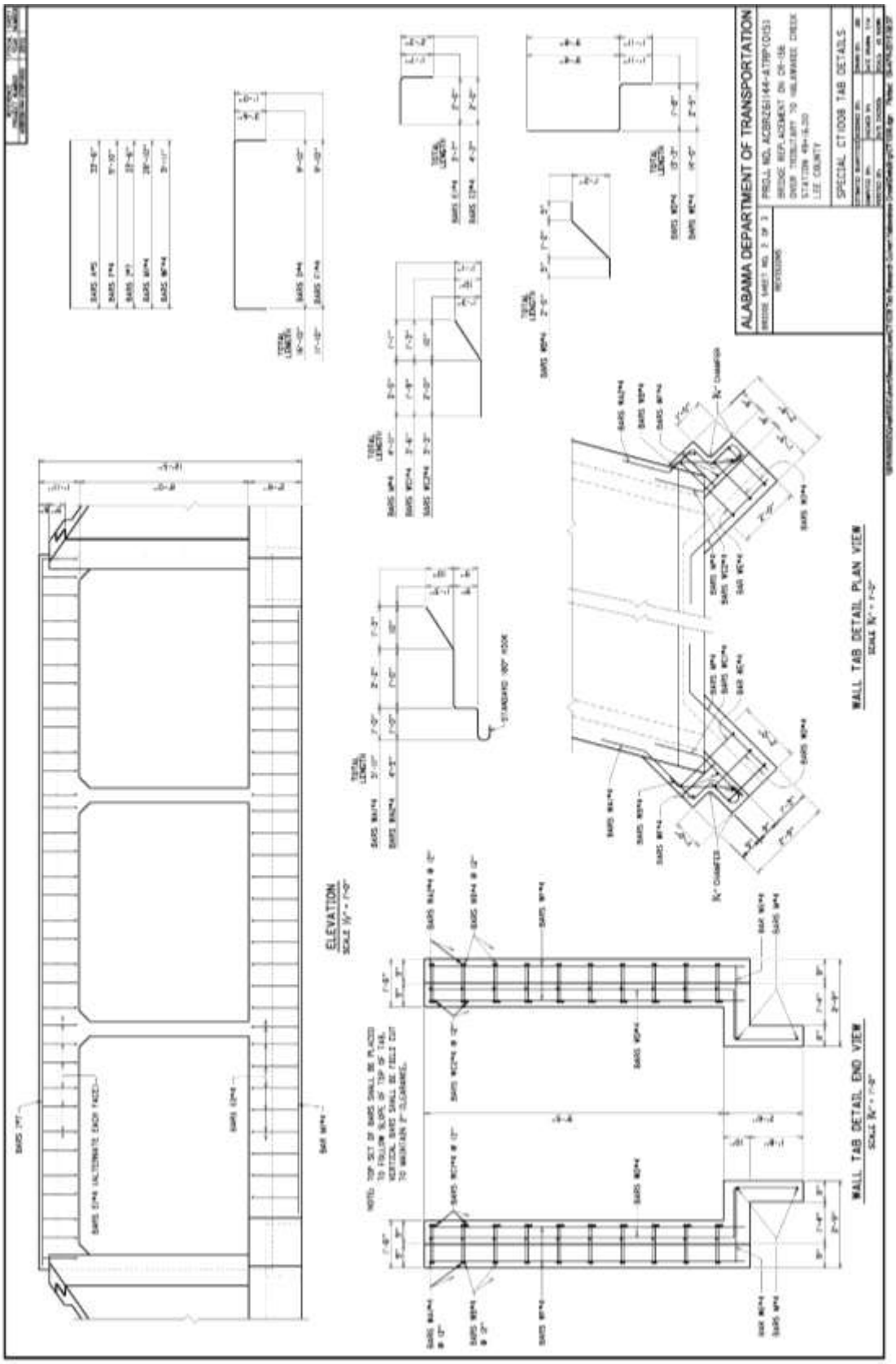

Figure A-6. Lee County culver detail, sheet #2

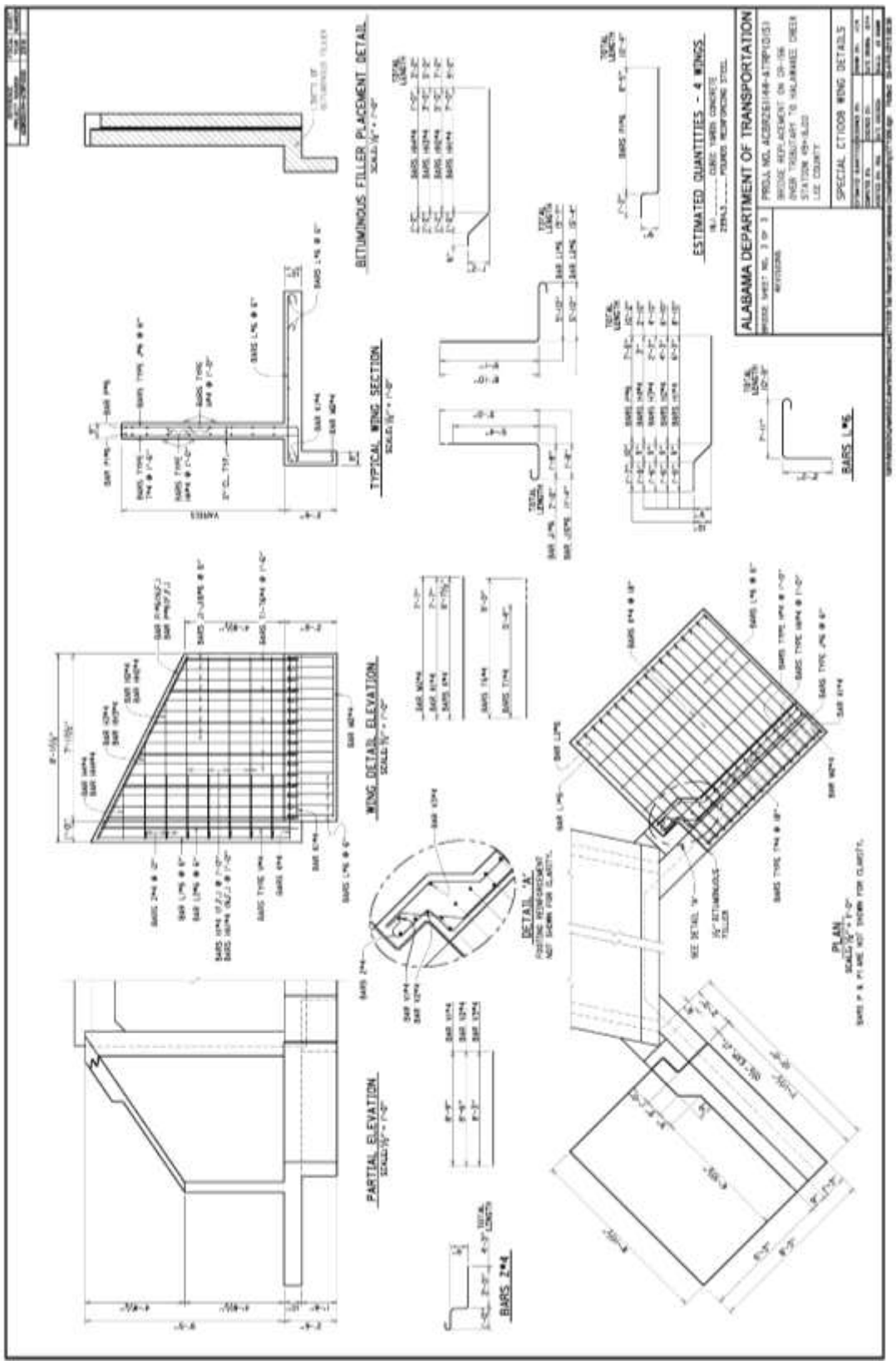

Figure A-7. Lee County culver detail, sheet #3

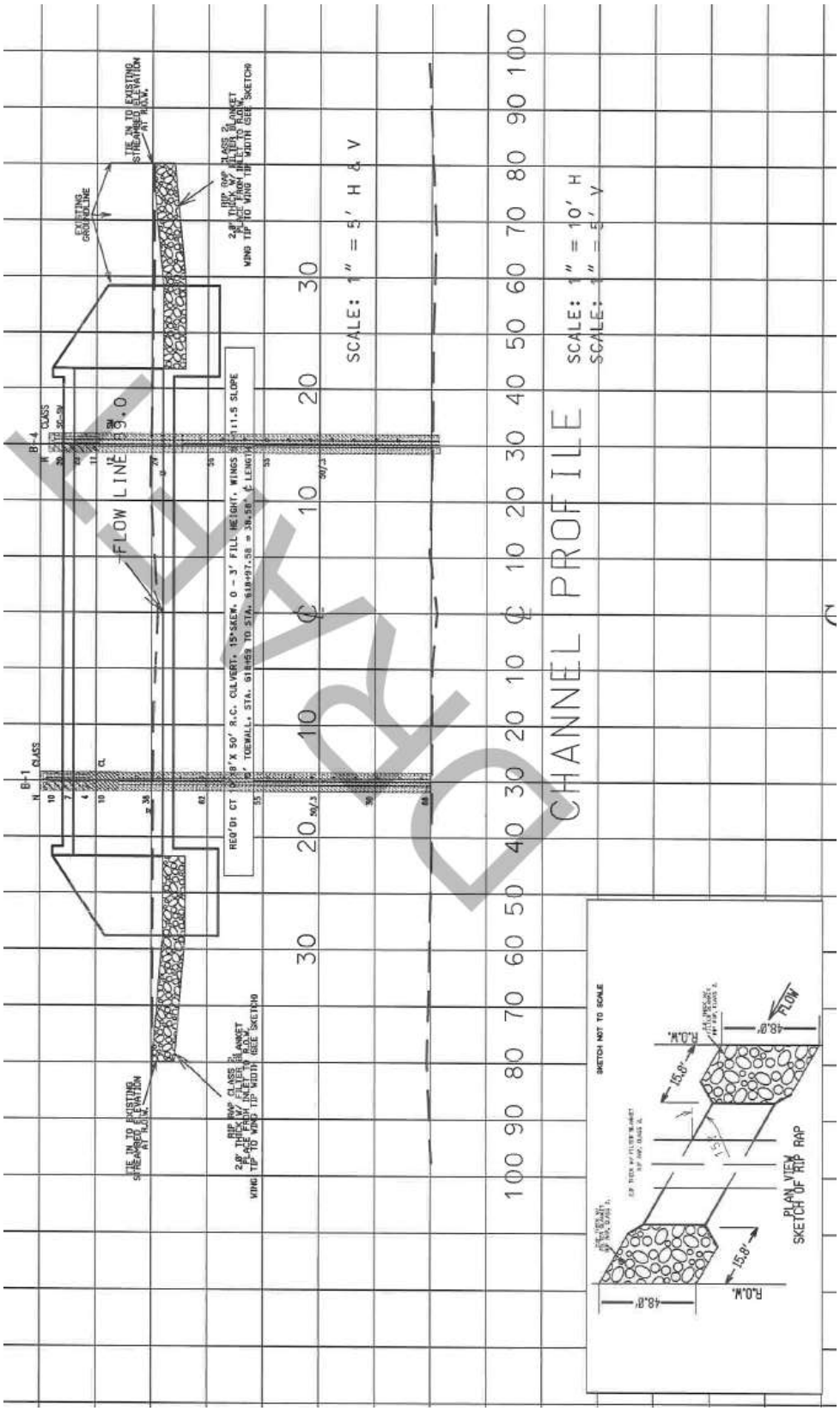

Figure A-8. Lee County culver drainage section and profile

Coosa County Culvert

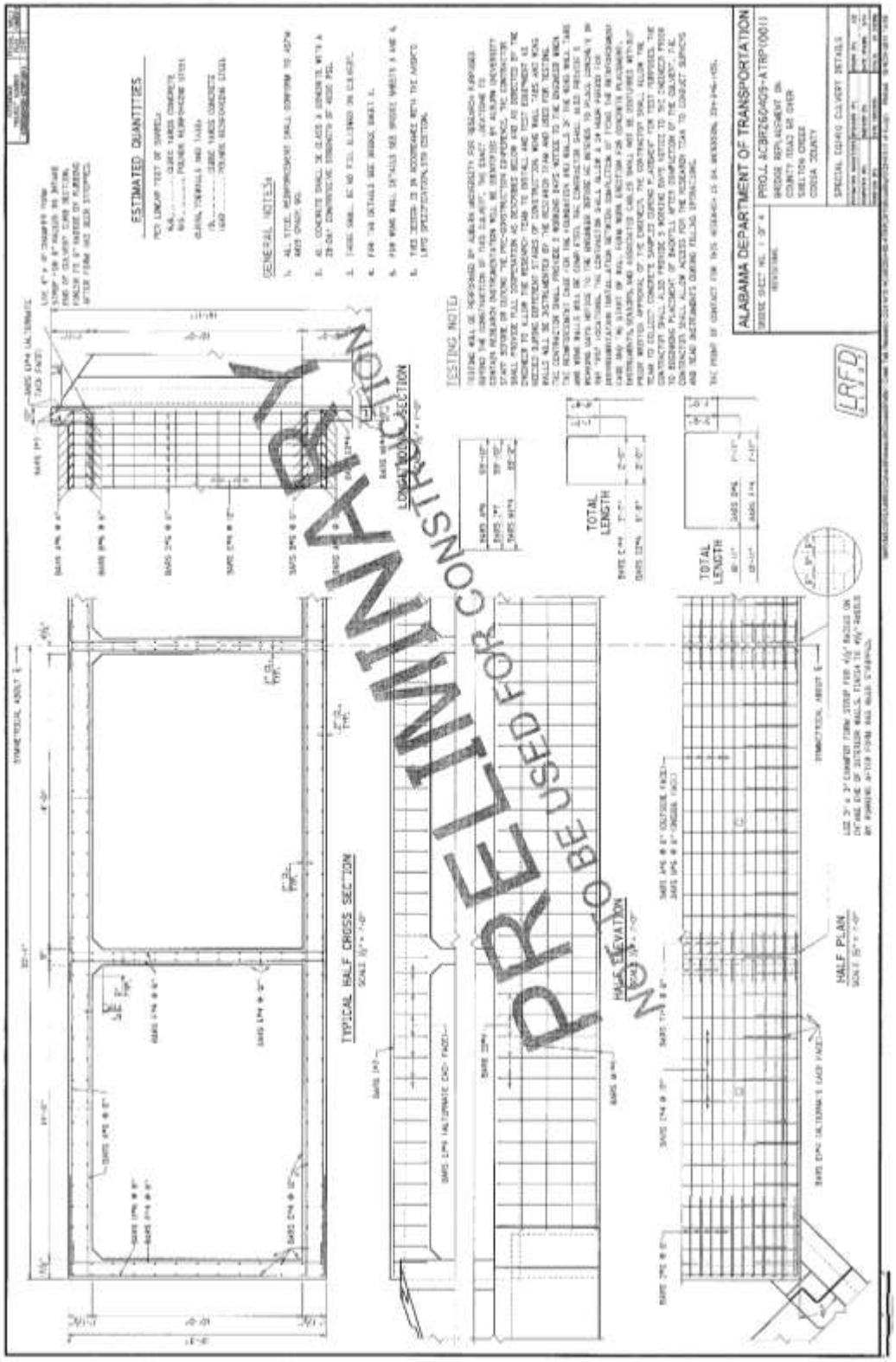

Figure A-9. Coosa County culver detail, sheet #1

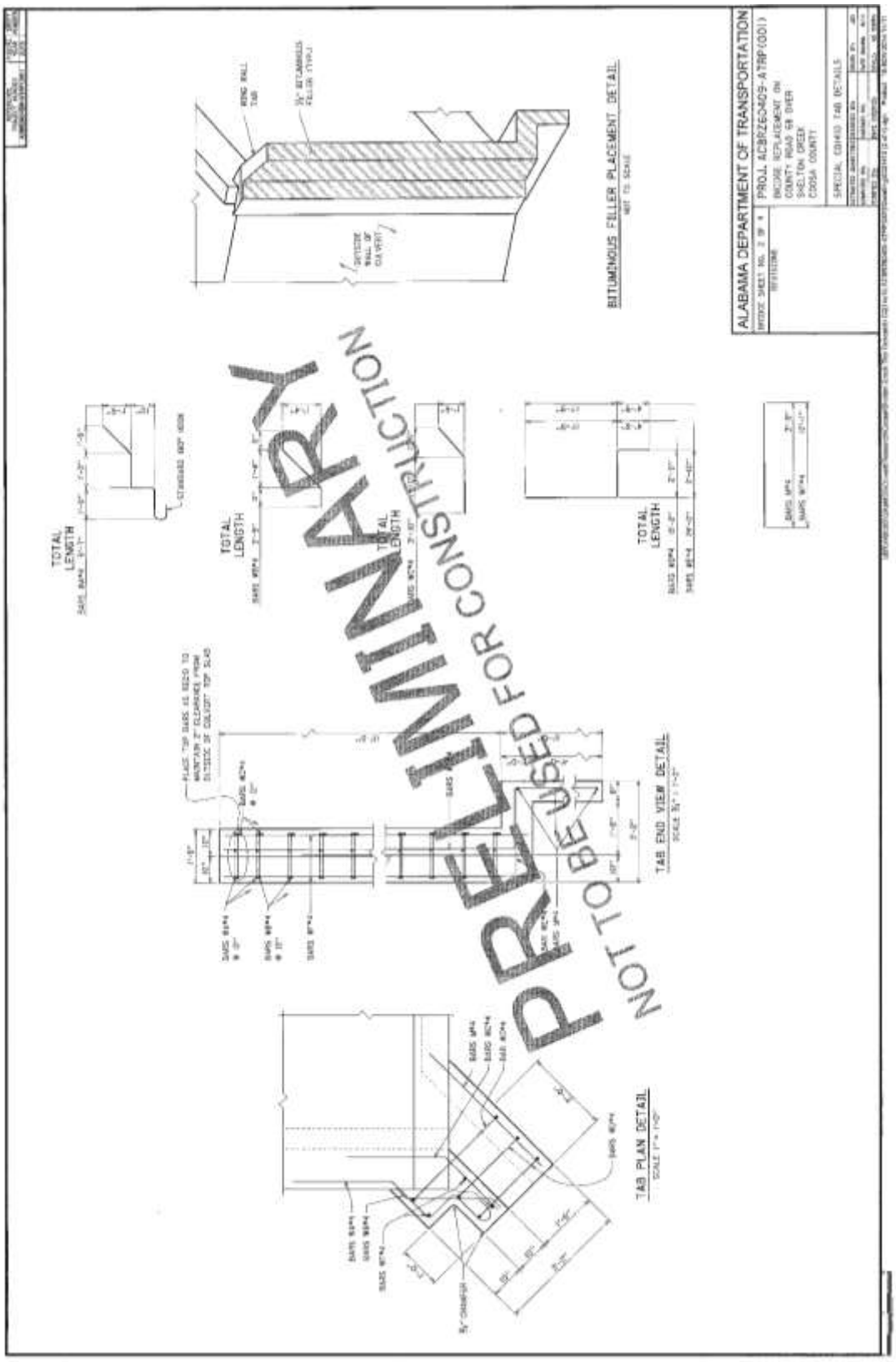

Figure A-10. Coosa County culver detail, sheet #2

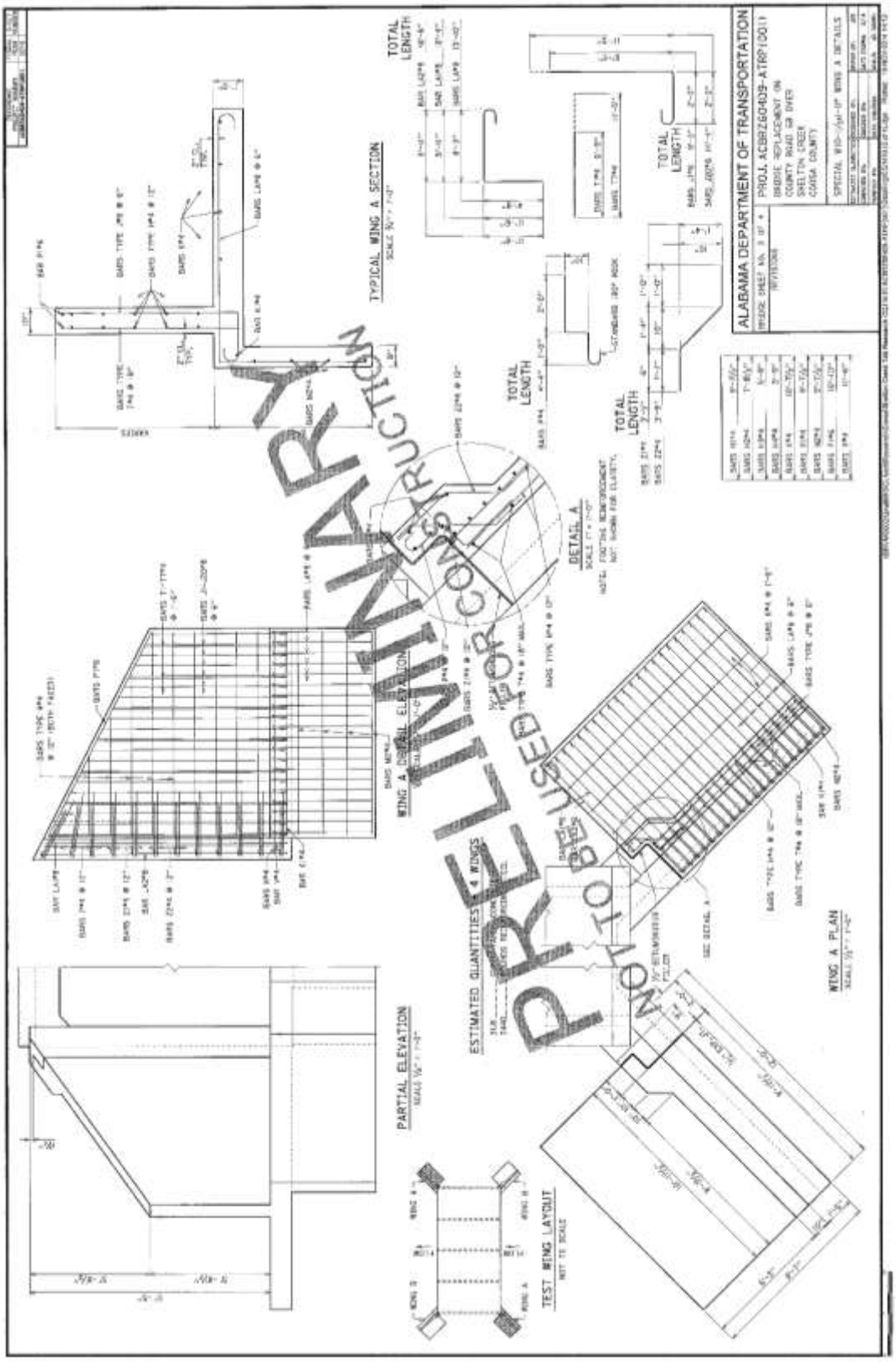

Figure A-11. Coosa County culver detail, sheet #3

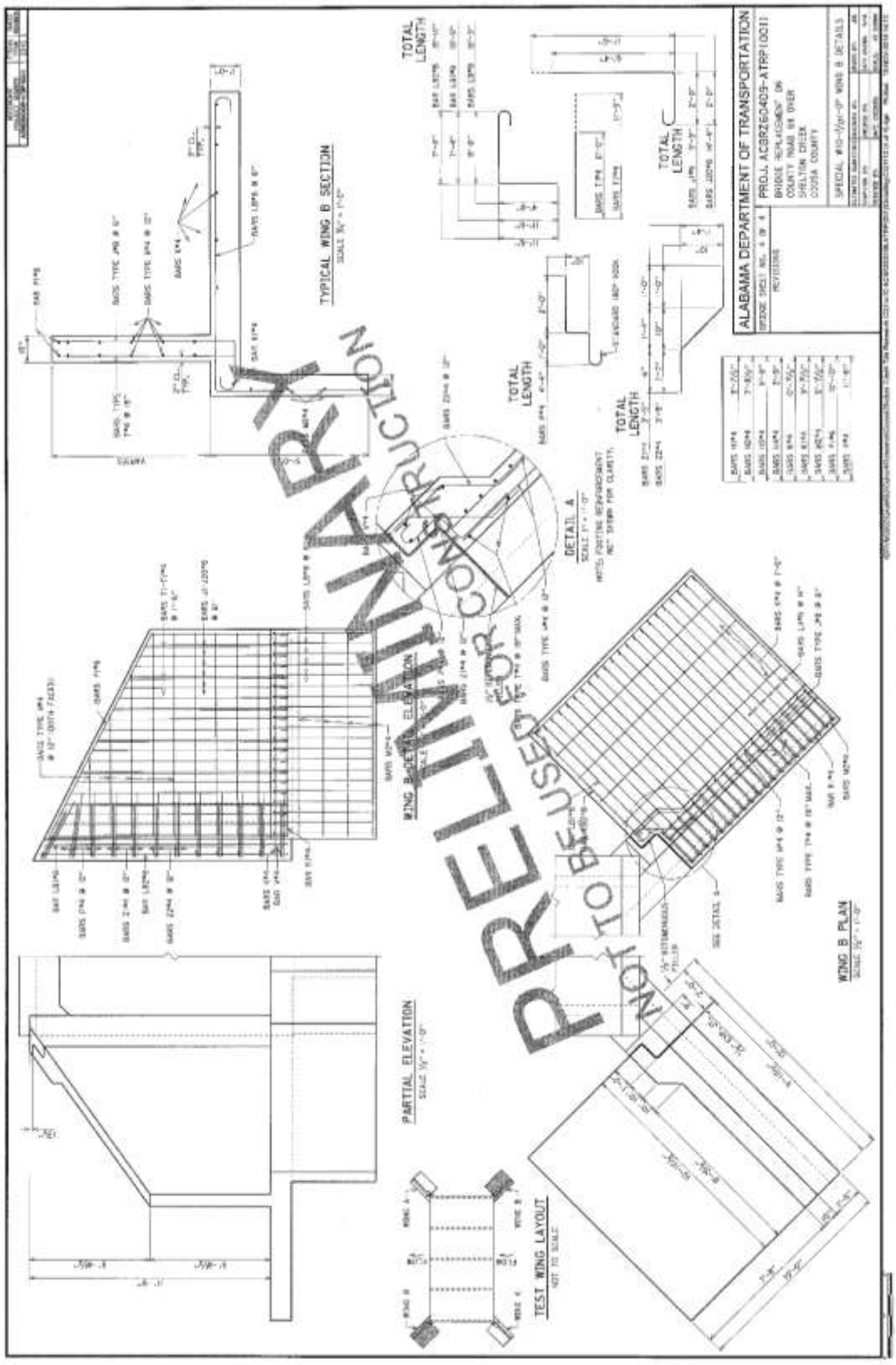

Figure A-12. Coosa County culver detail, sheet #4

B. APPENDIX B: Boring Logs

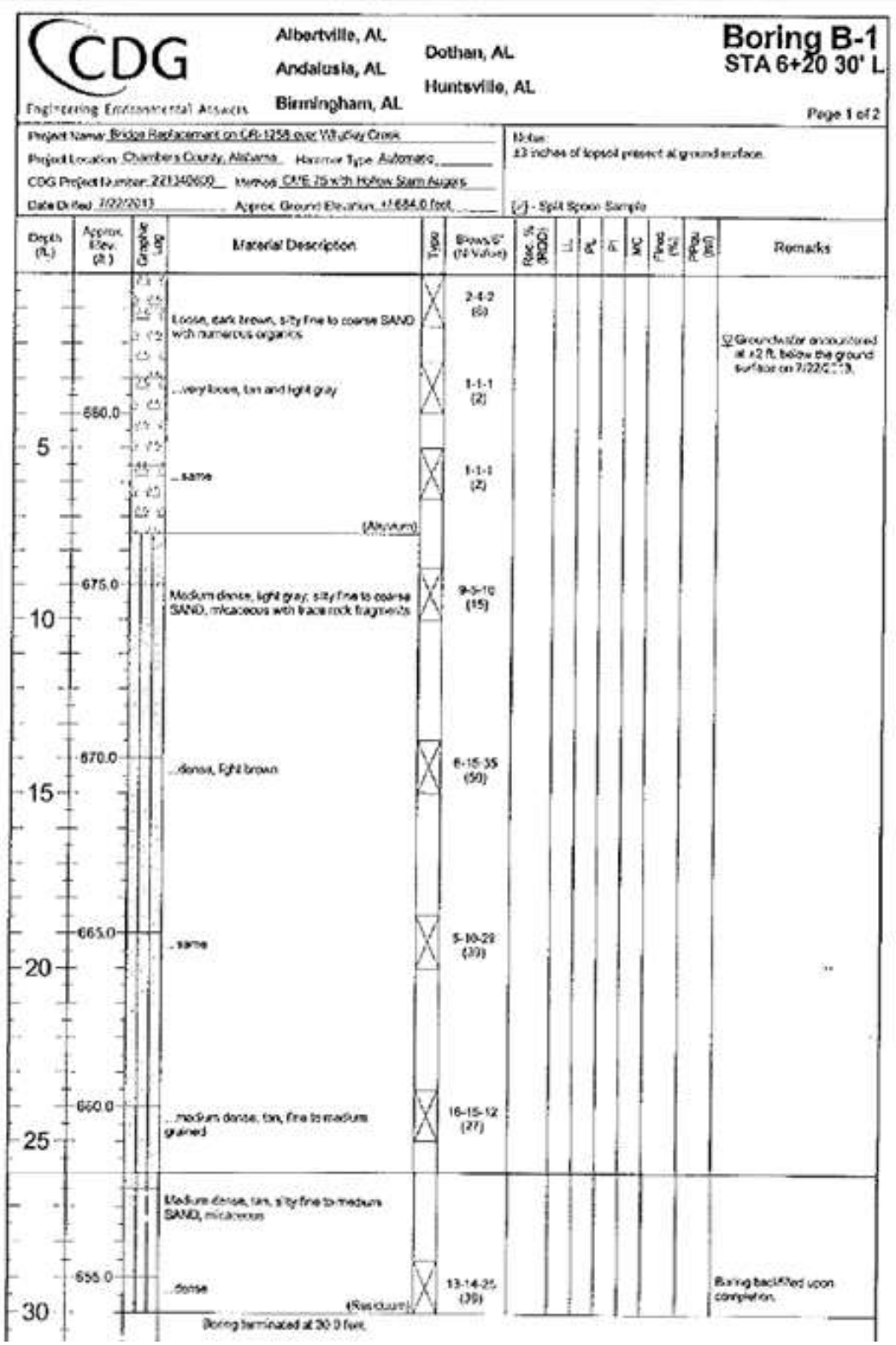

Figure B-1. Chambers County boring B-1 (0-30ft)

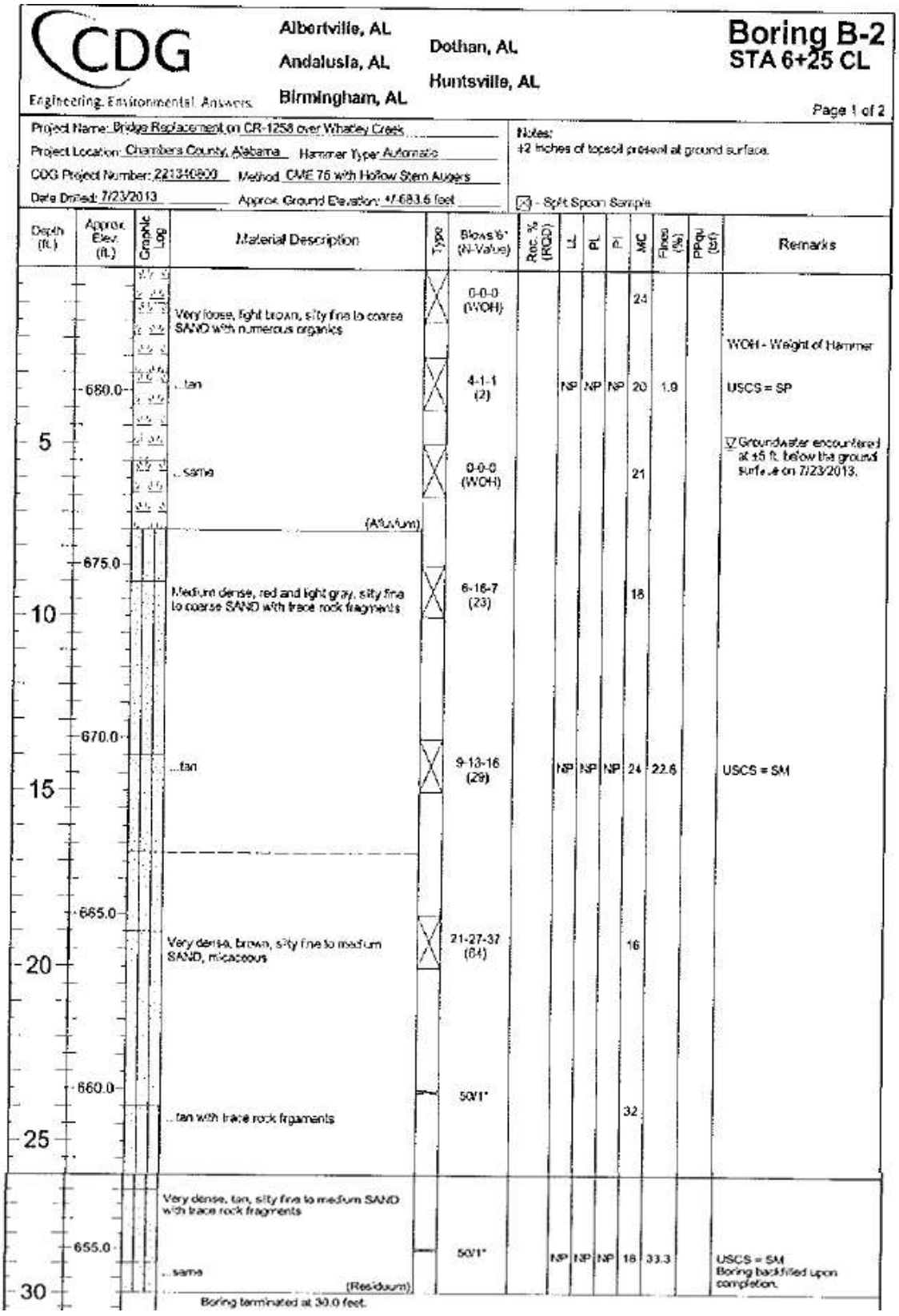

Figure B-2. Chambers County boring B-2 (25-30ft)

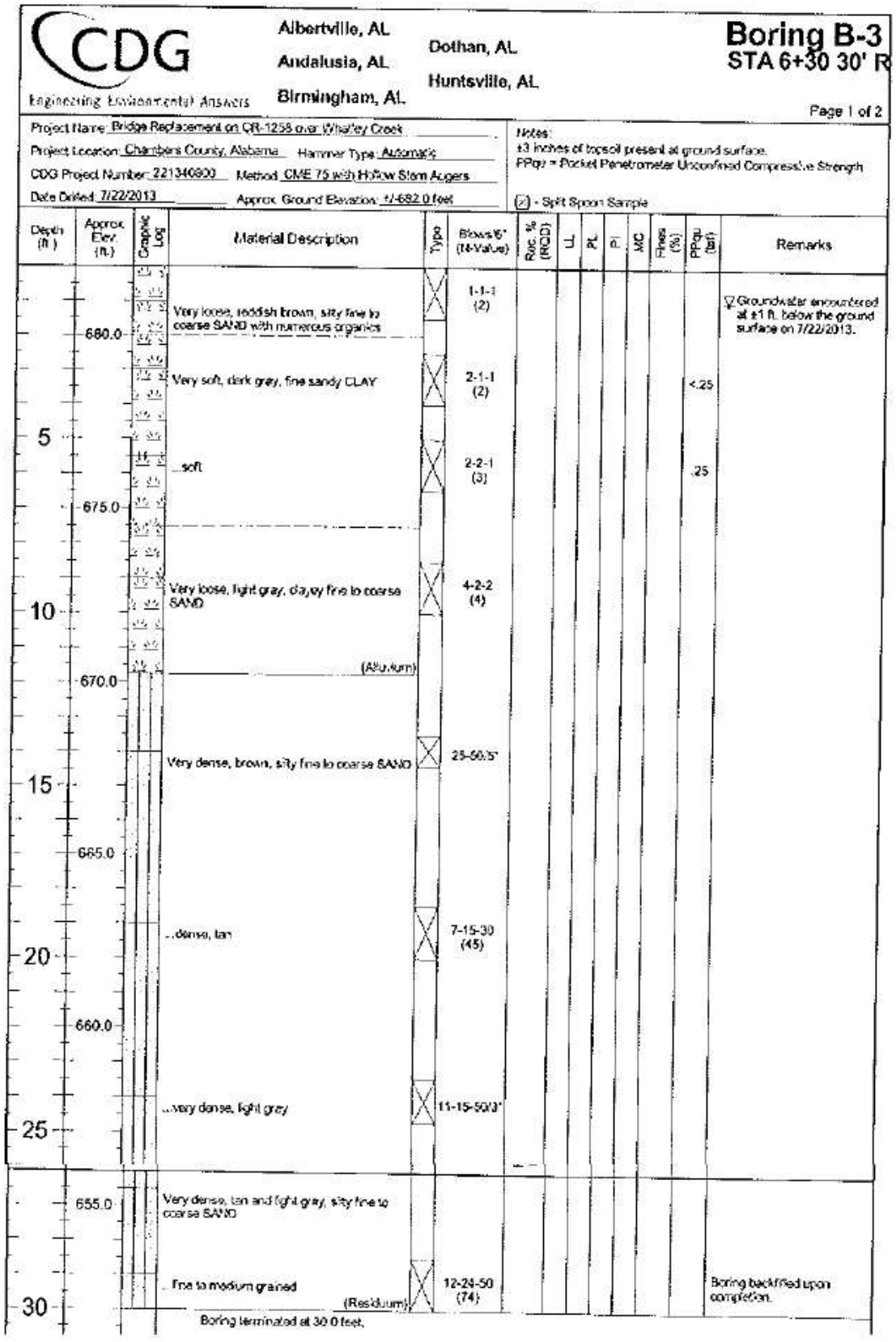

Figure B-3. Chambers County boring B-3 (25-30ft)

C. APPENDIX C: Tab Displacement

Chambers County Culvert

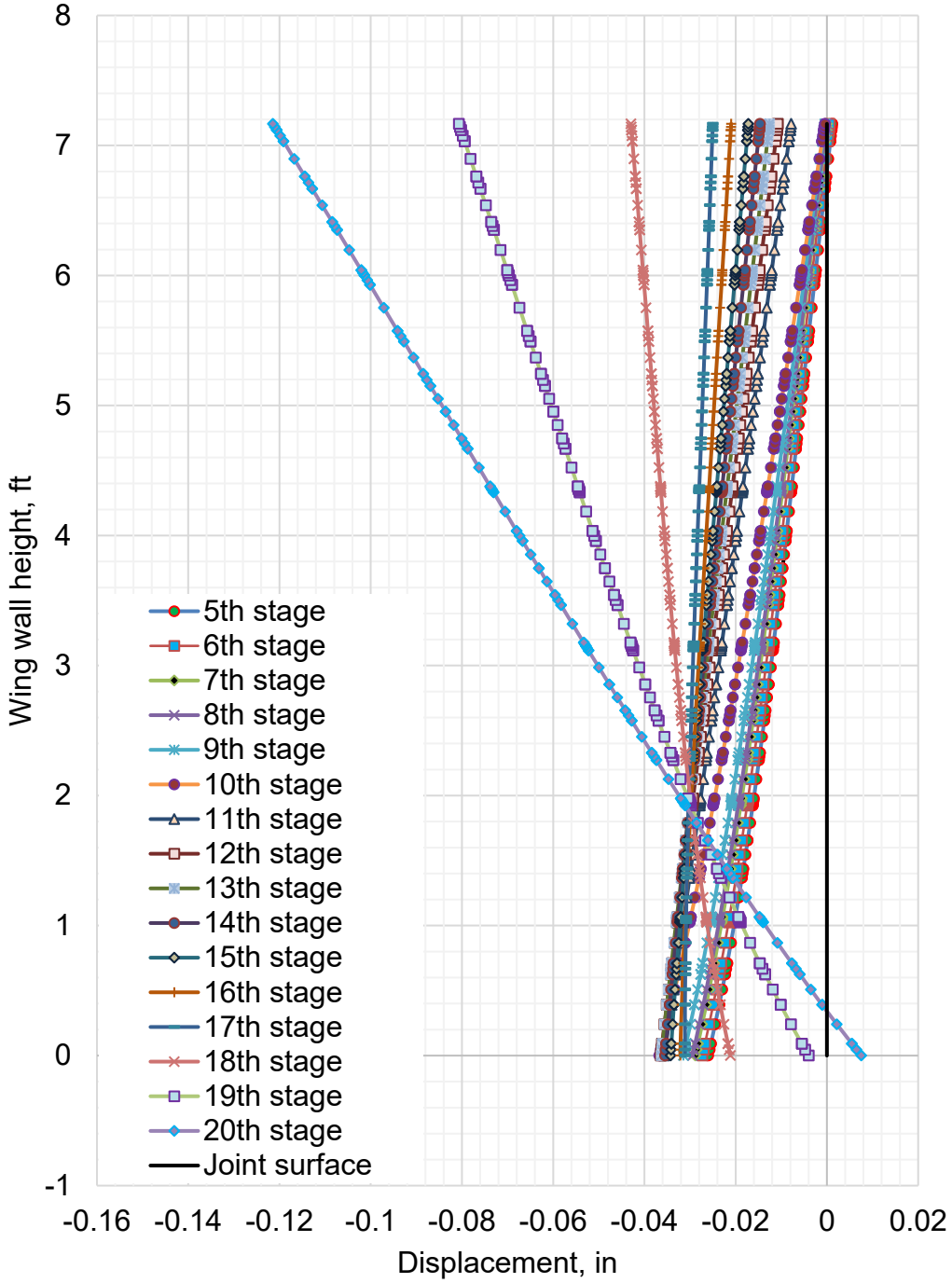

Figure C-1. Wing wall movement with scour development and 6-ft backfill over the culvert

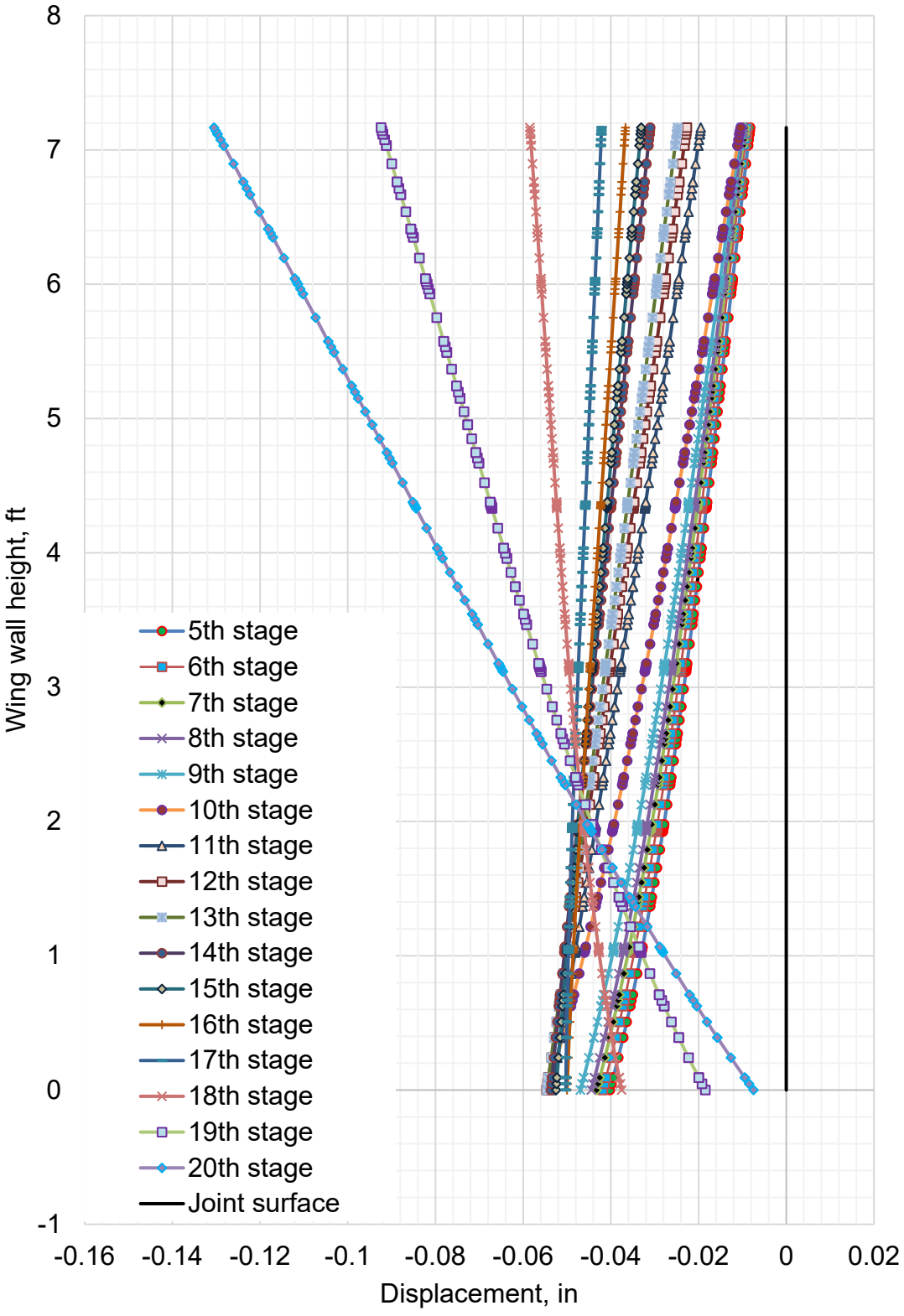

Figure C-2. Wing wall movement with scour development and 16-ft backfill over the culvert

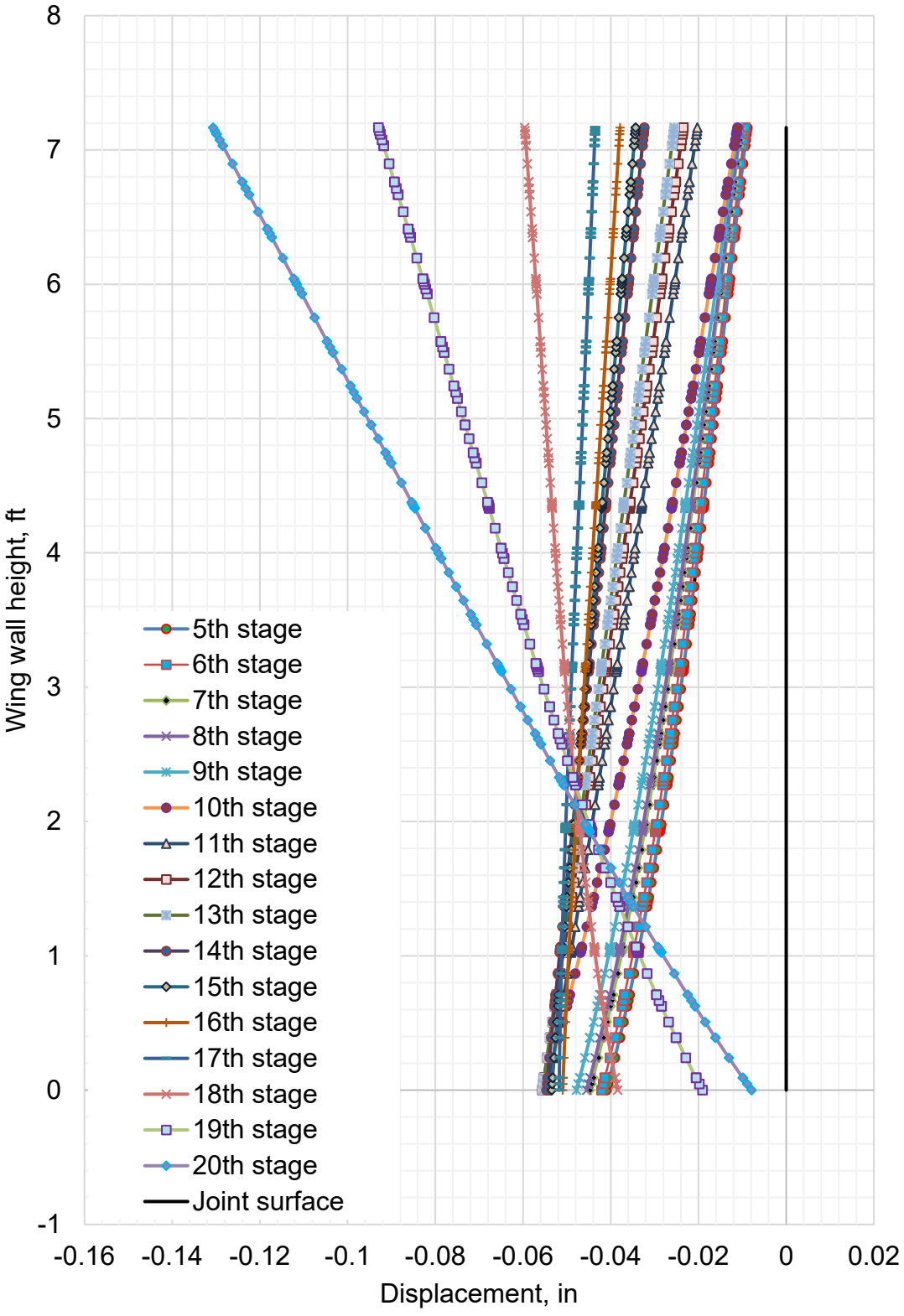

Figure C-3. Wing wall movement with scour development and 23-ft backfill over the culvert

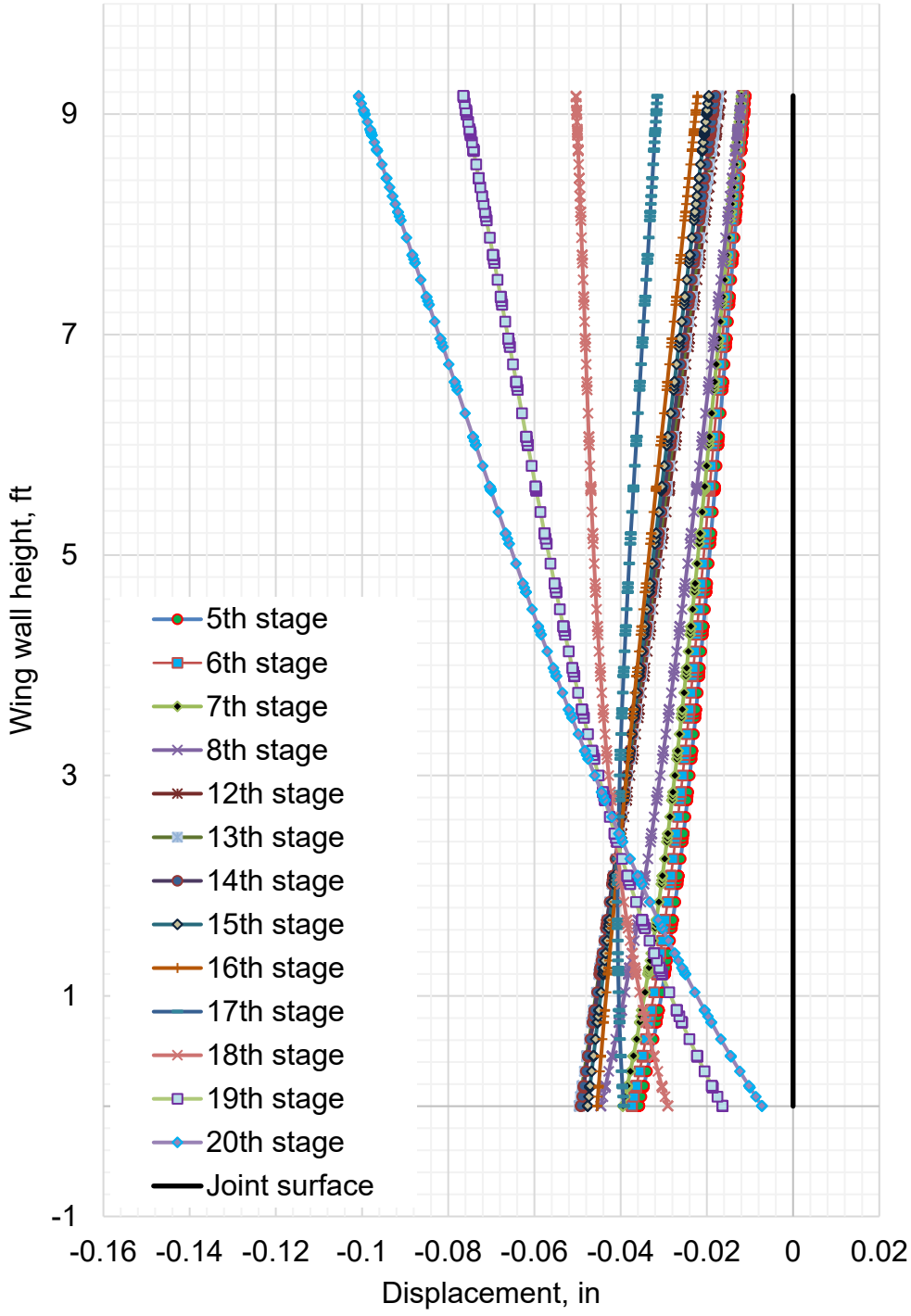

Figure C-4. Wing wall movement with scour development and 6-ft backfill over the culvert

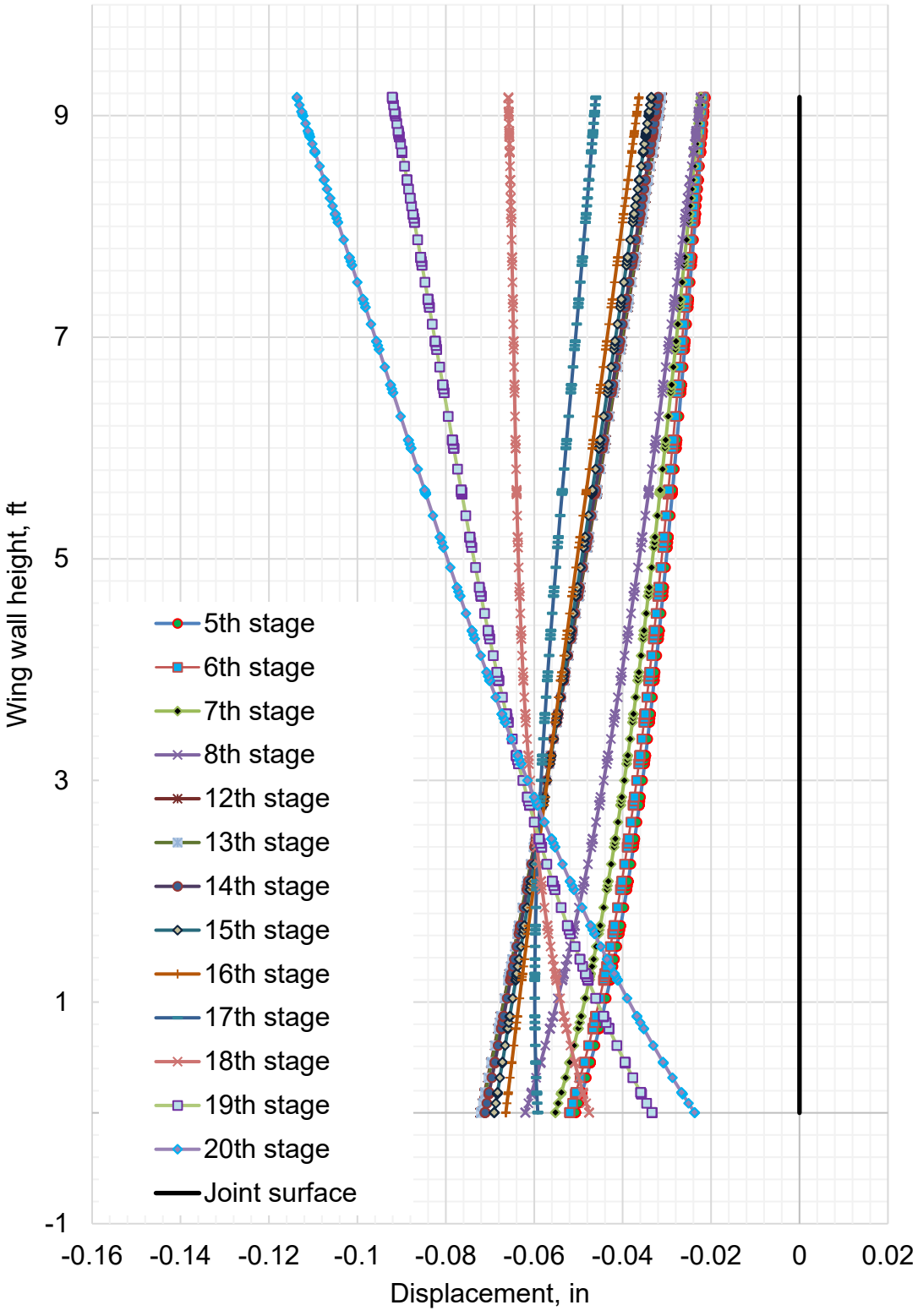

Figure C-5. Wing wall movement with scour development and 16-ft backfill over the culvert

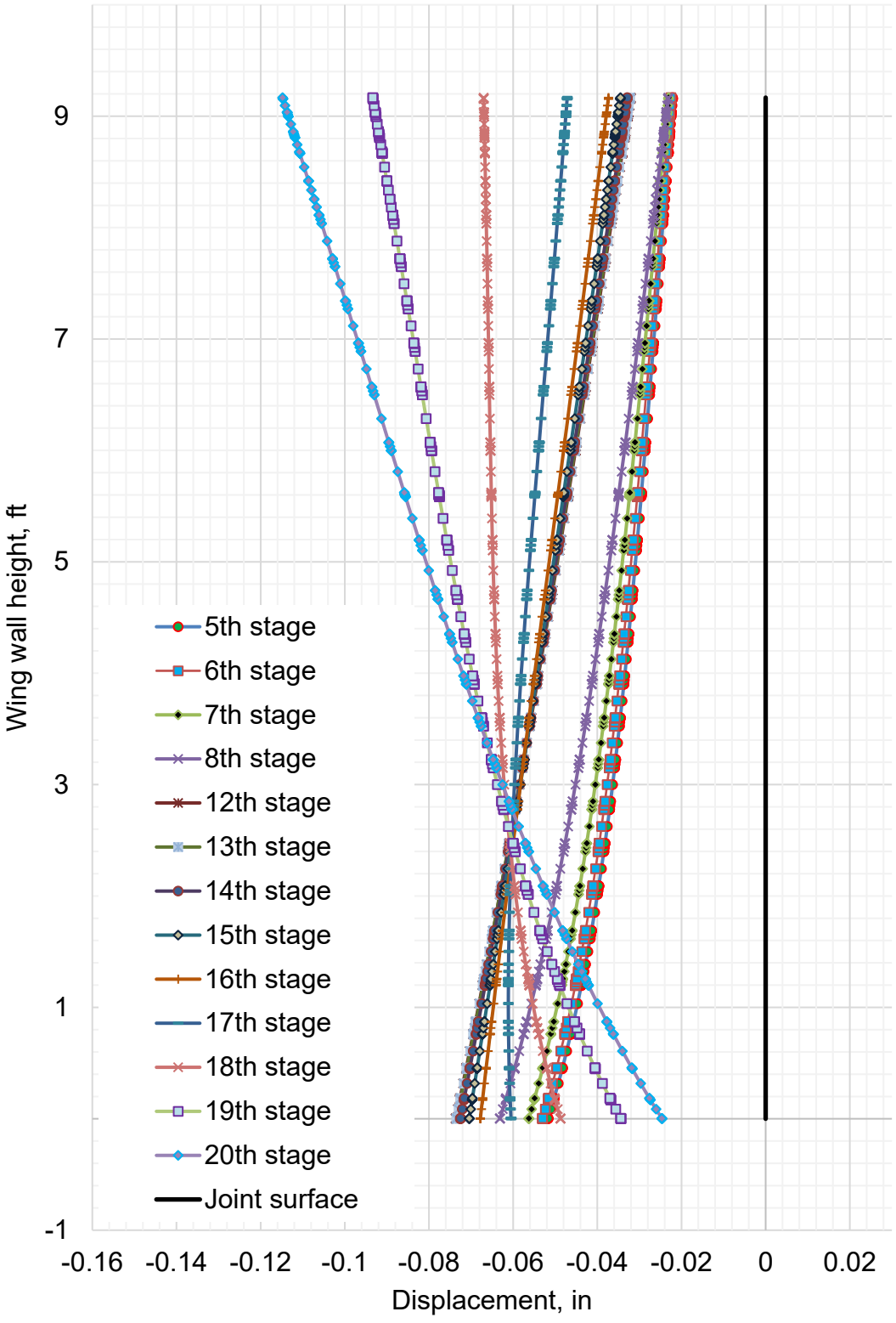

Figure C-6. Wing wall movement with scour development and 23-ft backfill over the culvert

Coosa County Culvert

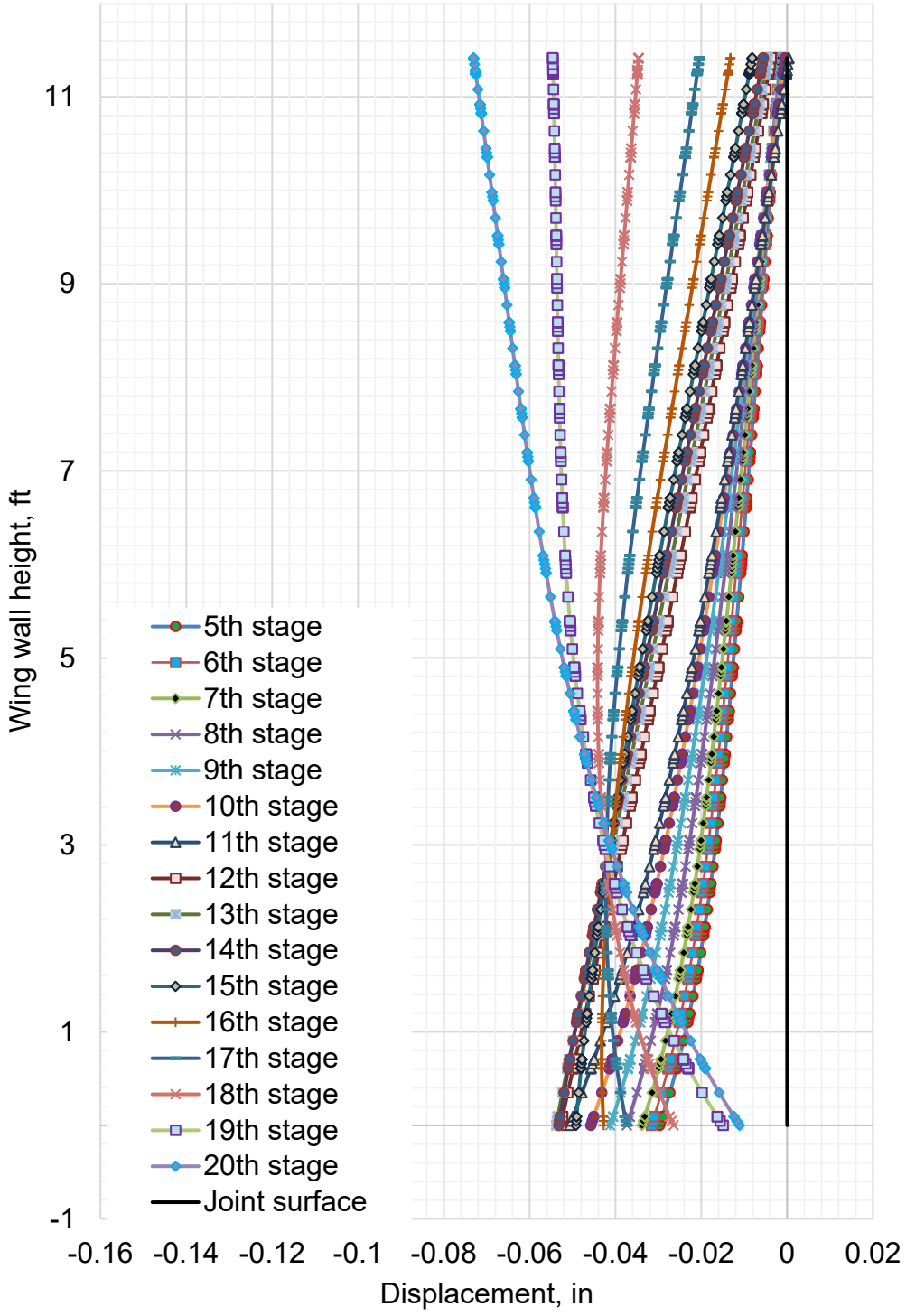

Figure C-7. Wing wall movement with scour development and 6-ft backfill over the culvert

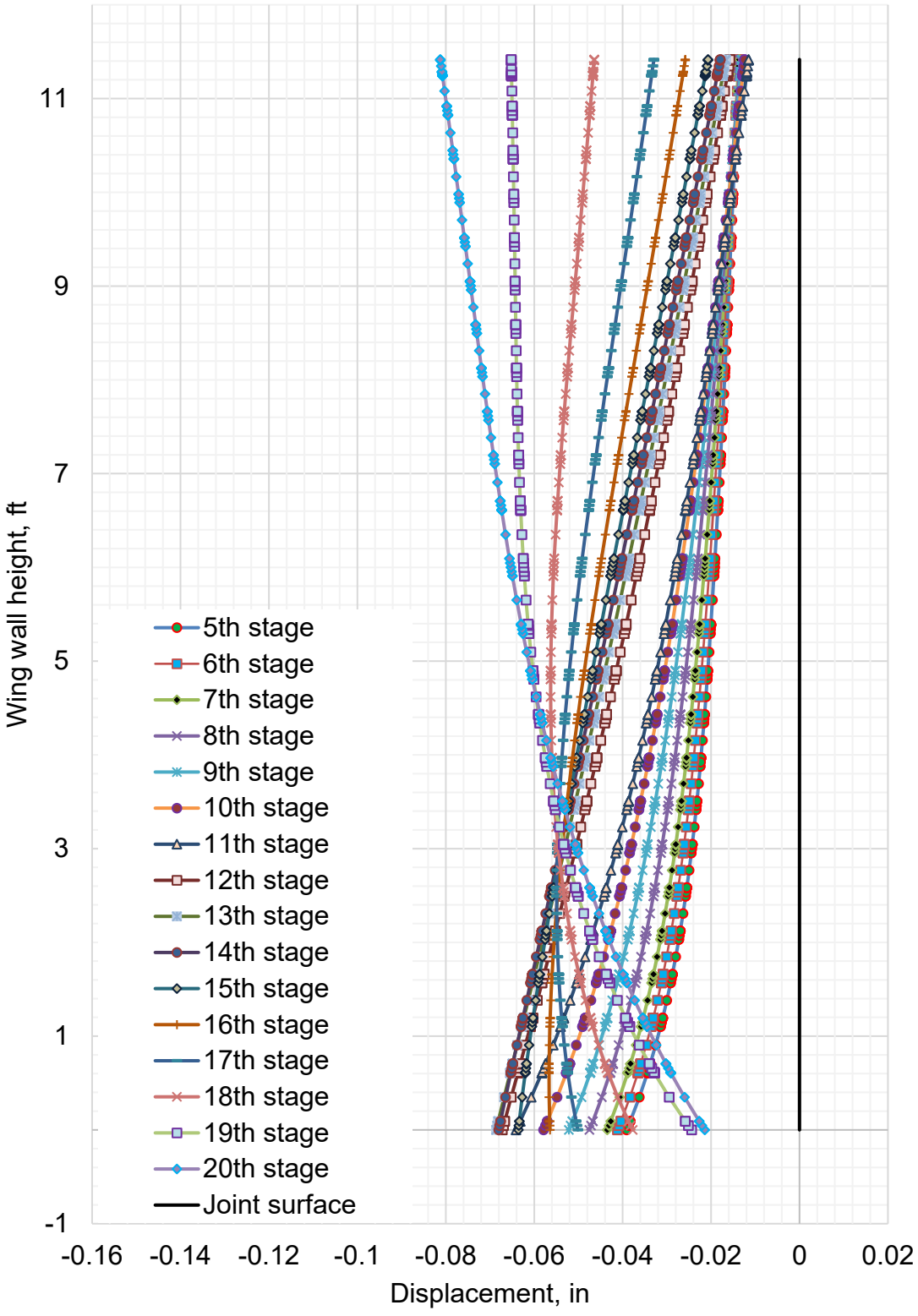

Figure C-8. Wing wall movement with scour development and 16-ft backfill over the culvert

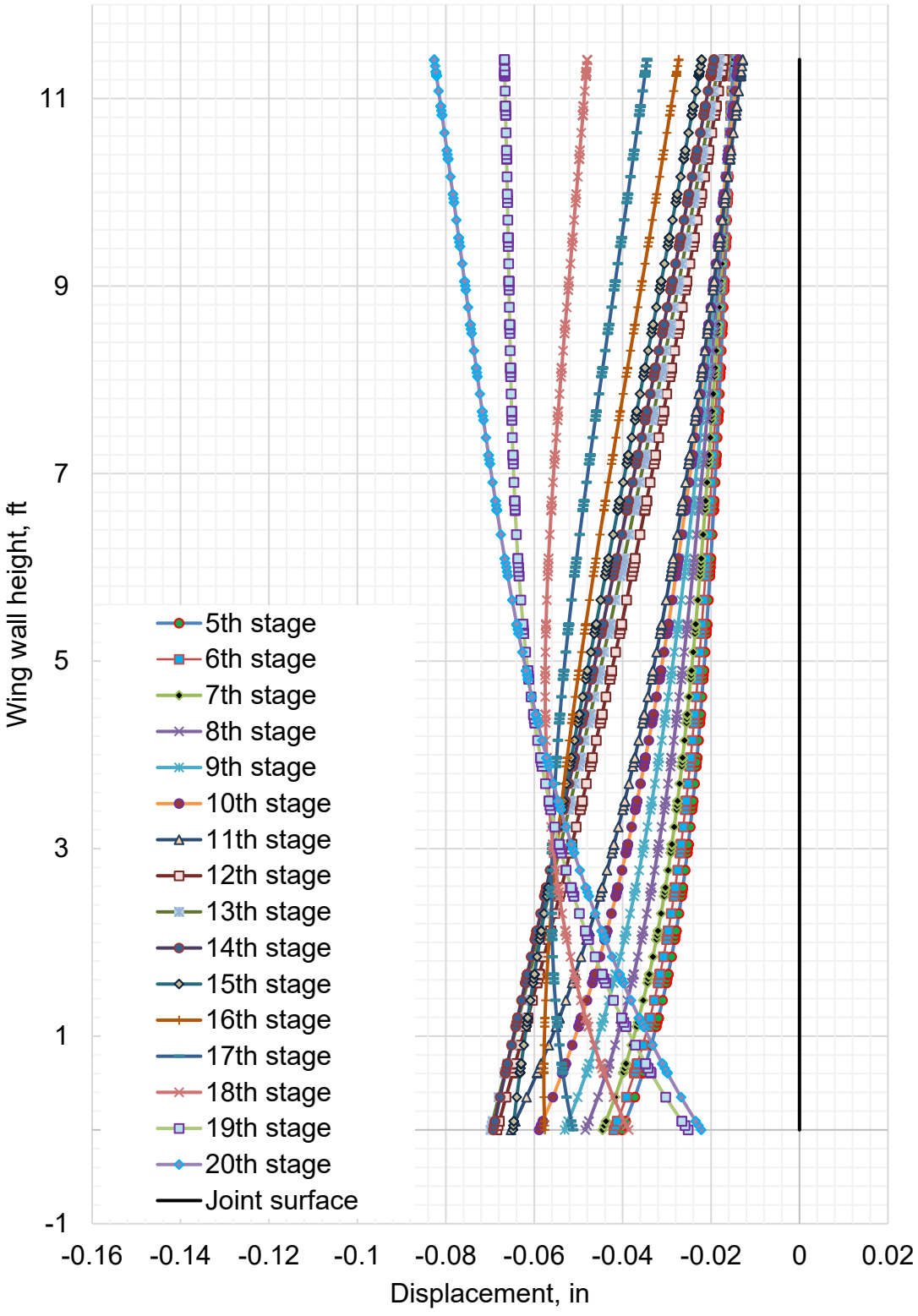

Figure C-9. Wing wall movement with scour development and 23-ft backfill over the culvert

D. APPENDIX D: Development of Stresses

Chambers County Culvert

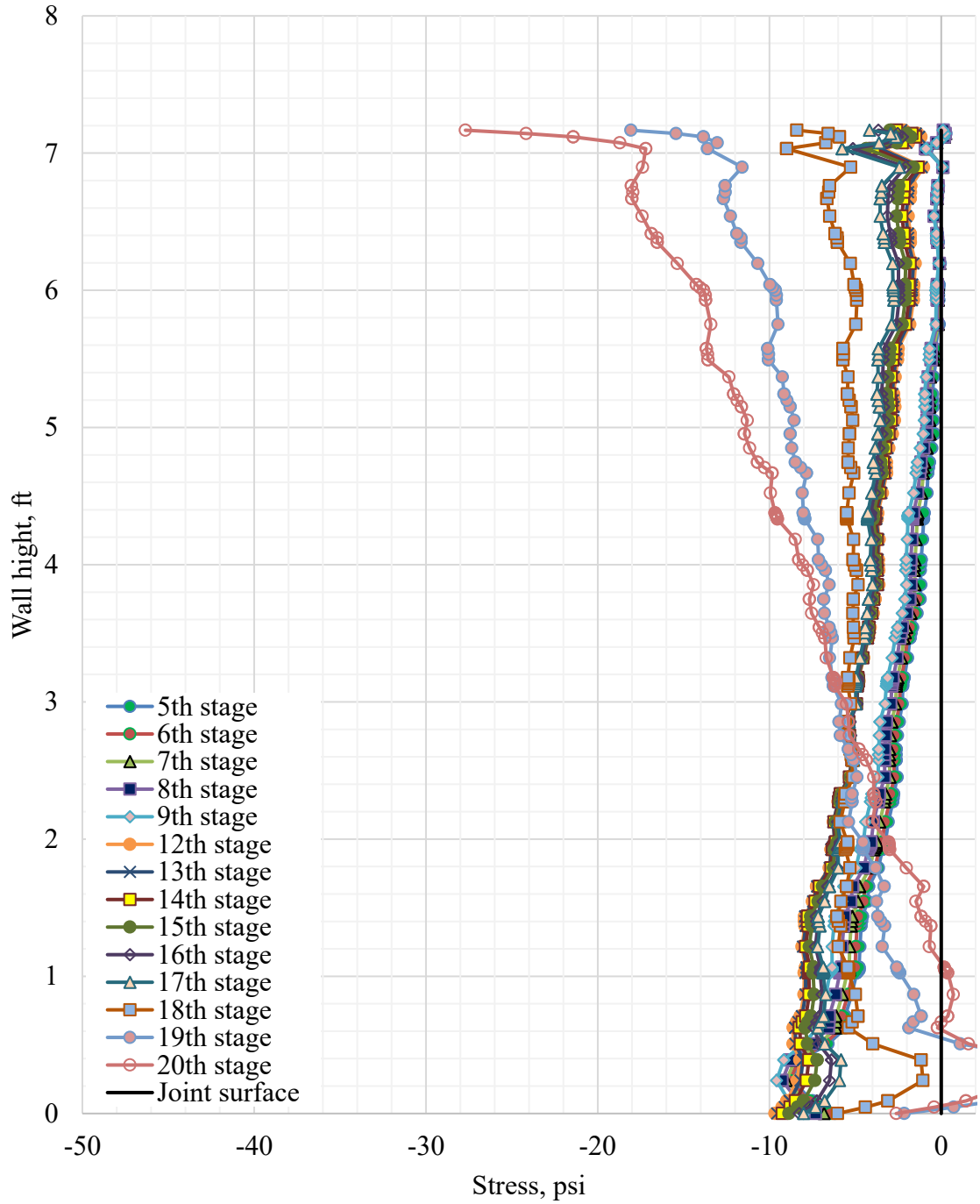

Figure D-1. Stresses along the tab surface with scour development and 6-ft backfill over the culvert

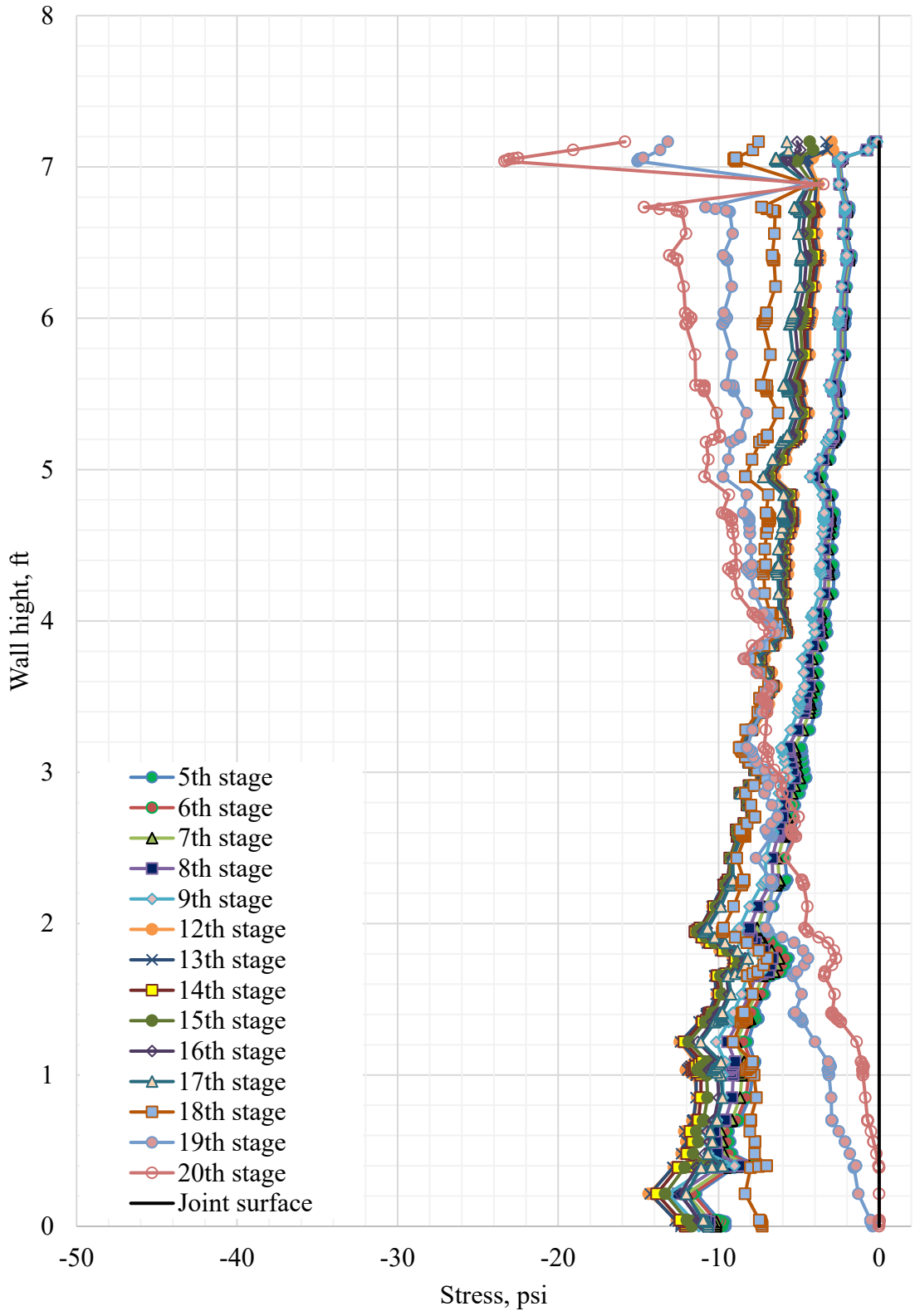

Figure D-2. Stresses along the tab surface with scour development and 16-ft backfill over the culvert

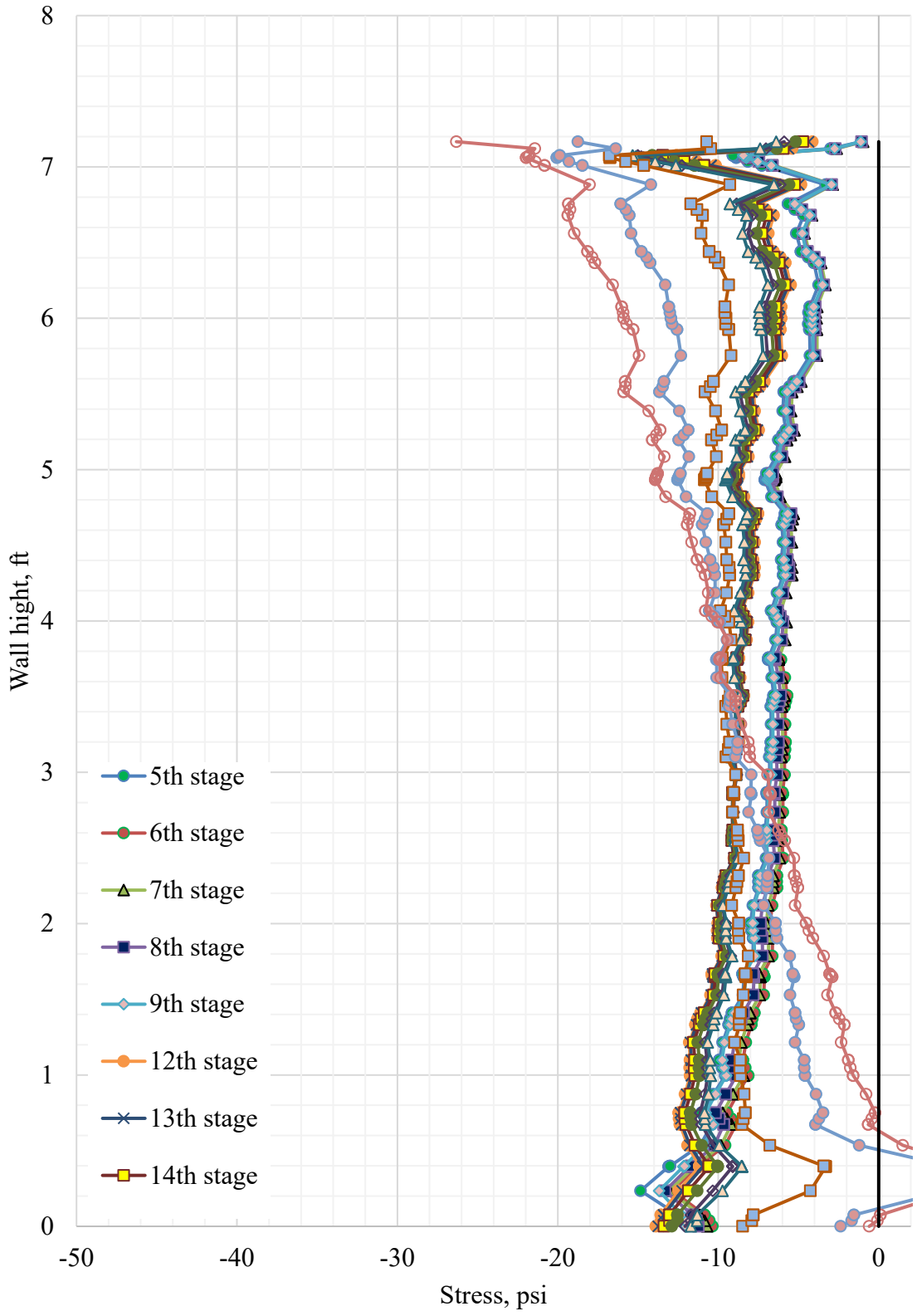

Figure D-3. Stresses along the tab surface with scour development and 23-ft backfill over the culvert

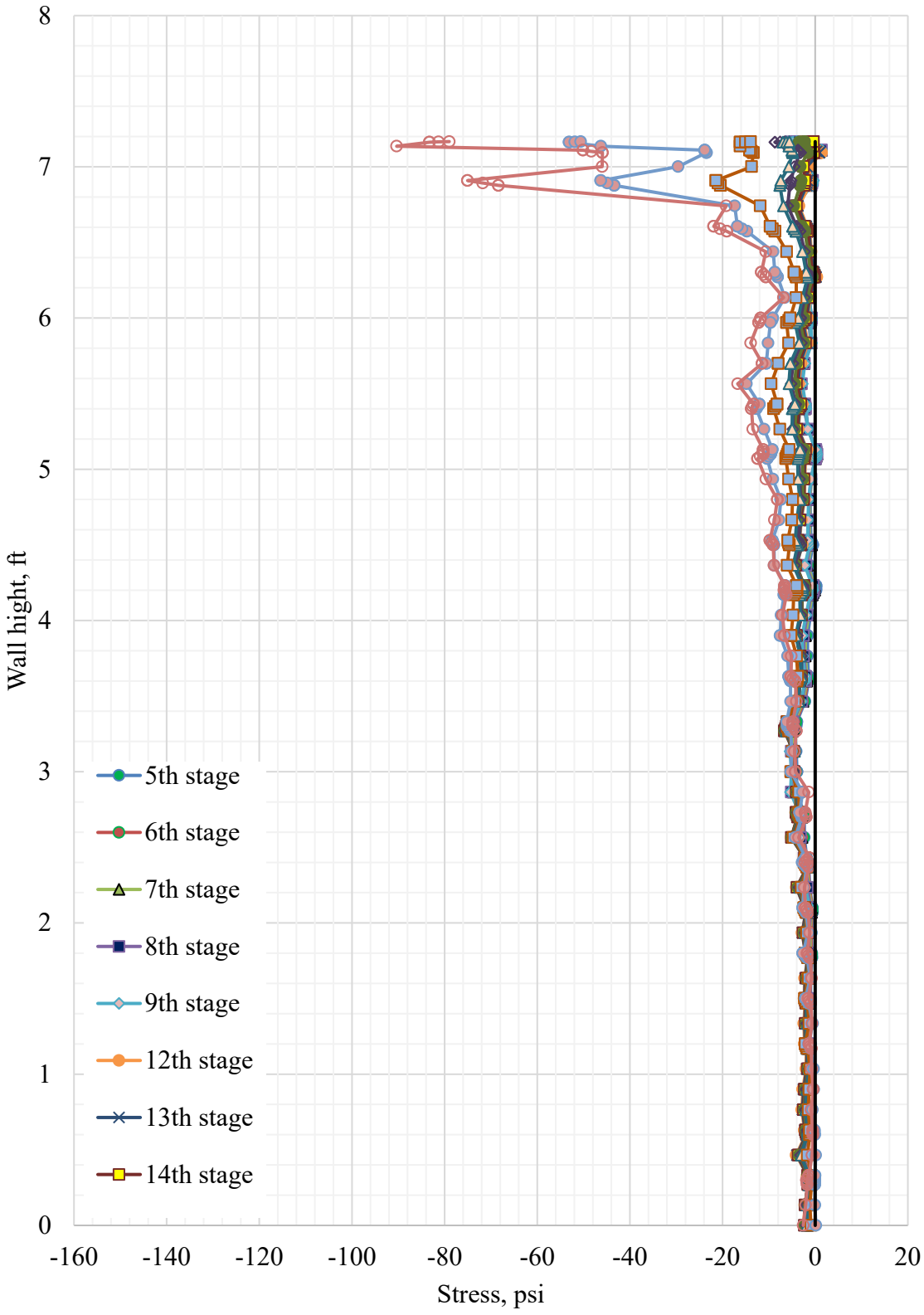

Figure D-4. Stresses along the tab extension with the locked tabs and 6-ft backfill over the culvert

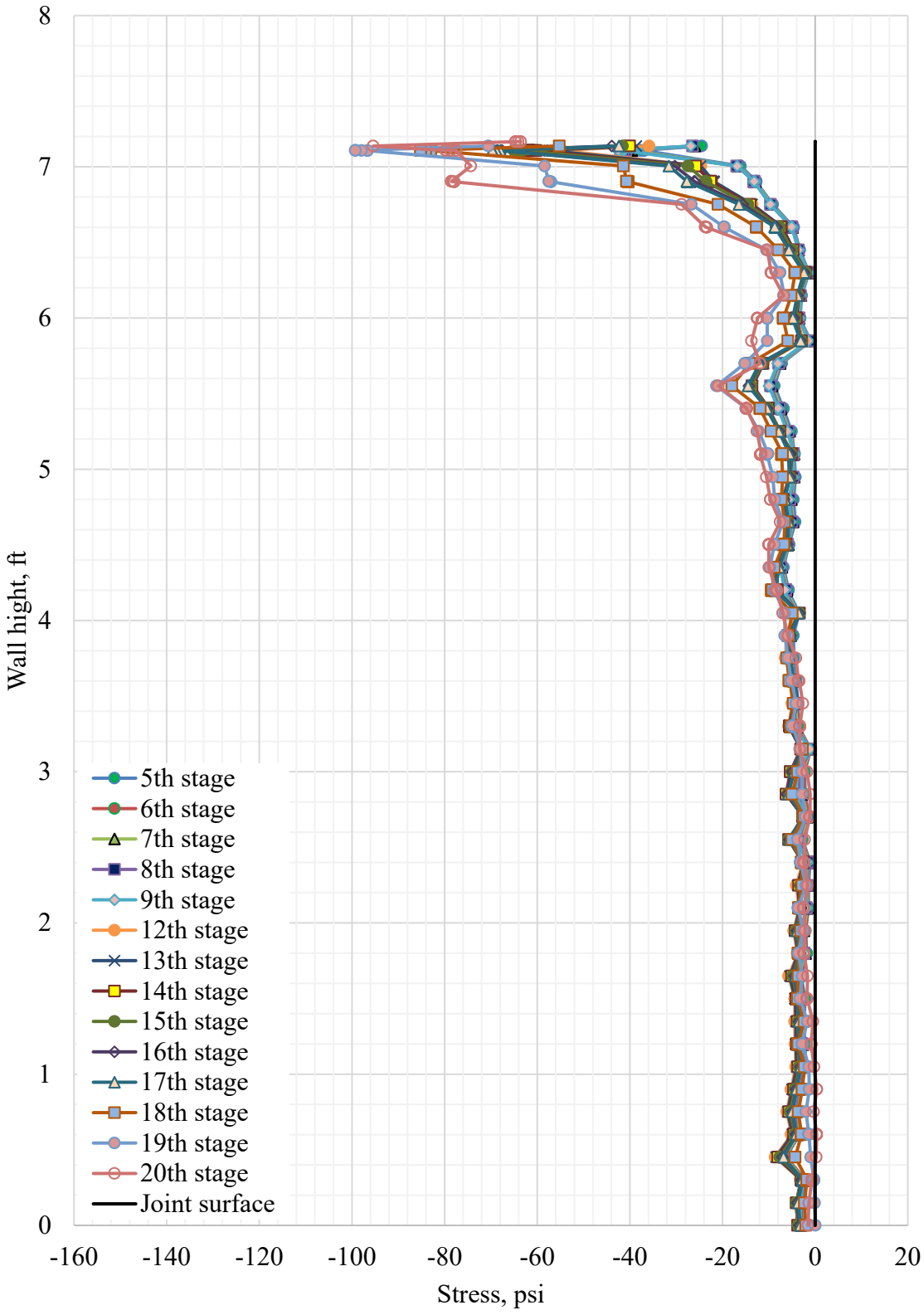

Figure D-5. Stresses along the tab extension with the locked tabs and 16-ft backfill over the culvert

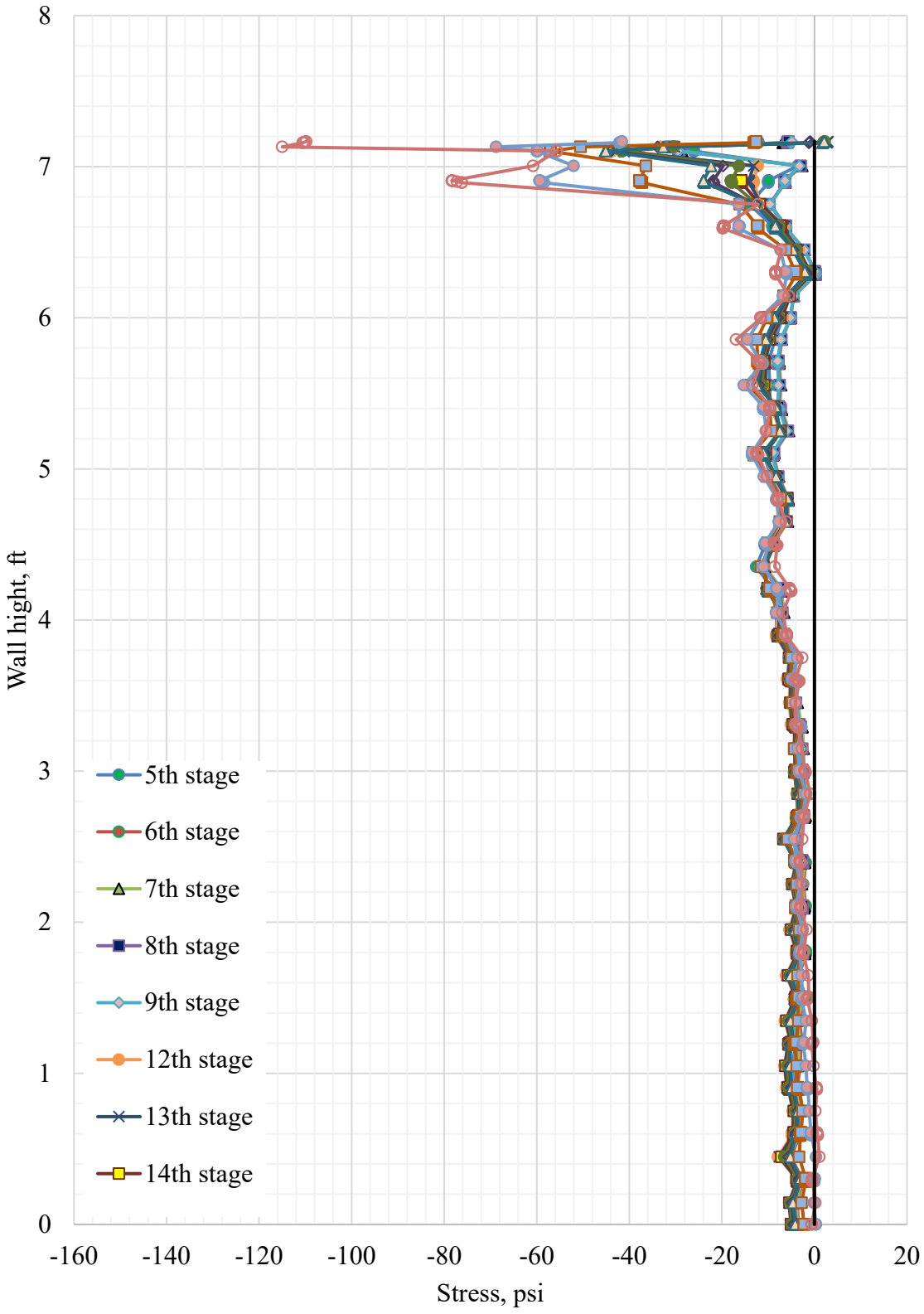

Figure D-6. Stresses along the tab extension with the locked tabs and 23-ft backfill over the culvert

Lee County Culvert

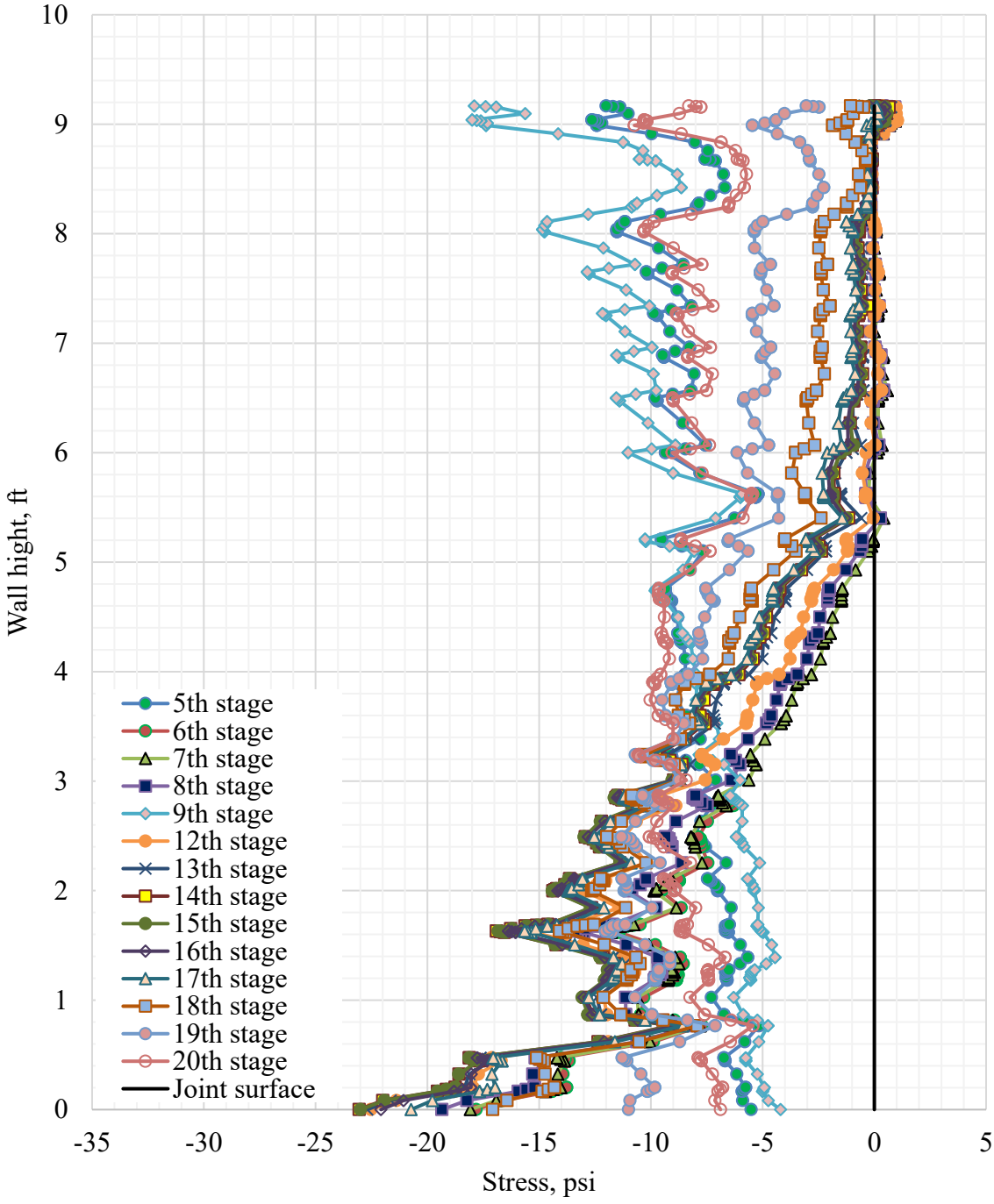

Figure D-7. Stresses along the tab surface with scour development and 6-ft backfill over the culvert

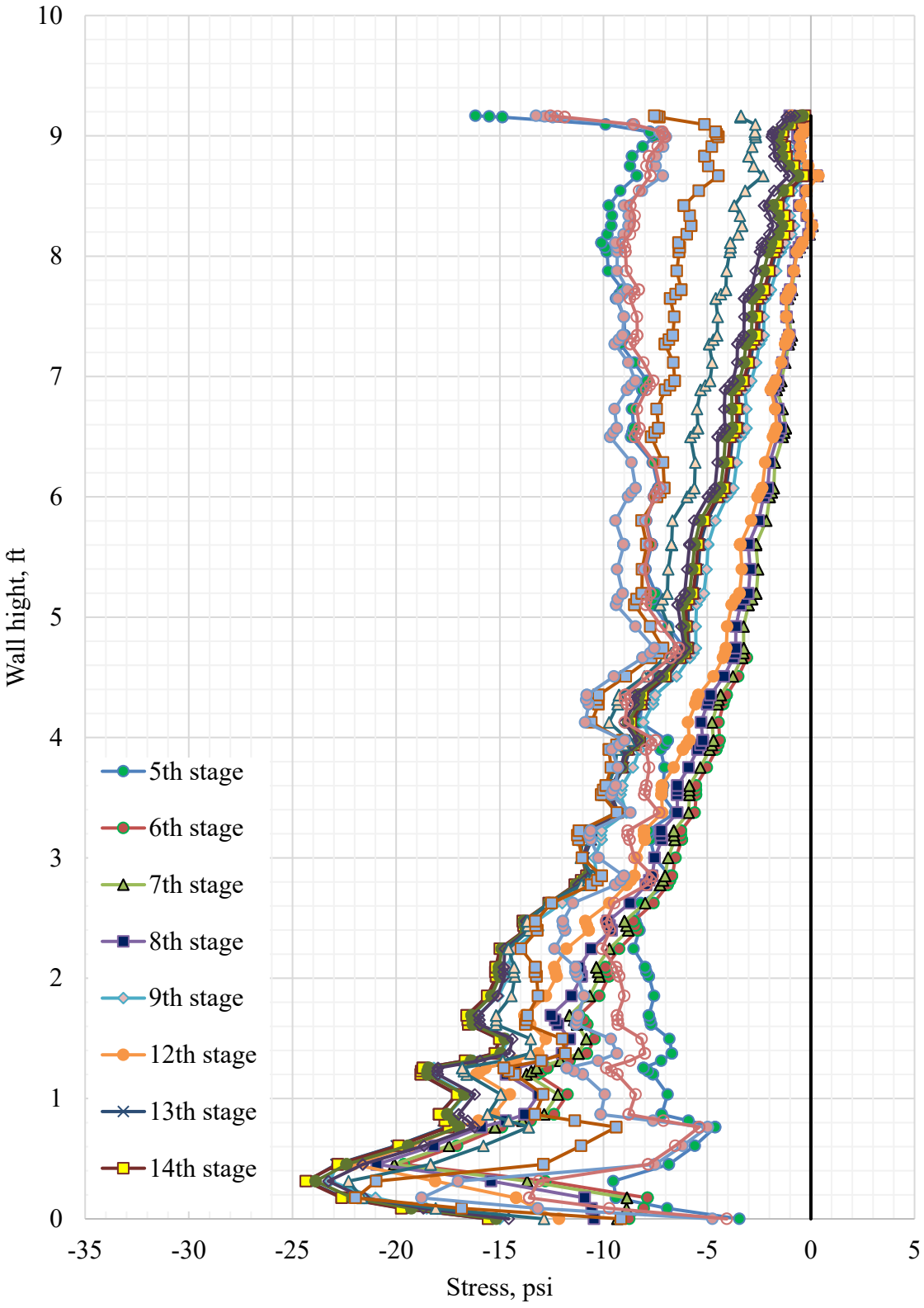

Figure D-8. Stresses along the tab surface with scour development and 16-ft backfill over the culvert

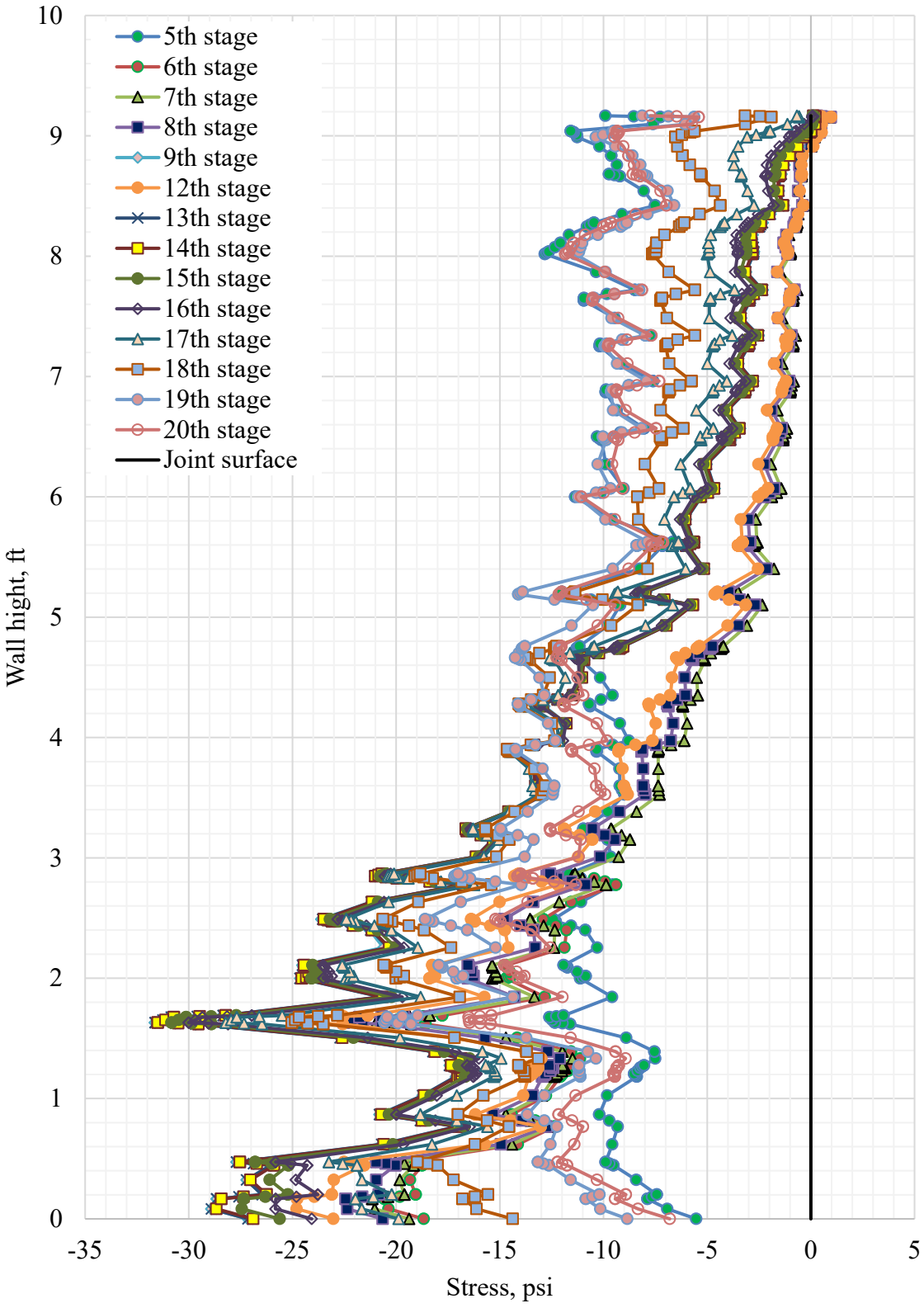

Figure D-9. Stresses along the tab surface with scour development and 23-ft backfill over the culvert

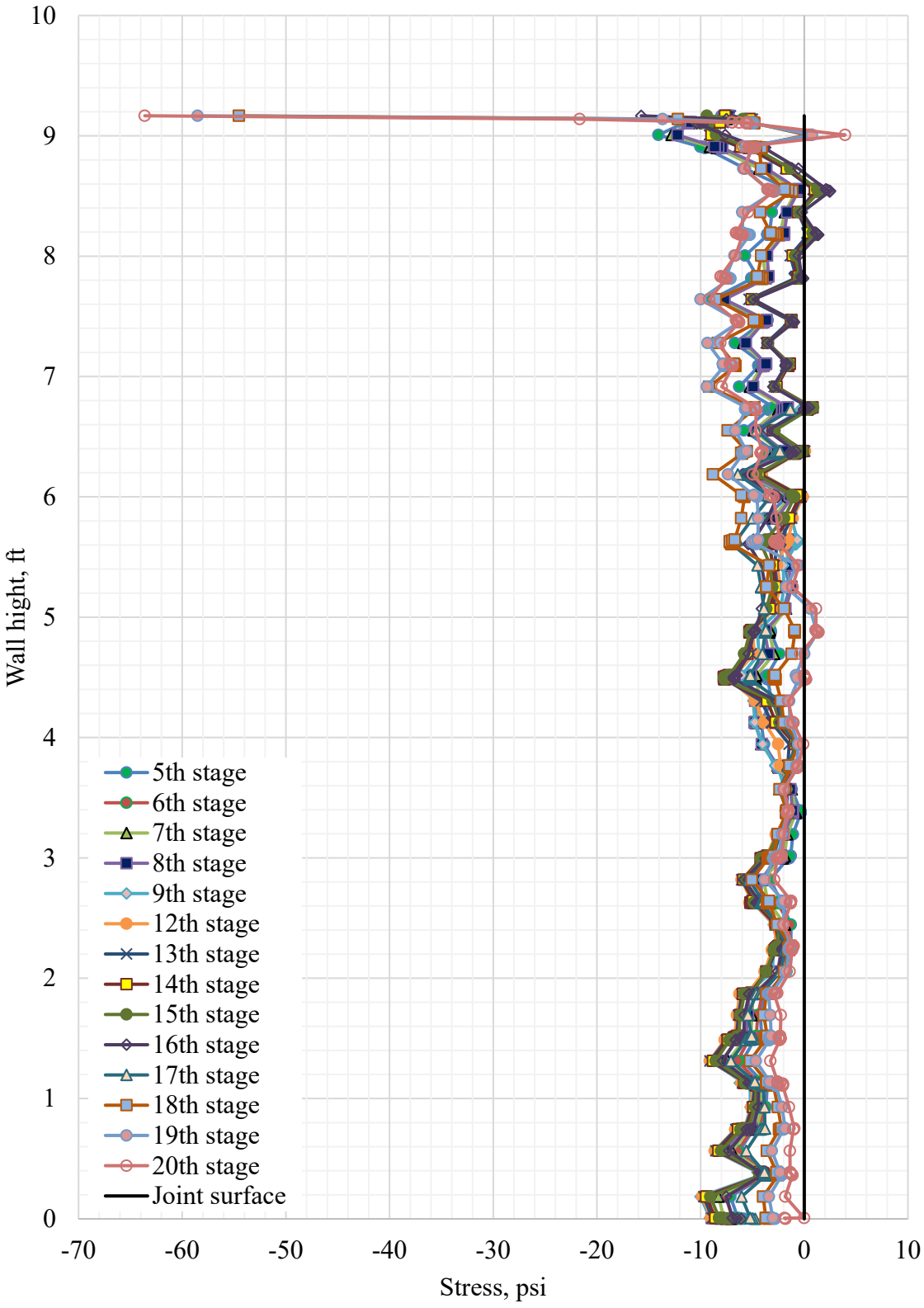

Figure D-10. Stresses along the tab extension with the locked tabs and 6-ft backfill over the culvert

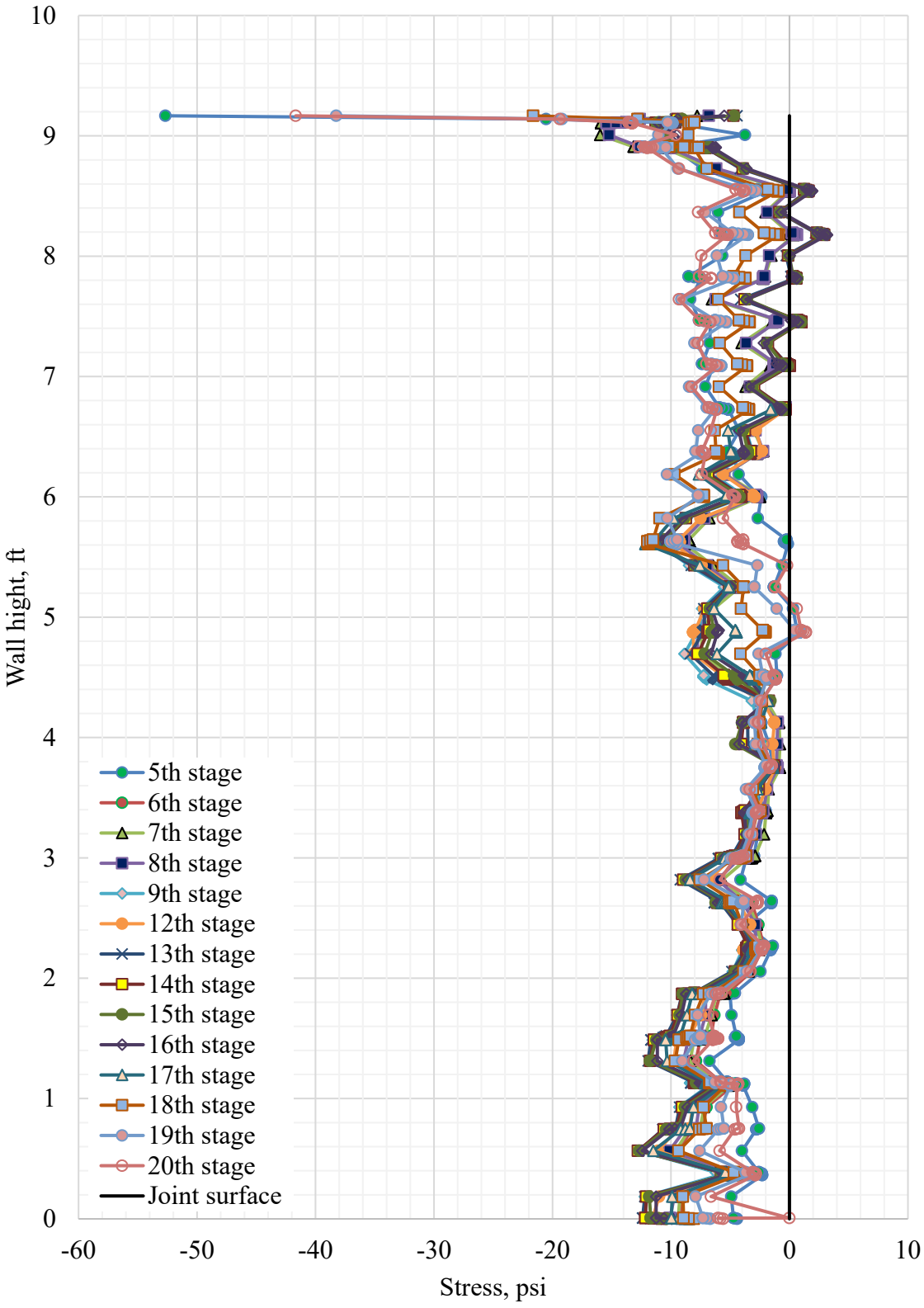

Figure D-11. Stresses along the tab extension with the locked tabs and 16-ft backfill over the culvert

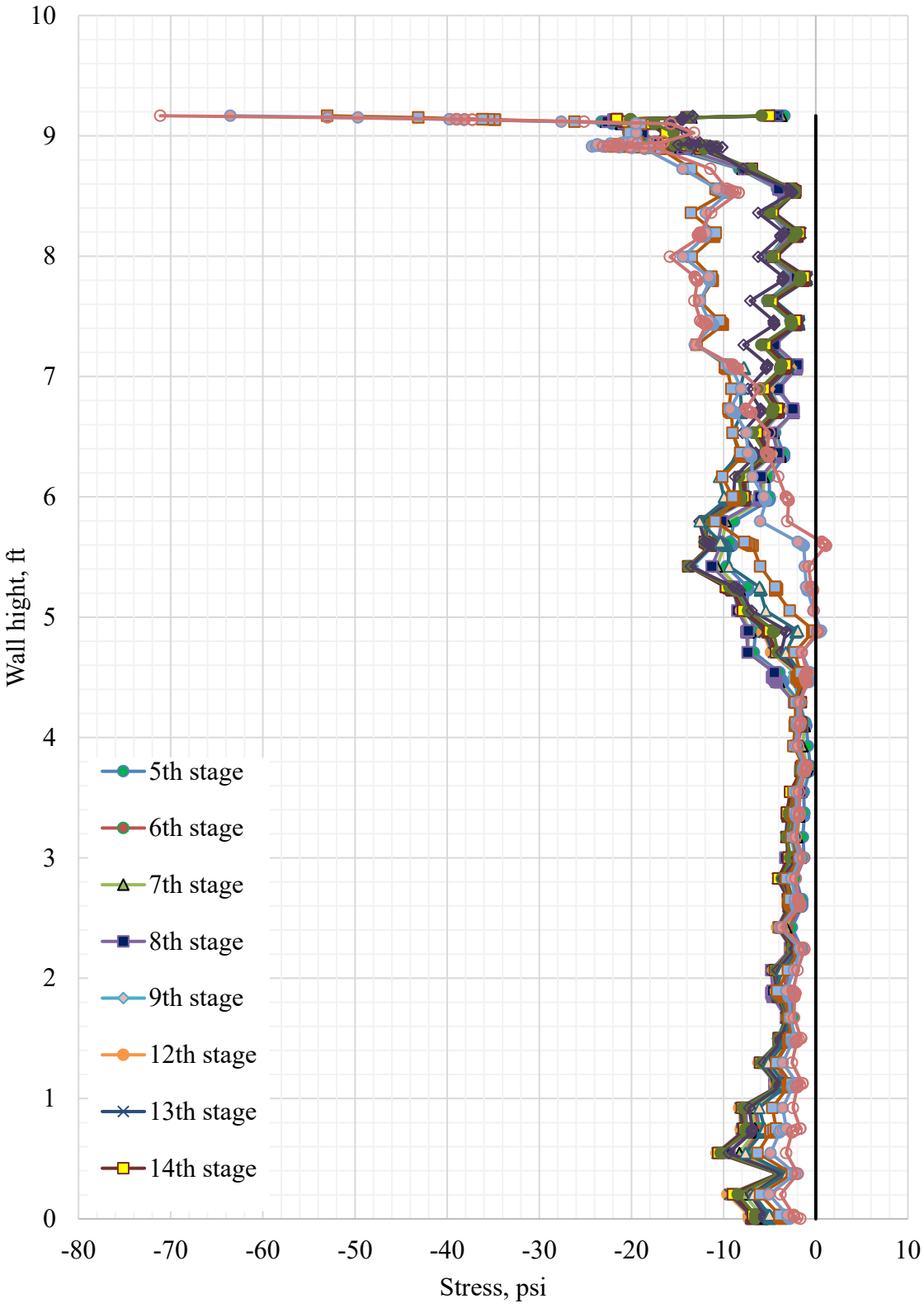

Figure D-12. Stresses along the tab extension with the locked tabs and 23-ft backfill over the culvert

Coosa County Culvert

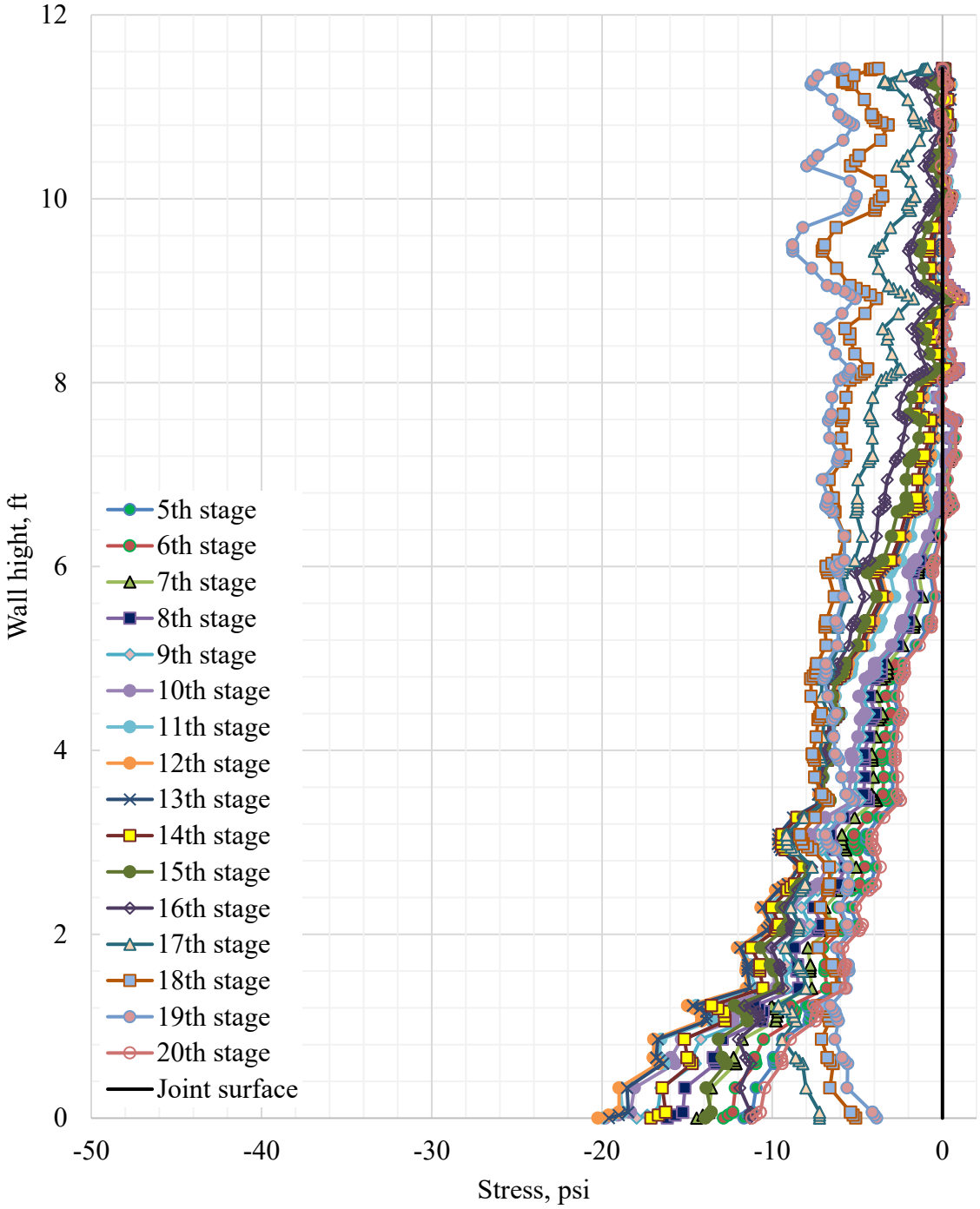

Figure D-13. Stresses along the tab surface with scour development and 6-ft backfill over the culvert

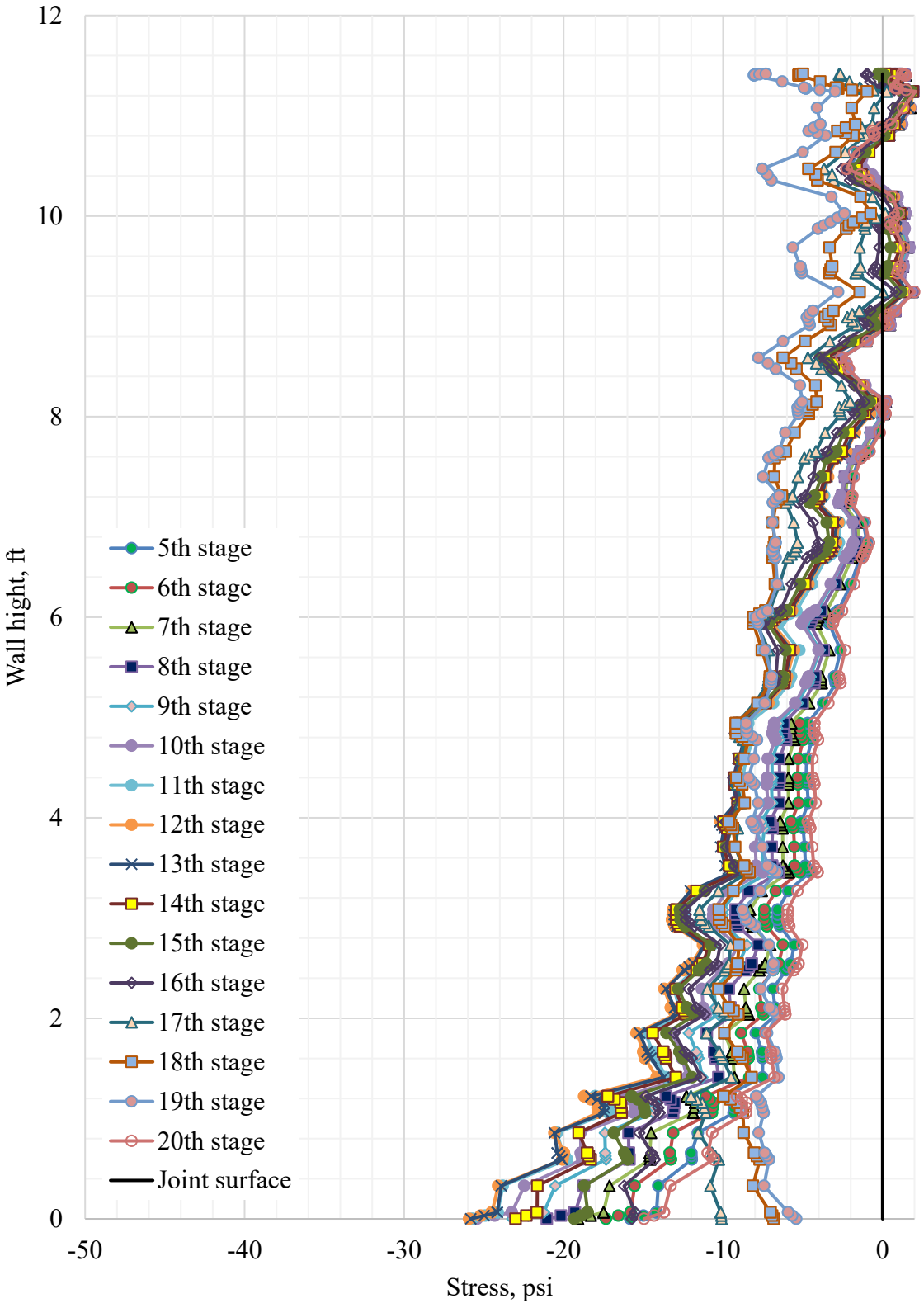

Figure D-14. Stresses along the tab surface with scour development and 16-ft backfill over the culvert

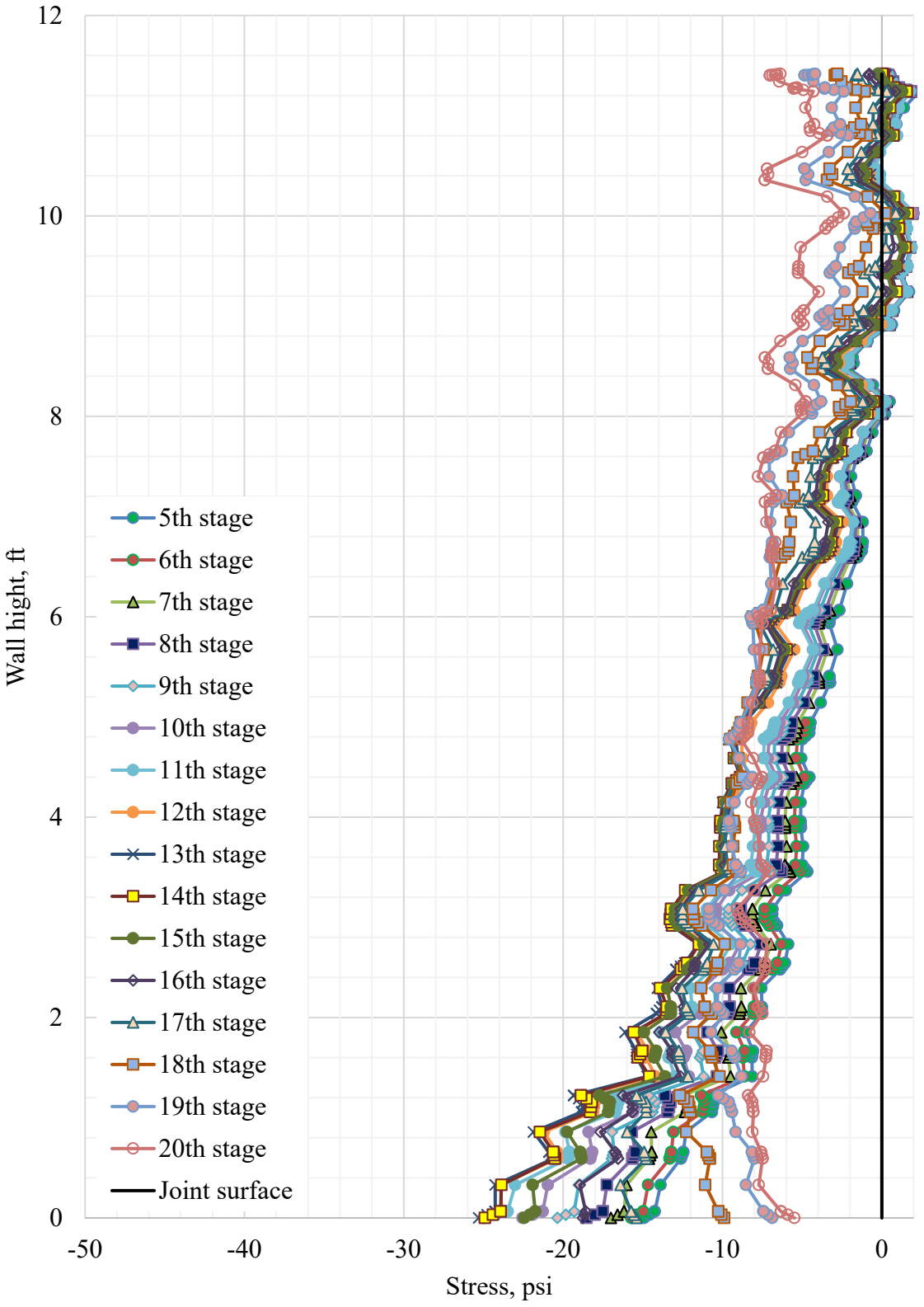

Figure D-15. Stresses along the tab surface with scour development and 23-ft backfill over the culvert

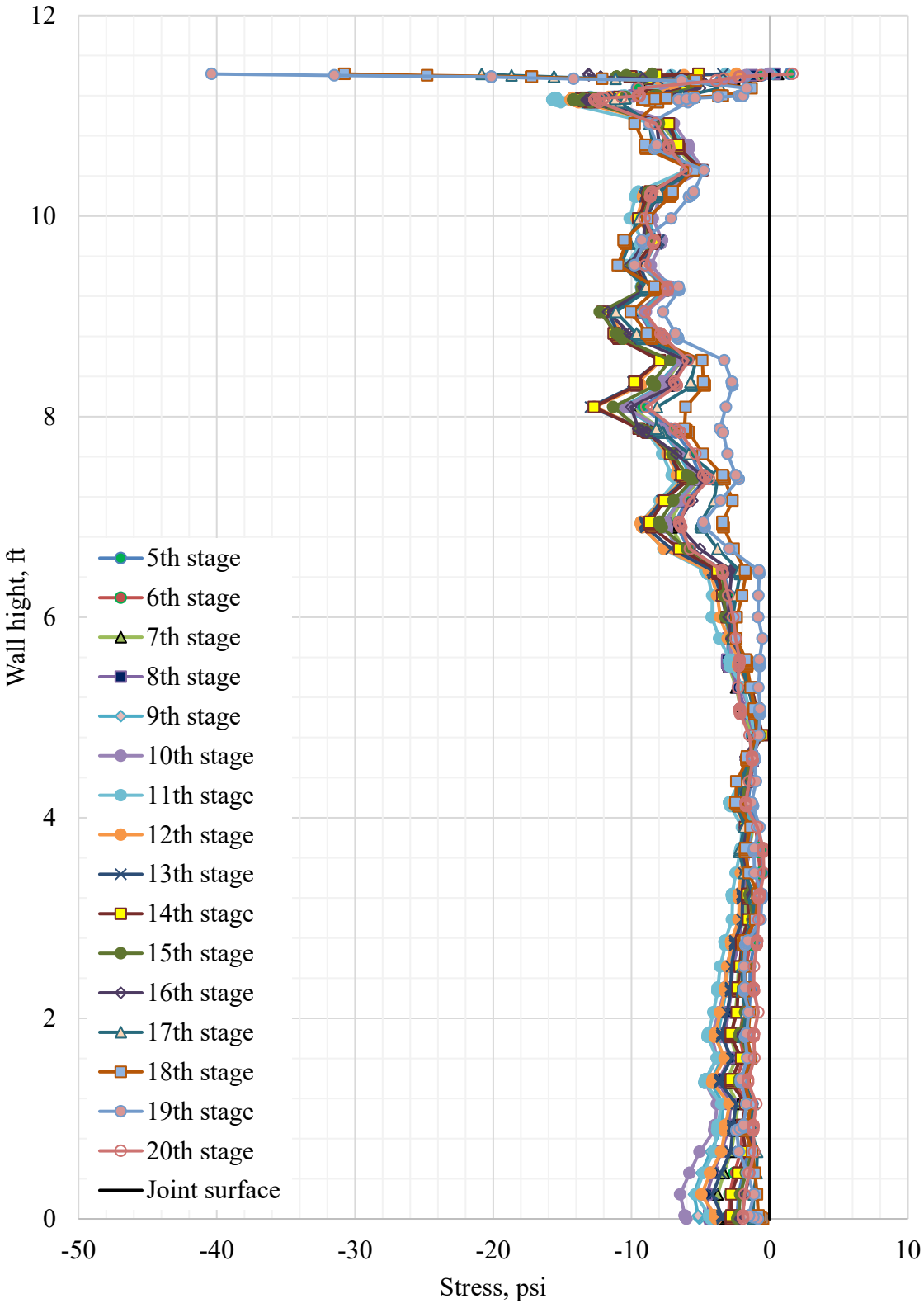

Figure D-16. Stresses along the tab extension with the locked tabs and 6-ft backfill over the culvert

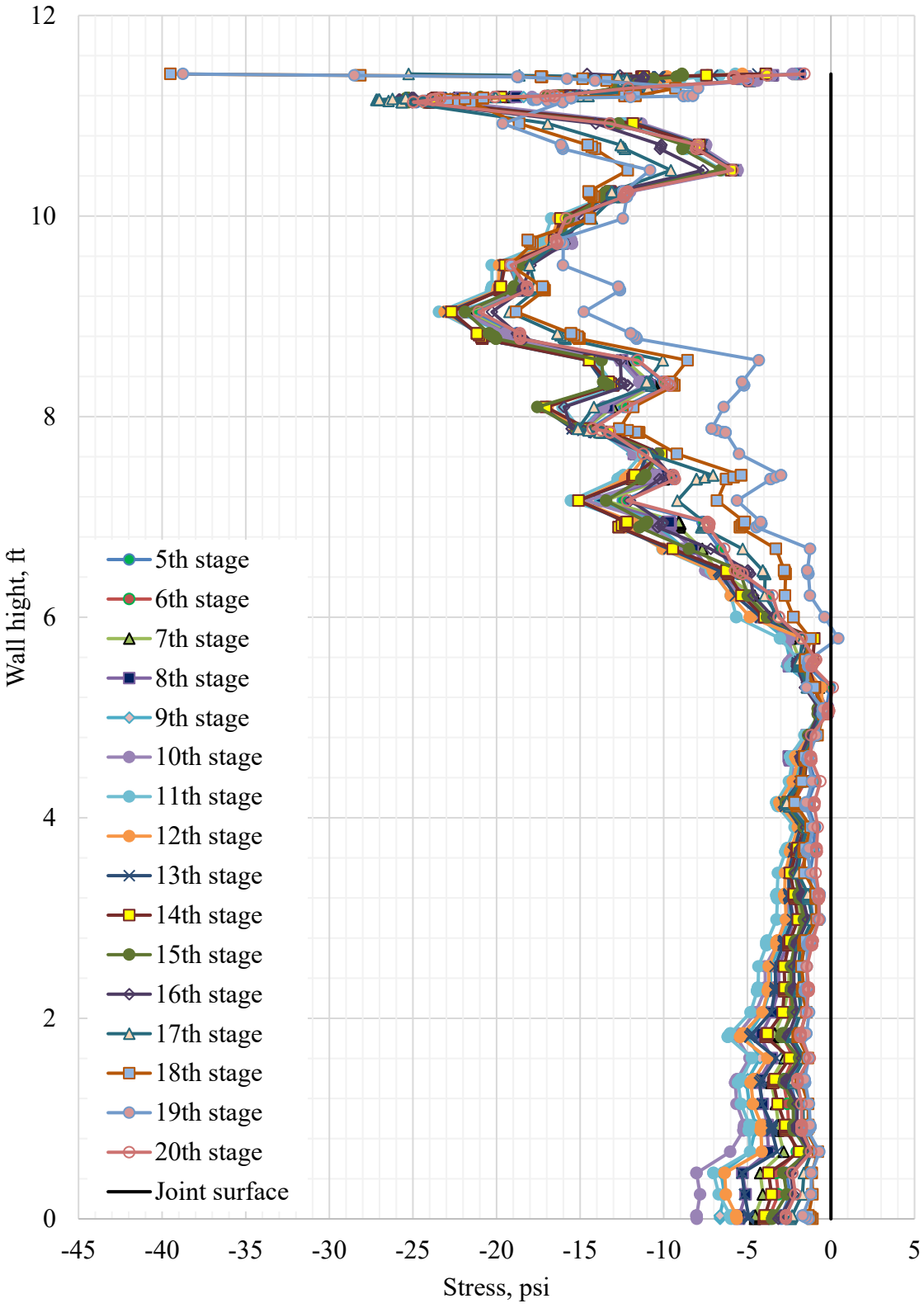

Figure D-17. Stresses along the tab extension with the locked tabs and 16-ft backfill over the culvert

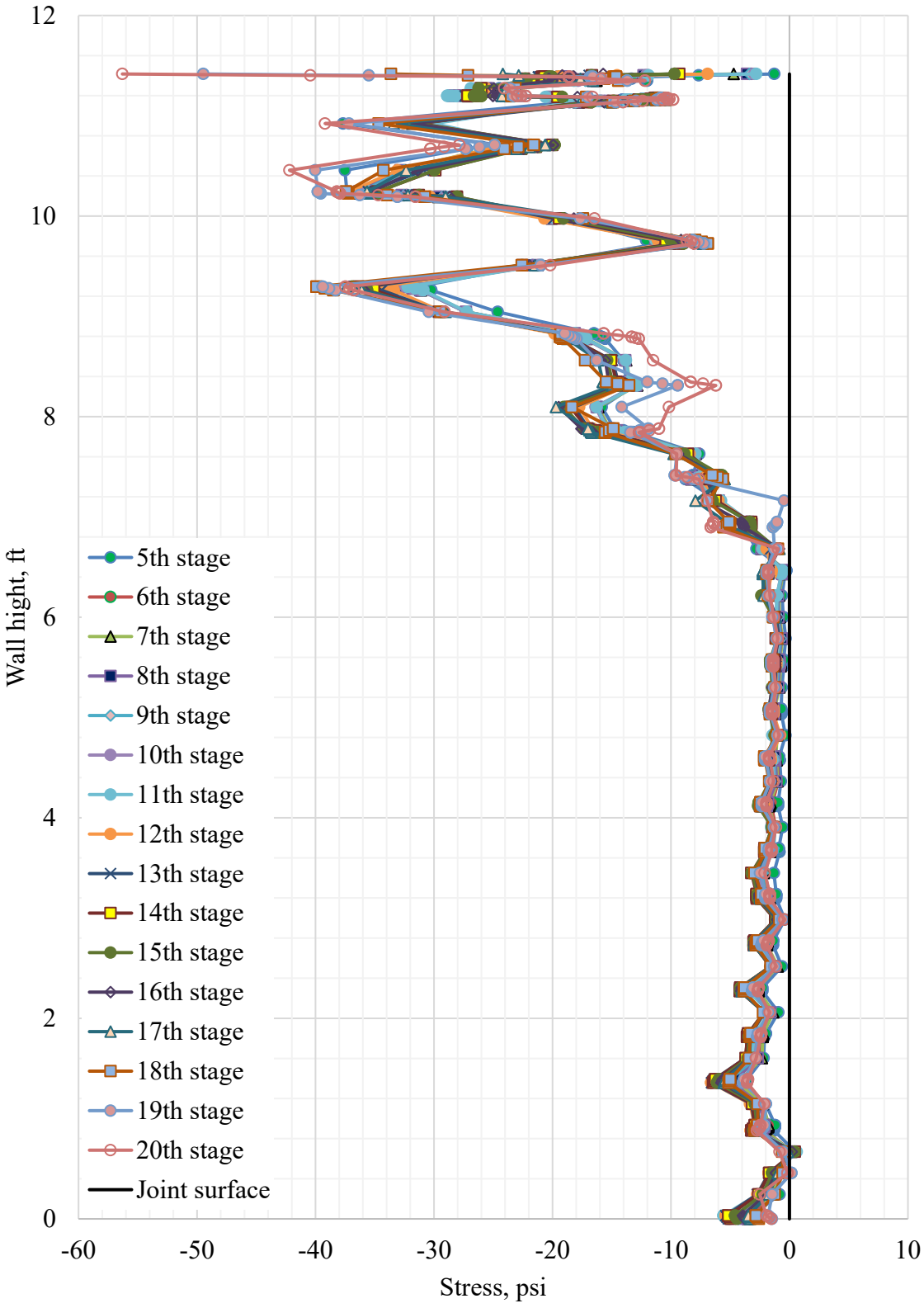

Figure D-18. Stresses along the tab extension with the locked tabs and 23-ft backfill over the culvert

E. APPENDIX E: Summarized Maximum Pressure in the Tab

Table E-1. Summarized compression stresses in the tab, psi.

			Steps of analysis					
								Scour
			Design Load					
			1	2	3	4	5	6
Type of measurments	Culvert location	Backfill height (ft)	No backfill	0-ft	0+truck load	+6-ft	+16-ft	+23-ft
Measured on the field	Chambers County			-5.7				
	Lee County			-11.2	-19.0			
	Coosa County			-6.9				
Calculated with backfill load	Chambers County		-1.3	-4.6	-10.3	-9.3	-11.2	-11.1
	Lee County		-1.4	-5.4	-12.6	-11.7	-14.9	-15.7
	Coosa County		-1.3	-9.1	-15.7	-14.2	-19.1	-19.8
Calculated with scour	Chambers County	0					-4.5	-4.7
		6					-8.7	-8.8
		16					-11.4	-11.6
		23					-14.8	-12.9
	Lee County	0					-7.5	-8.0
		6					-17.8	-18.1
		16					-19.6	-20.1
		23					-20.6	-21.2
	Coosa County	0					-7.9	-8.4
		6					-11.7	-12.9
		16					-15.0	-15.8
		23					-14.9	-15.7
Calculated with scour (locked tabs)	Chambers County	0					-2.1	-2.4
		6					-4.4	-4.6
		16					-37.9	-39.3
		23					-32.1	-31.7
	Lee County	0					-4.0	-5.4
		6					-14.1	-13.5
		16					-16.8	-16.0
		23					-23.3	-23.1
	Coosa County	0					-3.7	-3.6
		6					-13.1	-13.2
		16					-25.0	-24.8
		23					-37.7	-37.5

Table E-1. Continue

			Steps of analysis								
			Scour								
			Propagation around the key wall								
			7	8	9	10	11	12	13	14	15
Type of measurments	Culvert location	Backfill height (ft)									
Measured on the field	Chambers County										
	Lee County										
	Coosa County										
Calculated with backfill load	Chambers County										
	Lee County										
	Coosa County										
Calculated with scour	Chambers County	0	-5.0	-5.4	-5.9	-7.0	-6.9	-7.0	-6.9	-6.6	-6.2
		6	-9.0	-9.3	-9.6	-10.3	-9.5	-9.7	-9.5	-9.2	-8.9
		16	-12.0	-12.5	-13.2	-14.3	-13.8	-14.4	-14.3	-13.9	-13.3
		23	-13.0	-13.3	-13.7	-14.6	-13.6	-13.9	-13.7	-13.5	-14.1
	Lee County	0	-8.9	-10.3	-10.9			-11.1	-10.9	-10.0	-9.0
		6	-19.3	-22.5	-22.7			-23.0	-23.0	-22.1	-20.7
		16	-20.9	-22.1	-23.2			-24.3	-24.4	-23.9	-23.3
		23	-22.5	-24.8	-31.6			-31.6	-31.5	-30.8	-30.0
	Coosa County	0	-9.5	-10.7	-12.0	-13.4	-14.9	-14.4	-14.7	-14.4	-12.4
		6	-14.4	-16.2	-18.0	-19.8	-19.9	-20.2	-19.6	-17.1	-13.9
		16	-17.3	-19.1	-21.0	-23.2	-25.4	-25.7	-25.9	-25.8	-23.0
		23	-17.0	-18.5	-20.4	-22.5	-25.0	-25.0	-25.3	-24.9	-22.4
Calculated with scour (locked tabs)	Chambers County	0	-2.8	-3.2	-3.4	-3.6	-5.6	-6.7	-7.5	-8.9	-11.3
		6	-4.9	-5.3	-5.6	-5.9	-6.5	-6.6	-6.6	-6.6	-6.6
		16	-40.7	-42.0	-42.5	-39.9	-59.0	-56.1	-58.9	-61.8	-65.0
		23	-30.8	-30.5	-30.0	-28.6	-44.0	-43.8	-41.2	-40.4	-41.6
	Lee County	0	-4.0	-4.2	-5.1			-6.5	-7.7	-8.3	-10.9
		6	-12.8	-12.2	-10.0			-9.8	-9.7	-9.5	-10.0
		16	-15.4	-14.8	-12.7			-12.7	-12.8	-12.7	-12.4
		23	-22.8	-22.6	-22.9			-21.8	-21.7	-21.6	-20.1
	Coosa County	0	-3.4	-3.4	-3.3	-4.0	-4.9	-4.7	-4.8	-4.8	-4.8
		6	-13.1	-12.9	-12.5	-12.0	-15.7	-14.4	-13.8	-13.8	-14.2
		16	-24.5	-24.1	-23.6	-23.0	-22.4	-24.4	-24.3	-23.8	-24.0
		23	-36.5	-36.3	-36.1	-35.8	-35.4	-37.1	-35.7	-36.4	-36.9

Table E-1. Continue

			Steps of analysis				
			Scour				
			propagation under the footing				
			16	17	18	19	20
Type of measurments	Culvert location	Backfill height (ft)					
Measured on the field	Chambers County						
	Lee County						
	Coosa County						
Calculated with backfill load	Chambers County						
	Lee County						
	Coosa County						
Calculated with scour	Chambers County	0	-5.4	-5.8	-12.9	-28.4	-44.3
		6	-8.3	-8.0	-9.0	-18.1	-27.7
		16	-12.4	-12.0	-9.8	-15.0	-23.3
		23	-15.0	-15.3	-16.8	-20.1	-26.3
	Lee County	0	-6.3	-9.2	-18.6	-25.6	-30.8
		6	-17.1	-12.0	-10.7	-12.6	-18.0
		16	-22.3	-22.0	-18.8	-13.6	-16.2
		23	-28.2	-25.0	-20.6	-16.5	-12.8
	Coosa County	0	-9.9	-7.7	-6.2	-8.2	-11.2
		6	-12.0	-9.6	-8.4	-8.8	-11.2
		16	-19.3	-16.2	-12.0	-10.3	-8.8
		23	-19.0	-16.4	-12.7	-10.8	-9.1
Calculated with scour (locked tabs)	Chambers County	0	-14.9	-17.7	-29.3	-75.4	-154.6
		6	-8.7	-7.6	-21.4	-53.1	-90.3
		16	-69.4	-69.7	-85.2	-99.2	-95.4
		23	-44.1	-45.2	-57.1	-68.8	-115.0
	Lee County	0	-33.3	-64.8	-96.6	-106.1	-92.8
		6	-15.7	-27.3	-54.5	-58.5	-63.6
		16	-12.2	-21.6	-38.2	-41.7	-52.7
		23	-15.9	-33.9	-53.0	-63.5	-71.1
	Coosa County	0	-7.9	-12.2	-16.8	-30.0	-37.8
		6	-13.2	-20.8	-30.8	-40.4	-12.6
		16	-25.5	-25.9	-27.2	-39.5	-38.8
		23	-37.2	-37.4	-39.9	-49.5	-56.3